

## REPORT DOCUMENTATION PAGE

AFRL-SR-BL-TR-02-

Public reporting burden for this collection of information is estimated to average 1 hour per response, including the time for reviewing this collection of information. Send comments regarding this burden estimate or any aspect of this collection of information, including suggestions for reducing this burden to Washington Headquarters Services, Directorate for Information Operations and Reports, 1215 Jefferson Davis Highway, Suite 1204, Arlington, VA 22202-4302, and to the Office of Management and Budget, Paperwork Reduction Project (0704-0188), Washington, DC 20503

and maintaining  
registrations for  
the Office of

0121

|   |   |  |                            |  |  |
|---|---|--|----------------------------|--|--|
| 1. AGENCY USE ONLY (Leave blank)  |   | 2. REPORT DATE 15 Mar '02                  |                            | 3. REPORT TYPE AND DATES COVERED   |  |
| 4. TITLE AND SUBTITLE<br>COMPUTATIONAL FILM COOLING METHODS FOR GAS TURBINE AIRFOILS  |   |  |                            | 5. FUNDING NUMBERS<br>F49620-98-1-0479   |  |
| 6. AUTHOR(S)<br>PI: Prof. James H. Leylek<br>Graduate Students: D. Keith Walters, William D. York, D. Scott Holloway, Jeffrey D. Ferguson, E. Lee McGrath, and Catish Undapalli   |   |  |                            |  |  |
| 7. PERFORMING ORGANIZATION NAME(S) AND ADDRESS(ES)<br>Clemson University<br>Department of Mechanical Engineering<br>College of Engineering and Science<br>102 Fluor-Daniel EIB<br>Clemson, SC 29634-0921  |   |  |                            | 8. PERFORMING ORGANIZATION<br>REPORT NUMBER<br>AFOSR/PKC<br>801 North Randolph Street, Room 732<br>Arlington, VA 22203-1977  |  |
| 9. SPONSORING / MONITORING AGENCY NAME(S) AND ADDRESS(ES)<br>Dr. Len Sakell<br>Program Manager<br><br>Ms. Wendy M. Veon,<br>Administrative Contracting Officer  |   |  |                            | 10. SPONSORING / MONITORING<br>AGENCY REPORT NUMBER  |  |
| 11. SUPPLEMENTARY NOTES   |   |  |                            |  |  |
| 12a. DISTRIBUTION / AVAILABILITY STATEMENT<br>Approved for public release,<br>Distribution Unlimited  |   |  |                            | 12b. DISTRIBUTION CODE<br>AIR FORCE OFFICE OF SCIENTIFIC RESEARCH (AFOSR)<br>NOTICE OF TRANSMITTAL DTIC. THIS TECHNICAL REPORT<br>HAS BEEN REVIEWED AND IS APPROVED FOR PUBLIC RELEASE<br>LAW AFR 190-12. DISTRIBUTION IS UNLIMITED. |  |
| 13. ABSTRACT (Maximum 200 Words)<br>A previously documented CFD methodology is further generalized and applied to realistic turbine airfoil film cooling test cases. First, a series of fundamental test cases are examined in order to document the ability of the robust and practical CFD methodology to deal with the effects of the individually isolated key physics mechanisms on film cooling. These include: (1) favorable and adverse pressure gradients; (2) convex curvature; (3) horseshoe vortex; (4) profile losses with and without coolant jets; (5) laminar-to-turbulent boundary layer transition; and (6) discontinuities. Second, in addition to the fundamental flow test cases, two turbine airfoil cascade, one low subsonic and another transonic, configurations were modeled. The subsonic cascade case was designed to study the aerodynamics losses with and without film cooling jets, as well as, the adiabatic effectiveness for a range of parameters. The transonic turbine cascade represents a truly modern design at realistic engine conditions. A total of 18 test configurations, corresponding to compound-round, axial-shaped, and compound-shaped film holes, are simulated in order to document in detail the current state of the readily available robust and practical CFD technology for use by the gas turbine design community. |   |  |                            |  |  |
| 14. SUBJECT TERMS   |   |  |                            | 15. NUMBER OF PAGES<br>175   |  |
|   |   |  |                            | 16. PRICE CODE   |  |
| 17. SECURITY CLASSIFICATION<br>OF REPORT  | 18. SECURITY CLASSIFICATION<br>OF THIS PAGE | 19. SECURITY CLASSIFICATION<br>OF ABSTRACT | 20. LIMITATION OF ABSTRACT |  |  |

20020402 088

# **Computational Film Cooling Methods for Gas Turbine Airfoils**

## **Final Report**

March 1, 1998 – March 1, 2001

Contract Number: F49620-98-1-0479

Dr. Len Skelly, Program Manager  
AFOSR/PKC  
801 North Randolph Street, Room 732  
Arlington, VA 22203-1977

Principal Investigator: Prof. James H. Leylek

Graduate Students: D. Keith Walters, William D. York, Jeffrey D.  
Ferguson, E. Lee McGrath, Satish Undapalli,  
and D. Scott Holloway

Advanced Computational Research Laboratory  
Department of Mechanical Engineering  
College of Engineering and Science  
CLEMSON UNIVERSITY  
Clemson, SC 29634-0921

March 15, 2002

## TABLE OF CONTENTS

|   |    |
|---|----|
| <b>Chapter 1. Numerical Study on the Effects of Mainstream Pressure Gradient Effects on Film Cooling</b> .....                                    | 1  |
| Nomenclature.....   | 1  |
| Introduction.....   | 2  |
| Literature Review .....   | 2  |
| Simulation Details .....  | 4  |
| Results and Discussion .....  | 7  |
| Conclusions.....  | 10 |
| References.....   | 11 |
| <br><b>Chapter 2. Numerical Study on the Effects of Convex Curvature on Film Cooling</b> .....  | 22 |
| Nomenclature.....   | 22 |
| Introduction.....   | 22 |
| Literature Review .....   | 23 |
| Experimental Test Case .....  | 26 |
| Simulation Details .....  | 27 |
| Results and Discussion .....  | 30 |
| Conclusions.....  | 37 |
| References.....   | 38 |
| <br><b>Chapter 3. Computational Study of Film-Cooling Effectiveness on a Low-Speed Airfoil Cascade – Part I: Methodology and Validation</b> ..... | 57 |
| Nomenclature.....   | 57 |
| Introduction.....   | 58 |
| Literature Review .....   | 58 |
| Experimental Test Case .....  | 60 |
| Simulation Details .....  | 61 |
| Results and Discussion .....  | 64 |
| Conclusions.....  | 65 |
| References.....   | 66 |
| <br><b>Chapter 4. Computational Study of Film-Cooling Effectiveness on a Low-Speed Airfoil Cascade – Part II: Discussion of Physics</b> .....     | 76 |
| Nomenclature.....   | 76 |
| Introduction.....   | 77 |
| Test Case.....  | 77 |
| Simulation Details .....  | 78 |
| Results and Discussion .....  | 79 |
| Conclusions.....  | 85 |
| References.....   | 85 |

|  |     |
|--|-----|
| <b>Chapter 5. Film Cooling on a Modern HP Turbine Blade -- Part I:</b>             |     |
| <b>Methodology and Validation</b> .....  | 97  |
| Nomenclature.....  | 97  |
| Introduction.....  | 98  |
| Literature Review .....  | 98  |
| Present Contributions.....   | 100 |
| Experimental Methodology .....   | 100 |
| Computational Methodology .....  | 104 |
| Results.....   | 107 |
| Conclusions.....   | 109 |
| References.....  | 110 |
| <br><b>Chapter 6. Film Cooling on a Modern HP Turbine Blade -- Part II:</b>        |     |
| <b>Compound-Angle Round Holes</b> .....  | 123 |
| Nomenclature.....  | 123 |
| Introduction.....  | 124 |
| Present Contributions.....   | 124 |
| Simulation Details .....   | 125 |
| Results and Discussion .....   | 126 |
| Conclusions.....   | 130 |
| References.....  | 131 |
| <br><b>Chapter 7. Film Cooling on a Modern HP Turbine Blade -- Part III: Axial</b> |     |
| <b>Shaped Holes</b> .....  | 138 |
| Nomenclature.....  | 138 |
| Introduction.....  | 139 |
| Present Contributions.....   | 139 |
| Simulation Details .....   | 140 |
| Results and Discussion .....   | 141 |
| Conclusions.....   | 146 |
| References.....  | 147 |
| <br><b>Chapter 8. Film Cooling on a Modern HP Turbine Blade -- Part IV:</b>        |     |
| <b>Compound-Angle Shaped Holes</b> .....   | 157 |
| Nomenclature.....  | 157 |
| Introduction.....  | 158 |
| Objectives .....   | 158 |
| Computational Details .....  | 158 |
| Results.....   | 159 |
| Conclusions.....   | 163 |
| References.....  | 164 |



## CHAPTER 1

### NUMERICAL STUDY ON THE EFFECTS OF MAINSTREAM PRESSURE GRADIENTS ON FILM COOLING

William D. York and James H. Leylek

#### NOMENCLATURE

|              |   |
|--------------|---|
| D            | film-cooling hole diameter = 11.1 mm  |
| $dp/dx$      | simulation with mainstream pressure gradients   |
| DR           | coolant-to-mainstream density ratio = $\rho_j/\rho_\infty$                                    |
| I            | coolant-to-mainstream momentum flux ratio = $\rho_j U_j^2 / \rho_\infty U_\infty^2$           |
| k            | turbulent kinetic energy [ $m^2/s^2$ ]  |
| K            | nondimensional acceleration parameter = $(v_e/U_e^2) \cdot dU_e/dx$                           |
| L            | film-cooling hole length  |
| M            | coolant to mainstream mass flux ratio = $\rho_j U_j / \rho_\infty U_\infty$                   |
| $Re_D$       | Reynolds number based on film hole diameter   |
| REF          | zero-pressure gradient reference case   |
| RKE          | Realizable k- $\epsilon$ turbulence model   |
| S            | Film-cooling hole lateral spacing   |
| T            | static temperature [K]  |
| TL           | turbulence level (%) based on $U_e$ at injection<br>$= (100 \cdot (2/3 \cdot k)^{0.5}) / U_e$ |
| U            | x-velocity [m/s]  |
| x            | streamwise coordinate originating at trailing edge of holes [m]                               |
| y            | coordinate normal to test surface [m]   |
| $y^+$        | nondimensional distance from wall   |
| z            | spanwise coordinate originating at hole centerline  |
| $\alpha$     | injection angle with respect to film-cooled surface   |
| $\delta$     | boundary layer thickness at injection [m]   |
| $\epsilon$   | dissipation rate of turbulent kinetic energy [ $m^2/s^3$ ]                                    |
| $\eta$       | adiabatic effectiveness = $(T_{aw} - T_\infty) / (T_j - T_\infty)$                            |
| $\bar{\eta}$ | laterally averaged adiabatic effectiveness  |
| $\nu$        | kinematic viscosity [ $m^2/s$ ]   |
| $\rho$       | density [ $kg/m^3$ ]  |

#### Subscripts

|          |  |
|----------|--|
| $\infty$ | mainstream conditions at crossflow inlet plane |
| aw       | adiabatic wall                                 |
| e        | condition at boundary layer edge               |
| j        | coolant jet conditions                         |

## INTRODUCTION

Film cooling is commonly used in modern gas turbine engines to protect hot section components from the elevated temperature of combustion gases. As designers pursue greater efficiency, turbine inlet temperatures rise and coolant flow rates decrease, and a thorough understanding of film-cooling physics has become crucial to making further advances in cooling technology. The current empirical design methodology is proving to be too costly and time consuming in the highly competitive market, and there is a great need for a predictive, physics-based design tool. Computational fluid dynamics (CFD) has the potential to deliver detailed results to film-cooling problems quickly and economically.

Recent studies have demonstrated the predictive capability of CFD for flat-plate film cooling problems. As knowledge and computational resources advance, attention has generally turned to more complex problems involving full turbine airfoil geometries, multiple rows of cooling holes, and innovative cooling designs. However, before this type of problem can be fully analyzed, there is a need to singularly examine the fundamental parameters involved in turbine airfoil film cooling, including pressure gradients, surface curvature, freestream turbulence, and approach boundary layer characteristics. The present study isolates and analyzes the effects of mainstream pressure gradients in discrete-jet film cooling by employing a well-tested, reliable computational methodology to model a flat-plate experimental study. The bottom-line adiabatic effectiveness results are given in the context of extensive field data that highlights the physical mechanisms involved, and the performance of the computational methodology is discussed. Lastly, future directions in this area of computational research are suggested based on lessons learned.

## LITERATURE REVIEW

### Experimental Studies

There have been relatively few published studies of flat-plate film cooling in the presence of a mainstream pressure gradient, and there is some discrepancy as to the effects of mainstream acceleration on film-cooling effectiveness. Launder and York (1974) found for several rows of streamwise-injected ( $\alpha=45^\circ$ ) coolant jets that a constant acceleration parameter of  $K=2 \times 10^{-6}$  improved effectiveness by 30 percent for a range of blowing ratios at a station 8 diameters downstream of injection. They attributed the results to the suppression of mainstream turbulence by the strong favorable pressure gradient. It was also discovered that the favorable pressure gradient reduced the lateral spread of the coolant.

Several studies have been made of pressure gradient effects on film cooling from a single row of holes. Jabbari and Goldstein (1978) observed a slight increase in centerline effectiveness with increasing strength of the mainstream acceleration for  $K \leq 1.0 \times 10^{-6}$ . At higher values of  $K$ , a small decrease in  $\eta$  was seen. The coolant delivery tubes had an injection angle of  $35^\circ$ , a lateral spacing of  $3D$ , and a very large length-to-diameter ratio. In this study, the mainstream boundary layer thickness at injection varied

with  $K$ , and much of the results were attributed to this fact and not to the effect of mainstream acceleration on the coolant jet as it traveled downstream. Kruse (1985) found for a single row of  $\alpha=45^\circ$  and  $S/D=1.5$  a small advantage in laterally averaged effectiveness for an adverse pressure gradient as compared to a favorable gradient, but only at low mass flux ratios. The study concluded that the adverse gradient increased the tendency of the coolant to separate from the wall immediately downstream of injection, reducing effectiveness in this region, but increased the effectiveness further downstream. This was attributed to a greater jet penetration and thicker coolant layer caused by the adverse pressure gradient.

The work of Teekaram, Forth, and Jones (1991) indicated an increase of up to 20 percent in the laterally averaged isothermal effectiveness in a strong favorable pressure gradient, which varied from  $K=2.26 \times 10^{-6}$  at injection to  $K=0.6 \times 10^{-6}$  at  $x/D=30$ , over the zero gradient case at high blowing ratios. This was again attributed to the decreased tendency for coolant jet detachment in a favorable pressure gradient environment. A small decrease in effectiveness over the zero gradient case was found for a mild adverse pressure gradient ( $K=-0.22 \times 10^{-6}$ ). A row of  $30^\circ$  inclined holes of spacing  $3D$  and  $DR=1.2$  and  $0.8$  were used in the study. No consistent variation of the film-cooling effectiveness was observed far downstream of injection.

A recent study by Schmidt and Bogard (1995) modeled the suction surface of a typical turbine airfoil, with a favorable pressure gradient region of  $K=1.5 \times 10^{-6}$  at injection, transitioning to an adverse pressure gradient region with  $K=-0.5 \times 10^{-6}$  at  $50D$  downstream. A single row of holes of spacing  $3D$ , length-to-diameter ratio of  $4$ ,  $\alpha=35^\circ$ , and a density ratio of  $1.6$  was fairly representative of gas turbine conditions. The study found that the pressure gradient caused a greater streamwise decay rate of the laterally averaged effectiveness due to increased diffusion of the coolant jet with downstream distance. They attributed this phenomenon to a greater acceleration of the lower density mainstream than the coolant by the pressure gradient, thereby increasing the shear and turbulence between the mainstream and the jet. Additionally, with the pressure gradient imposed, a wider spread of the coolant jet very near the hole was observed, improving the lateral effectiveness in this region. The authors could not conclude on the physical mechanisms behind this occurrence from the available data.

## Computational Studies

To this date, no computational studies of film cooling in the presence of mainstream pressure gradients exist in the open literature. However, CFD has been employed for general film-cooling investigations, including the effects of curvature, film-hole exit-plane profiles, and vortex formation and mixing by Berhe and Patankar (1998), Garg and Gaugler (1997), and Vogel (1998), respectively. A comprehensive computational methodology for flat-plate film-cooling simulations is presented in Walters and Leylek (1997).

## Outstanding Issues

The survey of existing literature reveals several outstanding issues. Because of the conflicting results in the experimental studies, there is a need to further study the

effect of favorable and adverse pressure gradients on film cooling physics, and to describe the mechanisms behind the experimental results obtained. CFD has the potential to clearly show the effects of pressure gradients by allowing a thorough description of the physics involved. Additionally, there is need for a fundamental computational study of pressure gradient effects on film cooling to serve as a validation for future simulations. The present study addresses all of these issues.

## **SIMULATION DETAILS**

The methodology used in the present study is fully outlined in Walters and Leylek (1997), which describes the four critical issues in effective computational modeling of the three-dimensional film cooling flowfield: (1) proper computational modeling of flow physics; (2) exact geometry and high-quality grid generation; (3) use of a higher-order discretization scheme; and (4) effective turbulence modeling. This section outlines the best-practice techniques that are implemented at each step.

### **Computational Model and Boundary Conditions**

The present computational simulations are modeled after the experimental study of Schmidt and Bogard (1995), which was chosen for realistic parameters and the ability for computational replication. Following the model of Leylek and Zerkle (1994), the plenum, film-hole, and crossflow regions for each case were included in the computational domain. The experimental study employed a single row of holes with a lateral spacing of  $3D$ ,  $L/D=4$ , and  $\alpha=35^\circ$ . To reduce grid size and computation time, the computational domain encompasses one-half of the pitch and uses symmetry planes to model a row of holes of  $D=11.1$  mm. The coordinate origin in all cases is located at the trailing (downstream) edge of the film hole. The test surface began 23.1 diameters upstream of the hole ( $x/D=-23.1$ ), where boundary layer suction and a sharp test plate leading edge resulted in new boundary layer growth, and it extended to  $x/D=50$  in the downstream direction. Plenum dimensions were 101.6 mm in the  $x$ -direction and 50.8 mm in the  $y$ -direction, with the film hole entrance centered in the upper plenum wall. The computational geometry was created with GAMBIT, a pre-processing package from Fluent, Inc. The lower boundary of the plenum was a uniform-velocity inlet, and the entire plenum was set as a laminar flow zone to eliminate unrealistic turbulence generation. The density ratio of 1.6 was achieved by setting the crossflow inlet temperature at 300 K and the coolant at 187.5 K.

### **Pressure Gradient Cases**

The pressure gradient was established by contouring the wall opposite the film-cooled surface. The resulting mainstream acceleration is typical of the suction surface of a high-pressure turbine airfoil, with a strong favorable pressure gradient ( $K=1.5 \times 10^{-6}$  at  $x/D=0$ ) transitioning to a mild adverse gradient beyond  $x/D=30$ . Several steps were taken to reproduce the pressure gradient in the present study. First, point coordinates were taken from a digitized scale plot of the contoured wall given in Ellis et al (1991), and a

spline, shown in Figure 1, was created through these points in the computational model. In the experiments, the contoured upper wall began upstream of the test plate leading edge, and no inlet velocity profile was provided in the literature. A two-dimensional (2-d) test simulation with no film cooling was created to determine this profile and also to verify the  $K$  distribution. The test case domain was a vertical slice of the entire experimental test section from  $40D$  upstream of the test plate to the downstream edge of the test surface. A boundary layer bleed with a pressure outlet condition was located at the test-plate leading edge. The 2-d grid, employing the two-layer model, was approximately 80,000 cells at grid independence. The solution was iterated by adjusting the boundary layer bleed pressure and the inlet velocity until streamlines at the test plate leading edge were completely flat and  $U_e$  was 19 m/s at  $x/D=0$  to match the experiment. The distribution of the acceleration parameter over the flat plate is given in Figure 2, showing excellent agreement with the experimentally measured profile. A plot of streamwise  $U_e$  in Figure 3 is further proof of accuracy in matching the experimental pressure gradient.

In order to reduce the grid size, the three-dimensional (3-d) computational domain, shown in Figure 4, extended from  $x/D=-10$  (velocity inlet condition) to  $x/D=52$  (convection outlet condition), and it incorporated the validated contoured upper wall directly from the 2-d test case. The inlet  $x$ - and  $y$ - velocity profiles were taken from the test case at  $x/D=-10$  and employed as the velocity inlet condition in the 3-d simulations. The crossflow had a turbulence level of 0.2%. Mass flux ratios simulated were  $M=0.6$ , 1.0, and 1.5, corresponding to respective momentum flux ratios of  $I=0.23$ , 0.63, and 1.41.

#### Zero-Pressure Gradient Reference Cases

To provide a valid comparison of computational results for film cooling in the presence of a mainstream pressure gradient, a reference case (REF) with zero mainstream acceleration was simulated with parameters identical to the pressure gradient cases. A symmetry plane was located parallel to the film-cooled surface at a distance of  $y/D=17$  to replace the contoured upper boundary. It should be noted that for the REF cases of the experimental study, the coolant flow rate was held constant while varying the freestream velocity to produce desired mass flux ratios. Thus for the same mass flux ratios,  $Re_D$  and  $\delta$  in the experimental REF cases were different from that of the experimental pressure gradient cases, and a comparison must be interpreted accordingly. To eliminate these variables from the present analysis, the REF cases of this numerical study employed a turbulent velocity profile at the crossflow inlet that would result in the same  $U_e$  (19 m/s) and  $\delta/D$  (0.62) at  $x/D=0$ . As in the pressure gradient cases, the coolant flow rate was varied to give the same mass flux ratios.

#### **Numerical Grid**

The computational grid was also created using the GAMBIT from Fluent, Inc, and the background grid consisted of 1.0 million finite-volumes. The multi-topology grid was built with a multi-block technique to maximize cell quality throughout the domain. A combination of hexahedra and tetrahedra cell blocks were employed, and cells were concentrated in the area of the film-hole breakout in order to capture the complex flow

physics of the jet-crossflow interaction. The mesh on the centerline plane through the film hole is shown in Figure 5.

### **Solution Details**

In order to solve the time-averaged, steady Navier-Stokes equations, the multi-topology, unstructured/adaptive, pressure-correction code Fluent 5 from Fluent, Inc. with a multi-grid convergence accelerator was employed. The two-layer near-wall treatment was used to resolve the viscous sublayers, and a maximum  $y^+$  of 1.0 was targeted for the first grid point adjacent to all walls. A realizable  $k$ - $\epsilon$  (RKE) turbulence model, available in Fluent 5 and documented in Shih et al. (1995), was employed to eliminate the unrealistic turbulence generation of the  $k$ - $\epsilon$  model in regions of large irrotational strain. The RKE model was found through in house film cooling simulations to yield economical results that were far superior to the standard  $k$ - $\epsilon$  model. Additional details on the performance of the RKE model for turbomachinery applications are provided by Walters and Leylek (2000).

Convergence was declared when the following conditions were met: (i) global mass and energy imbalances dropped below 0.01%; (ii) the residuals of all governing equations, normalized by their relevant inlet fluxes, fell below 0.1%; (iii) profiles of the dependent variables, monitored in critical areas of the flowfield, were unchanged with additional iterations; and (iv) the surface effectiveness distribution was shown to not change with further iterations. After obtaining a solution with the background grid, the grid was refined in areas of large gradients of flowfield variables, specifically velocity,  $P$ ,  $T$ ,  $k$ , and  $\epsilon$ . Additionally, the small percentage of the cells along the walls that did not meet the target  $y^+$  were refined to bring this measure to an acceptable level. The hanging node adaption technique was used in order to preserve the quality of the background grid. A new converged solution was obtained with the refined grid, and this process was repeated until there were no observable changes in the field and surface results with further refinements. All cases in the present study required only one refinement to reach grid independence. The final grid contained 1.3 million cells.

The simulations were run on a Sun Ultra Enterprise 4000 computer with 10 processors and 5 GB of RAM. For the initial grid, each iteration took approximately 30 seconds, and 1000 to 1200 iterations were typically required to reach convergence. Results were post-processed on a Sun Ultra 10 workstation with 1 GB of RAM and the Creator 3-d Graphics system.

## RESULTS AND DISCUSSION

In this section, the flowfield physics and the surface results relevant to the effects of mainstream pressure gradients are discussed.

### Flowfield Results

Mainstream acceleration was found to have no effect on flow within the film hole, and therefore this portion of the flowfield will not be discussed. The physics followed those documented by Walters and Leylek (1997) in a cylindrical film hole.

The strong favorable pressure gradient near injection was seen to have little effect on the jet exit condition, notably its initial trajectory and penetration into the crossflow boundary layer. This is expected because the boundary layer thickness and  $U_e$  are the same for the  $dp/dx$  and REF simulations. However, the favorable pressure gradient rapidly bends the coolant jet over. Thus, several diameters downstream, the shear layers above the jet are closer to the wall than in the REF case, as illustrated in Figure 6 by the contours of turbulence level on the centerline plane for  $M=1.0$ . By  $x/D=15$ , the height of this shear layer above the wall remains approximately constant in the  $dp/dx$  case, while it continues to increase slightly in the REF case. It may be noted that the turbulence levels are remarkably similar between the two cases in Figure 6. This is contrary to the postulation of Schmidt and Bogard (1995) that increased shear between the jet and the mainstream in the favorable pressure gradient caused jet degradation. The present results indicate that in the  $dp/dx$  case the coolant jet accelerates at approximately the same rate as the crossflow. Therefore, the velocity gradients above the coolant jet in the crossflow ( $y-z$ ) planes remain similar to the REF case, as seen in Figure 7 for  $M=1.0$  at  $x/D=15$ . Consequently, there is negligible shear-induced turbulence to influence the effectiveness in the favorable pressure gradient.

The effect of the favorable pressure gradient is to reduce the boundary layer thickness. When coolant is contained in the boundary layer, it is forced downwards toward the wall. It would be expected that reducing the vertical thickness of the coolant jet would cause greater lateral spreading over the surface, yet this is not the case. The counterrotating "kidney" vortices, which are a result of vorticity in the film hole, play a major role in jet diffusion as they are convected downstream. As the jet core is strongly accelerated, the vortex pair are "stretched" in the streamwise direction, causing them to become smaller. Consequently, the vortex strength increases due to momentum conservation in this plane. This effect is easily seen when velocity vectors are displayed on crossflow planes, as done in Figure 8 for the case of  $M=0.6$  at downstream stations of  $x/D=5, 10$ , and  $15$ . At five diameters downstream there is already a large reduction in the size of the vortex for the  $dp/dx$  case. The fluid above the jet core is observed to move toward the wall due to the thinning boundary layer, forcing the coolant toward the wall, and slightly "flattening" the vortex pair. In contrast, the velocity vectors above the jet in the REF case are observed to point upward due to the momentum of the unconstrained secondary flow. Because of their greater strength, the vortex pair in a favorable pressure gradient has greater resistance to being damped out. At  $x/D=15$ , it is observed to be fairly well defined, while there are only remnants of the secondary flow existing for the REF case.

The physical mechanisms described above have a large effect on the downstream temperature distribution. Figure 9 provides a comparison of temperature contours for  $M=0.6$ , shown on crossflow planes at  $x/D=5, 10$ , and  $20$ . The decreased coolant diffusion in the favorable pressure gradient case is very evident as the jet progresses downstream, and by  $20$  diameters downstream, a significant difference in the contours is observed. The greatest reduction in diffusion occurs in the vertical direction, and is a combination of the thinning boundary layer and the smaller, stronger vortex pair in the accelerating mainstream. The reduction in spanwise diffusion is less, and is a consequence of the latter mechanism. At all stations, the temperature near the centerline is lower for the  $dp/dx$  case, but spanwise coverage on the wall decreases.

## Surface Results

In this section, the numerically predicted centerline and laterally averaged effectiveness are compared and discussed, followed by a comparison of these results with the experiment. All experimental data are from the study of Schmidt and Bogard (1995), which claims an uncertainty of  $\pm 0.03$  for both  $\eta$  and  $\eta$ .

### Centerline Effectiveness

The centerline adiabatic effectiveness results are presented in Figure 10. For all mass flux ratios, the simulations revealed that the strong favorable pressure gradient did not change  $\eta$  in the near-field (from injection to approximately  $5$  diameters downstream), as compared to the REF cases.

For the case when  $M=0.6$ , beyond  $x/D=5$ , there is increasing streamwise improvement in  $\eta$  over the REF case, which reaches a maximum of approximately  $15\%$  at  $x/D=20$ . This is due to the reduced lateral and vertical spreading of the jet caused by the large mainstream acceleration, which results in more coolant being concentrated at the centerline and drawn towards the surface. Lateral profiles of  $\eta$  for  $M=0.6$  in Figure 11 at streamwise stations of  $x/D=3, 10$ , and  $20$  give a better illustration of this effect. At  $x/D=3$ , the spanwise distributions of  $\eta$  are identical for the  $dp/dx$  and REF simulations. By  $x/D=10$ , there is a noticeable advantage in  $\eta$  over the REF case close to the centerline, while the opposite is true towards the lateral extremes. This trend is more severe at  $x/D=20$ . Beyond  $x/D=20$ , the low value of  $K$  is insignificant to produce further improvement in  $\eta$  over the REF case, and it is observed that  $\eta$  begins to slightly approach the REF case in the mild adverse pressure gradient region, where the boundary layer thickens and coolant diffusion increases. The centerline effectiveness for  $M=1.0$  shows the same trends as the lower mass flux ratio. The advantage in  $\eta$  for the  $dp/dx$  case over REF reaches a maximum of approximately  $10\%$  at a streamwise distance of  $20D$  to  $25D$ . There is no change in the centerline effectiveness between the  $dp/dx$  and REF cases for  $M=1.5$ . Here the momentum flux ratio ( $I=1.4$ ) is large enough to produce a complete coolant jet lift-off, and hot crossflow is quickly tucked under the jet core by the strong kidney vortices. The jet core remains outside of the boundary layer, and therefore effectiveness is significantly reduced from the cases with a lower  $M$ , reaching a maximum of only  $0.2$  at  $x/D=10$ . The observed effect of the favorable pressure gradient, which is to shrink and strengthen the kidney vortices, and thereby reduce the size of the



jet core, has no effect on surface results in this case since the coolant core is not in contact with the wall. The effectiveness increases slightly with downstream distance between  $x/D=3$  and  $x/D=10$  as coolant diffuses toward the wall.

### Laterally Averaged Effectiveness

To determine the laterally averaged effectiveness, a simple trapezoidal integration of the lateral distribution of  $\eta$  was divided by the hole spacing. To match the experiments, lateral stations used in this procedure were  $z/D=-1.5, -1, -0.5, 0, 0.5, 1$ , and  $1.5$ . Results are shown for all three mass flux ratios in Figure 12.

Unlike the centerline effectiveness, the laterally averaged effectiveness results are lower downstream for the  $dp/dx$  case than the REF case, although this effect is small. As in the results for centerline effectiveness, there is no observable difference in the near-field laterally averaged effectiveness for the predicted  $dp/dx$  and REF cases, which follows the observation that the favorable pressure gradient does not affect the jet exit physics. Beyond approximately  $x/D=5$  for all mass flux ratios, there is a small advantage, increasing with streamwise distance, in  $\bar{\eta}$  for the REF cases over the  $dp/dx$  cases. The maximum advantage in  $\bar{\eta}$  in the REF cases is approximately 0.02 to 0.03 and occurs at the streamwise domain limit of  $50D$  in all cases. This occurrence is caused by the decreased lateral spreading of the coolant in the  $dp/dx$  cases. This reduced spreading is offset by the greater effectiveness around the centerline, resulting in only small drop in  $\bar{\eta}$ .

### Comparison with Experiments

The computed trends show reasonable agreement with the experimental results of Schmidt and Bogard (1995), with several key differences that are to be discussed. Examining centerline effectiveness (Figure 10), the present data compares well to experiments in the near-field for  $M=0.6$ , but agreement in this region decreases with increasing  $M$ . For the  $M=1.5$  cases (both  $dp/dx$  and REF), jet lift-off is clearly defined by a large penalty in  $\eta$  immediately after injection. The present study also revealed a very slight detachment/reattachment for  $M=1.0$ , which the thermocouple locations in the experiment could not resolve. The computationally predicted  $\eta$  is greater than the experiment beyond a streamwise distance of 5 to 10 diameters for all  $M$ . From the spanwise profiles of  $\eta$  in Figure 11, it is observed that the present study predicts a significant reduction in lateral spreading of the coolant compared to experiments, which results in the higher predicted centerline value. A likely cause of this disagreement is the inability of the steady computational solver to capture the inherently unsteady jet/mainstream interaction, which has been recognized as a major factor in film-cooling physics. Another likely factor is the use of an isotropic turbulence model. It is difficult to make comparisons between the two studies regarding the effects of the pressure gradient because the measurements are likely influenced by the varying  $\delta$  and  $Re_D$  in the experimental study.

Experimental laterally averaged effectiveness values were only given at  $x/D=3, 6, 10$ , and  $15$ , and therefore a comparison with the computed results is limited to this range. For all mass flux ratios, the computed results for laterally averaged effectiveness (Figure

12) are lower than the experimental data in this range. However the experiment showed a much greater decay rate, and by  $x/D=15$ , the trend of  $\bar{\eta}$  appears to match the simulation predictions well. Schmidt and Bogard (1995) also found a greater decay rate for  $\bar{\eta}$  in a favorable pressure gradient versus the REF case in the range of their measurements when jet detachment did not occur. This again may be an effect of the different conditions in the  $dp/dx$  and REF cases of the experimental study.

## CONCLUSIONS

A systematic computational methodology was applied to investigate film cooling in the presence of mainstream pressure gradients with realistic gas turbine parameters. Through isolation of this parameter, the effects of mainstream acceleration on flowfield physics and surface measurements were documented. Computed results were compared to results of a replicated experiment for validation purposes. Key conclusions drawn in this study are as follows:

- Mainstream acceleration has no effect on flow within the film hole or on the jet exit physics, and therefore  $\eta$  and  $\bar{\eta}$  do not vary from the zero-pressure gradient case immediately downstream of injection, within approximately 5 diameters.
- Due to a thinning boundary layer in the strong favorable pressure gradient, the coolant jet is forced towards the wall as it travels downstream, concentrating coolant near the centerline.
- As the coolant jet is accelerated by the pressure gradient, the counterrotating kidney vortex pair are stretched in the streamwise direction, reducing their size and significantly increasing their strength.
- A strong favorable pressure gradient was shown to gradually increase centerline effectiveness downstream, and the maximum advantage over the zero-pressure gradient case of 10 to 15 percent occurring near 20 diameters downstream. No change in centerline effectiveness was observed for  $M=1.5$ , when the coolant jet was detached.
- The applied pressure gradient had the effect of very slightly reducing the laterally averaged effectiveness over the zero-pressure gradient case due to decreased coolant lateral spreading.
- Recognizing the consistent trends of the numerical predictions, the present computational methodology is effective at simulating a film-cooling flowfield in the presence of mainstream pressure gradients. The major deficiency was the underprediction of lateral spreading of the coolant based on comparison with experiments. Though limited by its inability to resolve anisotropy, the realizable  $k-\epsilon$  turbulence model gave reasonable results economically, which is an important factor in the emerging trend of CFD as a design tool.

## Suggestions for Future Work

Though the present methodology performed reasonably well in general, it is evident that there are some voids that need to be filled in the area of CFD for turbine

cooling applications. The most notable discrepancy between computations and experiments in the present work was the spreading rates of the cooling jets. The predictions severely underpredict the spreading (Figure X), and this is due to two dominant issues.

First, the RKE turbulence model is based on Boussinesq's hypothesis, and is therefore isotropic in its prediction of the Reynolds stresses. The jet-in-crossflow interaction is known to cause an anisotropic turbulence field, and the variances in individual Reynolds stresses can have a large impact on the mean flow locally (such as jet spreading). A full Reynolds Stress Model (RSM) for turbulence closure would ameliorate this condition in the simulation, but this closure is very costly from a computational resources standpoint, with seven equations that must be solved versus two equations for the  $k$ - $\epsilon$  family. Additionally, the RSM results in a stiff set of equations, which are difficult to converge for a complex flow, a fact that is substantiated by in-house experience of the authors. Therefore, research needs to be conducted on advanced turbulence models that encapsulate correct physics, and which may be solved easily and efficiently for complex turbomachinery flows.

Another likely reason for the underprediction of jet spreading is the fact that the interaction of the jet with the crossflow is inherently unsteady, and the present work involves a steady model. Several experiments and flow visualizations have proven that the jets tend to exhibit unsteady fluctuations in the lateral and normal directions, and this would be expected to cause a "smearing" effect in the validation experiment, which used thermocouples to get essentially the time-averaged effectiveness values. With recent advances in computational infrastructure, unsteady simulations are rapidly becoming feasible, but there are numerous unresolved issues in this area. Thus, there is a great need for research to be conducted on methods development for unsteady simulations, such that in the near future unsteady models may be used in the design process in the gas turbine industry.

## REFERENCES

- Berhe, M. K. and Patankar, S. V., 1998, "Curvature Effects on Discrete-Hole Film Cooling," ASME Paper No. 98-GT-373.
- Ellis, S. E., Bogard, D. G., and Crawford, M. E., 1991, "Effects of a Streamwise Pressure Gradient on the Suction Surface Boundary Layer of a Turbine Airfoil," AIAA 27th Joint Propulsion Conference, Sacramento, CA, Paper No. AIAA-91-2030.
- Garg, V. K. and Gaugler, R. E., 1997, "Effect of Velocity and Temperature Distribution at the Hole Exit on Film Cooling of Turbine Blades," *ASME Journal of Turbomachinery*, Vol. 119, pp. 343-351.
- Jabbari, M. Y. and Goldstein, R. J., 1978, "Effect of Mainstream Acceleration on Adiabatic Wall Temperature and Heat Transfer Downstream of Gas Injection," *Heat Transfer 1978: Proceedings of the 6<sup>th</sup> International Heat Transfer Conference*, Vol. 5, pp. 249-254.

- Kruse, H., 1985, "Effects of Hole Geometry, Wall Curvature and Pressure Gradient on Film-Cooling Downstream of a Single Row," AGARD-CPP-390.
- Launder, B. E. and York, J., 1974, "Discrete-Hole Cooling in the Presence of Free Stream Turbulence and Strong Favourable Pressure Gradient," *International Journal of Heat and Mass Transfer*, Vol. 17, pp. 1403-1409.
- Leylek, J. H. and Zerkle, R., 1994, "Discrete-Jet Film Cooling: A Comparison of Computational Results with Experiments," *ASME Journal of Turbomachinery*, Vol. 116, pp. 358-368.
- Schmidt, D. L. and Bogard, D. G., 1995, "Pressure Gradient Effects on Film Cooling," ASME Paper No. 95-GT-18.
- Shih, T. -H., Liou, W. W., Shabbir, A., and Zhu, J., 1995, "A New k-e Eddy-Viscosity Model for High Reynold's Number Turbulent Flows: Model Development and Validation. *Computers and Fluids*, Vol. 24, No. 3, pp. 227-238.
- Teekaram, A. J. H., Forth, C. J. P., and Jones, T. V., 1991, "Film Cooling in the Presence of Mainstream Pressure Gradients," *ASME Journal of Turbomachinery*, Vol. 113, pp. 484-492.
- Vogel, D. T., 1998, "Numerical Investigation of the Influence of Specific Vortex Generation on the Mixing Process of Film Cooling Jets," ASME Paper No. 98-GT-210.
- Walters, D. K. and Leylek, J. H., 1997, "A Systematic Computational Methodology Applied to a Three-Dimensional Film-Cooling Flowfield," *ASME Journal of Turbomachinery*, Vol. 119, pp. 777-785.
- Walters, D.K. and Leylek, J.H., 2000, "Impact of Film-Cooling Jets on Turbine Aerodynamic Losses," *ASME Journal of Turbomachinery*, Vol. 122, pp. 537-545.

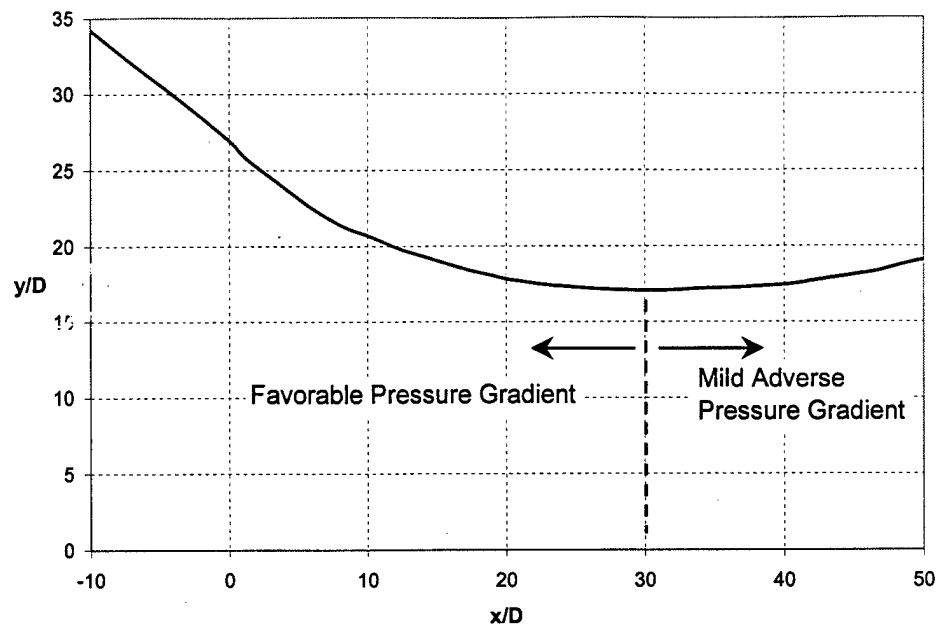


Figure 1. Contoured upper wall coordinates employed in the pressure gradient ( $dp/dx$ ) simulations.

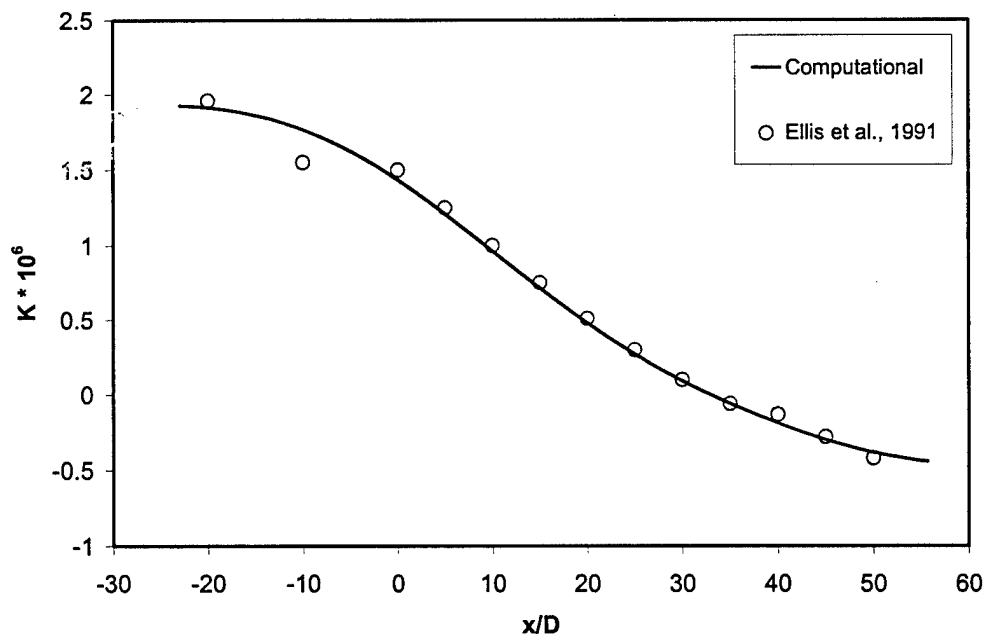


Figure 2. Streamwise acceleration parameter in 2-d simulations shows excellent agreement with experimental data.

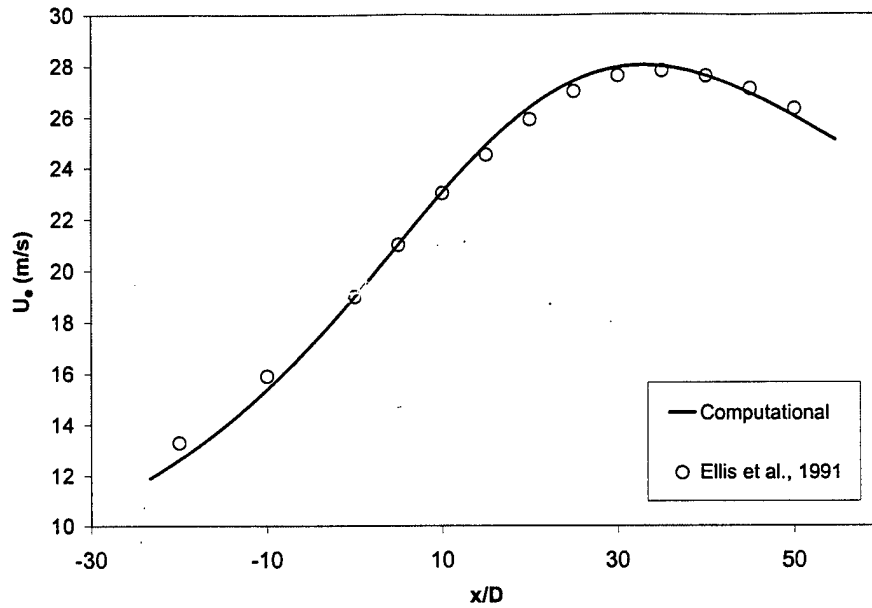


Figure 3. Streamwise velocity versus downstream distance in the 2-d simulations further validates the accuracy of the computational geometry.

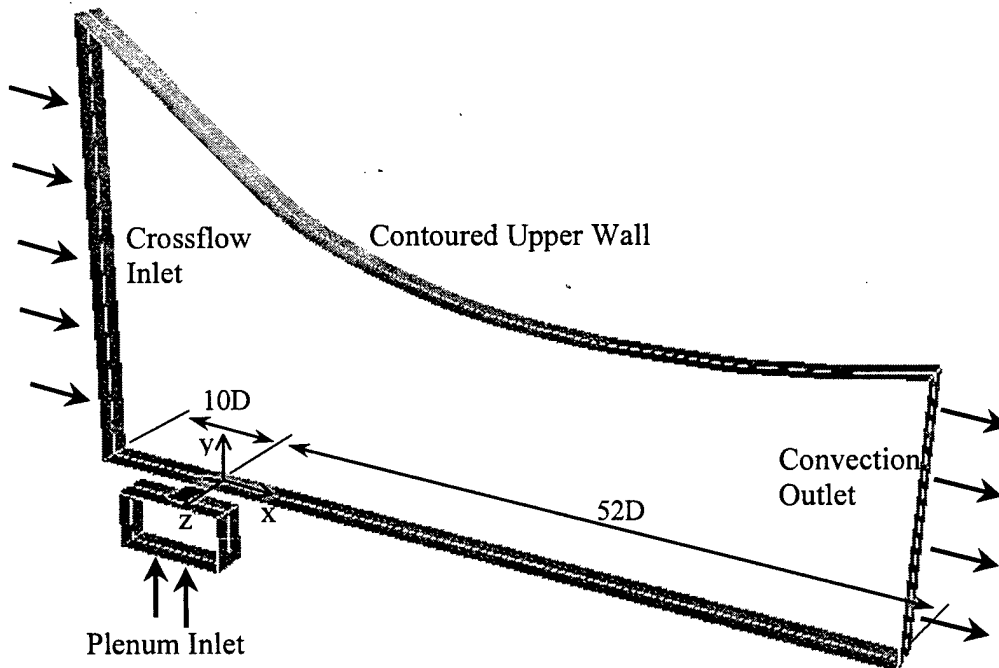


Figure 4. 3-d computational domain and boundary conditions.

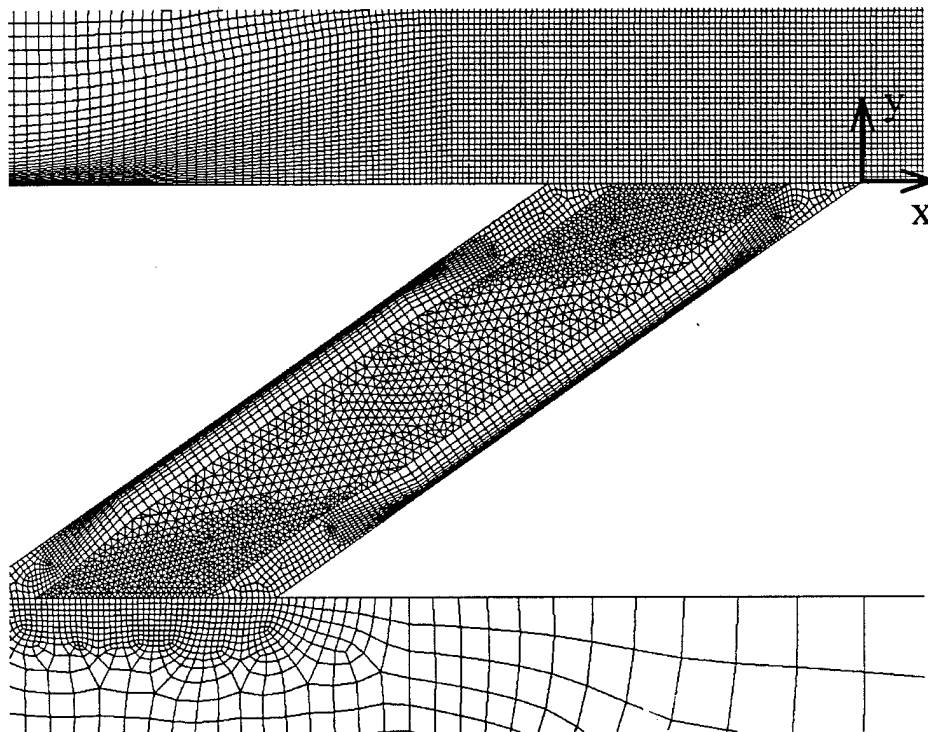


Figure 5. View of the background mesh on the film-hole centerline plane showing the very high resolution of cells in the film hole and at the breakout region.

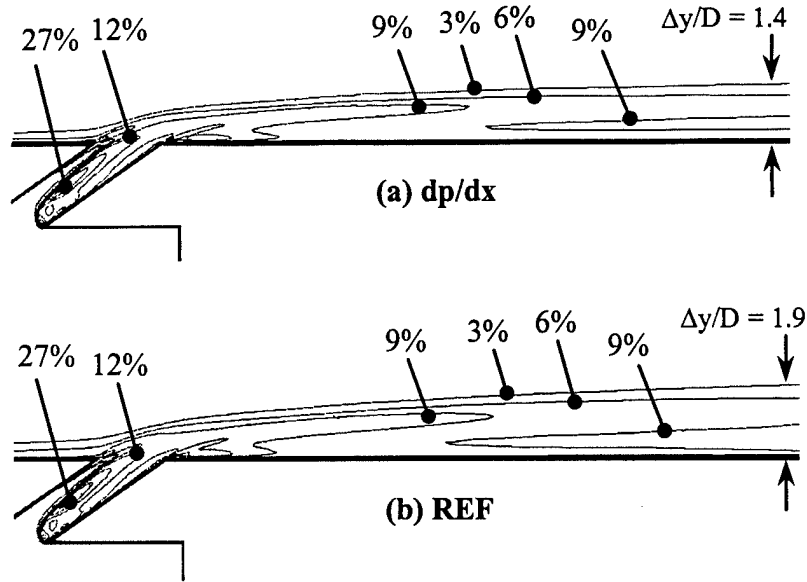


Figure 6. Contours of turbulence level (TL) for  $M=1.0$  on the jet centerline plane showing lower jet trajectory in the (a)  $dp/dx$  case versus the (b) REF case. The shear layer height at  $x/D=15$  is marked.

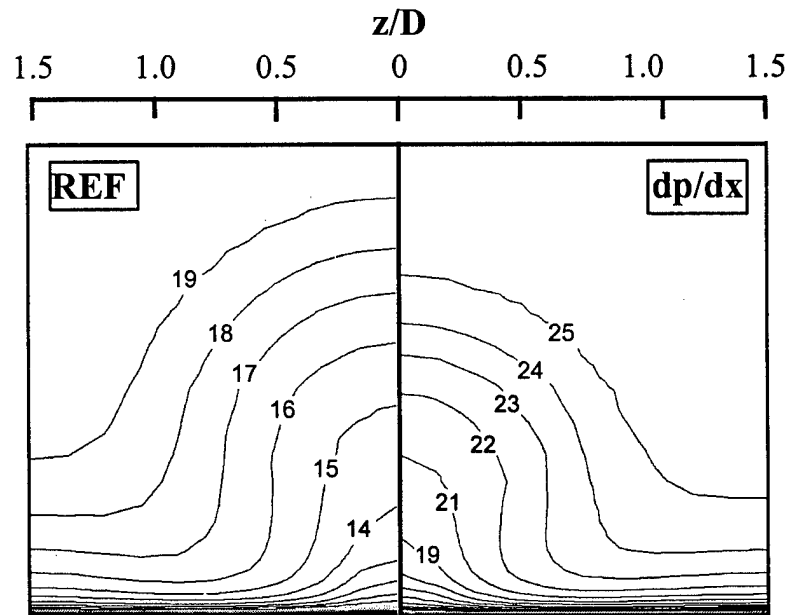
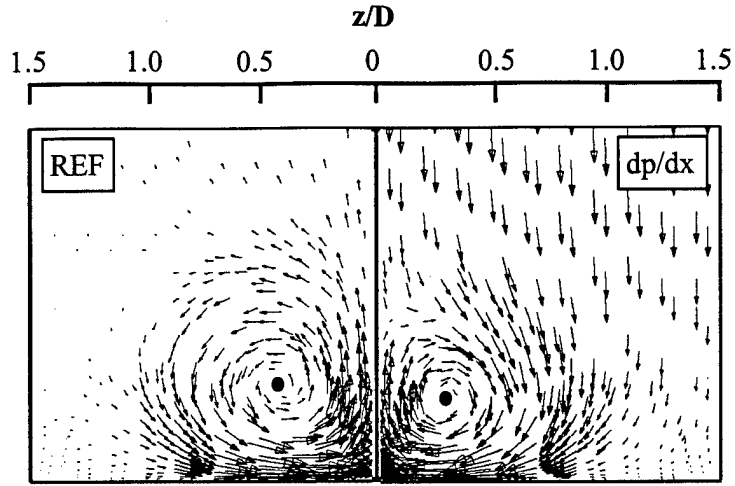
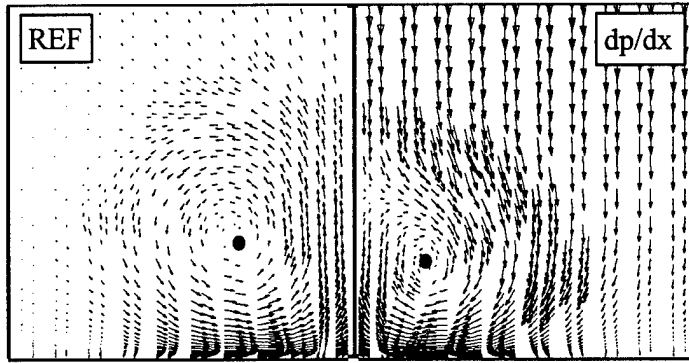


Figure 7. Lines of constant velocity magnitude (m/s) for  $M=1.0$  on a plane defined by  $x/D=15$  show similar velocity gradients in the jet for the  $dp/dx$  and REF cases.

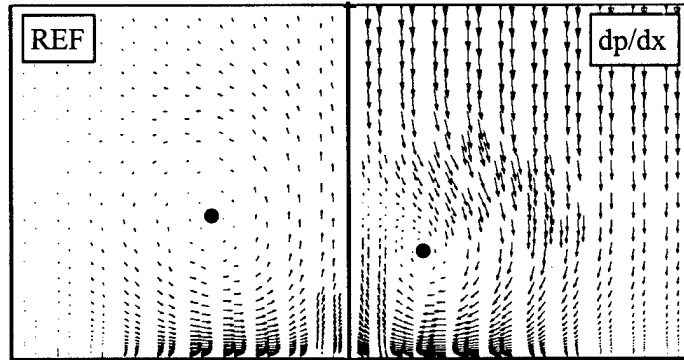




(a)  $x/D = 5$



(b)  $x/D = 10$



(c)  $x/D = 15$

Figure 8. Velocity vectors sized by in-plane velocity on planes of constant  $x$ -coordinate for the case of  $M=0.6$ . The vortex centers are marked with dots, and a reference vector is defined in (a).

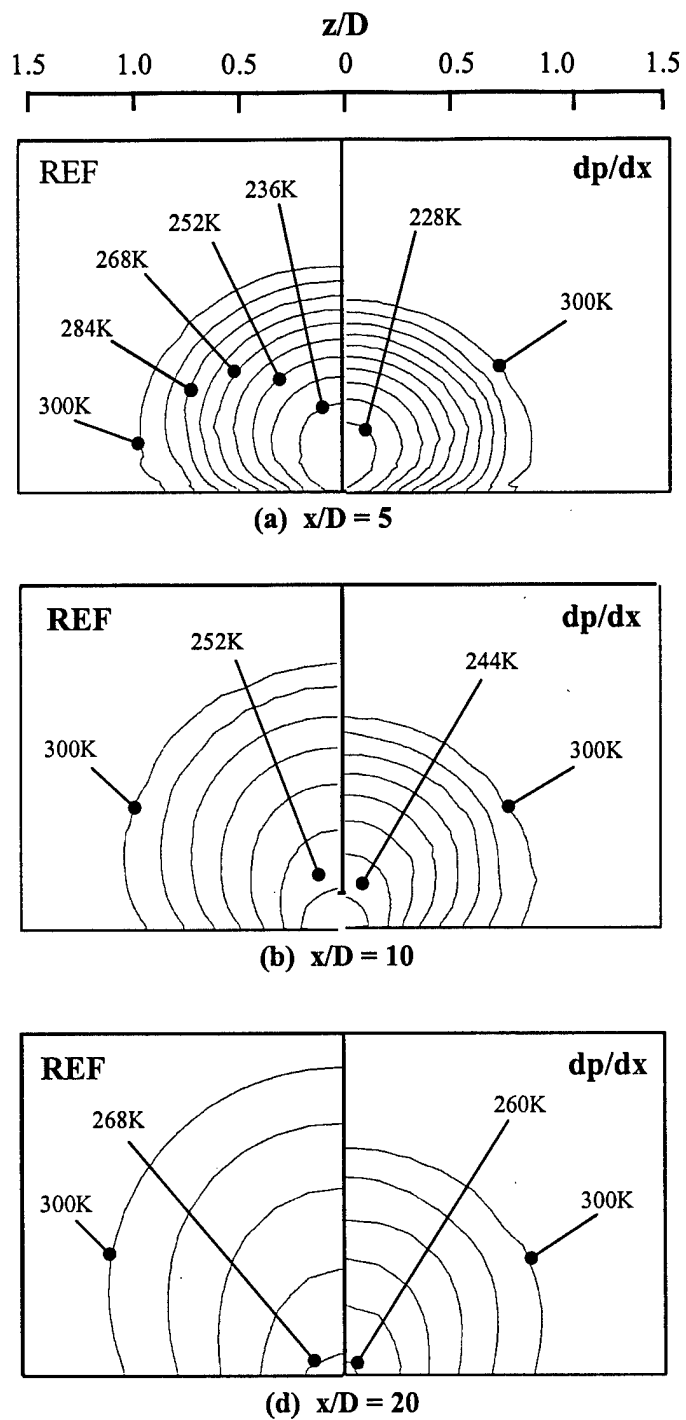
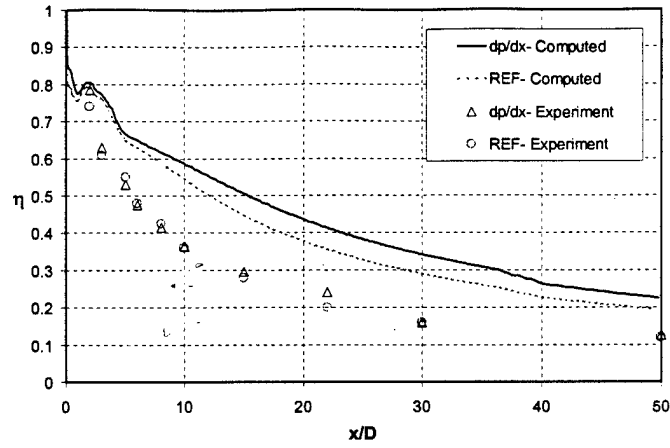
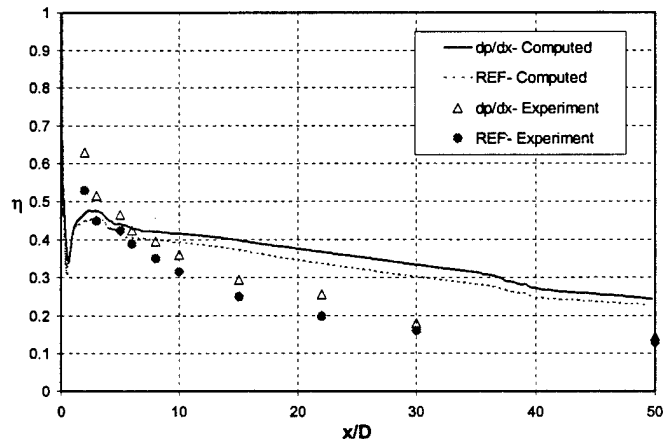


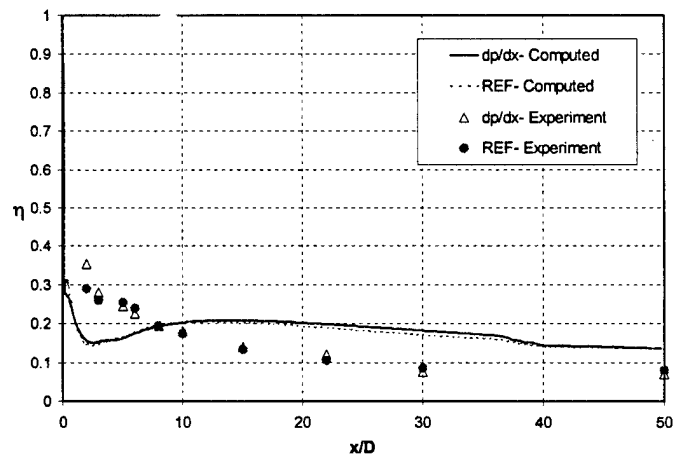
Figure 9. Contours of static temperature on planes defined by constant  $x$ -coordinate for  $M=0.6$ . The contour lines have a spacing of 8K.



(a)  $M=0.6$ ,  $I=0.23$

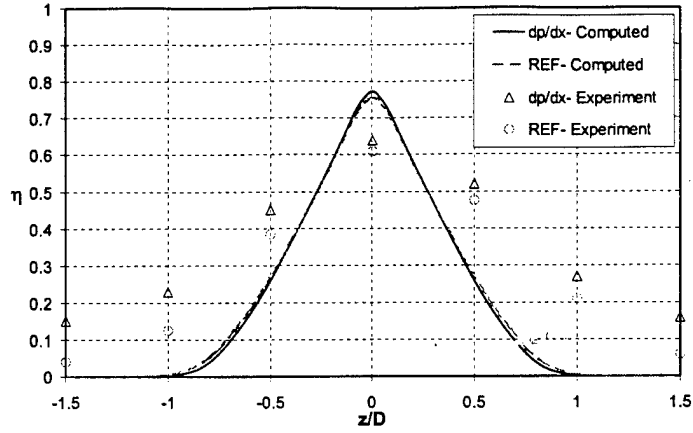


(b)  $M=1.0$ ,  $I=0.63$

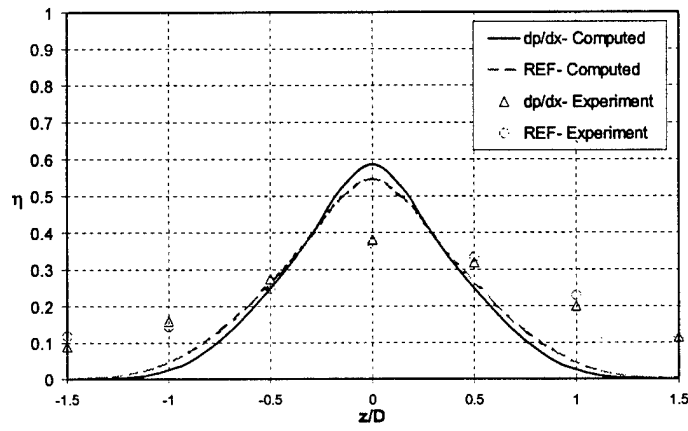


(c)  $M=1.5$ ,  $I=1.41$

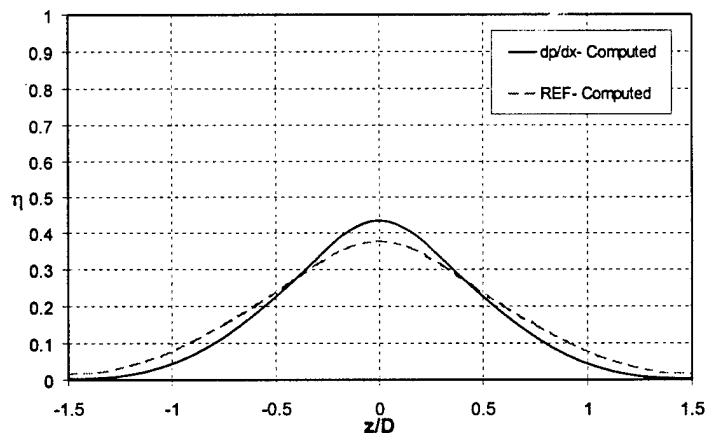
Figure 10. Centerline effectiveness versus downstream distance for (a)  $M = 0.6$  (b)  $M = 1.0$ , and (c)  $M = 1.5$ .



(a)  $x/D=3$

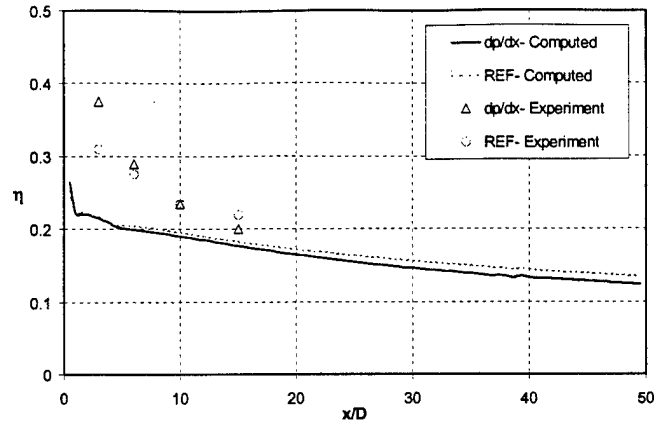


(b)  $x/D=10$

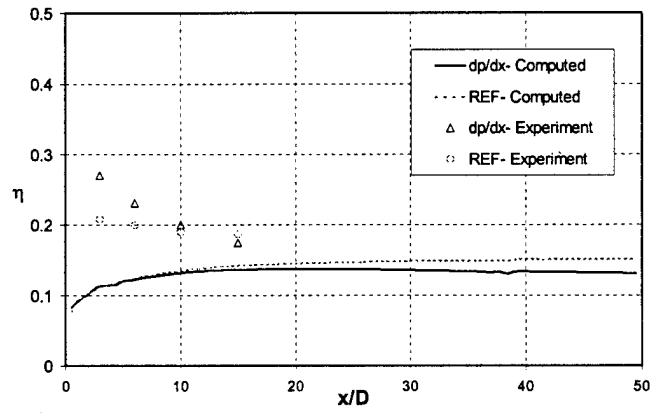


(c)  $x/D=20$

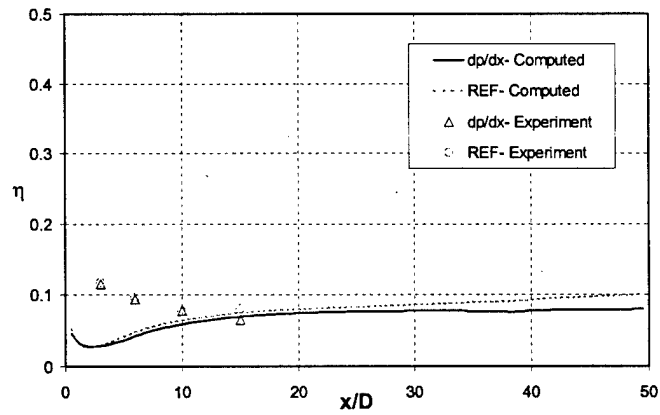
Figure 11. Spanwise distribution of local effectiveness for  $M = 0.6$  at (a)  $x/D = 3$ , (b)  $x/D = 10$ , and (c)  $x/D = 20$ .



(a)  $M=0.6$ ,  $I=0.23$



(b)  $M=1.0$ ,  $I=0.63$



(c)  $M=1.5$ ,  $I=1.41$

Figure 12. Laterally averaged effectiveness results for (a)  $M=0.6$ , (b)  $M=1.0$ , and (c)  $M=1.5$ .

## CHAPTER 2

### NUMERICAL STUDY ON THE EFFECTS OF CONVEX CURVATURE ON FILM COOLING

Satish Undapalli, D. Keith Walters and James H. Leylek

#### NOMENCLATURE

|              |   |
|--------------|---|
| D            | film-cooling hole diameter  |
| DR           | coolant-to-mainstream density ratio = $\rho_j/\rho_\infty$                        |
| I            | coolant-to-mainstream momentum flux ratio = $\rho_j U_j^2/\rho_\infty U_\infty^2$ |
| k            | turbulent kinetic energy [ $\text{m}^2/\text{s}^2$ ]                              |
| L            | film hole length  |
| M            | coolant to mainstream mass flux ratio = $\rho_j U_j/\rho_\infty U_\infty$         |
| Ma           | Mach number   |
| MF           | coolant mass fraction   |
| Re           | Reynolds number   |
| RKE          | Realizable k- $\epsilon$ turbulence model   |
| x            | streamwise coordinate originating at trailing edge of holes [m]                   |
| y            | coordinate normal to test surface [m]   |
| z            | spanwise coordinate originating at hole centerline                                |
| $\delta$     | boundary layer thickness at injection [m]   |
| $\epsilon$   | dissipation rate of turbulent kinetic energy [ $\text{m}^2/\text{s}^3$ ]          |
| $\eta$       | impermeable wall effectiveness = $(MF_w - MF_\infty)/(MF_j - MF_\infty)$          |
| $\bar{\eta}$ | laterally averaged impermeable effectiveness                                      |
| $\rho$       | density [ $\text{kg}/\text{m}^3$ ]  |

#### Subscripts

|          |  |
|----------|--|
| $\infty$ | mainstream conditions at crossflow inlet plane |
| j        | coolant jet conditions                         |
| w        | local wall value                               |

#### 1. INTRODUCTION

Film cooling is often used to protect gas turbine airfoils from exposure to hot combustion gases. It involves injecting a coolant gas, usually bled from the aft stages of the compressor, through holes in the surfaces of hollow turbine blades. This coolant spreads along the airfoil's outer surfaces, protecting them from the hot mainstream. There are several different kinds of film-cooling techniques, with typical film-cooling

geometries as shown in Figure 1. Of those shown, discrete film cooling is the most commonly used technique.

Because modern day gas turbine engines run with high turbine inlet temperatures in order to reach higher efficiencies, film cooling has become a critical technology for turbine design. Consequently, there is an urgent need to study the physical processes in film-cooling flows, and to develop predictive capability to be used in the design process.

Film cooling has been studied extensively for the past 30 years. Most of these studies can be divided into two main categories. The first includes experiments on specific airfoil geometries that are conducted close to engine boundary conditions. These studies, though very important to know the engine performance at the design conditions, often do not deliver enough information to study off-design conditions or variable geometries. The second category includes experiments that isolate the different features of the flow over an airfoil. These experiments try to resolve and explain the physics governing the film-cooling process. Some of the features investigated include streamwise pressure gradients, curvature (convex and concave), free-stream turbulence, and boundary-layer thickness. These fundamental studies are critical to understanding the overall physics involved in film cooling. These experiments are also useful as validation cases for studying computational approaches to film-cooling prediction, since any computational technique depends on the ability to correctly resolve the physical mechanisms in film-cooling flows.

The present work documents a numerical study of one of the above features, specifically the influence of convex curvature on film cooling. Simulations have been conducted to compute the adiabatic effectiveness on convex surfaces and results have been compared with experiments available in the open literature. The study aims for the understanding of curvature effects on film cooling and the physical mechanisms important to the process. Additionally, the performance of "current" turbulence modeling practice is evaluated, with the goal of highlighting weaknesses and recommending future improvements to turbulence prediction methods.

## **2. LITERATURE REVIEW**

### **2.1 Experimental Studies**

The effects of curvature on airfoil film cooling can be understood only if the streamline curvature effects on turbulent flow are understood. Numerous experiments can be found in the literature investigating these effects. These show that streamline curvature produces significant changes in the turbulence structure of shear layers. These changes are usually an order of magnitude more important than normal pressure gradients and other explicit terms appearing in the mean motion equations of shear layers. This was first stated by Bradshaw (1973) in his report on the effects of streamline curvature on turbulent flow. So and Mellor (1973) confirmed that curvature has a substantial effect on the nature of the mean flow and Reynolds stresses and, consequently, the wall shear

stress. Muck et al. (1986a,b) conducted experiments to determine the effect turbulence on boundary-layer development on convex and concave surfaces. They concluded that convex curvature has a stabilizing effect and concave curvature has a destabilizing effect in the boundary layer and that these effects are fundamentally different from one another. They found that even mild convex curvatures tend to attenuate the turbulence, while concave curvature results in quasi-inviscid generation of longitudinal vortices, together with significant enhancement in turbulence caused by both the curvature and the vortices. These vortices are called Taylor-Görtler vortices and have been observed in most experiments conducted on boundary layers on concave surfaces.

Mayle et al. (1977) conducted experiments to study the influence of streamline curvature on film-cooling effectiveness. Experiments were performed for air discharged through a slot and into a turbulent boundary layer along a flat, convex, and concave surface. Compared to the results for the flat surface, convex curvature was found to increase the adiabatic wall effectiveness whereas concave curvature was detrimental. The authors concluded that this behavior was caused by the influence of curvature on production, diffusion and dissipation of the Reynolds stresses and the turbulent heat flux, which determines the growth of thermal boundary layers.

Ito et al. (1978) measured local film-cooling effectiveness on a turbine airfoil geometry using a mass transfer technique. They explained the effects of curvature on film-cooling effectiveness by determining whether the injected fluid moves closer to or farther from the wall surface. The trend of the jet trajectory can be determined by considering the balance of forces exerted on the injected fluid of the jet by the static pressure and centrifugal force along the path of the injected coolant. They determined that curvature influences the mean flow independent of the Reynolds stresses, by forcing coolant jets toward a convex surface at low momentum-flux ratios ( $I$ ) and away from the wall at higher  $I$ . The trend was reversed on concave surfaces.

Schwarz and co-workers (1986,1988,1991) performed experiments on film cooling in curved passages. The studies focused on the influence of strength of curvature -- expressed by the parameter  $2r/D$  -- on the impermeable wall effectiveness. The effects of curvature were isolated by fixing both the radius of curvature and the boundary-layer displacement thickness at the point of injection for all the cases considered. Similar to Ito et al. (1978), the authors concluded that the tangential momentum of jets reduces effectiveness on the convex surface, and improves it on the concave. The radius of curvature of the jet trajectory is increased as tangential momentum is increased, pulling it away from a convex wall and pushing it into a concave wall. The normal momentum of jets degrades effectiveness on all surfaces by lifting the jet away from the wall in the near field. As a consequence, the convex surface shows better cooling performance than the concave at low momentum flux ratio, and the reverse is true for higher  $I$  value. Lateral profiles of local effectiveness are much flatter on the concave surface than on the convex, and this is attributed to lateral mixing caused by the unstable concave flow. Beyond a momentum flux ratio of 2, however, changes in curvature appeared to have little effect on cooling performance.



Goldstein and Stone (1997) conducted experiments with row-of-holes injection along a convex and a concave wall at different injection angles. Injection angle effects were found to vary with blowing rate. At low blowing rates, the injection angle is unimportant, while at moderate blowing rates the shallower angles provide better effectiveness, and at higher blowing rates a steeper injection angle may actually provide better results. The counter-rotating vortex motion was considered to explain these effects.

Recently, film-cooling experiments on convex surfaces were conducted by Lutum et al. (2000). The adiabatic film-cooling effectiveness and heat transfer increase due to film injection was investigated for a convex surface with zero streamwise pressure gradient. The effect of convex curvature was to decrease film-cooling effectiveness and increase heat transfer coefficient at moderate and high blowing rates.

## 2.2 Numerical Studies

Several numerical studies have been performed for film cooling on flat plates. Walters and Leylek (1997) documented a systematic computational methodology for this class of problems, in which turbulence model performance is isolated by minimizing errors arising from either inaccurate computational model or numerical viscosity.

Very few numerical studies on curvature effects are available in the open literature. One exception is the study of Berhe and Patankar (1999a,b), which compared computational simulations with selected experiments of Schwarz (1986). They modified the  $k$ - $\epsilon$  turbulence model to account for the curvature effects on the Reynolds stresses and turbulent heat fluxes. The results showed reasonable agreement with measured data. The simulations only considered relatively low trajectory jets, corresponding to blowing ratios equal to 0.5 and 1.0, and momentum flux ratios of 0.125 and 0.5, respectively. This does not allow an accurate judgment regarding model performance in cases with coolant jet lift-off. However, for the cases with attached coolant jets, the curvature-modified turbulence model appeared to yield some improvement over unmodified models.

Lin and Shih (1999) performed computational studies comparing flat and convex surfaces. They used a low Reynolds number  $k$ - $\omega$ /SST turbulence model (Menter, 1993) that was not modified to account for curvature effects on turbulence. The curved geometry was similar to the one used by Schwarz (1986). One significant departure of the computational model from the experiments was the use of a plug flow inlet boundary condition. The experiments had maintained the velocity profile at the injection location to yield a constant boundary layer thickness for each of the test cases. The results were only compared to experimental data for the case of flat-plate injection at the lowest blowing ratio ( $M = 0.5$ ), so an accurate assessment of the predictive capability was not possible for either curvature effects or significant jet lift-off.

## 2.3 Summary

Almost every study on curvature effects concludes that little progress has been made in quantifying the effects of curvature on turbulence despite the level of effort

devoted to the subject through laboratory, modeling and computational study. Some aspects are clear, however. Most specifically the conclusion that convex curvature tends to suppress boundary-layer turbulence, and that concave curvature tends to augment it.

Experimental studies of film cooling on curved surfaces have demonstrated two important yet separate effects: the influence of curvature on the mean flow characteristics (e.g. Ito et al., 1978), and the influence of curvature on the Reynolds stress and turbulent heat flux (e.g. Mayle et al., 1977). From a computational standpoint, one would expect current simulation techniques to resolve the former with at least reasonable accuracy, but resolving the latter depends greatly on the turbulence treatment used in the computations.

The very few computational studies on film cooling blame inadequate turbulence models for inability to resolve curvature effects. The present study uses a systematic methodology in order to provide a better understanding of the performance of turbulence models in simulations of film cooling on convex curved surfaces. Results are presented and compared to experimental data for a much wider range of conditions than has been found in the literature to date. This includes a range of blowing and momentum flux ratios to cover attached and highly lifted coolant jets, as well as examination of two different rates of curvature. Results will be examined in order to yield an evaluation of current modeling techniques, and to make suggestions for future improvements to computational capability.

### 3. EXPERIMENTAL TEST CASE

The present simulations are compared to the experiments of Schwarz (1986). The experimental apparatus is shown in Figure 2, and consists of five major components: wind tunnel, test section, secondary injection system, sampling system, and data acquisition/reduction system. The convex working surface had a radius of curvature of 10.10 cm and was 135° long in the streamwise direction. Stainless steel tubes of required film-hole diameter were epoxied into the holes drilled through the curved surfaces at an angle of 35° in the streamwise direction. The centers of the injection holes were located at 45° after the onset of convex curvature. Two different  $2r/D$  ratios with film-hole diameter .16 cm (lower strength of curvature,  $2r/D = 126$ ) and .333 cm (higher strength of curvature,  $2r/D = 61$ ) are considered for the present simulations. Effectiveness measurements along the convex wall of the test section were made using a foreign gas injection technique. Air mixed with freon-12 was injected through the row of holes in the curved surfaces. Detailed velocity profiles, and a description of how they were obtained, can be found in Schwarz (1986).

In order to represent a range of coolant conditions, the following experimental test cases were simulated in the present study: (1) lower strength-of-curvature ( $2r/D=126$ ),  $M = 0.99, 1.21, 1.59$ , and  $2.48$ ; (2) higher strength-of-curvature ( $2r/D=61$ ),  $M=1.00, 1.33$ , and  $1.90$ . All cases simulated had a coolant-to-mainstream density ratio (DR) of 2.

## 4. SIMULATION DETAILS

In an effort to support the overall objective of developing robust, practical, and fast turn-around time design tools for the gas turbine industry, attention is focused in the present study on RANS-based turbulence models. One major goal of the present study is to isolate turbulence model performance by minimizing errors from other sources. For this purpose, a systematic methodology was employed which includes: (1) accurate computational model of the physical problem; (2) accurate geometry representation and high quality grid generation; and (3) second-order discretization scheme to reduce numerical viscosity. In the past, erroneous conclusions may have been drawn regarding turbulence model performance based on an ineffective treatment of the above three issues. Details are presented in the following sections.

### 4.1 Computational Model and Boundary Conditions

Figure 3 shows the computational domain for the present simulations. It includes three main zones: the curved passage region, the film hole, and the coolant supply plenum. Each of the three zones must be modeled for accurate simulation, since there is a strong coupling between the three regions and a very complex flow structure in the film hole that cause the jet exit conditions to change dramatically with blowing ratio (Walters and Leylek, 1997; Lin and Shih, 1998). For the present simulations, the different non-dimensional curvature strengths ( $2r/D$ ) are implemented by changing the film-hole diameter, and maintaining the passage curvature for each case, exactly as in the experiments. Unlike most other film-cooling cases, the film holes in the present geometry have a projection into the plenum. The film holes also have a relatively high length-to-diameter ratio ( $L/D$ ) of 10. Both of these characteristics have a significant effect on the film-hole flowfield, discussed in the results section below. The actual computational domain only includes one-half pitch in the lateral (spanwise) direction. Symmetry conditions are applied at both the film-hole centerline plane (centerplane) and the mid-pitch plane between adjacent film holes, in order to simulate an infinite row of cooling holes.

It is important to use the appropriate boundary conditions to ensure that an accurate analog to the experiments is simulated. For the main passage flow, an inlet velocity profile is used in the current study in order to include any upstream boundary-layer history effects on the mean velocity field. This profile was modified from that of a uniform plug flow to a profile that showed good agreement with the experimental data provided at the injection location without film cooling. Numerical experiments on the passage flow studies were iteratively performed at Clemson University in order to obtain the correct profile. The resulting velocity profile at the injection location is shown in Figure 4 both for the case of uniform inlet flow and for the inlet profile used in this study. The profiles for turbulent kinetic energy and turbulent dissipation rate were also taken from the numerical experiments and applied to the film-cooled cases. The above procedure requires extra effort, but was deemed necessary since the boundary-layer thickness to film-hole diameter ratio ( $\delta/D$ ), as well as the mean velocity profile shape, are demonstrated to be important parameters in film-cooling performance.

The other boundary conditions are relatively straightforward. A constant pressure was applied at the outlet in order to avoid any recirculation. While a constant pressure condition may be an idealization, it was determined that spatial variations in the outlet conditions had little impact on the upstream film-cooling effectiveness. The plenum is specified as a velocity inlet. Because the plenum “pressurized” during the simulations, resulting in a changed inlet density, an iteration procedure was adopted to exactly match the experimental mass flow rate at the plenum inlet. The shape of the plenum inlet and the sufficiently low velocity magnitude ensured that there was no secondary flow within the plenum. A secondary coolant gas consisting of air and Freon was introduced at the plenum inlet to match the experimental secondary gas. All the walls were declared adiabatic and impermeable. All of the fluid properties were assumed to follow ideal gas mixture behavior, and Sutherland’s law for temperature dependent molecular viscosity was used. The Reynolds number based on the passage freestream velocity and film-hole diameter ranged from 430,000 for the weak curvature case to 890,000 for the strong curvature case. The inlet passage Mach number was 0.116 for all cases.

## 4.2 Grid

The computational grid must be constructed to meet several objectives. The grid must completely and accurately resolve the computational domain, avoiding as much as possible either stair-step or faceted boundary definition. The grid should be fine in critical areas of the flowfield and in areas where there are steep gradients of the flow variables. At the same time, grid quality must be maintained, in terms of aspect ratio, stretching ratio, and cell skewness factors. To meet these objectives, the current study implements a grid methodology that is multi-block, multi-topology, unstructured, and adaptive. First, the domain is subdivided into several smaller sub-domains, each of which is meshed using an appropriate topology. Topologies used include hexahedra, tetrahedra, triangular prisms, and pyramids. Typically triangular prisms or hexahedra are used in attached boundary layers where cells of large aspect ratio may be effectively implemented. Tetrahedral cells are used to fill complex volumes and near walls in regions where flow separation is likely to occur (e.g. film-hole inlet and exit) in order to maintain aspect ratios near unity. Pyramid cells are used for a transition from hexahedra to tetrahedra.

Two separate background meshes were generated, one for each strength of curvature investigated. The size of the background grid was approximately 3.3 million cells. Figures 5-7 show different views of the background grid, and highlight the use of the multi-block, multi-topology approach. For each simulation, grid independence was obtained by solution-based adaption. Once convergence was obtained on the background grid, the mesh was refined based on gradients of all primary variables, with an increase in mesh size of approximately 20%. The solution was then converged on the new grid and compared to the previous result. The process was repeated until the change in local film-cooling effectiveness everywhere on the downstream surface was negligible. For the

present simulations, it was found that the initial background meshes in fact yielded grid independent solutions for all cases.

### 4.3 Solution Method

The background grid was generated using a combination of the I-DEAS solid modeling package from SDRC, Inc., and the Gambit and T-Grid pre-processing tools from Fluent, Inc. The solver was Fluent 5.5.14. Within Fluent, the segregated solver was implemented, which uses a pressure-correction algorithm along with an implicit calculation scheme, which is appropriate for the low Ma cases investigated herein. A second-order upwind scheme was used for spatial discretization of all flow variables. For all cases, the solution was declared converged using the following four criteria: first, a reduction in normalized residuals of at least three orders of magnitude along with the flattening of these quantities; second, a reduction of the global mass and energy imbalance to less than .01% of the plenum mass flow rate; third, monitoring of the local values of velocity magnitude and turbulence quantities ( $k$  and  $\epsilon$ ) at a point located in the critical portion of the computational domain to determine that they weren't changing with increasing iteration; and fourth by monitoring the above mentioned quantities at a plane location. As described in the above section, solution-based adaption was used to determine grid independence.

### 4.4 Turbulence Modeling

The present simulations make use of Reynolds averaging of the Navier-Stokes equations. This necessarily makes the choice of turbulence model critical to the computations. The most commonly used turbulence models for film-cooling problems are of the two-equation eddy-viscosity type. The most basic -- and popular -- of these is the standard  $k$ - $\epsilon$  model. Earlier studies by Walters and Leylek (2000a) show that this model tends to underpredict the turbulence levels near the film-hole exit and overpredict them farther downstream. It has also been pointed out by several authors (e.g. Durbin, 1996; Moore and Moore, 1999; Walters and Leylek, 2000b) that the standard  $k$ - $\epsilon$  model suffers from violation of the realizability constraints, and should not be used for problems in which the turbulence is expected to depart strongly from equilibrium. Walters and Leylek (2000b) examined the impact of film cooling on total pressure loss through a turbine cascade, and concluded that the realizable  $k$ - $\epsilon$  model (RKE, Shih et al., 1995) available in Fluent yielded results similar to a full differential Reynolds stress model (RSM) and was consequently the best choice of available eddy-viscosity model for this class of problems. Briefly, the realizable model incorporates the mathematical constraint on the Reynolds stresses that requires all normal stresses to remain positive, and that the shear stresses satisfy the Schwarz inequality. The reader is referred to Durbin (1996), Moore and Moore (1999), or Walters and Leylek (2000b) for more details.

It must be pointed out that the RKE model used in the present study is not modified in any way to account for streamline curvature effects. In fact, none of the commonly used two-equation models contain curvature corrections. The RKE model is implemented in its unmodified form in order to establish a reference for these models.

One of the questions this study hopes to answer, at least in part, is how necessary it is to include curvature modifications into this class of modeling, in order to resolve film cooling on curved surfaces. From the point of view of turbine designers, it is helpful to determine the accuracy of current modeling practice before insisting on more complicated models, which may suffer from numerical stiffness and increased computational expense.

In addition to the turbulence model used, the choice of wall treatment is critical to any RANS simulation. Typically, the wall treatment is implemented in such a way that the first node is located either in the inertial sublayer of the turbulent boundary layer or very close to the wall in the viscous sublayer. In the first case, the viscous sublayer and buffer region are bridged using wall functions, which relate the wall shear stress to the first cell velocity using some form of the law of the wall. In the second, the transport equations are integrated to the wall itself, and the viscous and buffer regions are fully resolved. For these sublayer-resolving methods, the high-Re forms of the turbulence models must be modified in some way to include the influence of wall proximity on turbulence quantities. Because film cooling involves complex interaction between the coolant jet and the oncoming crossflow, including separation of both the coolant and crossflow boundary layers, it is necessary to implement some type of sublayer-resolving model in order to accurately capture the details of the relevant physical mechanisms. In the present study, the two-layer model of Wolfstein (1969) is used for all simulations. This method represents a relatively simple approach to sublayer-based modeling, in which the near wall layer is treated with a one-equation model for the turbulent kinetic energy only, and the dissipation rate and turbulence length scale are algebraically related to the wall distance. This model has been shown to yield favorable results in near-wall flows, even when compared to more complex low-Re two-equation models (Chen and Patel, 1988). This model has also been shown to yield improved near-field results in film-cooling flows when compared to the wall function approach (Walters and Leylek, 2000a).

## **5. RESULTS AND DISCUSSION**

### **5.1 Comparison of CFD and Experimental Results**

This section compares the computational results in the present study with the experimental data from Schwarz (1986). The comparison highlights the applicability of the numerical method described above (section 4) to film cooling on convex surfaces. Of particular interest is the applicability of the realizable  $k$ - $\epsilon$  (RKE) model in predicting the turbulent mixing of the exiting coolant, and its impact on film-cooling performance. The results will be used to explain the strengths and weaknesses of this modeling approach, and to suggest improvement to future simulations. A more detailed discussion of the flow physics is found below in section 5.2.

The results from the lower strength-of-curvature case ( $2r/D = 126$ ) will be examined first. Figure 8 shows the laterally-averaged impermeable wall effectiveness for

Freon injection ( $DR = 2$ ) plotted versus  $x/D$  for blowing ratios ( $M$ ) ranging from 1 to 2.5. For the lowest  $M$ , the CFD results show a significant underprediction of the effectiveness in the near field, with improving agreement farther downstream. From about  $x/D = 20$  onward, the computations show only a slight underprediction of the experiments. This suggests that the computations are not correctly resolving the jet lift-off mechanism in the near field, but are able to predict the downstream mixing behavior with reasonable accuracy. This is likely due to the fact that the coolant remains within the passage boundary layer for this relatively low injection rate, and is discussed in more detail in the following section. The trends for the two highest  $M$  are considerably different. For these cases, the computations predict low effectiveness values similar to the experiments in the very near field ( $x/D \approx 6$ ), indicating a clearly detached coolant jet. However, the computations show a very rapid rise in effectiveness corresponding to the transport of coolant back toward the downstream surface, while the experiments indicate a very slow rise in effectiveness with increasing  $x/D$ . In fact, while the CFD results show decreasing effectiveness after about  $x/D = 30$ , the experiments never clearly indicate any region of decrease, up to  $x/D = 90$ . These discrepancies for the higher injection rates are discussed below.

Figure 9 shows streamwise variation of local impermeable effectiveness values for the two bounding cases,  $M = 1$  (a) and  $M = 2.5$  (b), at two different spanwise locations corresponding to  $z/D = 0$  (centerline) and  $z/D = 0.732$ . Results are for the lower strength of curvature,  $2r/D = 126$ . For the lower  $M$  case, the centerline effectiveness is well predicted, while the off-centerline values show significant underprediction in the near field, but good agreement downstream of about  $x/D = 20$ . This suggests that the near-field discrepancy in laterally-averaged effectiveness shown in Figure 8 is due primarily to initially too-slow lateral spreading of the coolant jet after injection. This perhaps points to isotropy of the turbulence modeling approach as a significant effect for near-field predictions at low blowing ratios. The higher  $M$  case shows results consistent with Figure 8 above. Specifically, the computations show a rapid rise in effectiveness such that a maximum is reached by about  $x/D = 30$ , while the experiments show much slower transport of the coolant back to the downstream surface.

Figure 10 shows the laterally-averaged impermeable wall effectiveness values for the higher strength-of-curvature case ( $2r/D = 61$ ). The plot indicates a range of blowing ratios from approximately 1 to 2. Note that the maximum dimensionless downstream distance,  $x/D$ , is smaller for these cases, since the same passage test section was used with a larger film-hole diameter. However, the plot abscissa is extended to  $x/D = 100$ , to allow easier visual comparison with Figures 8 and 9 above. Similarities between Figures 8 and 10 are apparent. As above, the computations show an underprediction of the experiments for the lowest  $M$  case, with the discrepancy more severe in the near-field region ( $x/D < 20$ ) than farther downstream. However, comparison with Figure 8 indicates that the CFD results are even lower, relative to the measurements, for the higher curvature case. Similarly, for the highest blowing ratio, the computations again show significant overprediction of the experiments over the entire surface, except for the very near field. Interestingly, however, the middle case,  $M = 1.33$ , shows the best agreement between CFD and experiments. Not coincidentally, it is this blowing ratio that yields a

momentum flux ratio closest to unity for all of the cases over both curvatures. As discussed in the literature review above, the effect of curvature on the mean flow due to cross-stream pressure gradients is in general a function of the momentum flux ratio,  $I$ , so that the curvature effect is effectively neutral for  $I = 1$ . The implications on the effectiveness comparisons is discussed in more detail in the following section.

Figure 11(a,b) shows the streamwise variation of local effectiveness for the curvature  $2r/D = 61$ , for cases  $M = 1$  and  $1.9$  respectively. The plots indicate spanwise locations of  $z = 0D$  (centerline), and  $z = 0.627D$ . For  $M = 1$ , the results are similar to Figure 9(a), although the decay rate of the CFD results at both spanwise locations appears to be noticeably more rapid than indicated by the experiments. For  $M = 1.9$ , the results are similar to those in Figure 9(b) above, indicating similar mechanisms are at work at higher blowing ratios, regardless of the degree of curvature.

The effects of curvature can be effectively isolated by comparing results at identical blowing ratios from two different curvature strengths. The laterally-averaged impermeable wall effectiveness is shown in Figure 12 for the lowest blowing ratio simulated for each curvature,  $M = 1$ . For this blowing ratio, the momentum-flux ratio is equal to  $0.5$ . As discussed above, convex curvature influences the mean flow by "pushing" the coolant towards the surface for  $I < 1$ , thus increasing the effectiveness over the expected flat-plate value. The plots indicate that this is indeed the case, with increased curvature resulting in higher effectiveness levels, for both computations and experiments. The fact that both respond in a similar manner suggests that the CFD is in fact resolving the physical mechanisms responsible for the film-cooling performance, at least in a qualitative sense. There are, however, obvious differences. The computations show much less of a response to the curvature than the experiments, indicating that the impact of curvature is not fully resolved. This is likely due to the fact that the turbulence model used in the present study is not sensitized to streamline curvature effects, and therefore is unable to correctly predict the influence of the convex curvature on the turbulence dynamics, including suppression of turbulence and therefore decreased coolant mixing.

Figure 13 shows a comparison of laterally-averaged effectiveness for the two different curvatures, at higher blowing ratios. For the higher curvature,  $M = 1.9$  is shown, and for the lower curvature two cases are shown,  $M = 1.6$  and  $M = 2.5$ , that bracket  $M = 1.9$ . There is little difference between the two lower curvature results, and so it may be inferred that they are both representative of the results at  $M = 1.9$ , and can be compared to the higher strength of curvature case. The experiments indicate the expected trend, namely, that an increase in strength of curvature results in a decrease in effectiveness for a momentum-flux ratio greater than unity. However, the computations not only indicate an overprediction of effectiveness for all cases, they also do not show the expected decrease in effectiveness that should arise from an increase in curvature. Since the solution of the mean flow equations in CFD simulations is well established, and since great care has been taken to minimize sources of error from computational model and grid, it must be deduced that the current turbulence modeling treatment leads to



serious deficiencies when the coolant jet lifts off and penetrates into the freestream. Further discussion is found in the following section.

## 5.2 Discussion of Physics

This paper focuses on the influence of convex curvature on film-cooling performance, and the ability of a "standard" turbulence modeling approach to predict this influence. Those mechanisms unrelated to streamline curvature, yet significant to film-cooling performance, also bear some discussion. This section is divided into two parts: a discussion of the mean-flow physics, as predicted by the CFD simulations, and a discussion of the predicted turbulent mixing effects. The two are strongly coupled in many cases, and as much as possible, the links between them are investigated.

### 5.2.1 Mean-Flow Physical Mechanisms

In a qualitative sense, the film-cooling flowfield on a curved surface is similar to that on a flat plate. Many of the same physical mechanisms are apparent in both cases. The present results therefore share many of the features discussed in Walters and Leylek (2000a), as well as those found in the other chapters of this report. One significant difference in the current simulations is the flowfield within the film-hole itself. The present test case includes a rather long film hole ( $L/D = 10$ ) that extends well into the coolant supply plenum. Because the film-hole inlet is axisymmetric, there is no preferred direction for the coolant to enter the film hole, and therefore no significant flow turning as shown in Walters and Leylek (2000a). As compared to cases with non-extended film holes, the separation at the film-hole inlet is much less severe, and occurs around the entire circumference of the inlet, as shown in Figure 14(a). The result, seen in Figure 14(b), is an almost completely aligned film-hole flow, with no significant secondary motion. Hyams and Leylek (2000) reported that minimization of secondary flow within the film hole by inlet shaping resulted in a slight degradation of downstream cooling effectiveness. It may be deduced from the current results that a similar degradation would occur due to the extension of the film hole into the plenum, since this configuration also serves to suppress the film-hole secondary flow.

Similar to the results in Chapter 3 for film cooling in an airfoil cascade, the current results show the presence of a horseshoe vortex upstream of the film-hole exit, illustrated in Figure 15. The horseshoe vortex forms due to the roll up of vorticity contained in the approaching crossflow boundary layer. The figure indicates the expected trend, that the strength of the vortex is greatest for low coolant injection rates, and is reduced as blowing ratio increases. It is shown in Chapter 3 that the horseshoe vortex may play a role in determining the film-cooling performance in the near field, since it may entrain coolant fluid and transport it upstream and to the sides of the film hole on the cooled surface. Because the first measurement station in the experiments is at approximately  $x/D = 3$  (highest curvature case), it is not possible to compare the very-near-field region with the computational results. However, it is shown in Chapter 3 that the horseshoe vortex and its impact on film cooling are sensitive to the boundary layer

state. It is also known that convex curvature impacts the developing boundary layer (Muck et al., 1986a). Since the current turbulence treatment does not respond to streamline curvature effects, it is likely that the boundary-layer history is not properly predicted, and therefore the influence of the horseshoe vortex not quantitatively resolved in the CFD simulations. This may explain, in part, the lack of lateral coolant spreading in the near field, as shown in Figures 9 and 11.

It is apparent from the results shown in section 5.2.1 that coolant-jet lift off plays a major role in the cooling effectiveness, as well as in the ability of the computations to reproduce the experimental results. In general, the lifting-off of the coolant results in dramatically reduced effectiveness levels, as well as significant overprediction of effectiveness by the simulations. The jet lift-off mechanism is closely related to the presence of counter-rotating vortices (CRV) downstream of coolant injection, one of the prominent features discussed in film-cooling studies. This motion is responsible for both the lifting of the jet as the coolant moves downstream and the entrainment of the hot crossflow beneath the jet in the higher blowing ratio cases. In general, the strength of this secondary motion increases with increasing momentum flux ratio,  $I$ . As discussed in Walters and Leylek (2000a), the primary source of vorticity in the near field is that contained in the film-hole boundary layers exiting the film hole. Some amount of vorticity is also generated at the jet-crossflow interface, due to pressure gradients acting normal to the coolant-freestream density gradients. One significant effect of curved surfaces is to redirect vorticity normal to the wall so that it is oriented in the direction of flow, and to likewise redirect vorticity oriented in the flow direction so that it is oriented normal to the wall. Due to this action, the CRVs may be strengthened or weakened. For flow over convex surfaces, the coolant is effectively pushed toward the surface for momentum flux ratios less than unity. In these cases, the strength of the CRVs is diminished by the effects of the curvature. In fact, as discussed in Chapter 3, the CRVs may actually change their orientation if the curvature is strong enough. For  $I > 1$ , on the other hand, the coolant is lifted away from the downstream surface due to centrifugal forces, and correspondingly the CRVs are strengthened by the effects of curvature. Figure 16 illustrates the CRV secondary flow superimposed on the contours of coolant species mass fraction at two different downstream locations ( $x/D = 2$  and  $10$ ) and two different blowing ratios ( $M = 1$  and  $2.5$ ) for the lower-curvature case ( $2r/D = 126$ ). It is apparent that immediately downstream of the film hole ( $x/D = 2$ ) both blowing ratios indicate the presence of CRVs and a corresponding impact on the distribution of the exiting coolant, including the familiar "pinching" effect near the surface. However, farther downstream, at  $x/D = 10$ , only the highest  $M$  case still clearly shows the presence of secondary motion. The CRVs persist farther downstream in this case due primarily to the effects of curvature. Figure 17 shows the secondary motion and species concentration for the higher curvature case. For this case ( $2r/D = 61$ ), the coolant is pushed more toward the convex surface due to the increased centrifugal forces. This results in more severe attenuation of the vorticity for the cases with low momentum flux ratio and more enhancement of the CRV's for the cases with high momentum flux ratio. The results are similar to those in Figure 16, although some differences are apparent. Comparing the results at  $x/D = 2$  and  $M = 1$ , it is clear that both the strength of the CRVs and the coolant lift-off are greater for the lower curvature case. At this location the influence of

increased curvature is already apparent. In addition, the figures show that for the higher  $M$  cases, the strength of the CRVs are almost equal at  $x/D = 10$ , despite the fact that  $I = 3.1$  for the lower-curvature case and  $I = 1.8$  for the higher curvature case. The greater streamline curvature results in CRVs that persist farther downstream, for cases with  $I > 1$ .

### 5.2.2 Turbulent Mixing

The effectiveness results presented in section 5.1 indicate that the computations generally underpredict the experiments for low blowing ratios, and overpredict the experiments for higher blowing ratios. Further, the degree of discrepancy is greater for higher blowing ratios. The latter observation suggests that the computations perform most favorably for cases when the coolant remains within the boundary layer, and does not lift off from the downstream surface. The source of the discrepancy is likely due to an incorrect representation of turbulent mixing by the current turbulence treatment. Comparison with results presented in Chapter 3 for film cooling on both pressure and suction surfaces of a turbine airfoil shows that discrepancies at high blowing ratios are present regardless of the curvature and/or pressure gradient effects. It may be reasoned that there is a fundamental shortcoming to this modeling approach independent of curvature effects, for cases involving significant jet lift off. This shortcoming is likely traced to the traditionally poor performance of steady RANS models for flows with significant flow separation. In film-cooling flows, strong jet lift-off and penetration into the freestream is essentially a three-dimensional separation process. On the other hand, when the coolant remains within the attached boundary layer, at lower blowing ratios, the RANS modeling approach is much more capable of resolving the turbulence mixing dynamics, since these models have in fact been developed primarily to reproduce simple boundary-layer type flows.

As an example, consider Figure 18, which shows the contours of coolant mass fraction on the film-hole centerplane. The figure shows contours for each of the different curvatures, with bounding blowing ratios for each curvature. It should be pointed out that the figure shows an equal downstream extent for both cases, but the non-dimensional downstream extent ( $x/D$ ) is twice as great for the lower-curvature case ( $2r/D = 126$ ). All of the contours show qualitatively similar results, regardless of the blowing ratio and degree of curvature. This indicates that the pronounced change in turbulent mixing that occurs as blowing ratio is increased, as indicated by the experiments, does not occur for the CFD results. In fact, the CFD results force a boundary-layer-like behavior, even for the extreme case of  $M = 2.5$  ( $I = 3.1$ ).

One of the reasons for the disappointing performance of the simulations for lifted-off cases may be related to the fact that all RANS models are calibrated to yield results in turbulent flows that are at or near equilibrium. These include the inertial layer in turbulent boundary layers, decaying freestream turbulence, and the far-field regions of free jets and wakes. These flows typically generate a turbulence structure that is close to universal, and is essentially independent of the details of the upstream geometry. In flows with massive separation, including the near-field region of jets, the turbulence

structure may be said to more closely resemble an unsteady periodic or quasi-periodic fluctuation, with the energy concentrated at or near one or more characteristic frequencies (Yule, 1978), and the dynamics very closely related to the problem geometry. This type of unsteady behavior has been documented experimentally in the near-field region of film-cooling flows (Kohli and Bogard, 1998). It is possible that real improvement in the predictive capability of CFD for high  $M$  will necessarily require a methodology that moves beyond typical steady Reynolds-averaged simulations, and included the resolution of the fluctuating flowfield in the vicinity of the jet exit. Therefore, one major conclusion of this study is that steady, RANS-based modeling approaches as they currently exist are unlikely to yield consistently accurate results for film cooling with highly detached coolant jets, regardless of streamline curvature, freestream turbulence, and/or streamwise pressure gradient effects.

Another well-known limitation of the current turbulence treatment is the lack of anisotropy in the eddy-viscosity approach. Both the Reynolds stress tensor and the turbulent heat flux vector are based on simple gradient-based approximations, with a single scalar turbulent viscosity (diffusivity). The effect of this shortcoming is apparent in the lack of coolant spreading in the lateral direction, shown by the computational results in Figures 9 and 11 above, especially Figures 9(a) and 11(a). The lack of lateral coolant spreading is also apparent in Figure 19, which shows the contours of impermeable effectiveness on the downstream surface, for all blowing ratios examined on the lower-curvature (a) and higher-curvature (b) cases, respectively. It is possible that the effect of unsteady, non-equilibrium turbulence discussed above is closely related to turbulence anisotropy, and a methodology that resolves near-field unsteadiness would also improve the ability to resolve lateral coolant spreading. Regardless, improvements to the current turbulence modeling approach will almost certainly require some method of including anisotropy effects on the jet spreading rate. This conclusion has been drawn by previous researchers, and it is underscored yet again in the present study.

The impact of streamline curvature on the turbulent mixing -- and the subsequent impact on cooling effectiveness -- remains to be discussed. One of the primary goals of the present study was to isolate the response of the realizable  $k$ - $\epsilon$  turbulence model to the influence of convex curvature by minimizing all other sources of error. While we believe this has been done, it is unfortunately difficult to quantify what weaknesses in the current turbulence treatment are due to curvature effects and what weaknesses are due to other effects discussed above (unsteadiness, anisotropy, etc.). Clearly, since the turbulence model does not include any response to streamline curvature, it is expected that the impact on turbulent mixing in the CFD results should differ from experiments. As discussed above, cases with relatively high blowing ratios and coolant jet lift-off suffer from fundamental modeling problems, and it appears that curvature effects are only secondary. However, low  $M$  cases, in which the coolant remains attached within the boundary layer, show reasonable agreement with experiments, and it is these cases that highlight the effects of curvature on the turbulent mixing process. Consider Figure 12, which shows laterally-averaged effectiveness versus downstream distance at equivalent (low) blowing ratios, and two different rates of curvature. It is expected that an increase in convex curvature will suppress turbulence in the boundary layer and therefore

turbulent mixing of the coolant. This should result in an increased value of downstream effectiveness, assuming other governing parameters remain unchanged. This effect is dramatically visible in the experimental data. The computations, however, show only a slight response to the increased curvature effect. It is likely that the computations are resolving only the curvature effect on mean-flow physics, and so underpredict the curvature response. In contrast, Figure 13 shows that both computations and experiments show much less response to an increase in curvature for cases when the coolant jet is lifted far from the downstream surface. The significant difference between the CFD and experimental results must be due to other mechanisms, as discussed above.

## 6. CONCLUSIONS

This study documents the computational simulation of film-cooling flow over a convex curved downstream surface. Results have been presented and compared to available code-validation quality experimental data, in order to determine the accuracy of the numerical method, and to elucidate the pertinent physical mechanisms in this class of problems. The study utilized a systematic computational methodology to minimize errors due to computational model, grid, and discretization scheme, and to place the results firmly against the limits of the turbulence modeling technique. The turbulence modeling in the present study was representative of currently popular two-equation modeling practice, and was accomplished using the realizable  $k$ - $\epsilon$  model (RKE) of Shih et al. (1995), and two-layer near-wall treatment of Wolfstein (1969). Examination of the results yield the following conclusions:

- The physical mechanisms responsible for film-cooling performance have been identified by careful examination of the computational results. The ability to accurately resolve the quantitative effects of these mechanisms, however, is dependent upon the flow conditions examined.
- The downstream cooling performance is dominated primarily by the counter-rotating vortex structure in the near field, which governs the lift off of the coolant jet and the entrainment of crossflow fluid near the surface, and the downstream turbulent mixing, which governs the transport of coolant away from or towards the downstream surface. The current simulations help to explain the influence of streamline curvature on the streamwise vortex development.
- The current simulations indicate the presence of a horseshoe vortex upstream of the film-hole exit. The strength of the upstream vortex varies inversely with coolant injection rate.
- The simulations demonstrated an ability to resolve downstream film-cooling performance with reasonable accuracy for cases with low blowing ratios, i.e. cases in which the coolant jet did not lift off from the downstream surface, but remained within the boundary layer.
- For cases with relatively high blowing ratios, the coolant lifted off from the downstream surface, and the computations were unable to accurately resolve the downstream cooling effectiveness.

- For cases with low blowing ratio, the computations indicated the correct qualitative response to an increase in convex curvature, i.e. an increase in downstream cooling performance. The level of increase was underpredicted, however, due to the lack of response by the RKE turbulence model to streamline curvature effects. Future improvements to predictive capability will likely require either the use of more advanced models (differential or algebraic Reynolds stress models) or the modification of eddy-viscosity models to include the effects of curvature.
- For cases with high blowing ratio, the influence of curvature appeared to be secondary to other likely sources of discrepancy. Specifically, these include unsteady (non-equilibrium) influences in the near-field region associated with jet lift off, and turbulence anisotropy. Future modeling improvements for simulation of highly lifted-off coolant jets will likely require some method of including these effects, either through improved steady modeling capability or through the use of time-resolved (unsteady) modeling approaches.
- Overall, the current study indicates that current modeling practice is adequate to predict film-cooling performance on convex curved surfaces to a useful level of accuracy, provided two conditions are met. First, that the blowing ratio be low enough that the coolant jet is not lifted far from the surface. Second, that the surface curvature is relatively mild, so that the major influence of curvature is on the mean-flow, and not on the Reynolds stresses and turbulent heat flux. Future improvements to modeling technology, as suggested above, will increase the general level of applicability of CFD to film-cooling problems.

## REFERENCES

- Berhe, M. K. and Patankar, S. V., 1999, "Curvature Effects on Discrete-Hole Film Cooling," ASME Journal of Turbomachinery, Vol. 121, pp. 781-791.
- Berhe, M. K. and Patankar, S. V., 1999, "Investigation of Discrete-Hole Film-Cooling Parameters Using Curved-Plate Models," ASME Journal of Turbomachinery, Vol. 121, pp. 792-803.
- Bradshaw, P., 1973, "Effects of Streamline Curvature on Turbulent Flow," AGARDograph, Vol. 169.
- Chen, H.C. and Patel, V.C., 1988, "Near-Wall Turbulence Models for Complex Flows Including Separation," AIAA Journal, Vol. 26, pp. 641-648.
- Durbin, P.A., 1996, "On the  $k$ - $\epsilon$  Stagnation Point Anomaly," International Journal of Heat and Fluid Flow, Vol. 17, pp. 89-90.
- Goldstein, R.J. and Stone, L.D., 1997, "Row-of-Holes Film Cooling of Curved Walls at Low Injection Angles," ASME Journal of Turbomachinery, Vol. 119, pp. 574-579.

- Hyams, D.G. and Leylek, J.H., 2000, "A Detailed Analysis of Film-Cooling Physics -- Part III: Streamwise Injection with Saped Holes," ASME Journal of Turbomachinery, Vol. 122, pp. 122-132.
- Ito, S., Goldstein, R.J. and Eckert, E.R.G., 1978, "Film Cooling of a Gas Turbine Blade," ASME Journal of Engineering for Power, Vol. 100, pp. 476-481.
- Kohli, A. and Bogard, D.G., 1998, "Effects of Very High Free-Stream Turbulence on the Jet-Mainstream Interaction in a Film-Cooling Flow," ASME Journal of Turbomachinery, Vol. 120, pp. 785-790.
- Lin, Y.L. and Shih, T. I-P., 1998, "Computations of Discrete-Hole Film Cooling Over Flat and Convex Surfaces," ASME Paper No. 98-GT-436.
- Lutum, E., von Wolfersdorf, J., Weigand, B. and Semmler, K., 2000, "Film Cooling on a Convex Surface with Zero Pressure Gradient Flow," International Journal of Heat and Mass Transfer, Vol. 43, pp. 2973-2987.
- Mayle, R.E., Kopper, F.C., Blair, M.F. and Bailey, D.A., 1977, "Effect of Streamline Curvature on Film Cooling," ASME Journal of Engineering for Power, Vol. 99, pp. 77-82.
- Menter, F.R., 1993, "Zonal Two-Equation  $k-\omega$  Turbulence Models for Aerodynamic Flows," AIAA Paper No. 93-2906.
- Moore, J. G. and Moore, J., 1999, "Realizability in Turbulence Modeling for Turbomachinery CFD," ASME paper no. 99-GT-24.
- Muck, K.C., Hoffmann, P.H. and Bradshaw, P., 1986, "The Effects of Convex Surface Curvature on Turbulent Boundary Layers," Journal of Fluid Mechanics, Vol. 161, pp. 347-369.
- Muck, K.C., Hoffmann, P.H. and Bradshaw, P., 1986, "The Effects of Concave Curvature on Turbulent Boundary Layers," Journal of Fluid Mechanics, Vol. 161, pp. 371-403.
- Schwarz, S.G., 1986, "Film Cooling of Curved Surfaces," Ph.D. Thesis, University of Minnesota.
- Schwarz, S.G. and Goldstein, R.J., "The Two-Dimensional Behavior of Film-Cooling Jets on Concave Surfaces," ASME Journal of Turbomachinery, Vol. 111, pp. 124-130.
- Schwarz, S.G., Goldstein, R.J. and Eckert, E.R.G., 1991, "The Influence of Curvature on Film-Cooling Performance," ASME Journal of Turbomachinery, Vol. 113, pp. 472-478.

Shih, T. -H., Liou, W. W., Shabbir, A., and Zhu, J., 1995, "A New  $k$ - $\epsilon$  Eddy-Viscosity Model for High Reynolds Number Turbulent Flows: Model Development and Validation," *Computers and Fluids*, Vol. 24, pp. 227-238.

So, R.M.C. and Mellor, G.L., 1973, "Experiments on Convex Curvature Effects in Turbulent Boundary Layers," *Journal of Fluid Mechanics*, Vol. 60, pp. 43-62.

Walters, D. K. and Leylek, J. H., 1997, "A Systematic Computational Methodology Applied to a Three-Dimensional Film-Cooling Flowfield," *ASME Journal of Turbomachinery*, Vol. 119, pp. 777-785.

Walters, D.K. and Leylek, J.H., 2000a, "A Detailed Analysis of Film-Cooling Physics -- Part1: Streamwise Injection with Cylindrical Holes," *ASME Journal of Turbomachinery*, Vol. 122, pp. 102-112.

Walters, D.K. and Leylek, J.H., 2000b, "Impact of Film-Cooling Jets on Turbine Aerodynamic Losses," *ASME Journal of Turbomachinery*, Vol. 122, pp.537-545.

Wolfstein, M., 1969, "The Velocity and Temperature Distribution of One-Dimensional Flow with Turbulence Augmentation and Pressure Gradient," *International Journal of Heat and Mass Transfer*, Vol. 12, pp. 301-318.

Yule, A.J., 1978, "Large-Scale Structure in the Mixing Layer of a Round Jet," *Journal of Fluid Mechanics*, Vol. 89, pp. 413-432.



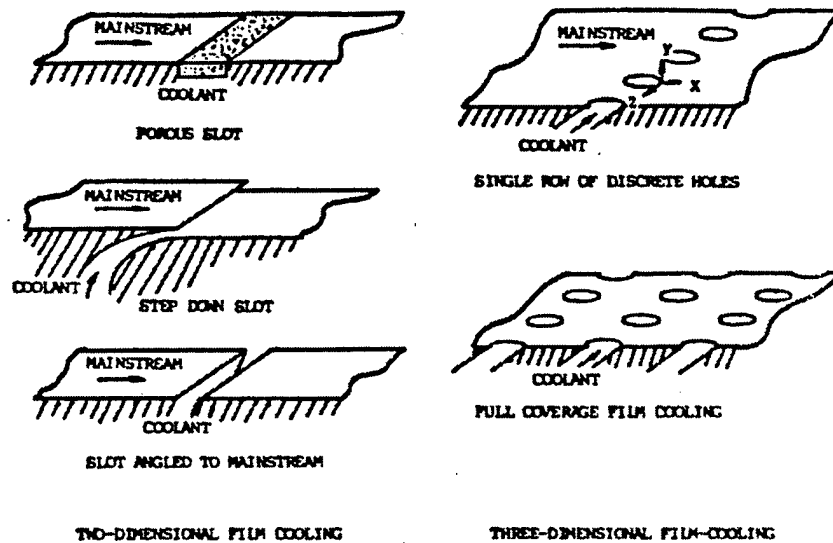


Figure 1. Illustration of different film-cooling methods (from Schwarz, 1986).

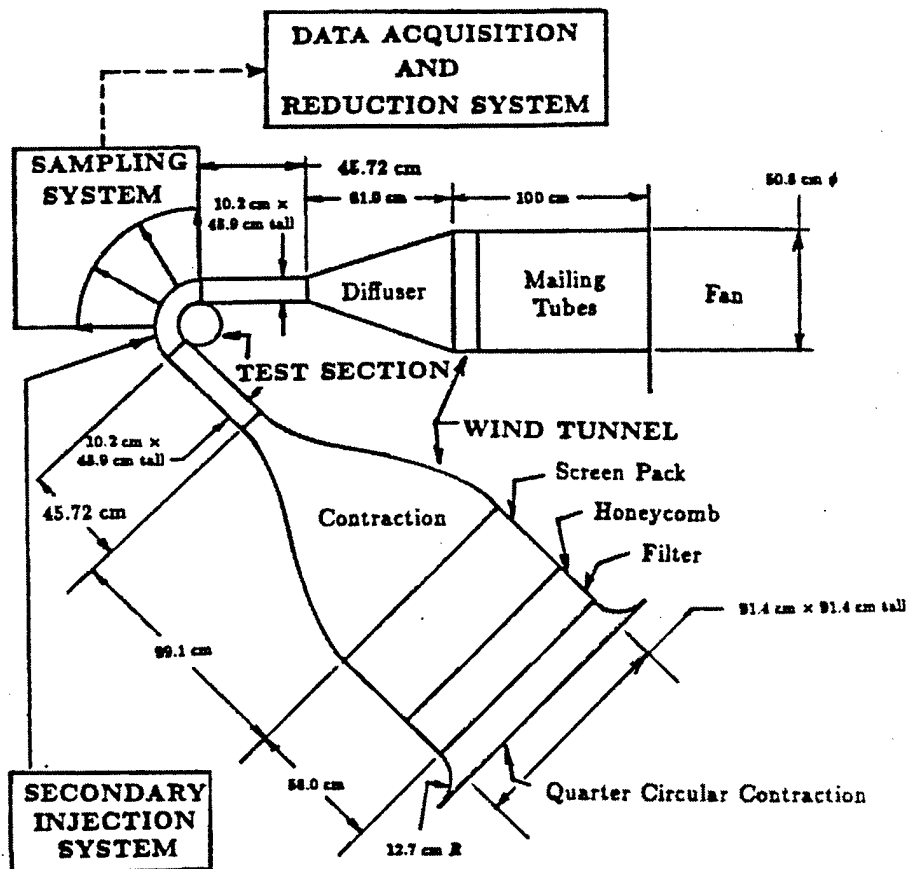


Figure 2. Illustration of experimental apparatus used in the experimental test cases (Schwarz, 1986).

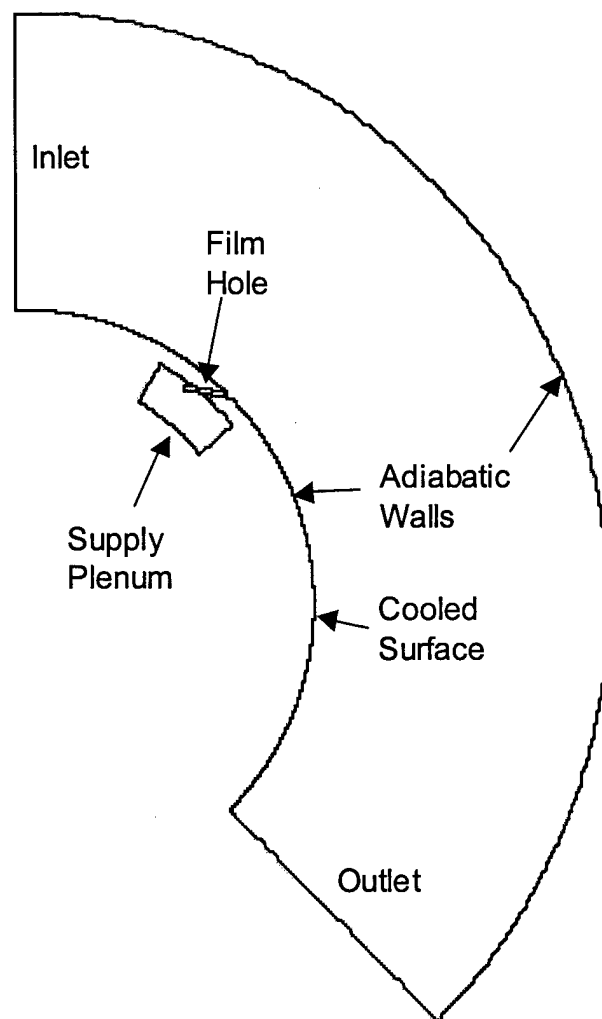


Figure 3. Illustration of the computational domain used in the current study.

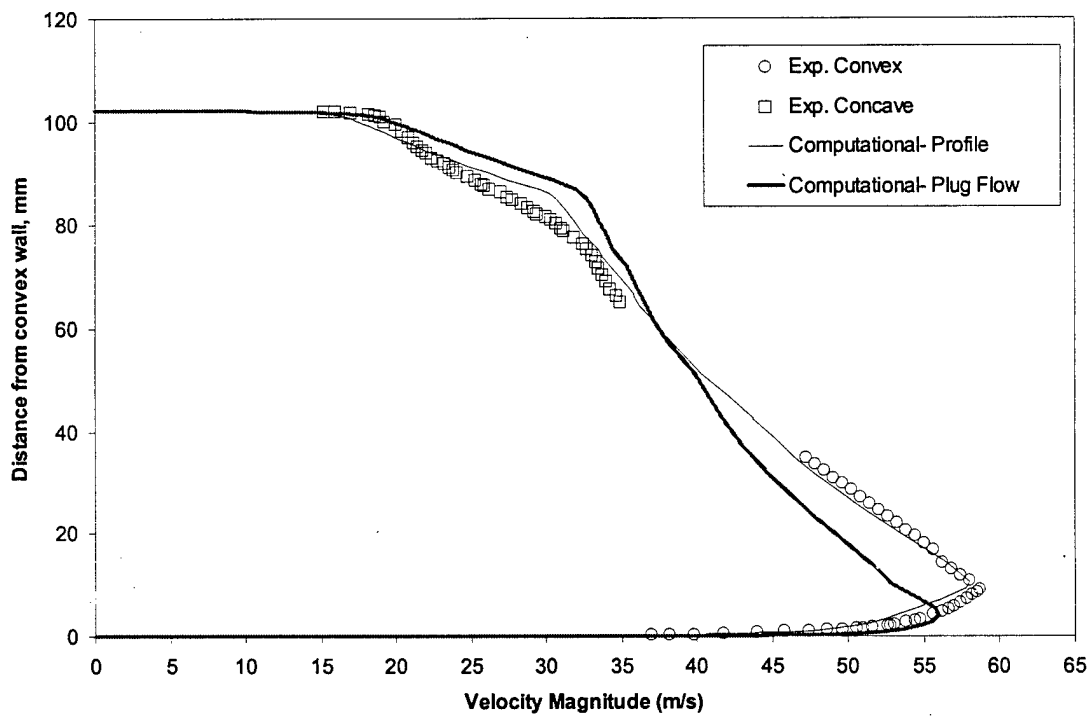


Figure 4. Velocity profile at the jet injection location for the present study. Comparison is shown between experimental data, present inlet profile, and plug-flow inlet.

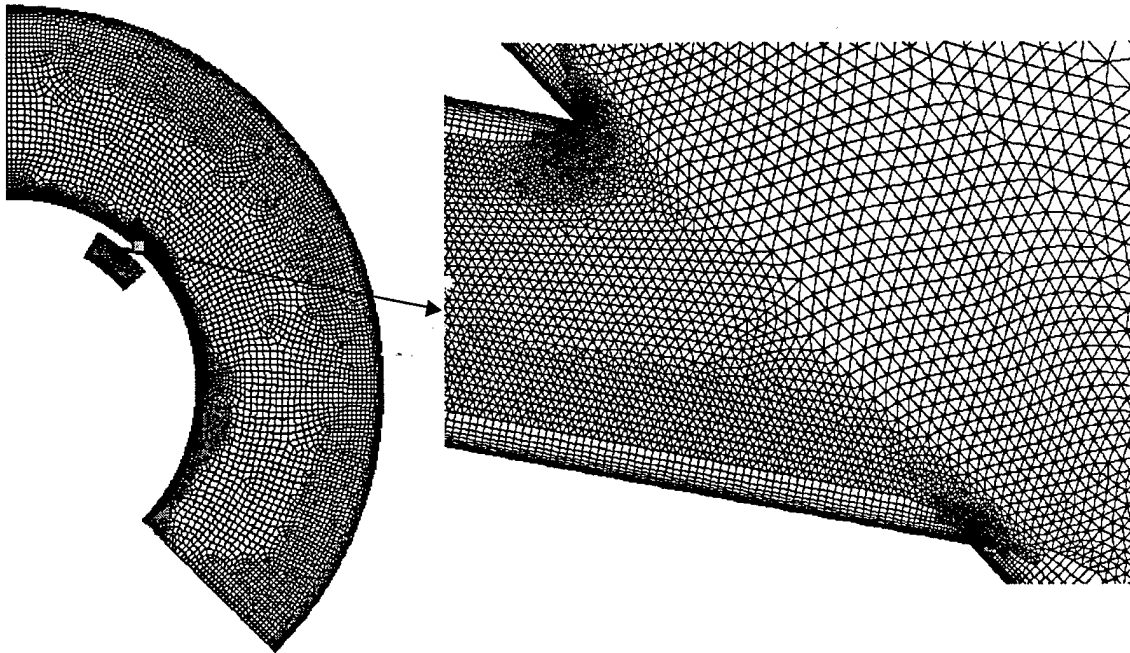


Figure 5. Centerplane background mesh used in the present study, including close-up of the film-hole exit.

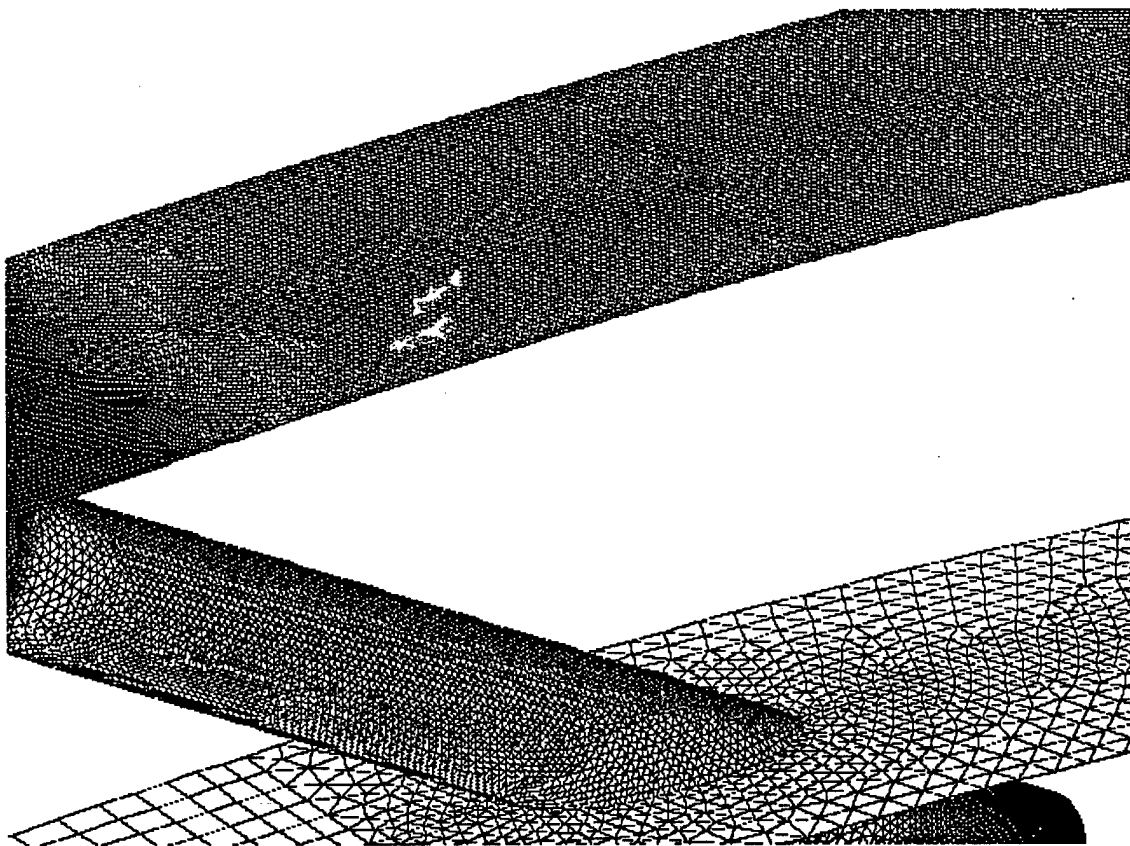


Figure 6. Surface mesh showing the film-hole inlet and supply plenum region.

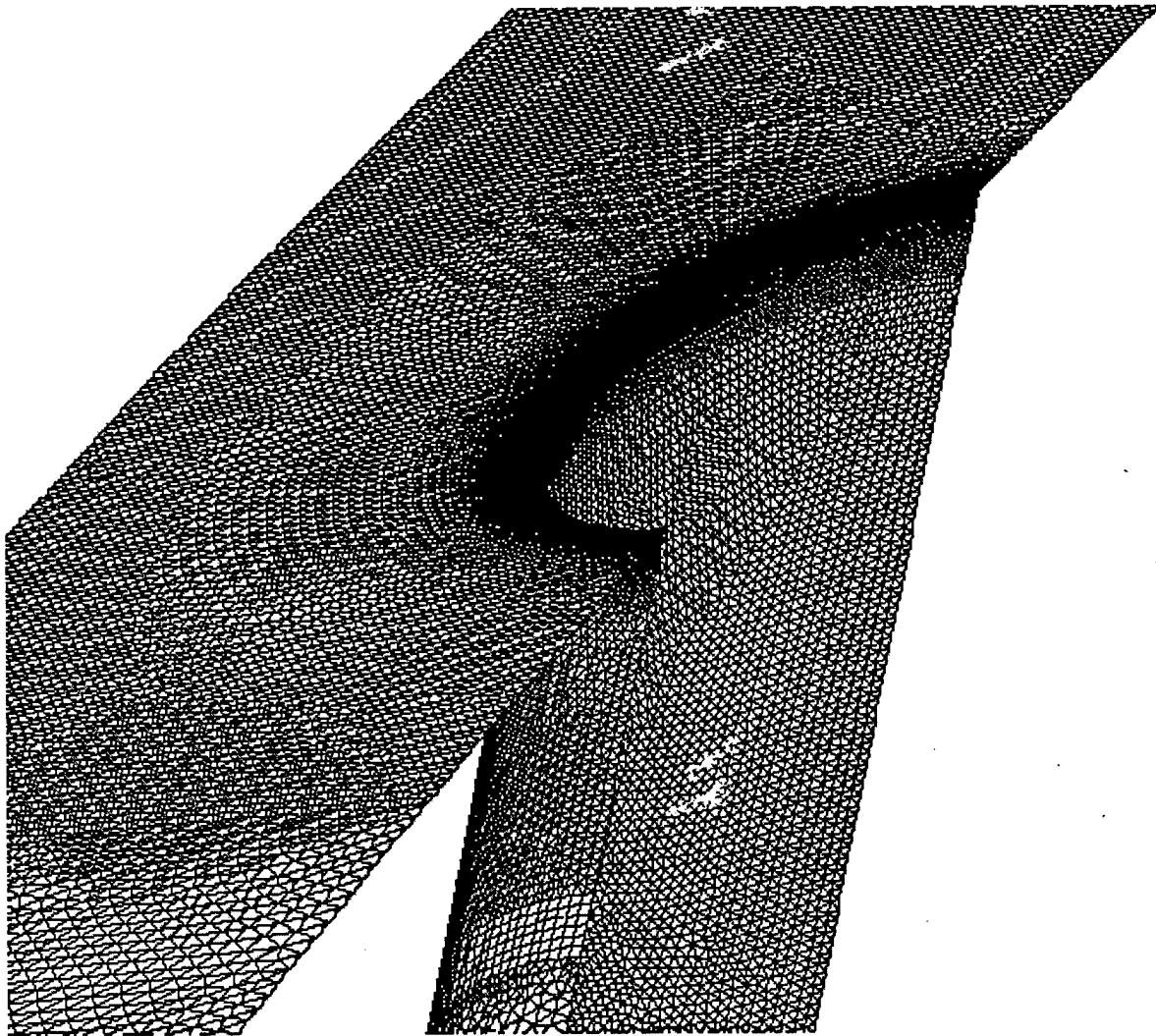


Figure 7. Close-up view of the surface mesh in the film-hole exit region.

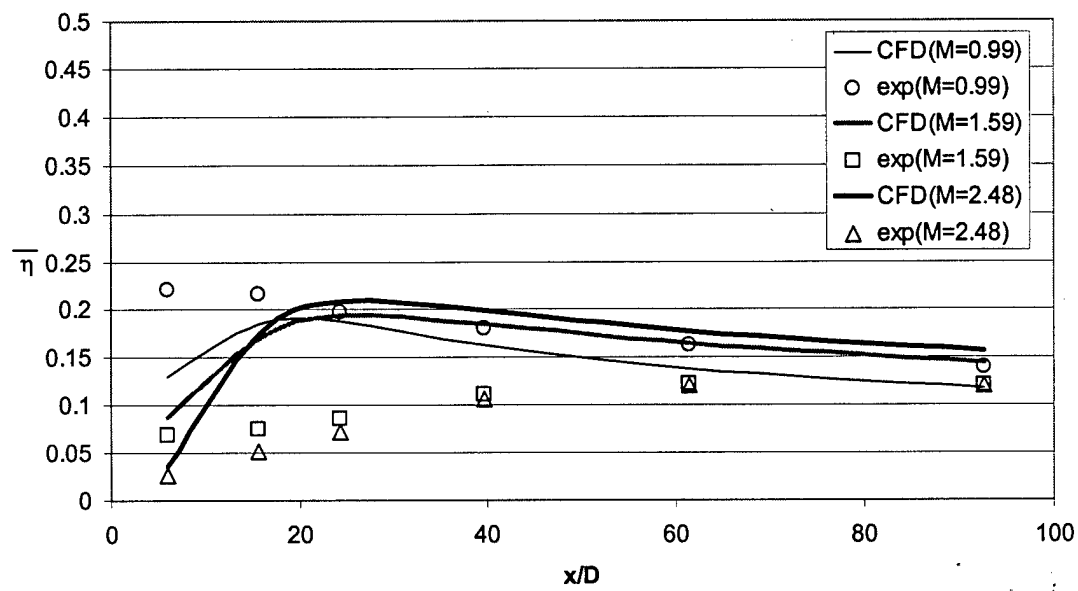
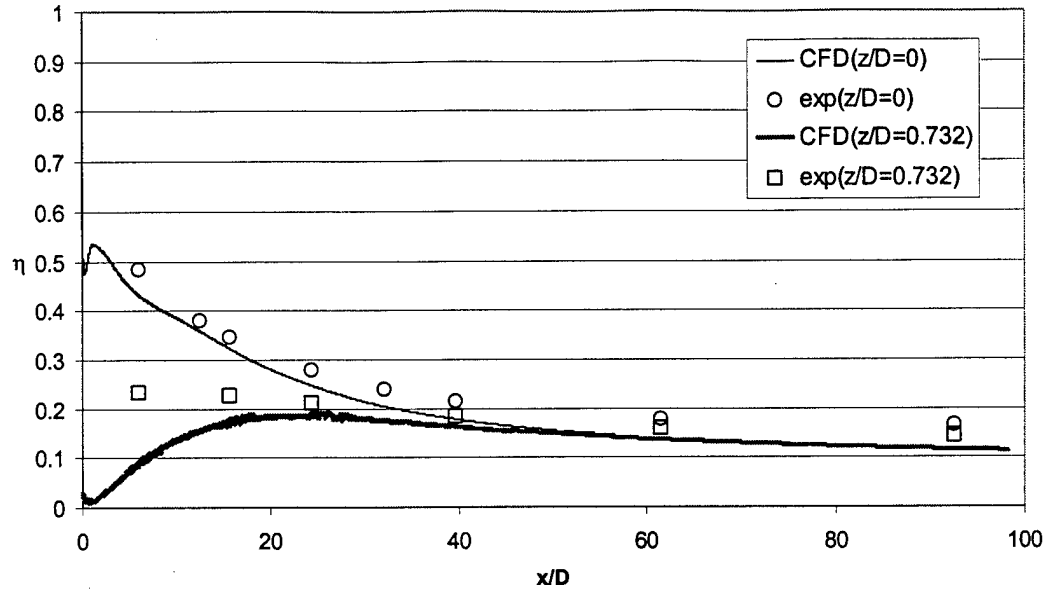
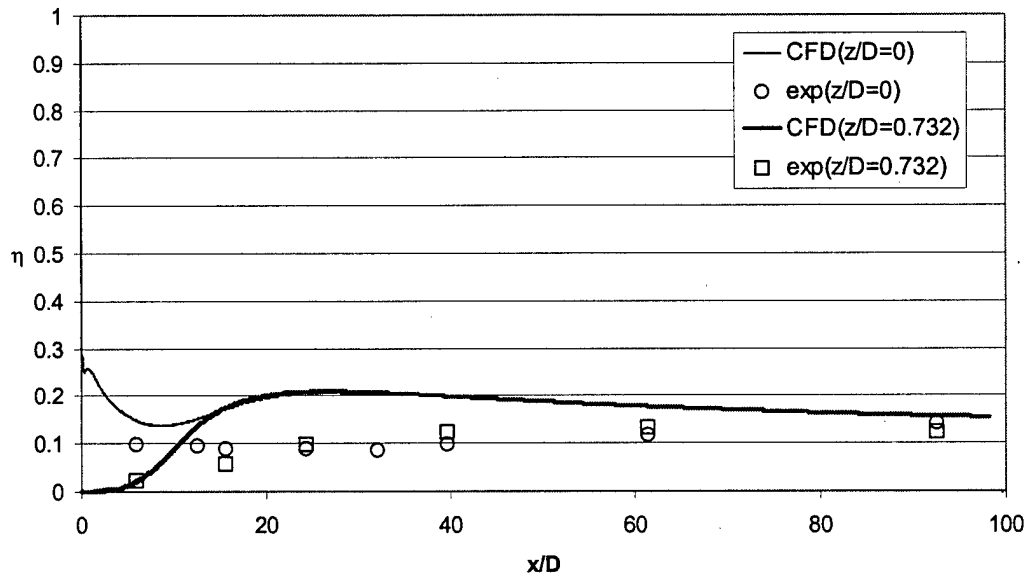


Figure 8. Laterally-averaged impermeable wall effectiveness versus downstream distance for the lower-curvature case ( $2r/D = 126$ ,  $DR = 2$ ).



(a)  $M = 1$ ,  $DR = 2$



(b)  $M = 2.5$ ,  $DR = 2$

Figure 9. Local variation of impermeable wall effectiveness versus downstream distance at two different spanwise locations. Lower-curvature case ( $2r/D = 126$ );  $M = 1$  (a) and  $M = 2.5$  (b).

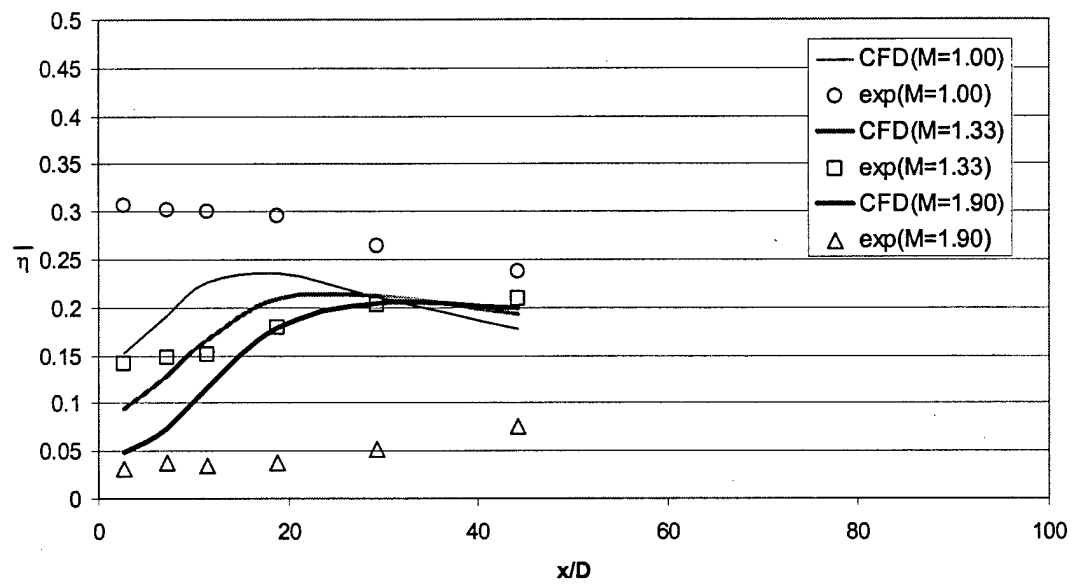
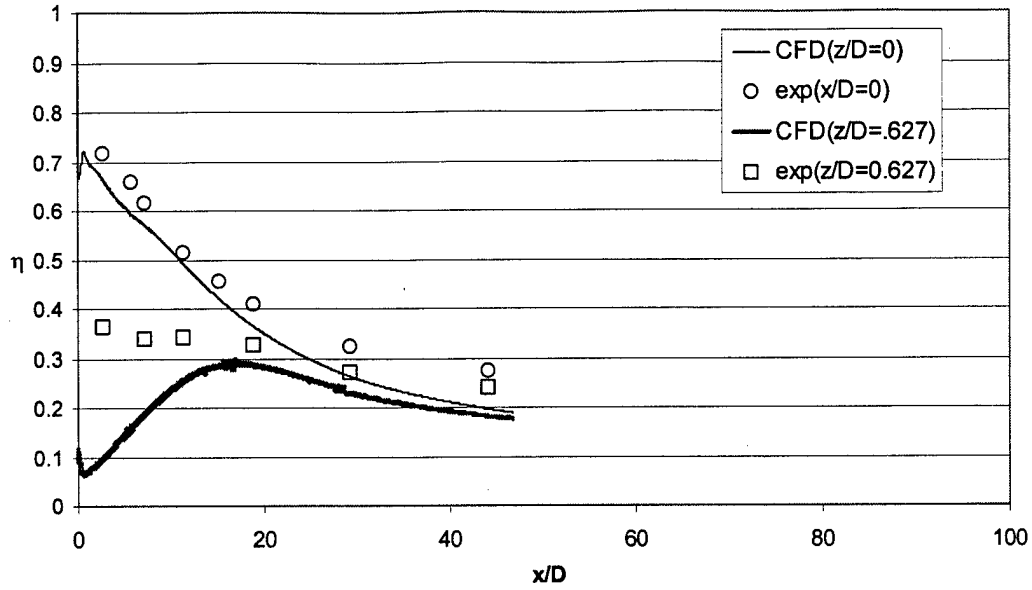
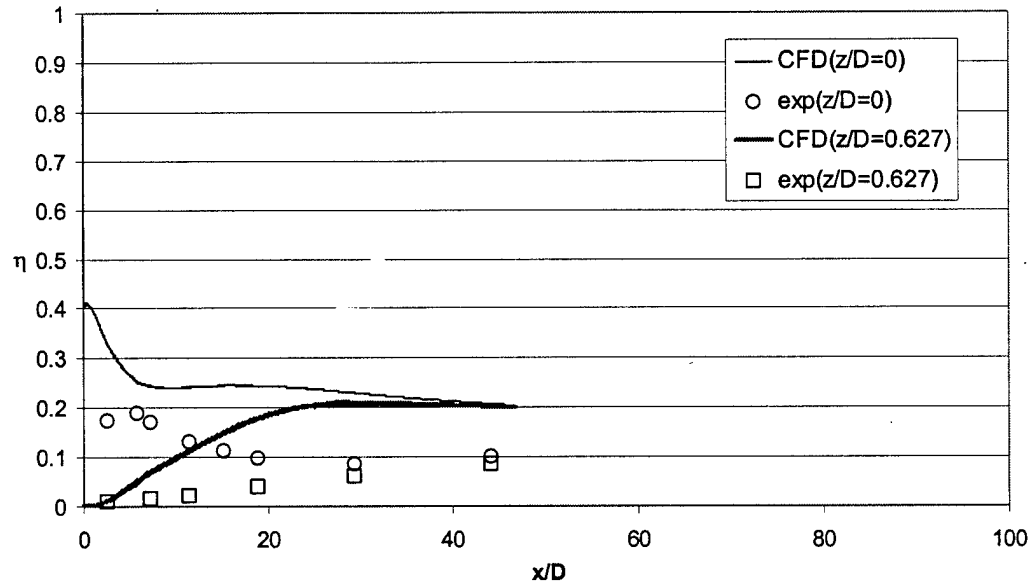


Figure 10. Laterally-averaged impermeable wall effectiveness for higher-curvature case ( $2r/D = 61$ ,  $DR = 2$ ).





(a)



(b)

Figure 11. Local variation of impermeable wall effectiveness versus downstream distance at two different spanwise locations. Higher-curvature case ( $2r/D = 61$ ,  $DR = 2$ );  $M = 1$  (a) and  $M = 1.9$  (b).

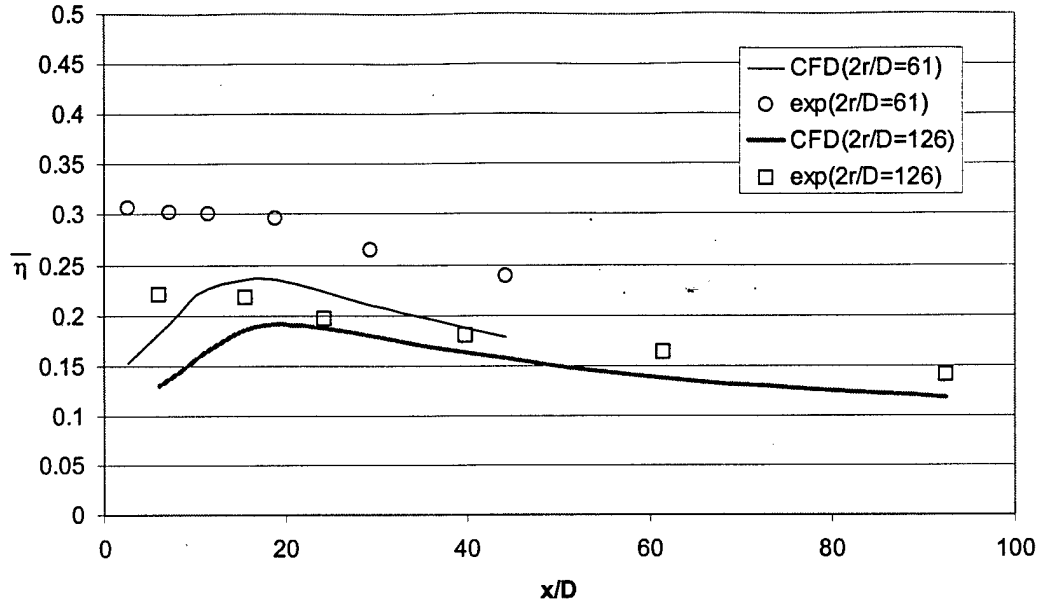


Figure 12. Comparison of laterally-averaged effectiveness for two different curvature strengths,  $M = 1$ ,  $DR = 2$ .

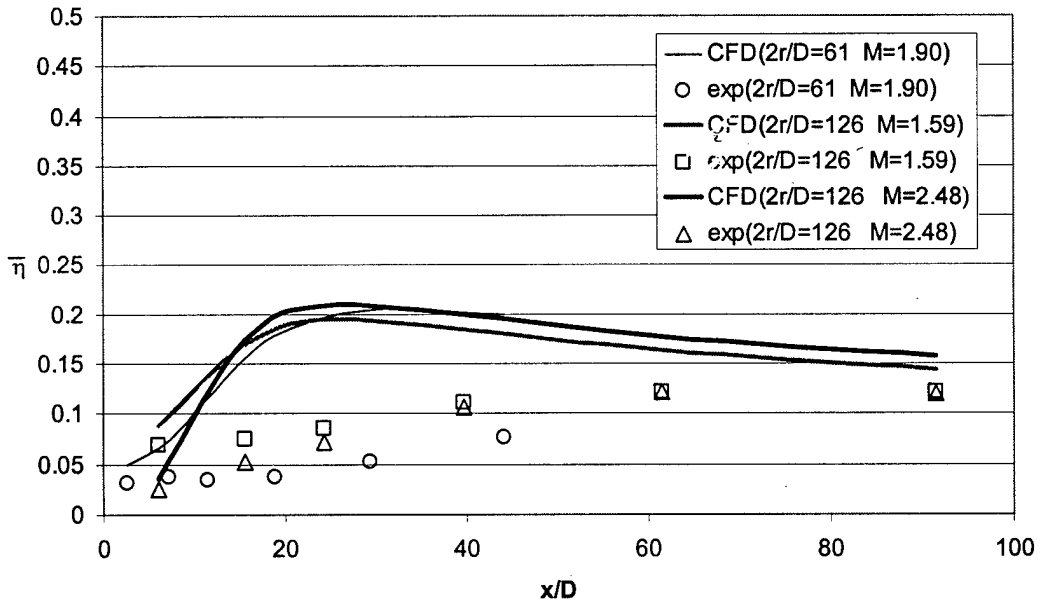
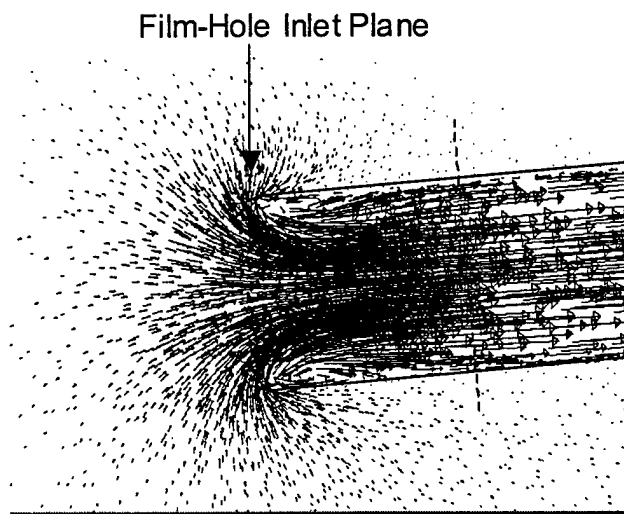
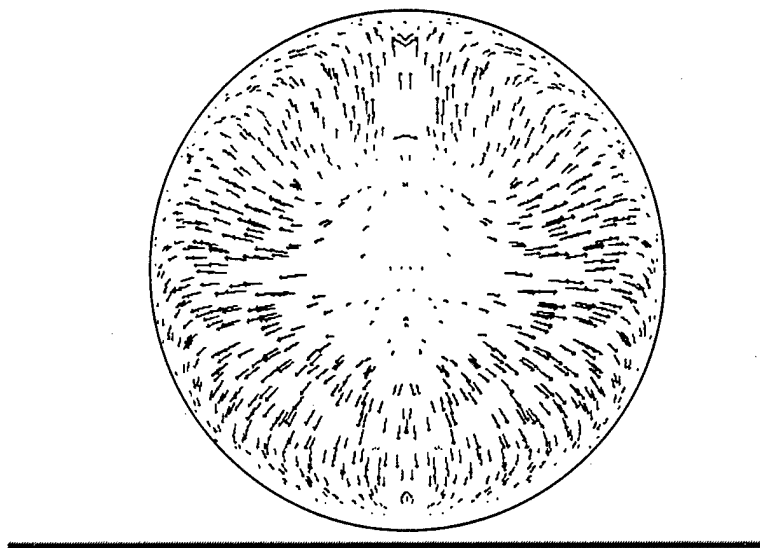


Figure 13. Comparison of laterally-averaged effectiveness for two different curvature strengths, for high blowing ratio ( $DR = 2$ ).

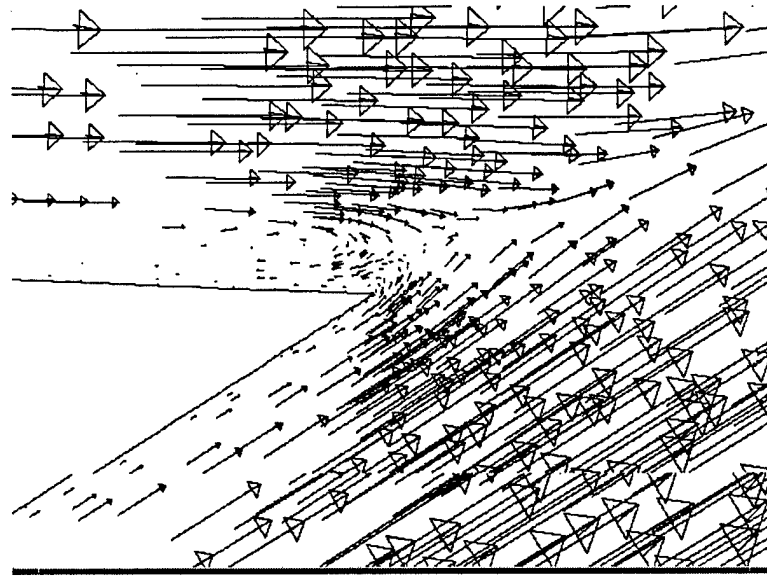


(a)

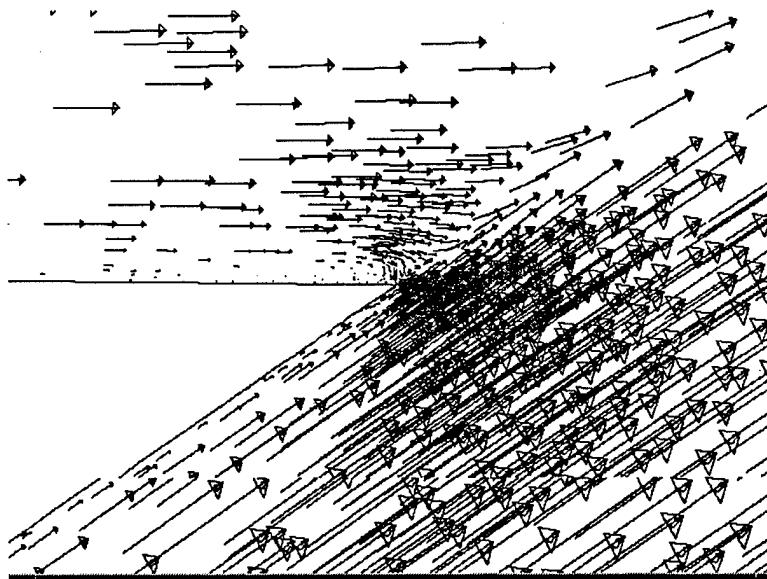


(b)

Figure 14. Velocity vectors illustrating the flowfield at the entrance to the film hole (a), and in a plane orthogonal to the film-hole axis (b). The viewing plane for (b) is indicated by the dashed line in (a).

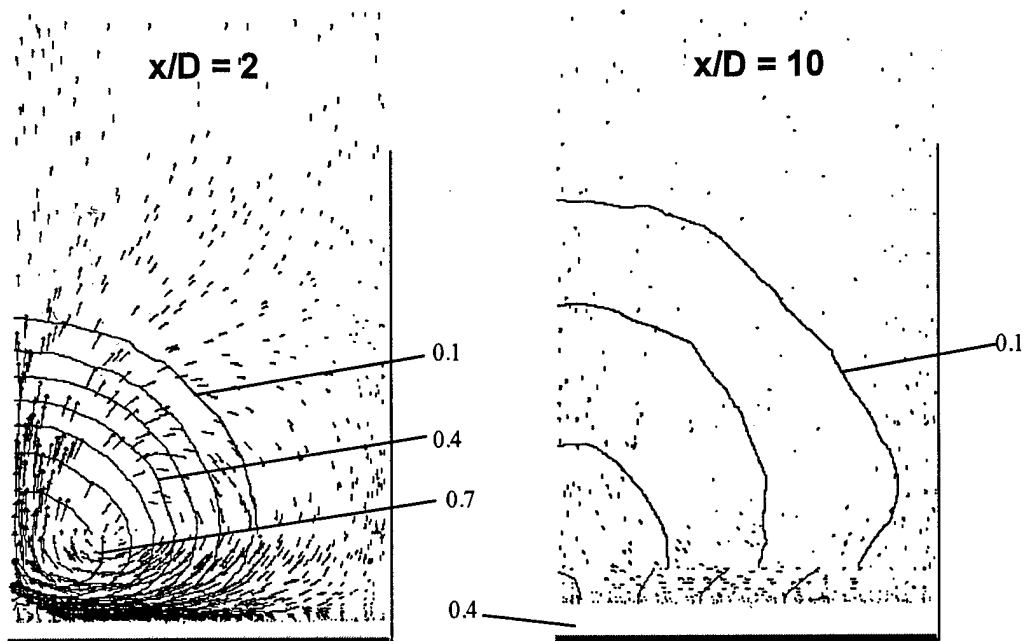


(a)

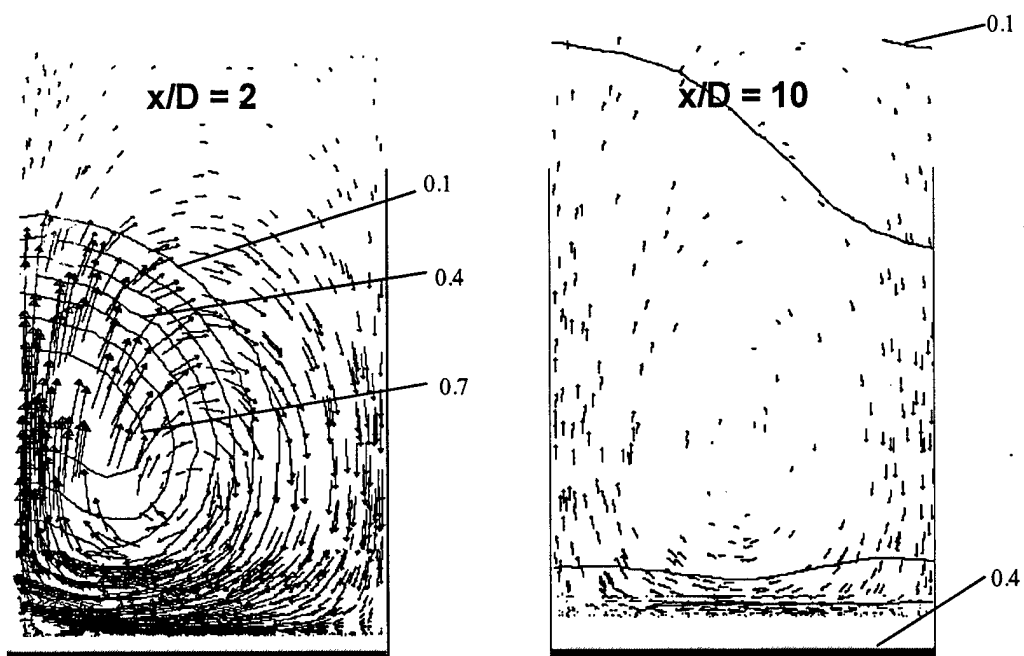


(b)

Figure 15. Velocity vectors showing horseshoe vortex formation upstream of the exiting coolant for the lower-curvature case. The horseshoe vortex is more pronounced for  $M = 1$  (a) than for  $M = 2.5$  (b).

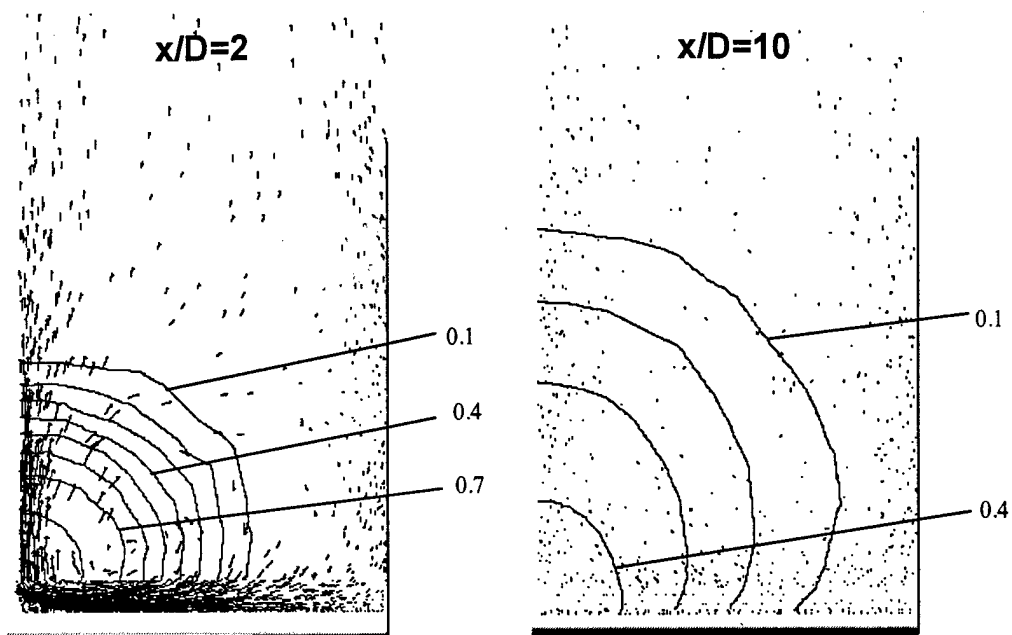


(a)

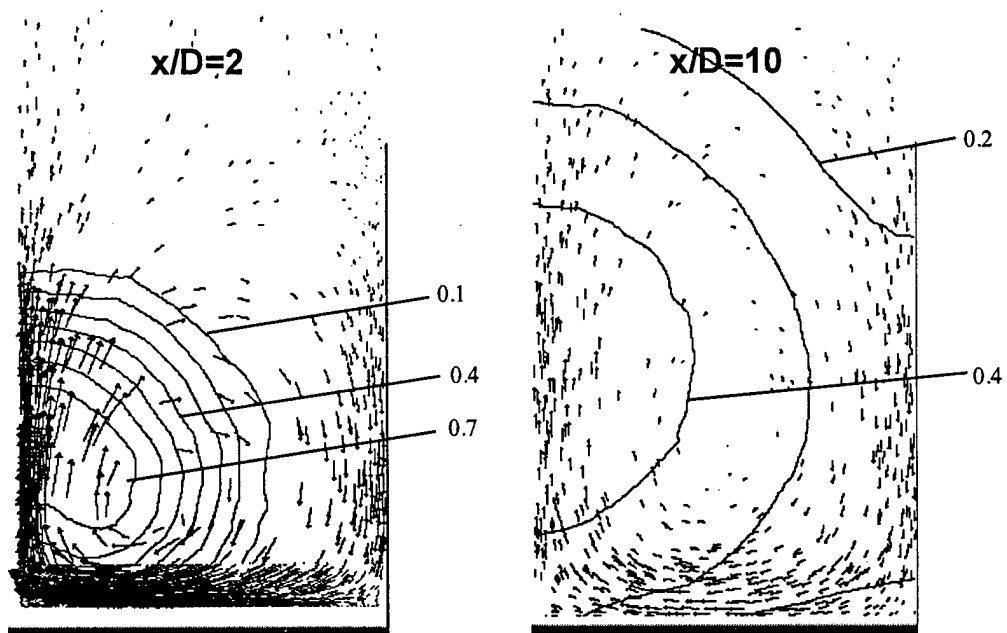


(b)

Figure 16. Contours of coolant mass fraction superimposed with velocity vectors in planes normal to the local streamwise direction at two different downstream locations. Cases shown are  $2r/D = 126$  and  $M = 1$  (a) and  $M = 2.5$  (b).

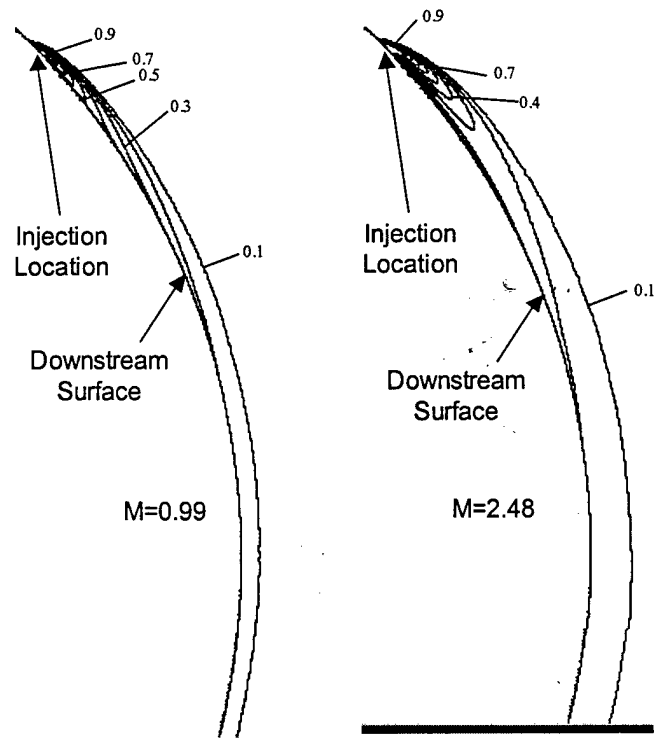


(a)

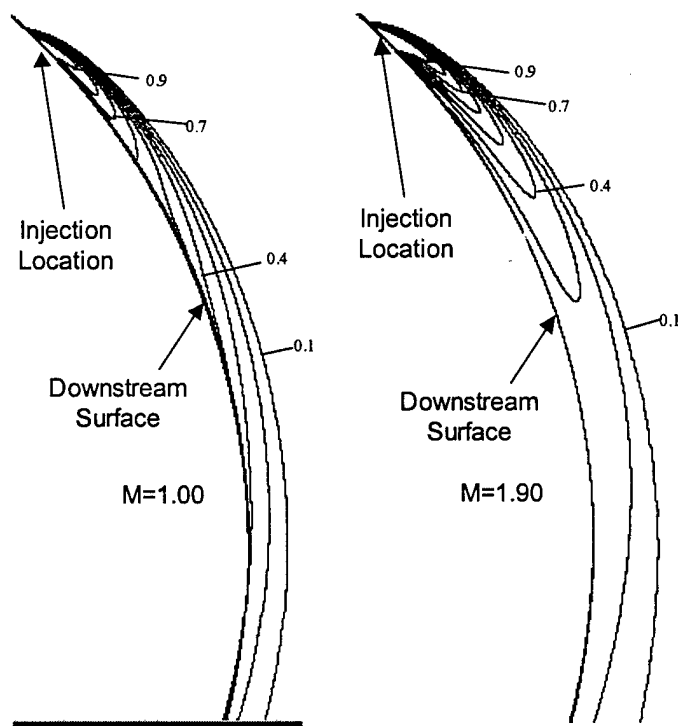


(b)

Figure 17. Contours of coolant mass fraction superimposed with velocity vectors in planes normal to the local streamwise direction at two different downstream locations. Cases shown are  $2r/D = 61$  and  $M = 1$  (a) and  $M = 1.9$  (b).



(a)



(b)

Figure 18. Contours of coolant mass fraction on the film-hole centerplane for lower-curvature (a) and higher-curvature (b) cases, for lowest and highest blowing ratios.

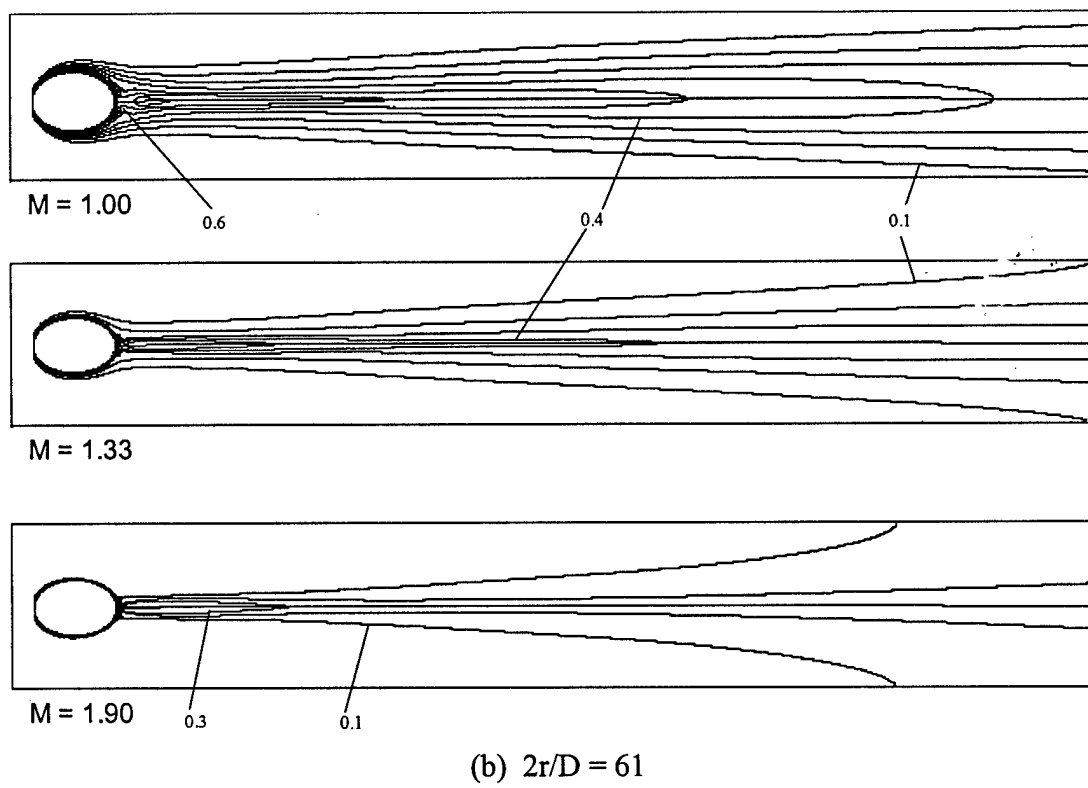
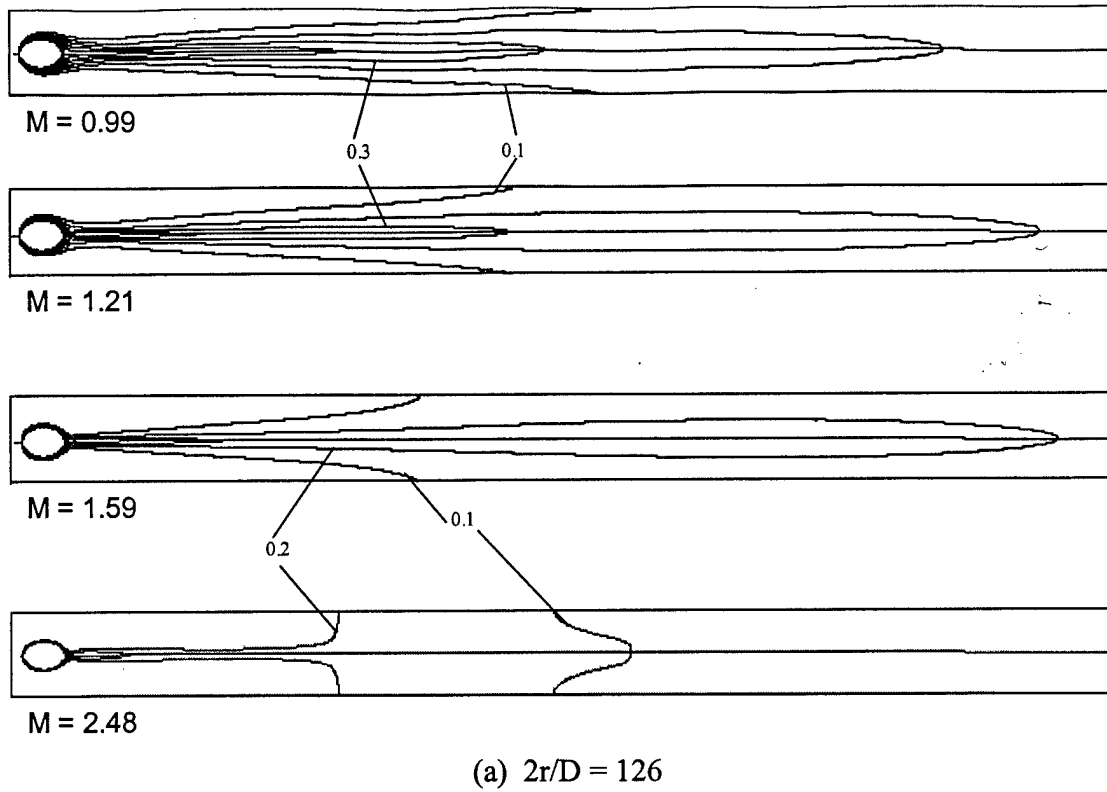


Figure 19. Contours of impermeable wall effectiveness for lower-curvature case (a) and higher-curvature case (b) for a range of blowing ratios.



## CHAPTER 3

### COMPUTATIONAL STUDY OF FILM-COOLING EFFECTIVENESS ON A LOW-SPEED AIRFOIL CASCADE – PART I: METHODOLOGY AND VALIDATION

D. Keith Walters and James H. Leylek

#### NOMENCLATURE

|              |  |
|--------------|--|
| D            | film-hole diameter   |
| DR           | density ratio = $\rho_j/\rho_\infty$                             |
| I            | momentum flux ratio = $(\rho u^2)_j/(\rho u^2)_\infty$           |
| k            | turbulent kinetic energy   |
| L            | film-hole length   |
| M            | blowing ratio = $(\rho u)_j/(\rho u)_\infty$                     |
| P            | film-hole pitch  |
| PS           | pressure surface   |
| Re           | Reynolds number  |
| RKE          | realizable $k$ - $\epsilon$ model                                |
| RNG          | <u>R</u> enormalization <u>G</u> roup $k$ - $\epsilon$ model     |
| RSM          | <u>R</u> eynolds <u>s</u> tress <u>m</u> odel                    |
| SKE          | standard $k$ - $\epsilon$  |
| SS           | suction surface  |
| T            | temperature  |
| u            | local velocity magnitude   |
| $y^+$        | non-dimensional wall distance                                    |
| $\alpha$     | injection angle  |
| $\delta$     | boundary layer thickness   |
| $\delta_0$   | boundary layer displacement thickness                            |
| $\epsilon$   | turbulence dissipation rate                                      |
| $\eta$       | adiabatic effectiveness = $(T_\infty - T_{aw})/(T_\infty - T_P)$ |
| $\bar{\eta}$ | laterally-averaged $\eta$  |
| $\rho$       | density  |

#### Subscripts

|          |  |
|----------|--|
| $\infty$ | free-stream condition at location of injection |
| aw       | adiabatic wall                                 |
| j        | jet conditions                                 |
| P        | plenum inlet conditions                        |

## 1. INTRODUCTION

Film cooling is a critical technology for modern gas turbine heat transfer design, yet the understanding of the complex fluid dynamic and heat transfer processes that govern film cooling is still limited. Research, both experimental and computational, is moving away from flat plates and toward realistic airfoil geometries in an attempt to increase understanding of these complex phenomena.

Film cooling on turbine airfoils remains primarily the interaction of an exiting coolant jet with a hot mainstream boundary layer, though it differs from flat-plate jet-crossflow interaction because of the influence of the more complex freestream (passage) flow. Specifically, the exiting jet is subjected to streamline curvature and streamwise pressure gradients caused by flow through the airfoil cascade. The downstream effectiveness is influenced by several physical mechanisms, including jet penetration into the freestream, formation of secondary flow structures, and turbulent mixing. The parameters which are generally recognized to govern the cooling performance include: the blowing ratio,  $M$ ; momentum flux ratio,  $I$ ; density ratio,  $DR$ ; the freestream boundary layer thickness relative to the film-hole diameter,  $\delta/D$  as well as the boundary layer condition (laminar or turbulent); the freestream and film-hole Reynolds and Mach numbers; the freestream turbulence intensity and length scale; and various parameters related to the coolant geometry, for example injection angle ( $\alpha$ ), compound angle,  $L/D$ ,  $P/D$  and hole shaping parameters. As mentioned above, airfoil film cooling is also influenced by the curvature of the freestream flow and by the presence of streamwise pressure gradients. On real airfoil geometries, neither of these will remain constant as the flow moves through the passage.

Because the overall research objective is to provide robust, economical design tools to the gas turbine industry, this paper seeks to provide a datum by which to judge the current capability of Reynolds-averaged Navier-Stokes (RANS) computational fluid dynamics (CFD) to effectively resolve these complex flows. It also seeks to document the physical mechanisms present in airfoil film cooling that significantly influence the cooling effectiveness, and to in part determine the effect of the above listed parameters on these physical mechanisms. To accomplish this, a 3-D Reynolds-Averaged Navier-Stokes simulation is performed on a well documented test from the open literature. Care is taken to ensure that all sources of error due to geometry modeling and grid are minimized, so that the performance of the simulations is placed squarely against the limitations of the turbulence models. The test geometry is a baseline case of a single row of streamwise injected, cylindrical holes, on both the pressure and suction surface of a realistic turbine airfoil.

## 2. LITERATURE REVIEW

This section highlights a few of the studies pertinent to the present work.

An early study of film cooling on an airfoil surface downstream of the leading edge region was documented in Ito (1976) and Ito et al. (1978), and forms the comparison data for the simulations presented herein. Measurements were taken on a linear airfoil cascade using a foreign gas injection technique, for a single row of streamwise-injected holes, and for a wide range of DR and M. The authors demonstrated the tendency of the coolant jet to react to the blade curvature effect depending on the coolant-to-mainstream momentum flux ratio. The pressure gradient normal to the flow direction tended to push a low momentum jet towards the convex surface and away from the concave surface, and vice versa for a high momentum jet.

A representative example of early CFD work on film cooling can be found in Bergeles et al. (1978). Typically, these first attempts were plagued with ineffective parabolic or semi-elliptic schemes that were incapable of resolving jet lift-off. They also suffered from insufficient grid resolution and quality, lower order discretization schemes, and overly simple turbulence models. Nevertheless, a great deal of useful information was gained from these first attempts, and applied to later efforts to improve computational capability.

Leylek and Zerkle (1994) used a flat plate film-cooling case to show that jet exit conditions were determined by the upstream flow in the film hole and coolant supply plenum, and as such these must be included to accurately resolve film-cooling flows. This point was underscored by Garg and Gaugler (1997) when they demonstrated that relatively small changes in applied jet exit conditions resulted in significant changes on the downstream airfoil surface. Several more recent computational film-cooling studies have also demonstrated the importance of modeling the coolant supply geometry in numerical simulations (Lin et al., 1997; Berhe and Patankar, 1998; Chernobrovkin and Lakshminarayana, 1998; Garg and Rigby, 1998).

A series of papers were presented by Leylek and co-workers (Walters and Leylek, 1997; McGovern and Leylek, 1997; Hyams and Leylek, 1997; Brittingham and Leylek, 1997) which analyzed the physical mechanisms governing film-cooling performance for four different cooling configurations. The results were analyzed by tracking vorticity to determine the source of secondary flow structures, and was an extension of the technique used by Moussa et al. (1977) in their experimental study of a normal jet in a crossflow. It was shown that the boundary layer vorticity within the film hole was the major source for the counter-rotating "kidney vortex" downstream of injection, a point that has also been underscored recently by the experimental work of Haven et al. (1997). The results of Part I also indicated that wall functions mask important small-scale flow features, and that low-Re or two-layer models should be used instead in the film-hole and near-field regions. As in all previous computational studies, the lateral spreading of the coolant jets was underpredicted.

A vorticity-based post-processing methodology was also used by Chernobrovkin and Lakshminarayana (1998) for their analysis of leading-edge airfoil film cooling. The computational domain included the coolant supply geometry, and downstream effectiveness results agreed well with the data of Cruse et al. (1997).

Lin and Shih (1998) simulated film cooling on flat and convex surfaces. The coolant supply geometry was modeled, and a low-Re  $k$ - $\epsilon$  model was used to effectively resolve the near-wall region. The film-cooling performance was explained in terms of the physical mechanisms, and the free-stream curvature was shown to alter the flow within the film hole relative to the flat plate case. Flat plate results compared to the experiments of Kohli and Bogard (1997) showed underprediction of downstream effectiveness near injection ( $x/D < 10$ ). The authors note that previous simulations using the standard  $k$ - $\epsilon$  model overpredicted the effectiveness in this region. The difference was attributed to the fact that wall functions in the previous cases induced artificially high turbulent diffusivity as well as numerical viscosity in the near-hole region.

The impact of turbulence models on flat plate film cooling was assessed by Ferguson et al. (1998). Previously, turbulence modeling influence on film cooling had been studied by Garg and Ameri (1997), but their simulation had not included the coolant supply geometry, and since grid independence was not addressed, grid-based errors may have affected the solutions. Ferguson et al. (1998) showed that near-wall resolution (via low-Re or two-layer models) was critical for accurately capturing downstream effectiveness.

The above review helps highlight outstanding issues for computational studies of airfoil film cooling. First, the fluid physics of airfoil film cooling is still not well understood. The impact of the acceleration and turning of the mainflow on film cooling, and vice-versa, has yet to be documented in detail, either experimentally or computationally. Also, the vorticity-based approach to analysis has not been applied to airfoil film cooling downstream of the leading-edge region, to see if it provides any insight into the complex physics. The influence of different turbulence modeling strategies has yet to be thoroughly documented for film-cooling problems, and has not been documented at all for airfoil film cooling. These issues form the motivation for the present work, which applies a systematic computational methodology to an airfoil film-cooling problem in order that all significant errors may be attributed to the turbulence treatment, allowing a realistic assessment of currently available models. The computational results will be used in combination with experiments to elucidate the underlying physical mechanisms responsible for airfoil film-cooling performance.

### 3. EXPERIMENTAL TEST CASE

The test case matches the experimental study documented in Ito (1976) and Ito et al. (1978). That study showed results for a single row of streamwise-injected film-cooling holes on both the pressure and suction surfaces of a linear airfoil cascade, illustrated in Figure 1. This figure shows the experimental configuration (a) as well as the geometry of the test blades (b). The cooling holes were located 10% (SS) and 15% (PS) of axial chord (145.3 mm) from the airfoil leading edge. The blade-to-blade distance of the cascade was 131.1 mm. The film holes had diameter ( $D$ ) of 2.38 mm, with  $P/D = 3$  and  $L/D \cong 4.4$ . The injection angle,  $\alpha$ , was  $35^\circ$ .

Results were obtained using a foreign gas injection technique, in which sample taps were located at several locations downstream of injection. Samples were drawn during steady state operation, and the concentration of foreign gas at the downstream locations was determined using gas chromatography. The analogous values for adiabatic effectiveness ( $\eta$ ) were obtained by application of the mass-heat transfer analogy, and the reader is referred to Ito (1976) for the details.

For all cases, both computational and experimental, the cascade inlet velocity was 14.1 m/s and the exit velocity was approximately 22 m/s. Based on exit velocity and axial chord, the Reynolds number was about  $2.3 \times 10^5$  and the Mach number was 0.06. On the suction surface, the approaching airfoil boundary layer displacement thickness at the injection location was 0.22 mm, and the boundary layer was assumed laminar based on  $Re_{\delta_0}$  at that location. On the pressure surface, the approach boundary layer was assumed turbulent due to an adverse pressure gradient that was present just downstream of the leading edge, although measurements to support this were not reported.

Experimentally, several combinations of DR and M were examined. The following chart lists the combinations that were simulated in the present study. Note that in the experiments, the listed values were nominal only, and some error was present (up to 2.5% in DR and 3.5% in M).

Table 1. Test Cases in the Present Study, Including Relevant Parameters

| <u>Case</u> | <u>Surface</u> | <u>DR</u> | <u>M</u> | <u>I</u> |
|-------------|----------------|-----------|----------|----------|
| S1          | SS             | 2.0       | 0.5      | 0.125    |
| S2          | SS             | 2.0       | 1.0      | 0.5      |
| S3          | SS             | 2.0       | 2.0      | 2.0      |
| P1          | PS             | 2.0       | 0.5      | 0.125    |
| P2          | PS             | 2.0       | 1.0      | 0.5      |
| P3          | PS             | 2.0       | 2.0      | 2.0      |

## 4. SIMULATION DETAILS

### 4.1 Geometry

The computational domain included the airfoil passage, the film-hole, and the supply plenum regions, and was chosen to match as closely as possible the experimental domain shown in Figure 1. It extended approximately one axial chord length upstream and one axial chord length downstream of the airfoil. The assumption of periodicity in the blade-to-blade direction was used so that repeating planes were applied at locations midway between consecutive airfoils, approximating an infinite cascade. The assumption of spanwise periodicity was used along with the fact that injection is in the streamwise

direction, so that only 1/2 of the spanwise pitch was included in the domain, and symmetry planes were applied in the center of the film-hole and at the mid-pitch plane between holes. This effectively modeled a cascade with infinite span. The geometry was generated using the I-DEAS Solid Modeling and FEA package from SDRC, Inc.

## 4.2 Grid

A novel grid generation methodology was implemented in order to satisfy all requirements of grid resolution and grid quality, including the requirement that near-wall cell centers be at approximately  $y^+ = 1$  for the two-layer near-wall treatment. The technique used an unstructured, multi-topology, multi-block approach along with solution-based adaption to ensure grid independence. The domain was partitioned into several different subsections in order to achieve maximum control over the grid quality and density. Each of the subsections was then meshed using an appropriate topology. For example, hexahedra were placed in near wall zones in order to achieve high aspect ratios very near the wall and extend the grid through the sublayer. In regions where a Cartesian grid was not feasible, tetrahedra were used in order to maintain high grid quality (minimize cell skewness). In the passage region far from the jet-crossflow interaction, the flow was assumed to be approximately 2-D, so triangular prisms were placed in these regions in order to reduce the overall cell count. Layers of pyramids were used to transition from tetrahedra to either hexahedra or prisms. Figures 2 and 3 show the grid for the SS cases. Figure 2 shows the grid on the  $z=0$  symmetry plane that exactly divides the film hole in the spanwise direction. Figure 3 shows the airfoil, film-hole, and plenum walls. Both of the figures highlight the advantages of the multi-topology approach used in the current study.

The background grids contained approximately 600,000 cells, the majority of which were placed in the film-hole and jet-crossflow interaction regions. In order to check grid independence, the solution for Case 2 (SS injection,  $DR = 2$ ,  $M = 1$ ) was refined based on gradients of all primary variables and near the wall, with the new grid containing 950,000 cells. This resulted in a negligible change of computed downstream  $\eta$ , and the results on the initial grid were therefore judged to be grid independent. The results from the initial grid are presented here.

Gridding was performed using a combination of I-DEAS and T-Grid grid generation package from Fluent, Inc.

## 4.3 Boundary Conditions

Boundary conditions were chosen to match the experimental test cases as closely as possible. As mentioned above, periodic planes were applied between the blades and symmetry conditions were applied on both the plane through the film-hole center and the mid-pitch plane. Upstream of the cascade, a constant velocity inlet was applied, with magnitude and flow direction of 14.1 m/s and  $44.3^\circ$  (see Figure 1). Neither inlet turbulence intensity nor turbulent length scale were documented experimentally, so assumed values of 0.5% and 1/100th of the blade-to-blade height were used. Freestream

(passage) inlet temperature was 300K. In the plenum, constant velocity was applied so that the required blowing ratio was achieved, and turbulence intensity and length scale were assumed 2% and 1/100th of the plenum "height" respectively. The coolant temperature was 150K. All walls were no slip and adiabatic. The use of a two-layer near wall treatment eliminated the need for wall functions.

#### 4.4 Solver

The simulations were processed using the Fluent software from Fluent, Inc. The particular solver was pressure correction with multi-grid acceleration. The discretization was a second-order accurate scheme for use with unstructured grid. The details of the numerical scheme are available in the Fluent User's Manual (1998). The solver has been extensively validated at Clemson University for problems ranging from laminar 2-D flow past a cylinder to 3-D flat plate film-cooling problems (e.g. Walters and Leylek, 1997).

Convergence was determined three ways. First, the overall residual level for each of the primary variables was monitored until it was reduced three orders of magnitude and was no longer changing with successive iterations. Second, the overall mass imbalance in the domain was required to be less than 0.01% of the mass flow entering the passage. Third, different locations in the flowfield were monitored to ensure that no flow variables were changing with increasing iterations, and thus a "steady state" had been achieved.

#### 4.5 Turbulence Modeling

Turbulence modeling remains as the most significant unresolved issue for practical computational treatment of film-cooling problems. The current study seeks to answer some of the questions regarding turbulence modeling for computational film cooling. Most significantly, the use of a systematic methodology allows the deficiencies of the turbulence treatment to be effectively isolated.

For the present cases, three different variations of the  $k$ - $\epsilon$  model were used on a reference case with no film cooling (solid blade) and case S2: the standard  $k$ - $\epsilon$  model of Launder and Spalding (1974), the RNG  $k$ - $\epsilon$  model (Yakhot et al., 1992), and a realizable  $k$ - $\epsilon$  (RKE) model (Shih et al., 1995). These models by their nature suffer from inherent isotropic turbulent viscosity, lack of "history" effects on the individual Reynolds stresses, no sensitivity to streamline curvature, and inability to represent turbulence at multiple scales. So additionally, results have been obtained for the solid-blade reference case using a form of the full Reynolds-Stress model (RSM) similar to the model documented by Launder and Shima (1989), but using an isotropic eddy-diffusivity for scalar transport, and an algebraic formulation for dissipation rate near the wall (Wolfstein, 1969). The results from the two-equation models are compared to the RSM reference case in order to evaluate them more effectively.

The reader is referred to Ferguson et al. (1998) for details of the SKE, RNG, and RSM models. The major difference between models is that the first two use an eddy viscosity to relate Reynolds stresses to the mean flow velocity gradients, whereas the

RSM model uses a transport equation for each of the Reynolds stresses themselves. Among the two-equation models, the RNG model differs from the SKE model primarily because it contains an extra source term in the transport equation for turbulence dissipation rate ( $\epsilon$ ). This extra term has the effect of increasing the generation of  $\epsilon$  in regions with high rates-of-strain.

The key feature of the RKE model is that the Reynolds stresses are made to remain physically realistic (meet realizability constraints) even in regions of the flow with high rates of strain. This is accomplished through a variable coefficient  $C_\mu$  in the definition of eddy viscosity. The use of a realizable model has been shown to improve prediction of turbulent flows with regions of high irrotational strain (Moore and Moore, 1999). In fact, the RKE model was found to significantly improve the computation of airfoil profile loss -- both with and without film cooling -- on the geometry under consideration in this study (Walters and Leylek, 1999). Figure 4 shows contours of turbulence intensity in the passage for the solid blade reference case for the four different turbulence models used in this study. Of concern is the excessive amount of turbulence generated by both the SKE and RNG models near the suction surface of the airfoil. It was shown that this excess turbulence resulted in poor calculation of airfoil profile loss downstream, whereas the RSM and RKE models showed very good agreement with experiments, shown in Figure 5. Please refer to Walters and Leylek (1999) for a thorough discussion.

Figure 6 shows  $\eta$  for case S2 using each of the two-equation models. The results are similar, with both standard and RNG  $k$ - $\epsilon$  models showing lower effectiveness values downstream due to the spurious turbulence generated in the passage. It is believed that proper resolution of the airfoil passage turbulence field is necessary for accurate film-cooling results, therefore the RKE model has been used for all of the film-cooling results presented in this paper. As discussed in the literature review, previous work has shown the necessity of resolving the flow very near the wall, particularly in the area near the film-hole exit (e.g. Walters and Leylek, 1997; Lin and Shih, 1998). All cases in the present study were computed using a two-layer near-wall treatment (Wolfstein, 1969) to provide near-wall resolution, and more accurately capture lift off of the coolant in the near field.

## 5. RESULTS AND DISCUSSION

Figure 7 shows the laterally averaged adiabatic effectiveness ( $\bar{\eta}$ ) plotted versus normalized downstream distance for each of the three cases (S1-S3) on the suction surface. Shown for comparison are the measured data from Ito (1976). The computations show similar qualitative behavior as the experiments. Agreement is best for the lowest blowing ratio case S1 ( $M = 0.5$ ) and worst for the highest blowing ratio case S3 ( $M = 2$ ). This trend is consistent with most reported simulations of film cooling in the open literature. However, all cases underpredict  $\bar{\eta}$  in the near-field region, which is counter to results typically obtained with wall function simulations. This is evidence of the fact that wall functions may in fact "smear" the exiting coolant near the blade surface, and that a more refined near-wall model is necessary to accurately capture jet lift-off. It



also suggests that the two-layer RKE model used for these simulations is not diffusive enough to accurately represent turbulent mixing close to the surface in the near field.

Local adiabatic effectiveness,  $\eta$ , versus downstream distance is plotted in Figure 8 along four different spanwise locations for case S2. Comparison with experimental data indicates that the lateral spread rate of the coolant near the downstream wall is underpredicted. This was found to be true for all cases in this study, and is consistent with all computational film cooling studies found in the open literature that use two-equation eddy-viscosity turbulence models. Several experimental studies (e.g. Kaszeta and Simon, 1999) suggest that the use of an isotropic eddy viscosity is insufficient to resolve the lateral spreading of the coolant jet, so it is not surprising to see such a result repeated here. The spread rate was also underpredicted for all three cases on the pressure surface.

The laterally averaged adiabatic effectiveness for the three pressure surface cases is compared to experiments in Figure 9. As with the suction surface cases above, the qualitative trends are matched by the computations. Also similar is the fact that the agreement is best for the lowest blowing ratio case, and gets progressively worse as  $M$  increases. However, for the two lowest  $M$  cases on the PS, effectiveness is overpredicted downstream of the near field, while it is underpredicted in this region for the SS cases. Reasons for this different trend are addressed in Part II.

The footprint of adiabatic effectiveness on the airfoil surface for each case is shown in Figure 10. Comparison between SS and PS results indicates the improved cooling on the SS at  $M = 0.5$  and  $M = 1$ . The opposite trend is seen for the  $M = 2$  cases. This behavior is consistent with experimental studies, and is typically attributed to the tendency of a coolant jet to be pushed toward a convex wall at  $I < 1$  and away from a convex wall at  $I > 1$ , and vice-versa for a concave wall (e.g. Ito, 1976). Physical mechanisms responsible for this behavior are examined more thoroughly in Part II.

## 6. CONCLUSIONS

This paper, part one of two, has presented a computational simulation of film cooling on a realistic turbine airfoil geometry, downstream of the leading edge. The methodology was outlined in detail, and results were compared to a well-documented experimental test case found in the open literature. Specific highlights of the present methodology include careful treatment of geometry, grid, boundary conditions, and convergence, so that all errors can confidently be attributed to the turbulence treatment. A realizable  $k$ - $\epsilon$  eddy-viscosity model was chosen in order to accurately resolve the passage turbulence field, which is believed to be critical to accurate film-cooling simulations.

The results of the computations were able to accurately reproduce the trends of the measured data. Agreement was best at low blowing ratio, and became progressively worse as  $M$  increased. This suggests that the correct mean-flow physical mechanisms

were predicted, although not the correct magnitudes of these mechanisms. Part II of this paper will examine these mean-flow physical mechanisms in detail. In addition, part II will address known shortcomings in the turbulence treatment that may be responsible for differences between experiments and computations.

## REFERENCES

Bergeles, G., Gosman, A.D., and Launder, B.E., 1978, "The Turbulent Jet in a Cross Stream at Low Injection Rates: A Three-Dimensional Numerical Treatment." *Numerical Heat Transfer*, Vol. 1, pp. 217-242.

Berhe, M.K. and Patankar, S.V., 1998, "Curvature Effects on Discrete-Hole Film Cooling," ASME Paper No. 98-GT-373.

Brittingham, R.A. and Leylek, J.H., 1997, "A Detailed Analysis of Film Cooling Physics Part IV: Compound-Angle Injection with Shaped Holes," ASME Paper No. 97-GT-272.

Chernobrovkin, A. and Lakshminarayana, B., 1998, "Numerical Simulation and Aerothermal Physics of Leading Edge Film Cooling," ASME Paper No. 98-GT-504.

Cruse, M.W., Yuki, U.M., and Bogard, D.G., 1997, "Investigation of Various Parametric Influences on Leading Edge Film Cooling," ASME Paper No. 97-GT-296.

Ferguson, J.D., Walters, D.K., and Leylek, J.H., 1998, "Performance of Turbulence Models and Near-Wall Treatments in Discrete Jet Film Cooling Simulations," ASME Paper No. 98-GT-438.

Garg, V.K. and Ameri, A.A., 1997, "Comparison of Two-Equation Turbulence Models for Prediction of Heat Transfer on Film-Cooled Turbine Blades," ASME Paper No. 97-GT-24.

Garg, V.K. and Gaugler, R.E., 1997, "Effect of Velocity and Temperature Distribution at the Hole Exit on Film Cooling of Turbine Blades," ASME Journal of Turbomachinery, Vol. 119, pp. 343-351.

Garg, V.K. and Rigby, D.L., 1998, "Heat Transfer on a Film-Cooled Blade - Effect of Hole Physics," ASME Paper No. 98-GT-404.

Haven, B.A., Yamagata, D.K., Kurosaka, M., Yamawaki, S., and Maya, T., 1997, "Anti-Kidney Pair of Vortices in Shaped Holes," ASME Paper No. 97-GT-45.

Hyams, D.G. and Leylek, J.H., 1997, "A Detailed Analysis of Film-Cooling Physics Part III: Streamwise Injection with Shaped Holes," ASME Paper No. 97-GT-271.

Ito, S., 1976, "Film Cooling and Aerodynamic Loss in a Gas Turbine Cascade," Ph.D. Thesis, University of Minnesota.

Ito, S., Goldstein, R.J., and Eckert, E.R.G., 1978, "Film Cooling of a Gas Turbine Blade," ASME Journal of Engineering for Power, Vol. 100, pp. 476-481.

Kaszeta, R.W., and Simon, T.W., 1999, "Measurement of Eddy Diffusivity of Momentum in Film-Cooling Flows with Streamwise Injection," ASME Paper No. 99-GT-37.

Kohli, A. and Bogard, D.G., 1997, "Adiabatic Effectiveness, Thermal Fields, and Velocity Fields for Film Cooling with Large Angle Injections," ASME Journal of Turbomachinery, Vol. 119, pp. 352-358.

Launder, B.E. and Shima, N., 1989, "Second-Moment Closure for the Near-Wall Sublayer: Development and Application," AIAA Journal, Vol. 27, pp. 1319-1325.

Launder, B.E. and Spalding, D.B., 1974, "The Numerical Computation of Turbulent Flows," Computer Methods in Applied Mechanics and Engineering, Vol. 3, pp. 269-289.

Leylek, J., and Zerkle, R., 1994, "Discrete-Jet Film Cooling: A Comparison of computational Results with Experiments," *Journal of Turbomachinery*, Vol. 116, pp. 358-368.

Lin, Y.-L. and Shih, T. I-P., 1998, "Computations of Discrete-Hole Film Cooling over Flat and Convex Surfaces," ASME Paper No. 98-GT-436.

Lin, Y.-L., Stephens, M.A., and Shih, T. I-P., 1997, "Computation of Leading-Edge Film Cooling with Injection through Rows of Compound-Angle Holes," ASME Paper No. 97-GT-298.

McGovern, K.T. and Leylek, J.H., 1997, "A Detailed Analysis of Film-Cooling Physics Part II: Compound-Angle Injection with Cylindrical Holes," ASME Paper No. 97-GT-270.

Moore, J.G. and Moore, J., 1999, "Realizability in Turbulence Modeling for Turbomachinery CFD," ASME Paper No. 99-GT-24.

Moussa, Z.M., Trischka, J.W., and Eskinazi, S., 1977, "The Near Field in the Mixing of a Round Jet with a Cross-stream," *Journal of Fluid Mechanics*, Vol. 80, Part 1, pp. 49-80.

Shih, T.-H., Liou, W.W., Shabbir, A., and Zhu, J., 1995, "A New  $k-\epsilon$  Eddy-Viscosity Model for High Reynolds Number Turbulent Flows Model Development and Validation," *Computers in Fluids*, Vol. 24(3), pp. 227-238.

Walters, D., and Leylek, J., 1997, "A Detailed Analysis of Film-Cooling Physics -- Part I: Streamwise Injection with Cylindrical Holes," ASME Paper No. 97-GT-269.

Wolfstein, M., 1969, "The Velocity and Temperature Distribution of One-Dimensional Flow with Turbulence Augmentation and Pressure Gradient," *International Journal of Heat and Mass Transfer*, Vol. 12, pp. 301-318.

Yakhot, V., Orszag, S.A., Thangam, S.A., Gatski, T.B., and Speziale, C.G., 1992, "Development of Turbulence Models for Shear Flows by a Double Expansion Technique," *Physics of Fluids Part A*, Vol. 4, pp. 1510-1520.



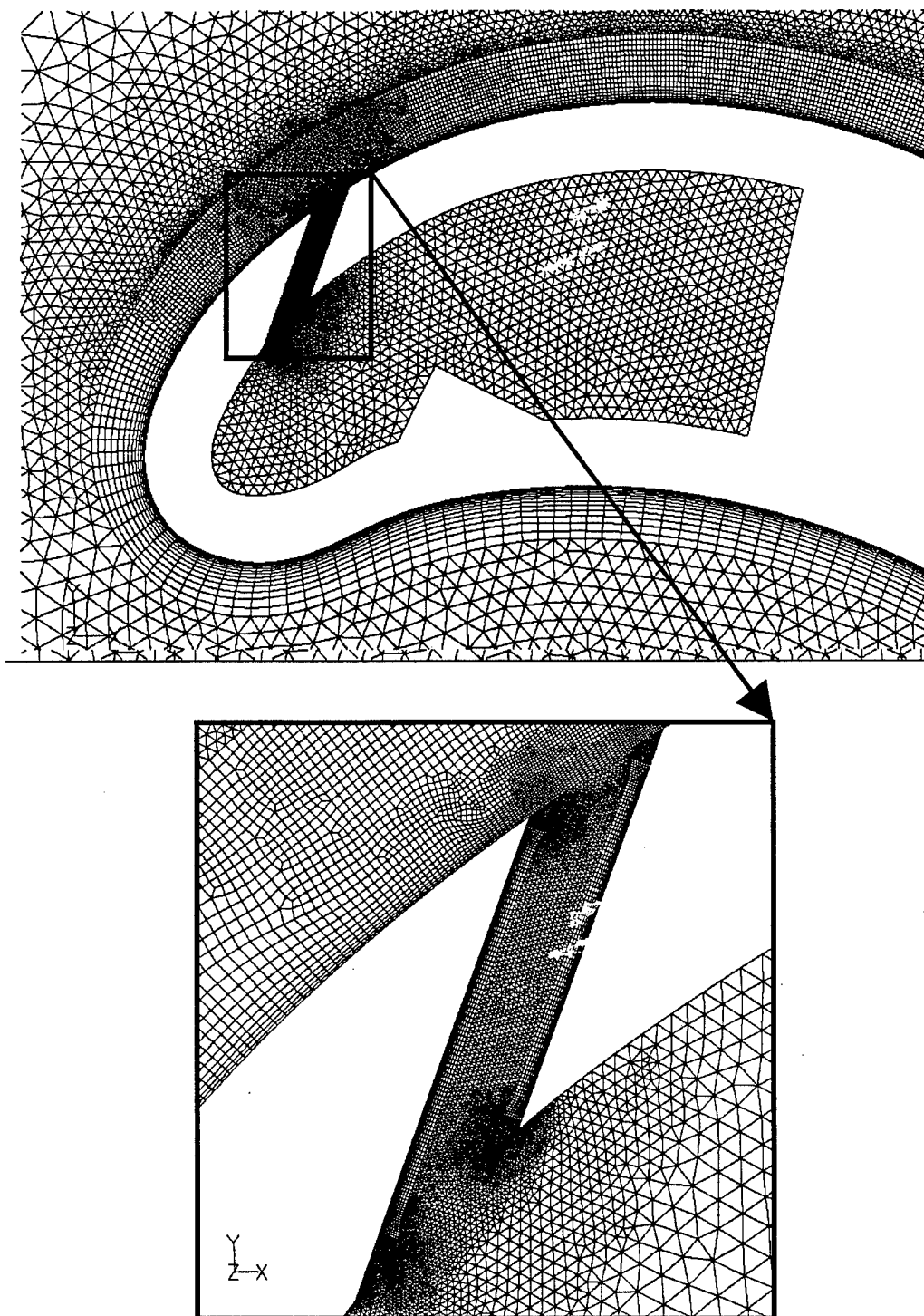


Figure 2. Illustration of mesh on centerline ( $z=0$ ) plane highlights the multi-topology approach and grid resolution in the film-hole region.

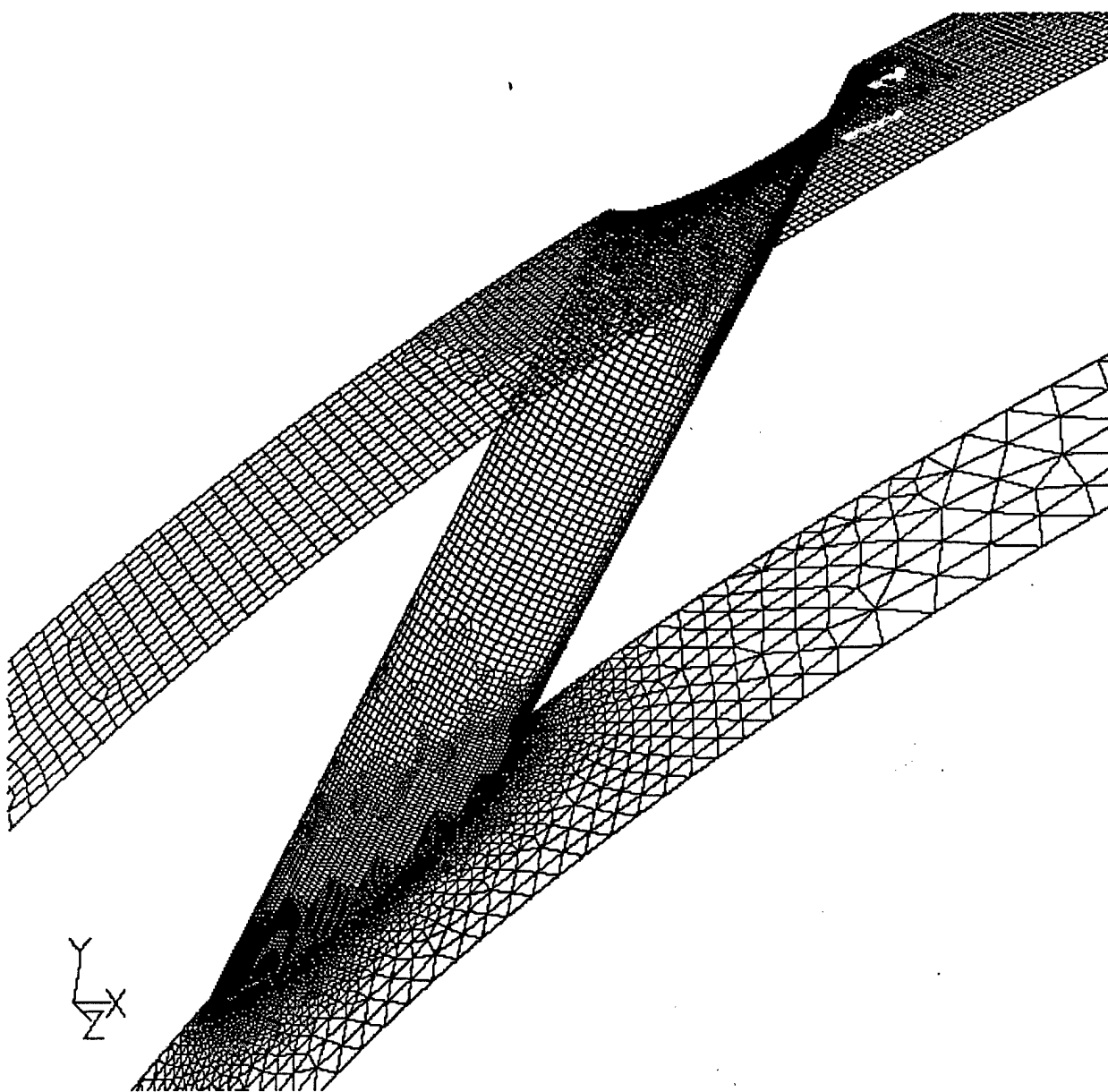


Figure 3. Multi-topology surface mesh showing the SS airfoil, film-hole, and plenum walls.

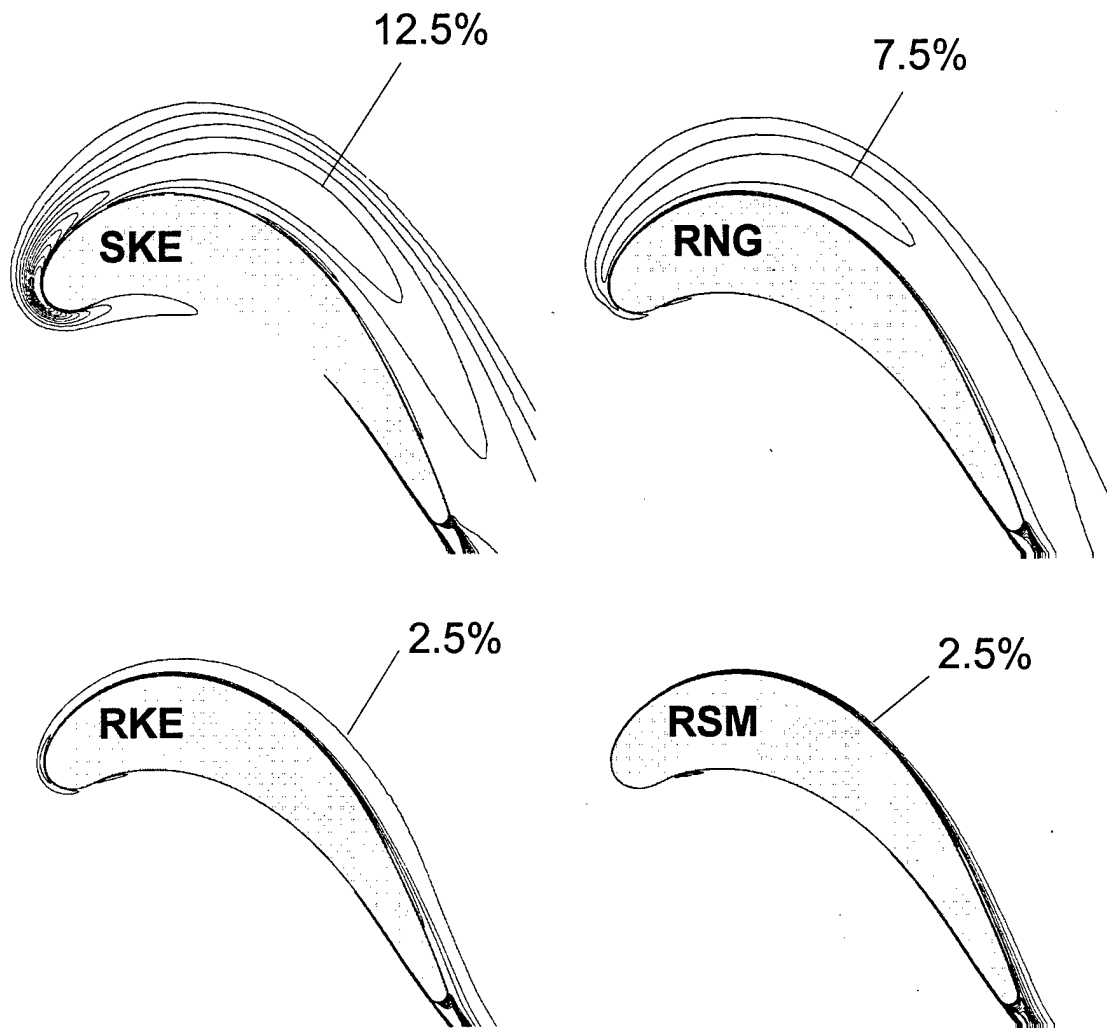


Figure 4. Contours of turbulence intensity for the solid blade reference case show the unrealistic passage turbulence field predicted by the SKE and RNG models.



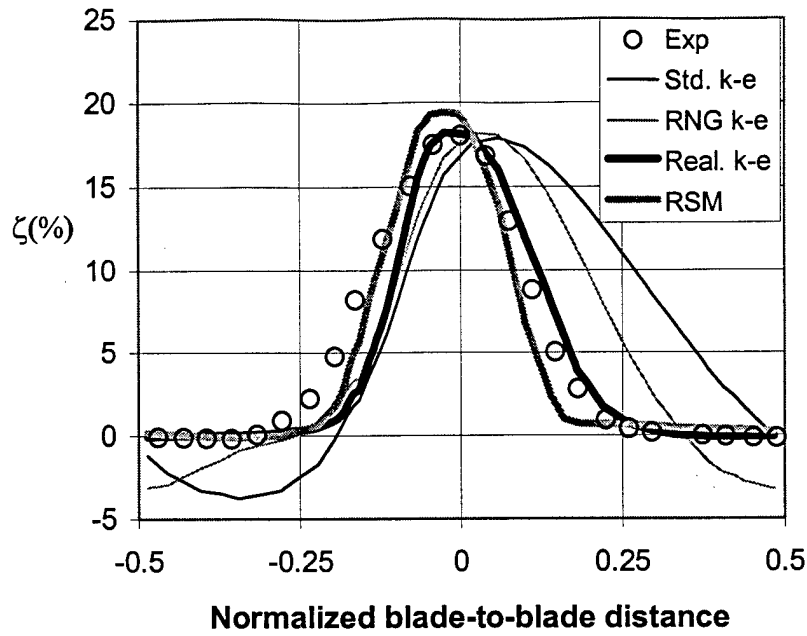


Figure 5. Prediction of primary loss coefficient on solid blade reference case shows best agreement using either RSM or RKE turbulence model.

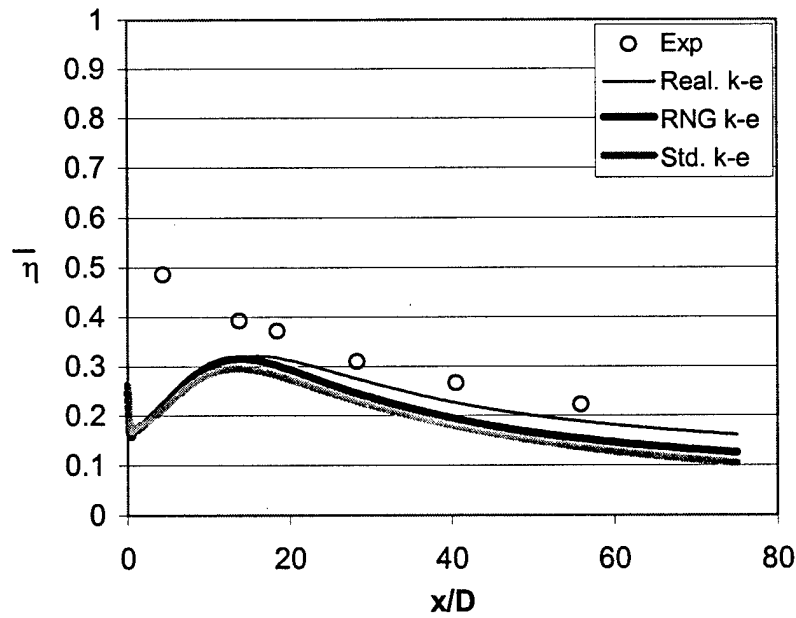


Figure 6. Laterally-averaged adiabatic effectiveness for case S2 (SS;  $M=1$ ) shows different values downstream due to passage turbulence field.

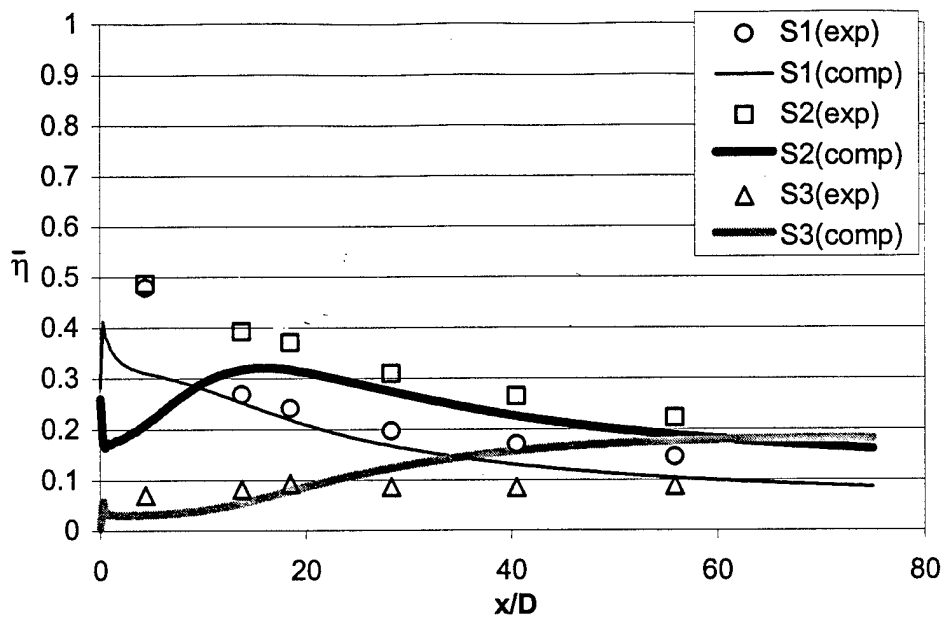


Figure 7. Laterally-averaged adiabatic effectiveness for the three SS cases shows agreement with experimental trends.

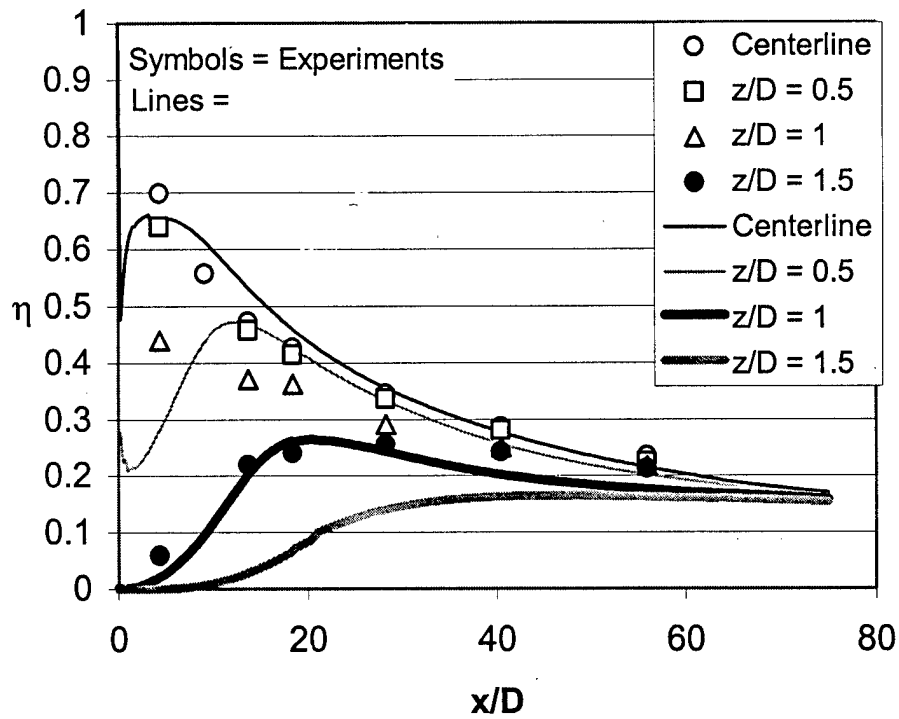


Figure 8. Adiabatic effectiveness at four spanwise stations highlights the underprediction of lateral spread rate in the computations.

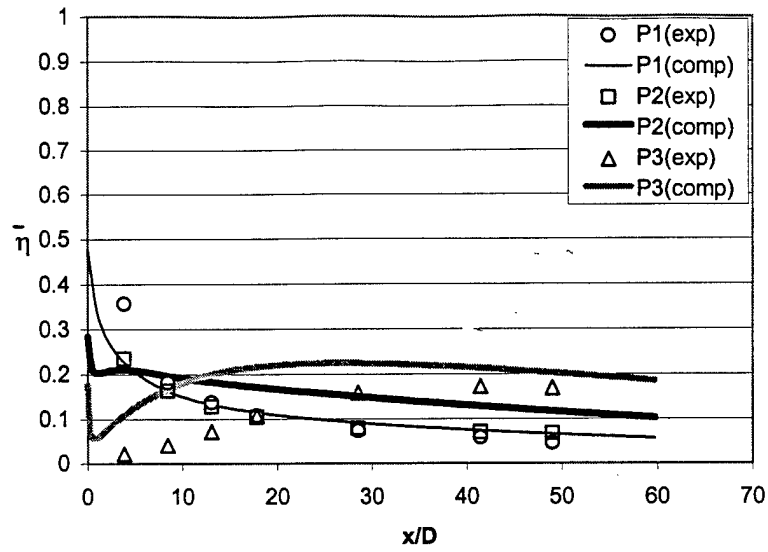
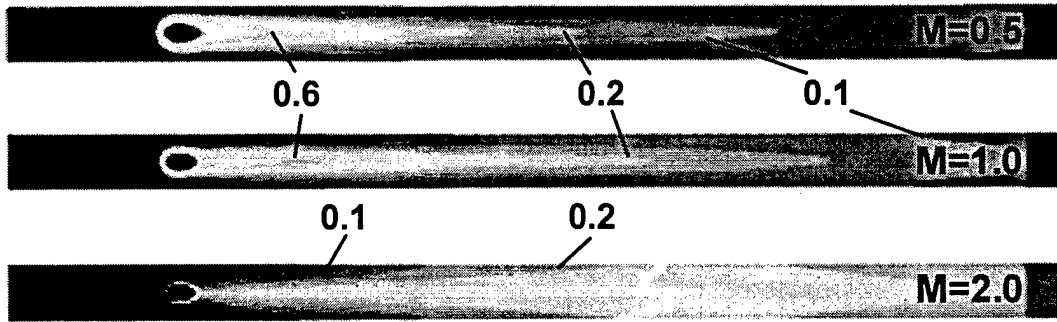
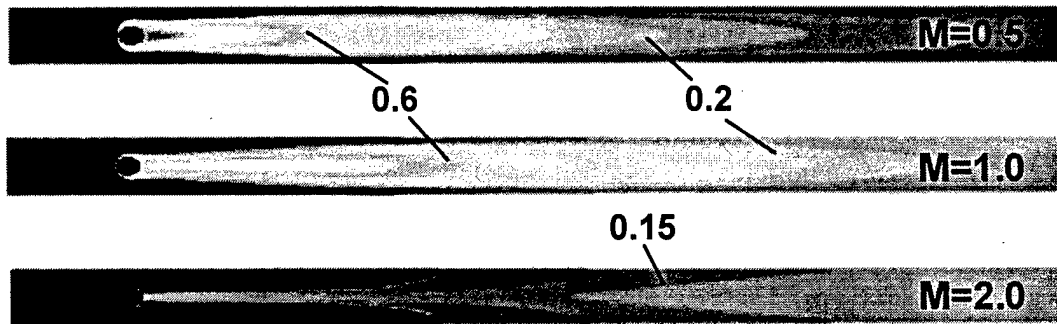


Figure 9. Laterally-averaged adiabatic effectiveness for the three PS cases show agreement with experimental trends, but significant overprediction as  $M$  increases.



(a) SS



(b) PS

Figure10. Contours of adiabatic effectiveness for all six cases in the present study.

## CHAPTER 4

### COMPUTATIONAL STUDY OF FILM-COOLING EFFECTIVENESS ON A LOW-SPEED AIRFOIL CASCADE – PART II: DISCUSSION OF PHYSICS

D. Keith Walters and James H. Leylek

#### NOMENCLATURE

|              |   |
|--------------|---|
| D            | film-hole diameter  |
| DR           | density ratio = $\rho_j/\rho_\infty$  |
| I            | momentum flux ratio = $(\rho u^2)_j/(\rho u^2)_\infty$                            |
| k            | turbulent kinetic energy  |
| L            | film-hole length  |
| M            | blowing ratio = $(\rho u)_j/(\rho u)_\infty$                                      |
| P            | film-hole pitch   |
| PS           | pressure surface  |
| Re           | Reynolds number   |
| R            | local airfoil radius of curvature   |
| RKE          | realizable $k$ - $\epsilon$ model   |
| RNG          | Renormalization Group $k$ - $\epsilon$ model                                      |
| RSM          | Reynolds stress model   |
| SKE          | standard $k$ - $\epsilon$   |
| SS           | suction surface   |
| T            | temperature   |
| u            | local velocity magnitude  |
| $y^+$        | non-dimensional wall distance   |
| $\alpha$     | injection angle   |
| $\delta$     | boundary layer thickness  |
| $\delta_0$   | boundary layer displacement thickness   |
| $\epsilon$   | turbulence dissipation rate   |
| $\eta$       | adiabatic effectiveness = $(T_\infty - T_{aw})/(T_\infty - T_p)$                  |
| $\bar{\eta}$ | laterally-averaged $\eta$   |
| $\kappa$     | acceleration parameter = $(v_\infty/u_\infty^2) * \partial u_\infty / \partial x$ |
| $\rho$       | density   |
| $\nu$        | fluid kinematic viscosity   |

#### Subscripts

|          |  |
|----------|--|
| $\infty$ | free-stream condition at location of injection |
| aw       | adiabatic wall                                 |
| j        | jet conditions                                 |
| P        | plenum inlet conditions                        |

## 1. INTRODUCTION

The physics of film cooling on airfoils is complex and not thoroughly understood. It is primarily concerned with the interaction of an exiting coolant jet with a hot mainstream boundary layer, though it differs from flat-plate jet-crossflow interaction because of the influence of the more complex freestream (passage) flow. Specifically, the exiting jet is subjected to streamline curvature and streamwise pressure gradients caused by flow through the airfoil cascade. The downstream effectiveness is influenced by several physical mechanisms, including jet penetration into the freestream, formation of secondary flow structures, and turbulent mixing. The parameters which are generally recognized to govern the cooling performance include: the blowing ratio,  $M$ ; momentum flux ratio,  $I$ ; density ratio,  $DR$ ; the freestream boundary layer thickness relative to the film-hole diameter,  $\delta/D$  as well as the boundary layer condition (laminar or turbulent); the freestream and film-hole Reynolds and Mach numbers; the freestream turbulence intensity and length scale; and various parameters related to the coolant geometry, for example injection angle ( $\alpha$ ), compound angle ( $\phi$ ),  $L/D$ ,  $P/D$  and hole shaping parameters. As mentioned above, airfoil film cooling is also influenced by the curvature of the freestream flow and by the presence of streamwise pressure gradients. On real airfoil geometries, neither of these will remain constant as the flow moves through the passage.

This two-part paper documents a computational study of film cooling on a modern turbine airfoil. Part I presented a review of available literature for airfoil film-cooling problems, details of the experimental test case and computational methodology, and a comparison of computed and measured results. The computational methodology systematically addresses common sources of error -- specifically geometry, grid quality, grid resolution (independence), boundary conditions, and convergence -- so that the simulations are believed to be truly limited only by the turbulence treatment. Comparison between simulation and experimental trends documented in Part I suggests that the mean-flow physical mechanisms are in fact reproduced in the computations, while highlighting specific deficiencies in the two-equation eddy-viscosity turbulence model. The current part examines the mean-flow physical mechanisms in detail, including their origin and impact on film-cooling performance. The current part also discusses the influence of the turbulence modeling at more length.

## 2. TEST CASE

As detailed in Part I, the test case is documented in Ito (1976) and Ito et al. (1978). Experimental results were obtained for a single row of streamwise-injected, cylindrical film holes on the suction and pressure surface of a turbine airfoil, downstream of the leading edge. The film holes had injection angle  $35^\circ$ ,  $L/D = 4.4$ , and  $P/D = 3$ . A schematic of the test case is shown in Figure 1.

Inlet velocity to the cascade was 14.1 m/s, and exit velocity was 22 m/s. Based on inlet velocity and axial chord, Reynolds number and Mach number were  $2.3 \times 10^5$  and 0.06 respectively. The boundary layer was assumed turbulent on the pressure surface due

to a small adverse pressure gradient near the leading edge, and the suction surface boundary layer was assumed laminar.

Combinations of nominal density ratio (DR), blowing ratio (M) and momentum-flux ratio (I) investigated in the present study are listed in Table 1.

Table 1. Test Cases in the Present Study

| <u>Case</u> | <u>Surface</u> | <u>DR</u> | <u>M</u> | <u>I</u> |
|-------------|----------------|-----------|----------|----------|
| S1          | SS             | 2.0       | 0.5      | 0.125    |
| S2          | SS             | 2.0       | 1.0      | 0.5      |
| S3          | SS             | 2.0       | 2.0      | 2.0      |
| P1          | PS             | 2.0       | 0.5      | 0.125    |
| P2          | PS             | 2.0       | 1.0      | 0.5      |
| P3          | PS             | 2.0       | 2.0      | 2.0      |

### 3 SIMULATION DETAILS

The computational methodology was outlined in Part I. The computational domain included one-half film-hole pitch in the passage, film-hole, and supply plenum regions, using symmetry and periodic boundary conditions to model an infinite length airfoil and infinite cascade, respectively. The grid was generated using an unstructured multi-topology approach that includes resolution of the near-wall regions for implementation of a two-layer turbulence treatment. Grid independence was checked using adaption based on gradients of primary variables in the background solution, as well as refinement near walls. The boundary conditions included constant velocity, temperature, turbulence kinetic energy ( $k$ ) and turbulence dissipation rate ( $\epsilon$ ) at both passage and plenum inlets. The passage freestream turbulence was low (0.5%). DR was applied through the use of different temperatures for passage and coolant flows, 300K and 150K respectively.

The simulations were processed using the Fluent 5.1 software from Fluent, Inc. A second-order accurate discretization scheme was used to reduce the influence of numerical viscosity. Care was taken to ensure that all results are fully converged and grid independent.

A discussion of turbulence modeling for the present cases was presented in Part I. Four different turbulence models were tested on a solid-blade reference case: standard  $k$ - $\epsilon$  (SKE), Renormalization Group  $k$ - $\epsilon$  (RNG), realizable  $k$ - $\epsilon$  (RKE), and a Reynolds stress model (RSM). Each of the two-equation models was also tested on film-cooling case S2. Among these, it was determined that the RKE model most successfully reproduced the passage turbulence field, and led to the most accurate downstream prediction of adiabatic

effectiveness. This model was then used to simulate the remaining cases in Table I, and the results obtained with RKE are presented in the current part of the paper. Although the RKE model most accurately computed the passage turbulence field, it still suffers from known deficiencies, including isotropic eddy viscosity, lack of history effects on Reynolds stresses, and no sensitivity to streamline curvature. These deficiencies are expected to influence the simulation results. The two-layer model was used to resolve the near-wall flow, in order to capture small-scale features of the flowfield near the jet-injection location.

## 4. RESULTS AND DISCUSSION

This section contains primarily a description of the mean-flow physical mechanisms influencing film-cooling performance for these cases. Comparison with the experimental data in Part I demonstrated that the computations appeared to capture the correct mean-flow physics, although turbulence model deficiencies resulted in discrepancy between computed and measured results. As such, useful qualitative descriptions of the origin and influence of various physical mechanisms is possible.

### 4.1 Suction Surface Versus Pressure Surface Cases

The freestream into which the coolant is exiting is quite different depending on which surface is being considered. Primarily, the differences have to do with streamline curvature, streamwise pressure gradient, and the approaching boundary layer. The curvature parameter  $2R/D$  is plotted for both surfaces in Figure 2. Both surfaces exhibit strong curvature -- convex on the SS and concave on the PS -- that varies in magnitude along the length of the blade. The impact of curvature on flow development downstream of coolant injection is highlighted below.

The airfoil loading curve for these cases is shown in Figure 3, and compared to experimental data. The excellent agreement indicates that the inviscid features of the flow are well captured by the computations. The presence of streamwise pressure gradients is apparent from the figure. In an attempt to quantify the influence of the streamwise pressure gradient, figure 4 shows the freestream acceleration parameter,  $\kappa$ , for both surfaces. On the SS,  $\kappa$  is relatively small ( $< 2.5 \times 10^{-7}$ ), and so streamwise pressure gradient effects are expected to be minimal. The simple reason for this is that over the region downstream of jet injection, freestream velocities are very high, while pressure remains relatively constant, as seen in Figure 3. On the PS, however, velocities are much lower, and the streamwise pressure gradient exerts more influence on the flow. There is a significant deceleration just downstream of the leading edge, which reaches a maximum in magnitude ( $\kappa = -7.0 \times 10^{-6}$ ) at the injection location. In fact, computations for the uncooled reference case showed a small zone of 2-D separation at the PS injection location. Around  $10D$  downstream of the film hole, however, a favorable pressure gradient causes relatively strong acceleration ( $\kappa \approx 2 \times 10^{-6}$ ) which persists over the remaining length of the airfoil.

The upstream boundary layer height,  $\delta_{99}$ , at the injection site was computed for SS as  $1.8D$ , and for the PS  $0.9D$ . There are expected to be differences in the state of the boundary layer between experiments and computations. Ito (1976) reported a laminar boundary layer at SS injection, and hypothesized that it was fully turbulent at PS injection due to the strong adverse pressure gradient. More likely, the boundary layer is in a state of transition at the pressure side injection location in the experiments. In the computations, the boundary layers are computed as fully turbulent. The influence of both state and height of the approach boundary layer is discussed in more detail below.

## 4.2 Adiabatic Effectiveness

Figure 5 shows the laterally-averaged adiabatic effectiveness for the SS cases. The results indicate underprediction by the computations in the near field for all three blowing ratios, with the most drastic occurring for  $M = 1$ . Far downstream, the results indicate good agreement for the  $M = 0.5$  and  $M = 1$  cases, although the  $M = 2$  case overpredicts downstream  $\eta$ . Figure 6 shows laterally-averaged effectiveness for the PS cases. Except for the lowest blowing ratio,  $M = 0.5$ , the computations overpredict the experimental data, and the degree of overprediction increases with increasing  $M$ . On both the SS and PS, however, the trends appear to be well predicted, indicating a resolution of the mean-flow behavior by the computations, if not accurate representation of the turbulent mixing by the current turbulence treatment.

The lateral distribution of effectiveness is illustrated for the lowest  $M$  cases on both SS and PS in Figure 7. The plot shows local  $\eta$  versus downstream distance at four different spanwise stations. It is clear from the experimental data that coolant is rapidly mixed laterally, and in both cases significant influence is seen close to the hole even at the mid-pitch ( $z/D = 1.5$ ) measuring station. The computations drastically underpredict this spreading, which is expected due to the inability of the turbulence model to account for anisotropic mixing. The current results also suggest that the upstream horseshoe vortex may be a significant contributor to lateral mixing close to the film hole, and this is discussed in section 4.4 below.

## 4.3 Near-Field Behavior

A qualitative illustration of the near-field mean-flow streamlines obtained in the present computations is shown in Figure 8. Streamline A, which emanates from the trailing point of the film-hole breakout, is the dividing streamline between coolant and entrained mainstream fluid in the film-hole centerplane ( $z=0$ ). When the exiting coolant has finite momentum, this streamline separates from the surface and the coolant jet lifts off. The fluid that is very near the wall in the approaching airfoil boundary layer is pushed into the region underneath the coolant, streamlines B, C, and D. The height to which the coolant lifts off and the amount of passage fluid entrained beneath increases with increasing momentum-flux ratio, and at very low  $I$ , there is no appreciable lift off. It is important to note that the coolant jet does not "reattach" in a hydrodynamic sense downstream, regardless of  $M$  or  $I$ , since there is no mechanism to force the coolant back towards the airfoil surface. The picture presented in Figure 8 agrees with the



experimental description of normal jets found in Andreopoulos and Rodi (1984) and Kelso et al. (1996).

Observation of adiabatic effectiveness for case S2 ( $M = 1$ ) in Figure 5 *suggests* that the coolant does lift off and reattach at approximately 16 diameters downstream, and similar results are often interpreted this way in the literature. However, Figure 9 indicates a different behavior, namely that the peak in  $\eta$  downstream of injection is a result of turbulent mixing of the coolant toward the wall, a diffusive process. In that figure, the streamlines exiting from the film-hole do not “reattach” downstream, but remain lifted off from the surface. Observing the temperature contours in planes normal to the passage flow direction, at  $x/D = 0.5$ , the location of minimum temperature is clearly removed from the airfoil surface. As the coolant jet travels downstream, the low temperature coolant mixes (diffuses) toward the wall, as seen at  $x/D = 7.5$ . Eventually, the minimum temperature in the crossflow plane will be located at the surface. This is the location of maximum  $\eta$  seen in Figure 5 at about  $x/D = 16$ , a “thermal reattachment”. Downstream of this point, the coolant will only diffuse outward, away from the surface, decreasing the effectiveness. For coolant jets with strong penetration into the freestream, no “thermal reattachment” will occur, and the coolant is said to be completely detached. We emphasize once more, however, that there does not appear to be a regime in which the coolant jet hydrodynamically reattaches downstream, and that diffusive rather than mean-flow convective processes are responsible for any “peaks” in downstream effectiveness distributions.

#### 4.4 Upstream Horseshoe Vortex

One explanation for the significant influence of coolant in the lateral direction near the holes (shown in Figure 7) is the presence of an upstream horseshoe vortex. This vortex is present in the computations and is illustrated in Figure 10 for case P1. It entrains coolant upstream and to the sides of the film-hole as the legs wrap around the exiting jet, increasing the lateral influence of the coolant in the near field. Although the influence of the horseshoe vortex is apparently underpredicted by the computations, it is clearly present in both experiments and computations. For the computations, the strength of the vortex varies inversely with blowing ratio, and at high  $M$  does not form at all, because the exiting jet actually accelerates the approaching crossflow boundary layer. Similarly, in the experiments, the lateral influence of the coolant in the near field decreases with increasing  $M$ , suggesting a decrease in the influence of the horseshoe vortex.

The strength of the horseshoe vortex will depend on the state of the approaching boundary layer. Ito (1976) documented in the experiments a laminar boundary layer on the suction surface at the coolant injection location, while the computational boundary layer is fully turbulent. A proof-of-concept simulation was run for case S1 in which the SS boundary layer was kept laminar, with point transition made to occur at the film-hole leading edge. The results, shown in Figure 11, indicate the increased influence of the horseshoe vortex on lateral distribution of coolant for the case with a laminar upstream boundary layer, and in fact move the computational results closer to the experiments.

Horseshoe vortex formation and upstream entrainment of coolant fluid has been visualized experimentally by Johnston and Khan (1997) for a compound-angle jet-in-crossflow at low  $Re$ . It has also been shown experimentally for normal jets (Fric and Roshko, 1994; Kelso et al., 1996) that the roll-up of the approaching crossflow boundary layer significantly influences mixing in the near field through the action of unsteady vortex structures. The unsteady character of the horseshoe vortex formation cannot be simulated with the current approach, and this source of coolant mixing in the near field may pose a limitation for future Reynolds-Averaged Navier Stokes computations of film-cooling flows. It should be noted, however, that the present study -- and those mentioned above -- are for relatively low-speed cases. The influence of the horseshoe vortex may be much less significant for cases at higher  $Re$  and  $Ma$ .

#### 4.5 Influence of Streamline Curvature

The influence of passage streamline curvature on the coolant trajectory was explained by Ito (1976) in terms of blade-normal pressure gradients acting on a high- or low-momentum coolant jet. Briefly, the cross-stream pressure gradient pushes lower momentum coolant toward a convex wall and away from a concave wall, and vice versa for high momentum coolant. Some recent film-cooling studies, both computational (e.g. Walters and Leylek, 1997; Chernobrovkin and Lakshminarayana, 1998) and experimental (e.g. Haven et al., 1997) have examined vorticity dynamics to gain insight into the mean-flow fluid physics. This section examines the role curvature plays in the vorticity dynamics in the current cases.

As documented in Walters and Leylek (1997), the most significant mean-flow structures governing streamwise-injected film cooling in the near field are the downstream counter rotating vortices (CRVs) or so-called "kidney vortices", which are responsible for the lift-off of the coolant and entrainment of hot crossflow fluid to the wall. The source of these vortices was found to be primarily the streamwise component of vorticity exiting the film hole in the coolant boundary layers. For the case of unity density ratio, the film-hole vorticity is the *only* source for the CRVs, since vorticity cannot be generated away from solid boundaries (see Panton, 1984). For flows with density gradients, vorticity can be generated when a pressure gradient acts normal to a density gradient in the flow. This occurs in film cooling for example when the coolant jet is bent over by the crossflow. The interaction of jet and crossflow results in a high-pressure region upstream and low-pressure region downstream of the exiting jet. For cases with  $DR > 1$ , this pressure gradient will act to strengthen the CRVs at the outer (lateral) shear layers between jet and crossflow, where density gradients are present. For cases with relatively shallow injection angles, such as those considered here, there is little bending of the jet by the crossflow, and thus a relatively weak pressure gradient and presumably small contribution to the CRVs by vorticity generation at the jet-crossflow boundary. These two contributors -- vorticity exiting in the film-hole boundary layers and vorticity generation due to density gradients in the shear layers -- combine to make the strength of the CRVs in general dependent on the jet momentum-flux ratio,  $I$ , which corresponds to the fact that jet penetration height also depends roughly on  $I$ .

After injection, the coolant jet is turned in the downstream direction, and the coolant cross-sectional shape is altered by the action of the CRVs. The strength of the vortices lessens in the downstream direction as the vorticity is diffused. One significant effect of curved surfaces is to redirect vorticity oriented normal to the wall so that it is oriented in the direction of flow, and to likewise redirect vorticity oriented in the flow direction so that it is oriented normal to the wall. Due to this action, the CRVs will be strengthened or weakened. In some cases the CRVs will actually die out and be replaced by vortices rotating in the opposite direction. This occurs for cases in which coolant is "pushed" toward the airfoil surface. Consider the illustration in Figure 12, which shows locations of both y-direction and z-direction vorticity. As the jet moves downstream, streamline curvature will act to reorient the y-direction vorticity at the sides of the jet to the streamwise (x-) direction, increasing or decreasing the strength of the CRVs. For low-momentum coolant on the SS, this reorientation will act to reduce the strength of the CRVs, since (considering Figure 12) negative  $\omega_y(\text{right})$  vorticity gets reoriented to negative  $\omega_x(\text{right})$  vorticity. For high-momentum coolant on the SS, positive  $\omega_y(\text{right})$  vorticity is reoriented to positive  $\omega_x(\text{right})$  vorticity, strengthening the CRVs. The opposite action occurs for film cooling on the PS. This effect is demonstrated in Figure 13, which shows velocity vectors in planes oriented normal to the passage flow, at two different downstream locations, for cases S1 and S3. Case S1 initially shows a streamwise oriented CRV, but as the coolant moves downstream, the reorientation of vorticity results in a reversal of the vortex structure, as shown. Case S3 has higher momentum flux ratio, and so maintains the CRV far downstream.

In addition to reorientation of already-present vorticity, downstream streamline curvature can also result in generation of new vorticity at the edges of the coolant jet, due to the action of the blade-normal pressure gradient on the density gradients, in a manner similar to that documented above. The net result is that the impact of streamline curvature on the CRVs is roughly dependent on the streamwise momentum-flux ratio between coolant and crossflow. Ito (1976) documented a similar relationship using momentum concepts in his discussion on downstream coolant jet dynamics. Some remarks regarding the ability of computations to accurately represent the dynamics discussed above are in order. Due to the lack of turbulent mixing computed for these cases, computations will tend to overpredict the vorticity concentration at downstream locations. Thus the magnitude of secondary flow, regardless of its orientation, is likely to be overstated by the computations. This underscores the importance of accurately predicting the downstream turbulence field, not only to correctly resolve coolant diffusion, but to accurately determine the magnitude of mean-flow mechanisms. It should also be pointed out that the RKE model, as it is implemented, does not include any terms to resolve the impact of curvature on the turbulence field. For example, the augmentation of turbulence in a boundary layer on a concave surface, or attenuation of turbulence on a convex surface, which is known to occur in real flows, will not be represented.

#### 4.6 Downstream Coolant Mixing

The adiabatic effectiveness results in Figure 7 suggest that coolant mixing is consistently underpredicted in the near field with the two-equation turbulence models used. One explanation is the upstream horseshoe vortex (see above), but it is expected, based on past computational studies, that lateral turbulent mixing is underpredicted as well. In addition, the underprediction of  $\eta$  in the near field for all but Case P3 suggest that computed turbulent mixing toward the wall is too low, yielding an unrealistically large thermal reattachment length in these cases. (Note that for previous cases using wall functions, the diffusion toward the wall in the very near field is likely overwhelmed by numerical viscosity due to large cell height.) Finally, the overprediction of  $\eta$  far downstream for Cases S3, P2, and P3 indicate that turbulent mixing away from the wall is too low for these cases. Interestingly, however, the effect on  $\eta$  is minimal for the cases with lower  $M$ . The reason for this can be seen in Figure 14. Shown are the temperature and total pressure contours in planes normal to the freestream flow direction at  $x/D = 10$  for cases S1 and P3. Clearly, for S1 the low-temperature coolant is located entirely within the boundary layer near the wall, while for P3 it is almost entirely outside the boundary layer. It is expected that the turbulent dynamics within the boundary layer are dominated by the presence of the wall, and that downstream of injection, the turbulent mixing is reasonably approximated by currently popular turbulence models, which are primarily designed to reproduce near-wall turbulence effects. For cases in which the coolant jets penetrate through the boundary layer, the turbulence model deficiencies play a major role in the prediction of downstream  $\eta$ . This is the likely reason that almost all documented computational film-cooling studies tend to perform far better for cases with low  $M$ . It is also the reason that  $\eta$  predictions for  $M = 1$  show an underprediction on the SS but overprediction on the PS. In the PS case, the boundary layer is considerably thinner, and much of the coolant penetrates into the freestream. This does not happen on the SS.

#### 4.7 Streamwise Pressure Gradient

As mentioned in section 4.1, there is little streamwise acceleration on the suction surface. On the pressure surface, because the influence of streamwise acceleration is not isolated, it is somewhat difficult to separate pressure gradient effects from other influences. As mentioned above there is a computed flow separation at the injection location due to the adverse pressure gradient, even for cases with no coolant injection. For the cases with film cooling, this separation is indistinguishable from the upstream horseshoe vortex, which is larger for the PS cases than for the corresponding SS cases. Downstream of about  $x/D = 10$ , where the acceleration is strongly favorable, the boundary layer on the PS becomes thinner. The thinning boundary layer compresses the counter-rotating vortices in the vertical direction and elongates them in the spanwise direction, effectively pushing coolant fluid outward, and increasing the lateral spread rate in the downstream regions. Note that the experiments also showed slightly more rapid lateral spreading for the PS cases (seen for example in Figure 7). This effect of streamwise pressure gradient has been documented in York and Leylek (1999), and in Chapter 1 of this report.

## 5. CONCLUSIONS

The present study has combined experimental data and computational results to document the flow physics of film cooling on realistic airfoil geometries. The combination of experiments and computations allows the strengths of each to be utilized and a clear picture of physical mechanisms to be drawn. Results have also been used to determine the shortcomings of widely-used two-equation eddy-viscosity turbulence models. Based on the results presented, the following conclusions can be drawn.

- The airfoil passage flow can significantly impact film-cooling performance. Passage flow conditions on SS and PS can be characterized by streamline curvature, streamwise pressure gradient, and size and state of the crossflow boundary layer.
- The current results indicate jet lift-off at sufficiently high blowing ratios, but not jet reattachment. The apparent reattachment indicated by adiabatic effectiveness results is in fact due to coolant mixing (diffusion) toward the airfoil surface.
- The upstream horseshoe vortex may be a significant contributor to coolant spreading in the near field. The influence of the horseshoe vortex is dependent on momentum flux ratio ( $I$ ) and the crossflow boundary layer size and state. For the present cases, computations consistently underpredict this influence.
- Streamline curvature on both the concave and convex surfaces influence the downstream secondary flow by reorienting already present vorticity to (or away from) the streamwise direction, and by generating (or reducing) vorticity at the coolant jet boundaries for cases with  $DR \neq 1$ . This influence can include a reversal of the well-known counter-rotating vortex structure.
- Current results indicate that downstream coolant mixing is underpredicted with the current turbulence treatment. Future work will include implementation of more advanced turbulence models which accurately reproduce downstream turbulent mixing.

## REFERENCES

- Andreopoulos, J. and Rodi, W., 1984, "Experimental Investigation of Jets in a Crossflow," *Journal of Fluid Mechanics*, Vol. 138, pp. 93-127.
- Chernobrovkin, A. and Lakshminarayana, B., 1998, "Numerical Simulation and Aerothermal Physics of Leading Edge Film Cooling," ASME Paper No. 98-GT-504.
- Fric, T.F. and Roshko, A., 1994, "Vortical Structure in the Wake of a Transverse Jet," *Journal of Fluid Mechanics*, Vol. 279, pp. 1-47.
- Haven, B.A., Yamagata, D.K., Kurosaka, M., Yamawaki, S., and Maya, T., 1997, "Anti-Kidney Pair of Vortices in Shaped Holes," ASME Paper No. 97-GT-45.

Ito, S., 1976, "Film Cooling and Aerodynamic Loss in a Gas Turbine Cascade," Ph.D. Thesis, University of Minnesota.

Ito, S., Goldstein, R.J., and Eckert, E.R.G., 1978, "Film Cooling of a Gas Turbine Blade," ASME Journal of Engineering for Power, Vol. 100, pp. 476-481.

Johnston, J.P. and Khan, Z., 1997, "The Origins of the Dominant Vortex From a Pitched and Skewed Jet," Presented at International Conference on Fluids Engineering, JSME, Tokyo, July 13-18, 1997.

Kelso, R.M., Lim, T.T., and Perry, A.E., 1996, "An Experimental Study of Round Jets in Cross-Flow," Journal of Fluid Mechanics, Vol. 306, pp. 111-144.

Panton, R.L., 1984, Incompressible Flow, John Wiley & Sons, Inc., Ch. 13.

Walters, D.K., and Leylek, J.H., 1997, "A Detailed Analysis of Film-Cooling Physics -- Part I: Streamwise Injection with Cylindrical Holes," ASME Paper No. 97-GT-269.



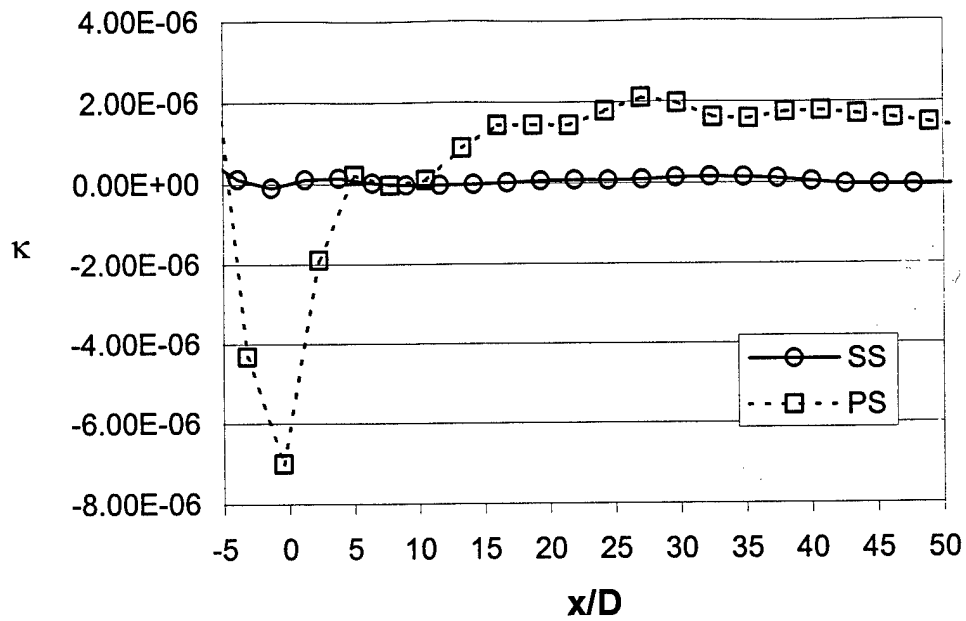


Figure 4. Downstream variation of streamwise acceleration parameter, highlighting the strong influence on the PS, but relatively weak influence on the SS.

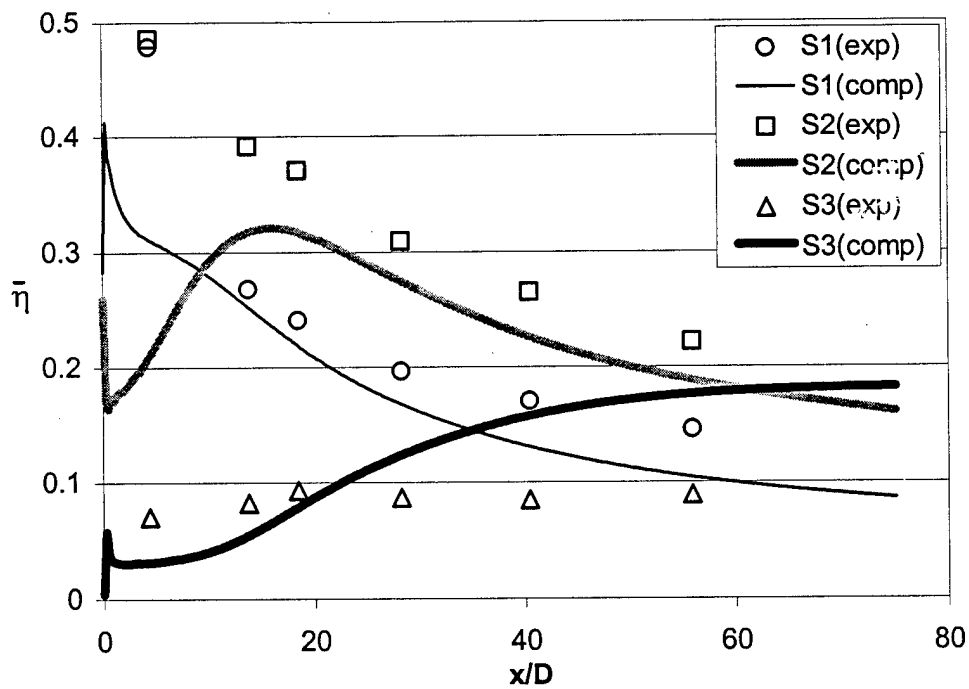


Figure 5. Laterally-averaged adiabatic effectiveness on the suction surface, downstream of coolant injection.



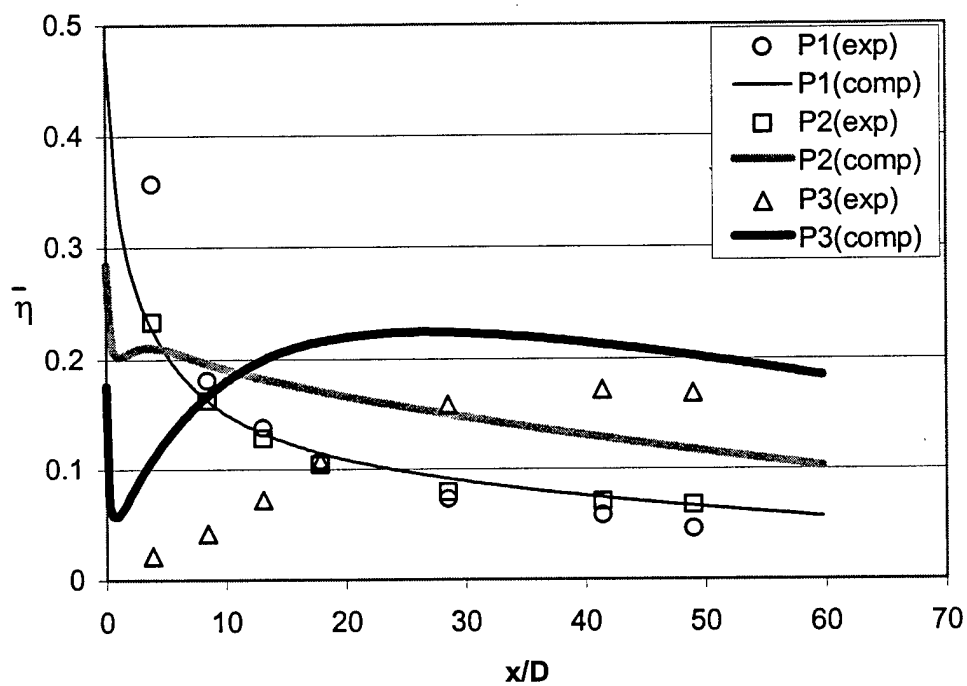


Figure 6. Laterally-averaged adiabatic effectiveness on the pressure surface, downstream of coolant injection.

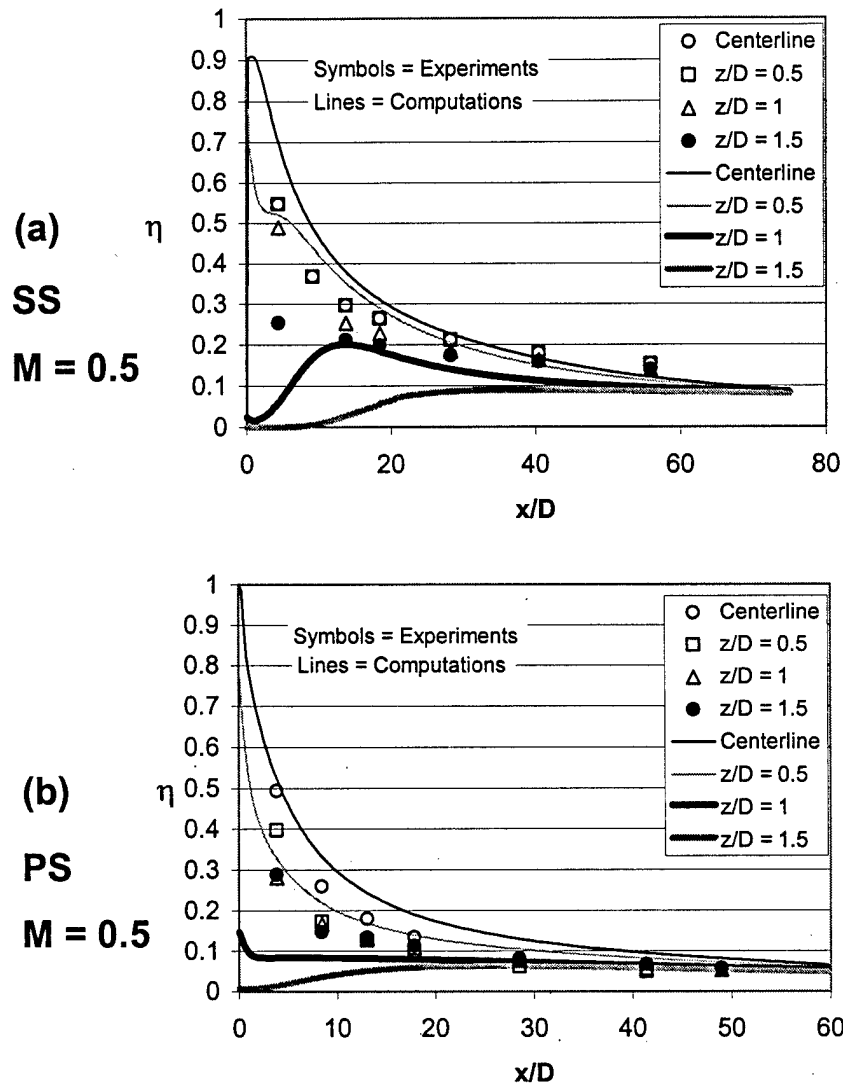


Figure 7. Local adiabatic effectiveness at four spanwise stations for case S1 (a) and P1 (b) show underprediction of lateral spread rate by the computations.

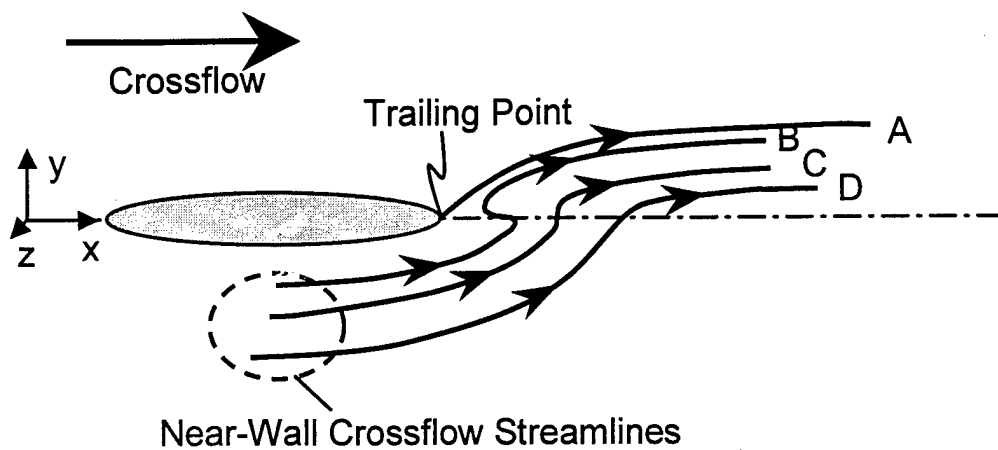


Figure 8. Mean-flow streamline pattern near the film-hole exit shows lift-off of coolant jet and entrainment of passage fluid beneath.

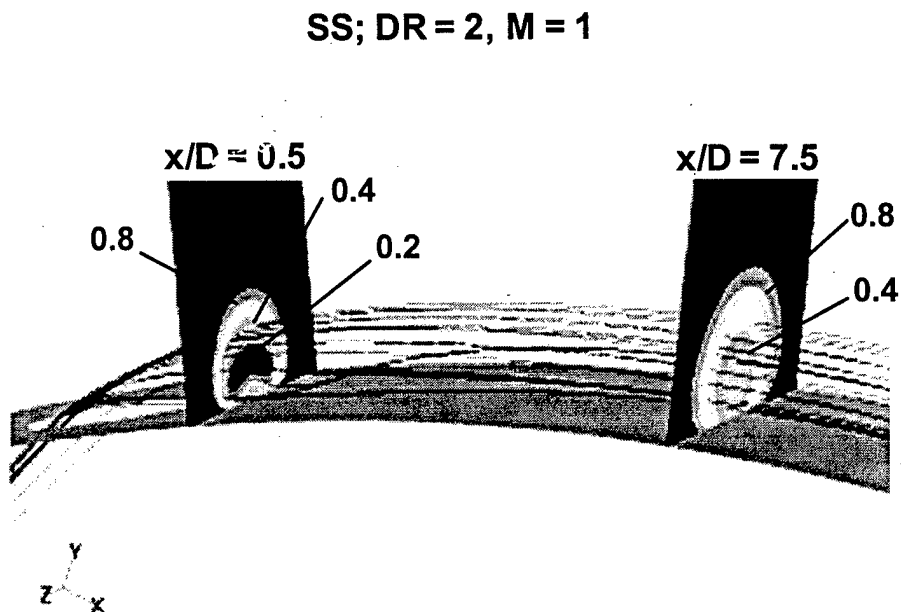


Figure 9. Temperature contours in planes normal to the passage flow and coolant streamlines for case S2.

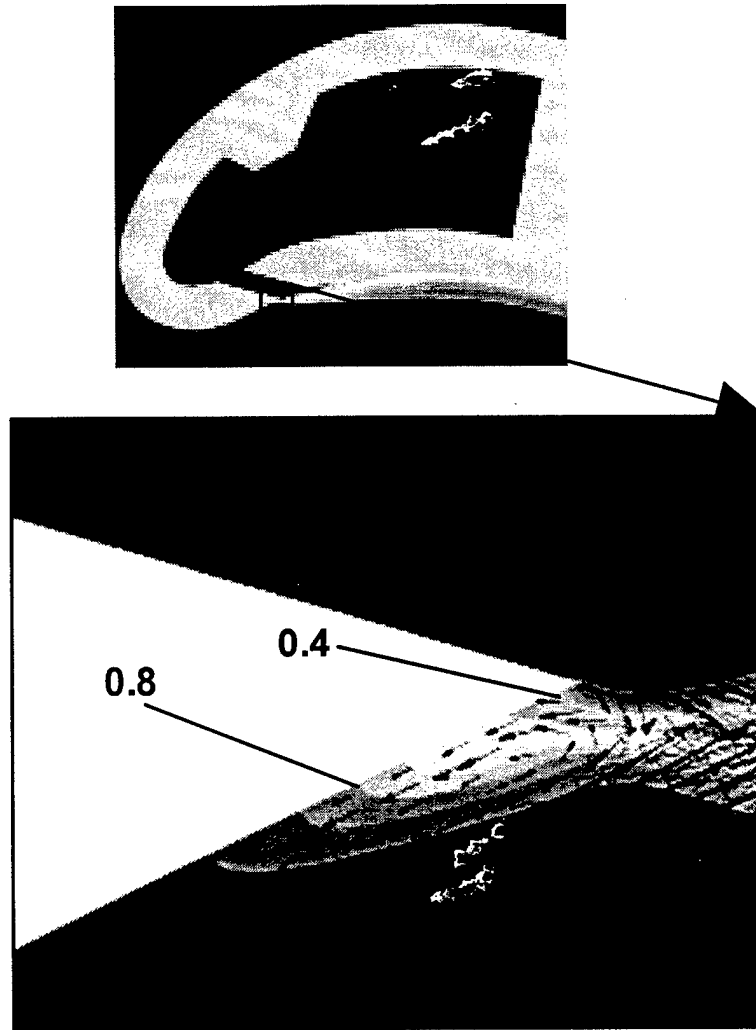


Figure10. Velocity vectors and  $\theta$  contours on the  $z=0$  centerline plane, showing the presence and influence of the upstream horseshoe vortex.

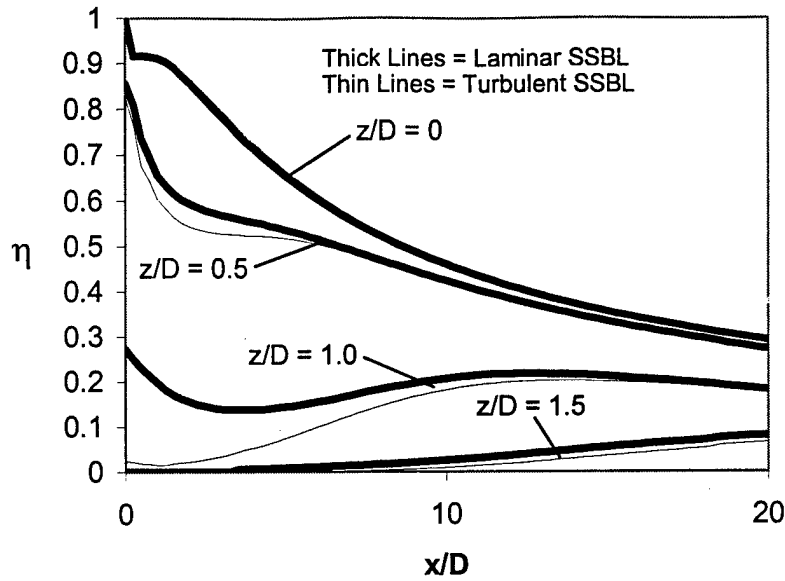


Figure 11. A proof-of-concept simulation for case S1 employing a laminar boundary layer upstream of coolant injection results in more lateral spreading of the coolant in the near field.

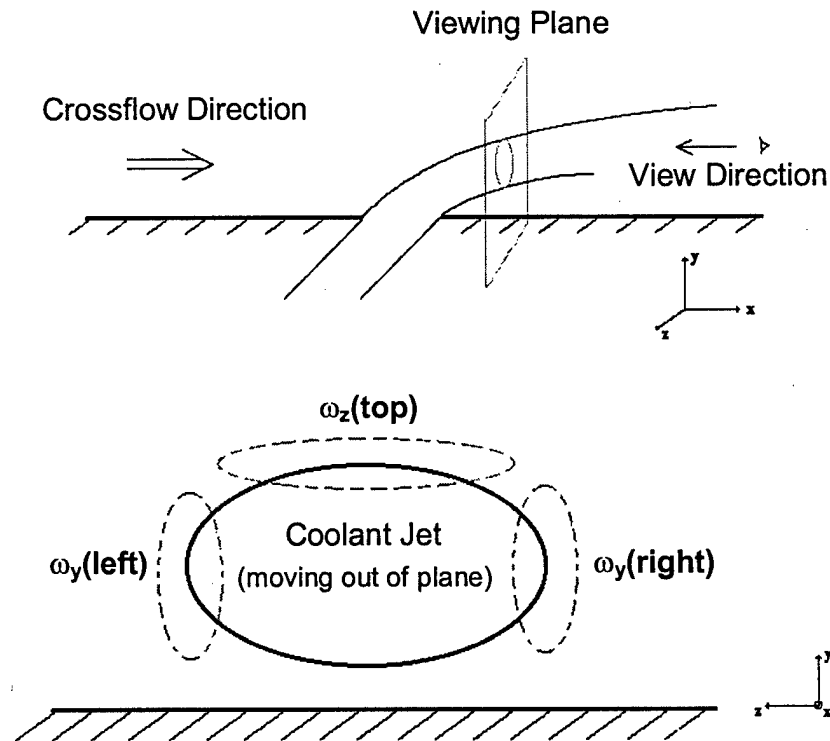


Figure 12. Illustration of near-field vorticity distribution at the edges of the coolant jet.

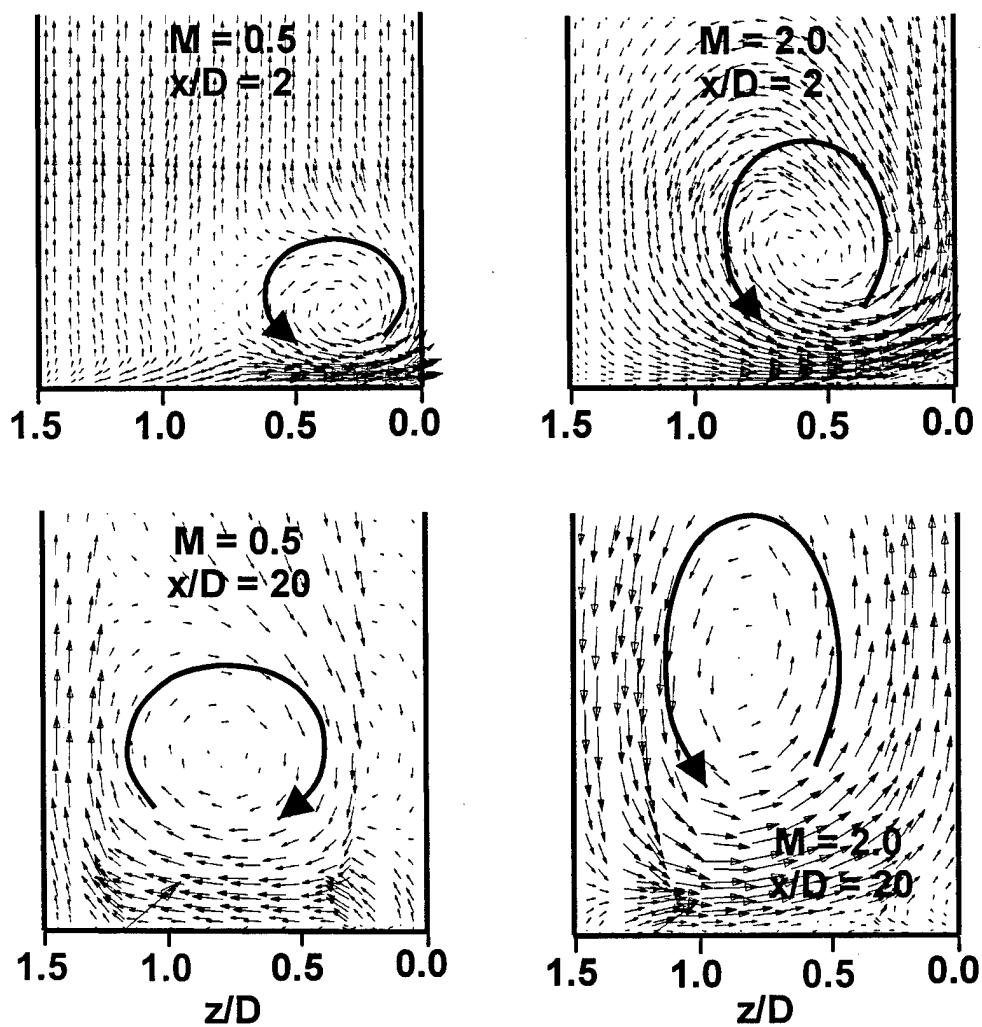


Figure 13. Velocity vectors in planes normal to the passage flow, at two downstream locations, for case S1 and S3.

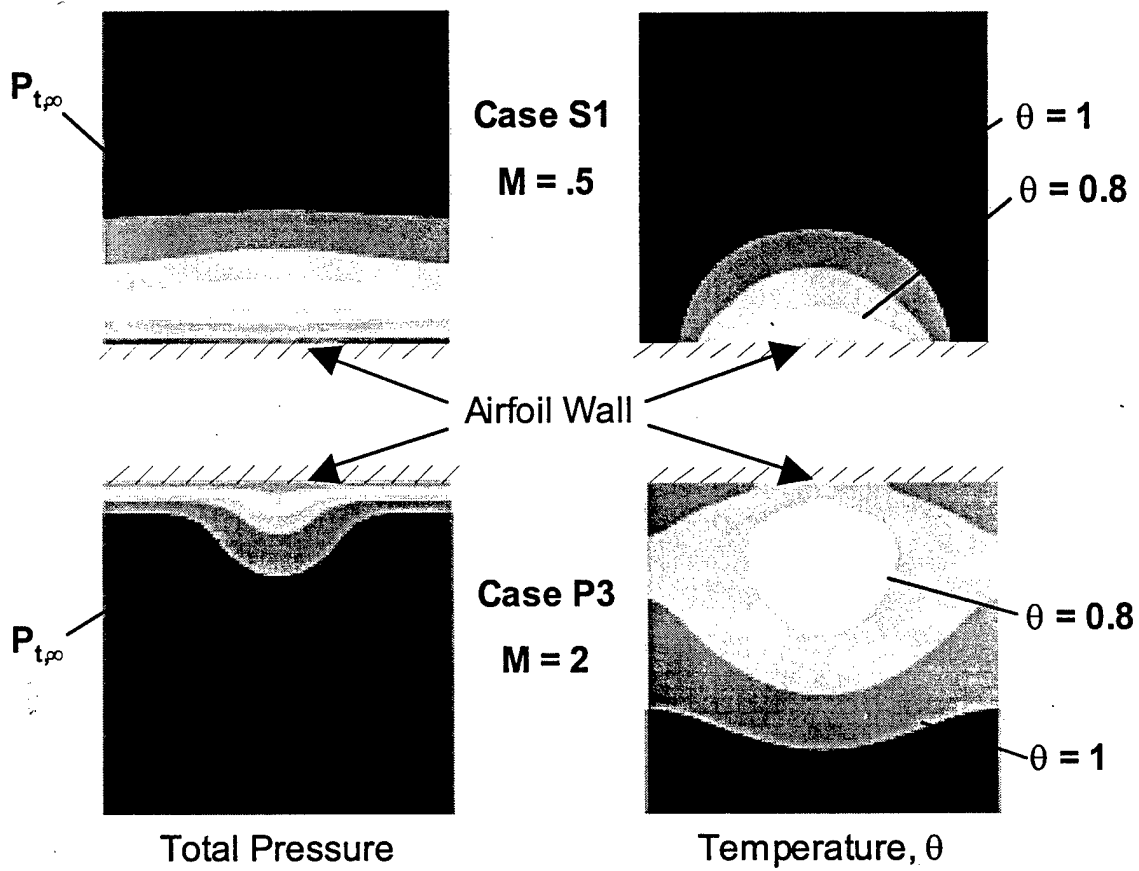


Figure 14. Contours of total pressure (left) and temperature (right) show coolant remaining within the boundary layer for case S1, but penetrating into the freestream for case P3.

## CHAPTER 5

### FILM COOLING ON A MODERN HP TURBINE BLADE PART I: EXPERIMENTAL & COMPUTATIONAL METHODOLOGY AND VALIDATION

Frederick A. Buck, D. Keith Walters, Jeffrey D. Ferguson, E. Lee McGrath and  
James H. Leylek

#### NOMENCLATURE

|               |  |
|---------------|--|
| ASH           | <u>a</u> xial <u>s</u> haped <u>h</u> oles                         |
| C             | mass <u>c</u> oncentration   |
| CAR           | <u>c</u> ompound- <u>a</u> ngle <u>r</u> ound holes                |
| CASH          | <u>c</u> ompound- <u>a</u> ngle <u>s</u> haped <u>h</u> oles       |
| DR            | density ratio = $\rho_{pp}/\rho_{\infty}$                          |
| FHEP          | <u>f</u> ilm- <u>h</u> ole <u>e</u> xit <u>p</u> lane              |
| k             | turbulence kinetic energy  |
| <i>l</i>      | turbulence length scale  |
| LE            | <u>l</u> ea <u>e</u> ding <u>e</u> dge                             |
| M             | blowing ratio = $(\rho u)_{pp}/(\rho u)_{\infty}$                  |
| Ma            | Mach number  |
| PS            | <u>p</u> ressure <u>s</u> urface                                   |
| r             | recovery factor  |
| Re            | Reynolds number  |
| SS            | <u>s</u> uction <u>s</u> urface                                    |
| T             | temperature  |
| $T_{cool}$    | coolant recovery temperature = $T_{s,aw} + r (T_{T,P} - T_{s,aw})$ |
| TE            | <u>t</u> railing <u>e</u> dge                                      |
| TI            | turbulence intensity = $\sqrt{(2/3)k}/u$                           |
| u             | local velocity magnitude   |
| X             | length of film-cooled section of airfoil                           |
| $y^+$         | non-dimensional wall distance                                      |
| $\varepsilon$ | turbulence dissipation rate  |
| $\phi$        | compound angle   |
| $\gamma$      | injection angle  |
| $\eta$        | adiabatic effectiveness = $(T_r - T_{s,aw})/(T_r - T_{cool})$      |
| $\bar{\eta}$  | laterally- or spanwise-averaged $\eta$                             |
| $\rho$        | density  |

#### Subscripts

|          |                       |
|----------|-----------------------|
| $\infty$ | free-stream condition |
|----------|-----------------------|



|      |   |
|------|---|
| aw   | adiabatic wall                                  |
| cool | coolant   |
| in   | inlet conditions                                |
| pp   | conditions at pierce point (injection location) |
| r    | recovery  |
| s    | static quantity                                 |
| T    | total (stagnation) quantity                     |

## 1. INTRODUCTION

Current turbine heat transfer design methodology relies heavily on empirical correlations and relatively simple 2-D computational codes for prediction of the performance of new film-cooling designs. These design tools are often inadequate to describe the adiabatic effectiveness on film-cooled airfoils for complex film-hole geometries. The difficulty is compounded by the fact that adiabatic effectiveness is a strong function of many variables, including not only film-hole geometry (hole diameter, hole pitch, spacing, wall thickness, diffuser geometry and angular orientation), but also airfoil geometry (surface curvature), mainstream aerodynamics (pressure gradient, turbulence levels), and coolant flow conditions. A well-tested, robust methodology utilizing both experiments and computations can provide a powerful tool for the designer, and provide insight into improved cooling strategies.

At GE Aircraft Engines, an effort was initiated in 1993 to experimentally obtain the adiabatic film-cooling effectiveness design data for turbine airfoil applications using a single airfoil passage test model, with a gas analysis technique to measure film-cooling effectiveness. Buck and Prakash (1995) reported on the first of these tests. Since then, the single passage/gas analysis technique has been employed to obtain design data for several engine applications. This paper will report on the performance of three types of holes installed at identical locations on the pressure and suction sides of an airfoil shape. The film-hole geometries include: 1) compound-angle round (CAR) holes, for which the projection of the hole axis is not aligned with the flow; 2) axial shaped holes (ASH), which include a diffusing section at the downstream portion; and 3) compound-angle shaped holes (CASH), which combine the attributes of both. The measurements also provide high-quality experimental data in a "blind" test case to develop and validate a systematic computational methodology for use in simulations with high freestream turbulence intensity, pressure gradients, curvature, and strain rates found in actual engines.

## 2. LITERATURE REVIEW

The present study is one of the first to conduct a series of detailed examinations of multiple "complex" film-cooling geometries on a modern turbine airfoil. The brief review below highlights some of the pertinent work available in the open literature.

## 2.1 Experimental Studies

To date, most experimental film-cooling studies have been performed on flat plates, using the relatively simple injection geometry of a streamwise-injected, cylindrical hole. Some exceptions are discussed below.

A few authors, including Goldstein et al. (1974), and Gritsch et al. (1997a,b and 1998), have examined the film-cooling performance of streamwise-injected shaped holes, most notably highlighting the increase in downstream adiabatic effectiveness for shaped versus cylindrical film holes, at comparable blowing ratios. This improvement is generally attributed to reduced coolant momentum at the film-hole exit caused by hole shaping, although Haven et al. (1997) showed that hole shaping can inhibit jet lift-off by altering the vorticity distribution near the jet exit region. Similarly, several studies have been performed on compound-angle cylindrical-hole film cooling, for example Ligrani et al. (1992 and 1994a,b) and Ekkad et al. (1997a,b). These studies have documented an increase in adiabatic effectiveness for compound-angle versus streamwise injection. Honami et al. (1994) and Lee et al. (1997) showed that the flow physics in the near field are altered by compound angling, documenting for example the presence of a single, dominant downstream vortex, instead of the symmetric, counter-rotating vortex pair present with streamwise injected holes. Companion studies by Schmidt et al. (1996) and Sen et al. (1996) documented the adiabatic effectiveness and heat transfer for both compound-angle cylindrical and compound-angle shaped holes on a flat plate geometry.

Ito et al. (1978) examined film cooling on an airfoil cascade, with a single row of streamwise-injected cylindrical holes on both the pressure and suction surfaces. They documented the influence of streamline curvature on the downstream adiabatic effectiveness. Ames (1997a,b) recently documented a similar study, and examined particularly the influence of high freestream turbulence. Both the Ito and Ames studies were performed at relatively low Ma and Re, not indicative of realistic engine conditions, and included only streamwise-injected, cylindrical holes. Drost and Bolcs (1998) examined the effects of M, DR, Re, Ma, and freestream turbulence on airfoil film cooling, in one of the first documented experiments at engine-realistic operating conditions. They did not explore the influence of film-hole geometry on the cooling performance.

## 2.2 Numerical Studies

A few computational studies of complex film-cooling geometries on flat plates have been documented, including a four-part paper by this group (Walters and Leylek, 1997b; McGovern and Leylek, 1997; Hyams and Leylek, 1997; and Brittingham and Leylek, 1997) that thoroughly documented the effects of hole shaping and compound-angling, both separately and together. The improved performance of both shaped-hole and compound-angle geometries was discussed in terms of the momentum and vorticity distributions near the jet exit. Other authors (e.g. Geibert et al., 1997 and Kholi and Thole, 1998) have also used computational approaches to examine different aspects of shaped-hole film cooling on flat plates.

Few computational studies are available for airfoil film cooling downstream of the leading edge, exceptions being for example the work by Garg and Gaugler (1997) and Garg and Rigby (1998), who effectively demonstrated the need for including the film hole and coolant supply plenum in film-cooling simulations. No computational studies are known to the authors that examine the impact of film-hole geometry on film-cooling performance downstream of the airfoil leading edge.

## **2.3 Summary**

Based on the above, several outstanding issues can be identified, including a lack of data and/or simulations in the open literature regarding detailed airfoil film cooling with realistic engine operating conditions, and a lack of data and and/or simulations considering the effect of film-hole geometry on cooling performance. In addition, the physical mechanisms of airfoil film cooling remain to be thoroughly documented.

## **3. PRESENT CONTRIBUTIONS**

This work combines validation quality experimental data with state-of-the-art numerical techniques to analyze the physics of “complex geometry” film cooling on a modern turbine airfoil operating under realistic engine conditions. Specific contributions include:

- Documentation of the film-cooling performance of “complex geometry” film-hole configurations over a range of blowing ratios on both the suction and pressure surfaces;
- Identification of key physical mechanisms responsible for airfoil film-cooling performance of all configurations;
- Extension of the methodology developed in Walters and Leylek (1997a) to the current cases, which involve transonic blade passage flows;
- Evaluation of the ability of a currently popular, practical turbulence model to accurately capture the physics of these complex flows.

## **4. EXPERIMENTAL METHODOLOGY**

### **4.1 Test Model**

Figure 1 shows the cross-section of the single-airfoil-passage test model. The model features include: (1) a mainstream passage with a bellmouth-inlet; (2) boundary layer bleeds located immediately upstream of the airfoil leading edges; (3) airfoil walls scaled from engine airfoil pitch-line dimensions; and (4) adjustable trailing edge flaps. Flow restrictions were also used at the exit of the model to back pressure the mainstream flow. During the tests, the mainstream flow, boundary layer bleed flows, trailing edge flaps and backpressure levels were adjusted to produce the desired pressure distribution on the airfoil surfaces.

The secondary or film-cooling flow was injected into the mainstream flow through film holes emanating from cooling plenums on the backside of the airfoil walls. A foreign gas, usually pure carbon dioxide ( $\text{CO}_2$ ), but sometimes a mixture of carbon dioxide with other gases, was used as the "coolant". The film-cooling effectiveness was obtained from the  $\text{CO}_2$  concentration measurements made along the surface downstream of the coolant injection site. These measurements were made by extracting a small portion of the mainstream flow through static pressure taps installed along the surface of the model.

#### 4.2 Design, Fabrication, and Implementation

Each film-hole geometry was installed in a separate airfoil test piece to insure that there were no steps or surface discontinuities upstream or downstream of the hole breakout. The film holes were produced using electron-discharge machining (EDM) and the metering sections of the holes (i.e., the diameter of the round hole portion at the wall of the cooling plenum) were nominally equal. Actual metering hole diameters were determined from pinned measurements.

The projection of the hole axis of the ASH geometry onto the airfoil surface was aligned with the mainstream flow. The design intent hole angles for the CAR and CASH holes were identical, however a limited sample of hole angle measurements indicated that some angles differed by as much as 3.2 degrees. The hole exit for the axial diffuser was shaped using EDM to diffuse both perpendicular to and in-line with the direction of the mainstream flow. The compound-angled diffuser only diffused in a direction perpendicular to the flow.

For all pressure-side holes, the intended angles between the projections of the hole axis and surface tangent ( $\phi$ ) onto the cross-section plane (XY) were identical. This was done because of manufacturing limitations that typically exist when drilling holes into engine hardware at such a location. The resulting surface angle ( $\gamma$ ) for the axial diffuser is larger than would normally be desired from a pure film-cooling performance standpoint. Compound angling of the hole permitted a smaller surface angle as shown in Figure 2. The surface angle for the suction-side ASH hole was already reasonably shallow. Therefore, the compound-angled holes on the suction side were drilled with a steeper cross-section angle and were rotated to produce a slightly smaller surface angle than the axial shaped hole.

The as-built diffuser geometry details were reverse-engineered from a series of X-ray images made of the airfoil test pieces. The X-ray data was converted into a digital representation of the local mass density and an inflection edge-point-detection algorithm was used to determine the "skin" of the test piece. The result was a 3-dimensional "cloud" of edge points that clearly defined the walls of the film holes and the inside and outside walls of the test piece. Figure 3 shows one of these "cloud" images. These 3-D images were then manipulated to determine the film-hole angle and diffuser length and angle dimensions. In general, these dimensions were different than design intent and there were also substantial hole-to-hole variations. It is believed that these variations

were caused by EDM tool wear during the drilling process. A nominal hole geometry was constructed from the average of the each of the various dimensions and was used in the subsequent CFD simulations.

Each test piece was instrumented with 33 static pressure taps. One of these pressure taps was located upstream of the film-hole breakout along the mid-span of the airfoil wall. In the pressure-side tests, two of the rows of taps were located behind a centerline pierce point of an upstream film hole and the other two were located behind points mid-way between adjacent film-hole pierce points. In the suction-side tests, which had a larger pitch spacing between adjacent film holes, one row of taps was located in-line with a film-hole pierce point and the other three rows were located at 25%, 50%, and 75% of the span between adjacent film holes. All of the taps were used to record local static pressures during the aerodynamic flow tests. During the film cooling tests, the gas sampling was done using the 32 downstream taps, bleeding the sampling flow off one tap at a time to a ANARAD CO<sub>2</sub> analyzer. Following the recommendations of Pedersen (1972), the sampling flow rate was controlled to ensure that the extraction velocity at the pressure tap inlet was no more than 10% of the local mainstream velocity. The sampling tap diameters were larger the film-hole metering section diameter, so the use of a 10% sampling velocity had to be validated. First, the results were examined for a range of sampling velocities, and it was determined that negligible changes occurred between velocities of 5 and 15%. Further, the gas analysis results with 10% sampling velocity were compared to previous thermal tests as well as instrumented engine tests, and were shown to yield an excellent match.

### 4.3 Test Procedures

Orifice pressure measurements obtained upstream and downstream of a Daniels orifice together with the barometric pressure, fluid temperature and orifice plate diameter were then reduced to get the mainstream (i.e., air) flow using standard ASME orifice algorithms. The coolant flow measurement was obtained using a second orifice run in a similar manner taking into account the isentropic flow function characteristics of carbon dioxide. The tests were run using LABview-based data acquisition software that generated a continuous update of pertinent mainstream and secondary flow, temperature and pressure conditions and a chart of recent history of gas concentration output from the CO<sub>2</sub> analyzer. The operator simultaneously controlled both the mainstream and secondary flows and monitored the output from the CO<sub>2</sub> analyzer. Once the gas concentrations reached a steady-state condition, the LABview program recorded a sequence of 15 data sets (flows, pressures, temperatures and concentration) over a time period of approximately one-minute. This process was repeated for each of the 32 instrumentation taps while maintaining the desired mainstream and secondary flow conditions. The local adiabatic film-cooling effectiveness level  $\eta$  were calculated for each tap using the equation:

$$\eta = \frac{C_{\infty} - C_{aw}}{C_{\infty} - C_{cool}}$$

where  $C_\infty$  is the mass concentration of  $\text{CO}_2$  in the mainstream flow,  $C_{aw}$  is the concentration measured at each of the local instrumentation taps and  $C_{cool}$  is the concentration of the coolant. In these tests,  $C_\infty$  was essentially zero and  $C_{cool}$  was essentially 100%. In most cases, the designer is only concerned with the average film-cooling effectiveness as one progresses downstream of the film injection site. In these tests, the average  $\eta$  at a particular streamwise location was obtained by the simple average of the four span-wise local  $\eta$ 's measured at that location. The applicability of simple averaging was assumed valid due to the relatively large size of the sampling taps. The computational results were examined to verify this assumption, and the procedure is discussed in section 6.2 below.

#### 4.4 Test Conditions

Both simulations and experiments were intended to mimic realistic engine conditions. For the passage flow, the inlet Mach number was 0.2, and increased to slightly greater than one just downstream of the airfoil throat. The chord Reynolds number varied from 600,000 at the inlet of the domain to 2,000,000 at the throat. The coolant-to-mainstream density ratio was nominally 1.52 for all cases. The blowing ratio ( $M$ ) for each case was calculated based on the film-hole metering section cross-sectional area, and tests were performed at  $M = 1.5, 3.0$ , and  $4.5$  for pressure-surface injection, and  $M = 1.0, 1.5$ , and  $2.0$  for suction-surface injection.

#### 4.5 Experimental Uncertainties

The flow and effectiveness measurement uncertainties have been calculated from the individual instrument measurement uncertainties using the "classic" method of Kline and McClintock (1953). The uncertainties in the quoted mainstream and secondary flow measurements are 1.17 % and 1.79 % respectively. The uncertainty in the film-cooling effectiveness measurements based on instrument capability was 0.6 %. The repeatability and reproducibility characteristics of these measurements were also measured experimentally over a range of mainstream and secondary flow conditions. The 95 % confidence bands for maintaining the mainstream and coolant flow levels were  $\pm 0.1$  % and  $\pm 0.8$  % of the desired flows respectively.

Since each test piece has duplicate instrumentation (two taps in-line with the film-hole pierce point and two taps midway between adjacent pierce points), a value of the variation in the film cooling effectiveness measurements can be determined by comparing the results from similarly installed taps. The resulting 95 % confidence band,  $\pm 19.9$  % of the measured film cooling effectiveness, was significantly larger than the uncertainty level based on instrument capability for most of the test measurements. This is probably due to variations in the manufacture of the film holes and the instrumentation installation, especially the former. Averaging the results of the four taps at each axial location reduce the 95 % confidence band to  $\pm 9.9$  % of the quoted average effectiveness.

## 5. COMPUTATIONAL METHODOLOGY

The computational methodology developed in the present study is based on the work by Walters and Leylek (1997a). That study developed and applied a comprehensive computational methodology to discrete-jet film cooling on a flat surface in incompressible, low TI flow. In the present study, the existence of high TI, steep pressure gradients, high Mach numbers, and high curvature required some modifications to the Walters and Leylek (1997a) methodology. Nevertheless, both studies seek to address all the critical aspects of a simulation in order to minimize numerical errors and isolate the true performance of turbulence models.

### 5.1 Computational Model

The present computational study is a "blind" test case of the experimental work outlined above. Initially, only the geometric details and boundary conditions were released to the CFD team. Measured data were superimposed by the experimental team after they received the grid-independent and fully-converged results. The computational model carefully mimics the experiments described in the previous section, and the model was developed in three phases: (1) the passage domain, (2) the film-cooling domain, and (3) the boundary conditions.

#### 5.1.1 Passage Domain

Initially, a 2-D computational model was developed to match the test model shown in Figure 1, based on mid-span measurements of aerodynamics experiments on the single passage cascade. Because the flow was essentially 2-D along the pitch-line of the blade, the 2-D domain was optimized for computational efficiency and then extruded to 3-D to form the aero passage domain used in the film-cooling simulations.

The experimental study had several flow parameters that required accurate modeling in the computational simulations: the blade loading, the turbulence intensity at a monitor location, the inlet total pressure and temperature, and the inlet mass flow rate. However, other parameters, such as the static back pressure and bleed flows were not clearly defined. Therefore, iterative 2-D numerical experiments were run to isolate the most realistic boundary conditions for the full domain aero simulations. Convergence on the proper boundary conditions was declared when the blade loading curve, turbulent intensity at the monitor location, and mass flow rate through the passage were within 0.04% of the experimental values.

With the mainstream plenum and the boundary layer bleeds included in the computational model, the full 3-D domain would prove extraordinarily difficult and computationally expensive to construct, grid, and run. Isolating the stagnation streamlines upstream of the airfoil LE in the 2-D case and using them as boundary conditions eliminated the need to model the boundary layer bleeds, inlet plenum, and bellmouth assembly in the 3-D cases. The stagnation streamlines remain well outside of the bellmouth boundary layers and do not change position with changes in  $TI_{in}$ , so they

were used as boundaries in a new, optimized computational domain. Zero-gradient conditions were applied at these boundaries. The computational intensity of the simulations was further reduced by removing the mainstream plenum and bellmouth and using a new inlet location further downstream of the bellmouth, but far enough upstream of the blade LE to avoid altering the physics of the flow. The new inlet conditions were set by profiles of the dependent variables from the same position in the full domain. The optimized passage domain is shown in Figure 4.

### 5.1.2 Film-Cooling Domain

Because the passage flow is essentially 2-D, the same optimized domain outlined above can be extruded to 3-D and used to model the film cooling along the mid-span of the blade. The three-way coupling of the flow in the plenum, film-hole, and crossflow regions was modeled following the recommendations of Leylek and Zerkle (1994). Symmetry (ASH) or periodic (CAR and CASH) conditions were used to model a row of cooling holes. However, because of manufacturing limitations, the as-built film-hole geometries varied somewhat from hole to hole. Therefore, a nominal geometry based on averaged parameters from the as-built test sections was used in the simulations. Details of the individual film-hole geometries are included in the appropriate sections of this paper. Figure 5 shows the breakouts of the film holes for each configuration. For all simulations, the origin is located at the pierce point of the film hole on the blade. The pierce-point is the intersection of the film-hole metering section centerline and the film-hole exit plane (FHEP) and is at the same location on the blade for each configuration.

### 5.1.2 Boundary Conditions

For each configuration, three blowing ratios were examined for a total of 18 simulations. For the SS,  $M=1.0$ , 1.5, and 2.0 were the nominal blowing ratios studied. For the PS,  $M=1.5$ , 3.0, and 4.5 were the blowing ratios studied. All simulations used a nominal  $DR=1.52$ . Total pressure profiles were prescribed at the passage and plenum inlets. In the experiments, no turbulence generator was used, however the turbulence intensity of the mainstream flow was found to be non-negligible. The instantaneous velocity was measured using a hot film sensor at the leading-edge plane of the airfoil cascade, midway between the adjacent airfoil surfaces. The turbulence intensity (TI) was found to be 8% at this monitor location. Turbulence boundary conditions for the simulations were determined by matching the TI at the monitor location in the passage. Since the turbulence decayed upstream of the monitor location, the necessary inlet value was  $TI_{in}=10.8$ . The turbulence length scale was not available from the experiments, but was estimated in the computations as 5% of the passage height. The plenum was modeled as a laminar zone based on the recommendations of Ferguson, Walters, and Leylek (1997). All walls were adiabatic.

## **5.2 Geometry and Grid**

The present study employs a super-block, multi-topology, unstructured/adaptive, non-conformal, body-fitted mesh that allows the highest possible quality grid while



completely resolving the high-gradient regions with a reasonable number of cells. In the super-block approach, the domain is originally divided into many smaller domains, each of which contains a block of unstructured mesh, with any one of three topologies: hexahedra, tetrahedra, or triangular prisms. The blocks are then joined together directly or by a layer of pyramid cells for cases when two adjacent blocks contain tri and quad face topologies, respectively. The passage grid maintained  $y^+ \leq 1$  on all surfaces. Because of the complexity of the jet-in-crossflow interaction, the film-hole and breakout regions contained cells with aspect ratios near unity. Figure 6 highlights some of the PS CAR mesh, including the multi-topology approach and the resolution of the near-wall regions. Figure 7 shows a typical histogram of cell skewness for the grids, with 0 indicating a perfectly equiangular cell and 1 a completely degenerate cell. A combination of I-DEAS Master Series 6A, by SDRC, Inc., and GAMBIT and T-grid, by Fluent, Inc., were used to generate the geometry and grid for each configuration.

### 4.3 Solution Method

Because accurate solutions of complex flowfields were desired in the present work, the second-order, linear reconstruction finite volume spatial discretization scheme in Fluent 5, by Fluent, Inc., was employed (Fluent, 1997; Barth and Jespersen, 1989). This scheme calculates face values based on a linear extrapolation from the upstream cell center, and limits dispersion by enforcing monotonic behavior between adjacent cells. A combination of solvers provided in Fluent 5, including the fully-explicit, time-marching scheme and the fully-implicit, pressure-correction scheme, was used to minimize the convergence time for each simulation. Approximately 1,500 to 2,000 iterations were required to converge each simulation. For both solvers, under-relaxation techniques were implemented to increase simulation stability. Convergence at each level of grid refinement was established by the following set of strict criteria: (1) a drop in all residuals to 0.01% of the relevant inlet fluxes; (2) global mass and energy imbalances of less than 0.01%; (3) less than 0.01% change in the general flowfield and pertinent surface parameters (such as  $\eta$ ) upon further iteration; and (4) no change in velocity, total pressure, mass flow rate, temperature,  $k$ , and  $\epsilon$  profiles at selected stations in the domain. Once a converged solution was obtained on the initial grid, gradient-based adaption was used to add a significant increase of cells (at least 15-20%) in those regions of the flowfield where gradients of all primary variables were highest. The solution was then reconverged on the adapted grid, and the process repeated until no grid-to-grid variation in results was observed, indicating a grid independent result.

### 4.4 Turbulence Model

Turbulence modeling remains the weak link for computational simulation of film-cooling problems. The steps outlined above are intended to minimize errors due to other sources, and isolate turbulence model performance. Since more complex models in general lead to more accurate solutions, selection of a turbulence model typically represents a trade-off between accuracy and computational expense. The RNG  $k$ - $\epsilon$  model with a two-layer near-wall treatment is used in the present study, for reasons outlined below.

The major issues for turbulence modeling in the present study include accurate reproduction of the passage turbulence field, accurate reproduction of the turbulent mixing of coolant downstream of the jet exit, and accurate resolution of the near-wall features of the flow. The flow in the passage is subject to strong irrotational straining due to aerodynamic loading on the airfoils. This can result in unrealistic turbulence production in the passage flow. Walters and Leylek (2000) documented this effect for a low-speed ( $Ma < 0.1$ ) airfoil cascade, attributing it to violation of the realizability conditions in both the standard and Renormalization Group (RNG)  $k$ - $\epsilon$  models. As a result, that study recommended the use of either a full Reynolds stress model (RSM) or the realizable  $k$ - $\epsilon$  model of Shih et al. (1995). However, for the present case, which includes transonic passage flow and higher airfoil loading, the RNG  $k$ - $\epsilon$  model was better able to reproduce the passage turbulence field and the airfoil boundary layer development relative to the RSM results, for the 2-D aerodynamic test case mentioned in section 5.1.1 above. The well-known “rule of thumb” that is typically employed in CFD for the inlet turbulence length scale – 5% of the passage height – did provide the best agreement. This length scale was therefore applied as an inlet boundary condition for the 3-D film-cooling simulations.

Several computational film-cooling studies have pointed out the need to accurately resolve the flow in the viscous sublayer and buffer region of the turbulent boundary layer, especially in the near-field region of a jet/crossflow interaction zone (e.g. Ferguson et al., 1998). As such, the two-layer treatment first proposed by Wolfstein (1969) is used in the present study.

Nearly all computational film-cooling studies in the open literature cite the lack of anisotropic mixing in two-equation models to be a key shortcoming of the turbulence treatment. Obviously, the use of the RNG model will not resolve the issue in the present study. In addition, the RNG model does not contain terms to model the effect of streamline curvature on the turbulence field. Nevertheless, it is believed that the current results represent the limiting case of what can be accomplished for these problems using a relatively simple linear eddy-viscosity turbulence model. Additional improvement to the results will probably be accomplished through the use of either non-linear models or full Reynolds stress closure.

## 6. RESULTS

### 6.1 Airfoil Loading Curve

Figure 8 shows the comparison between the target airfoil pressure distribution, the experimental results from the single airfoil passage model, and the computational results from the 2-D domain. Except for a region near the trailing edge on the suction side, the agreement between the test results and the target were excellent. Likewise, the excellent agreement between computations and experiments suggests that the inviscid features of

the single passage model were accurately captured in the simulations, including the location and strength of the shock that is evident on the SS at  $x/X_{ss} = 0.7$ .

## 6.2 Lateral Averaging Comparison

Since lateral averages at each downstream location were calculated for the experiments using a simple average at the four tap locations, it is possible that comparisons to a full-pitch lateral average from the computations might lead to discrepancies. In order to confirm that this was not the case, the computational results were averaged using two different techniques: full-pitch averaging, and an average using only the surface area corresponding to the physical tap locations in the experiments. Figure 9 shows two representative comparisons, from the compound-angle round configuration. This configuration has the narrowest coolant footprint on the downstream surface and would presumably be most prone to averaging errors. While there is in fact a small discrepancy between the two averages in the near field, it is close to the experimental uncertainty. Farther downstream, the discrepancy is negligible. It was therefore deemed acceptable to compare full-pitch computational results to the experimental data, as in the following sections.

## 6.3 Compound-Angle Round Holes

Spanwise-averaged  $\eta$  for the SS cases is plotted versus normalized downstream distance in Figure 10. The figure indicates reasonably good agreement between experiments and computations. The effectiveness is slightly underpredicted in all cases, although agreement improves with increasing  $M$ . Qualitatively, the results show similar trends, effectiveness in the near field varies inversely with  $M$ , but varies directly with  $M$  far downstream. Note, however, that the location where  $\bar{\eta}$  for  $M = 1$  drops below  $\bar{\eta}$  for  $M = 2$  is at about  $x/X_{ss} = 0.2$  for the computations, but  $x/X_{ss} = 0.7$  for the experiments. Results for the PS cases are shown in Figure 11, and are similar to those for the ASH configuration below. Both experiments and computations show that the effectiveness varies inversely with  $M$  in the very near field, but farther downstream, effectiveness increases with increased coolant addition, and no blow-off is observed. The computational results approach the measured data far downstream, but overpredict  $\bar{\eta}$  closer to the film hole. It is also evident that agreement is best for the lowest  $M$  case, but gets progressively worse as  $M$  increases. The current approach evidently tends to overpredict  $\bar{\eta}$  when coolant penetrates through the boundary layer.

## 6.4 Axial Shaped Holes

A comparison with experiments of laterally-averaged adiabatic effectiveness in Figure 12 on the SS for different  $M$  shows reasonably good agreement for the two lowest blowing ratios. However, the experiments indicate that the  $M = 2$  case has blown-off, resulting in lower downstream effectiveness values than for the  $M = 1.5$  case, while the computations show a continued increase in effectiveness. As above, the computations tend to overpredict the cooling performance when the coolant penetrates the boundary layer. A similar comparison for the PS configuration in Figure 13 shows that the

computations capture the qualitative trends only. For  $M=1.5$  on the PS, the computations match the experiments very well. In the far-field, the agreement between computations and experiments is good for all cases. However, for the highest two  $M$  cases, the computations significantly over-predict in the near field. As will be discussed in the following sections of this paper, in the presence of crossflow ingestion and/or strong coolant penetration of the crossflow boundary layer, the computational methodology used in the present study tends to significantly over-predict surface cooling effectiveness. Nevertheless, for both PS and SS ASH configurations, the computational results may be used to gain insight into the physics of ASH film cooling.

### **6.5 Compound-Angle Shaped Holes**

Figures 14 and 15 show laterally averaged  $\eta$  for the CASH configurations on the SS and PS, respectively. Both the experimental data and computational results indicate that no coolant blow-off occurs over the entire range of blowing ratio. This configuration also shows the best overall agreement between computations and measurements, and the influence of  $M$  is well represented on both surfaces. For this configuration, the flow is well diffused by hole shaping, resulting in relatively low exit momentum, and more coolant remaining within the boundary layer, relative to either the CAR or ASH configurations. More detailed discussion is found in Part IV of this paper.

## **6. CONCLUSIONS**

This four-part paper describes a joint experimental and computational effort to analyze film-cooling performance of several complex film-hole geometries on a modern turbine airfoil, and to document the underlying physics responsible for that performance. The study models realistic engine conditions, including Reynolds and Mach numbers typical of those found in actual turbines. Validation quality experimental results have been obtained using a single passage cascade (SPC) model that reproduces the geometry and flow features of a highly loaded turbine cascade. A foreign gas sampling technique provides laterally-averaged adiabatic effectiveness data with uncertainty less than 10% at all downstream locations. The computational methodology as outlined is intended to minimize geometry and grid-based errors and place the simulations against the limits of a commonly used eddy-viscosity turbulence model, RNG, with a two-layer near-wall treatment.

This study highlights the manner in which experiments and CFD augment one another. The experimental results serve to anchor and validate the computations, while the CFD results provide detailed insight into complex physical mechanisms and aid in understanding the measurements.

Conclusions specific to the current part include the following:

- The turbine passage aerodynamics is well reproduced by both the experimental SPC model and the computational methodology, as indicated by the excellent agreement of the airfoil loading curves.
- For low blowing ratios, the computational results show good agreement with measurements. It appears that the turbulence modeling approach used in the current study performs well when coolant remains within the airfoil boundary layer, but is less accurate when coolant penetrates into the freestream.
- In general, better agreement between computations and experiments is obtained on the suction surface of the airfoil. This may be due in part to the fact that the blowing ratio ranges in the current study were lower on the SS than on the PS.
- Computations in general show better agreement with measured data for film-hole configurations with compound-angle injection.
- The results appear to indicate that the current computational methodology, specifically the turbulence treatment, is not yet capable of yielding consistently accurate film-cooling predictions for all combinations of geometry and blowing ratio. Predictive capability can be improved by addressing the weaknesses in the current standard of two-equation eddy-viscosity turbulence modeling, either through the use of more advanced models (e.g. differential Reynolds stress models) or improvement to existing eddy-viscosity models.

## REFERENCES

- Ames, F.E., 1997a, "Aspects of Vane Film Cooling with High Turbulence: Part I – Heat Transfer," ASME Paper No. 97-GT-239.
- Ames, F.E., 1997b, "Aspects of Vane Film Cooling with High Turbulence: Part II – Adiabatic Effectiveness," ASME Paper No. 97-GT-240.
- Barth, T.J. and Jespersen, K., 1989, "The Design and Application of Upwind Schemes on Unstructured Meshes," Technical Report AIAA-89-0366, AIAA 27th Aerospace Sciences Meeting, Reno, Nevada.
- Brittingham, R.A. and Leylek, J.H., 1997, "A Detailed Analysis of Film Cooling Physics Part IV: Compound-Angle Injection with Shaped Holes," ASME Paper No. 97-GT-272.
- Buck, F.A and Prakash, C., 1995, "Design and Evaluation of a Single Passage Test Model to Obtain Turbine Airfoil Film Cooling Effectiveness Data," ASME Paper 95-GT-19.
- Drost, U., and Bolcs, A., 1998, "Investigations of Detailed Film Cooling Effectiveness and Heat Transfer Distributions on a Gas Turbine Airfoil," ASME Paper No. 98-GT-20.

Ekkad, S.V., Zapata, D., and Han, J.C., 1997a, "Heat Transfer Coefficients Over a Flat Surface with Air and CO<sub>2</sub> Injection Through Compound Angle Holes Using a Transient Liquid Crystal Image Method," ASME J. of Turbomachinery, Vol. 119, pp. 580-586.

Ekkad, S.V., Zapata, D., and Han, J.C., 1997a, "Film Effectiveness Over a Flat Surface with Air and CO<sub>2</sub> Injection Through Compound Angle Holes Using a Transient Liquid Crystal Image Method," ASME J. of Turbomachinery, Vol. 119, pp. 587-593.

Ferguson, J.D., Walters, D.K. and Leylek, J.H., 1998, "Performance of Turbulence Models and Near-Wall Treatments in Discrete Jet Film-Cooling Simulations," ASME Paper No. 98-GT-438.

Garg, V.K. and Gaugler, R.E., 1997, "Effect of Velocity and Temperature Distribution at the Hole Exit on Film Cooling of Turbine Blades," ASME Journal of Turbomachinery, Vol. 119, pp. 343-351.

Garg, V.K. and Rigby, D.L., 1998, "Heat Transfer on a Film-Cooled Blade - Effect of Hole Physics," ASME Paper No. 98-GT-404.

Goldstein, R.J., Eckert, E.R.G., and Burggraf, F., 1974, "Effects of Hole Geometry and Density on Three-Dimensional Film Cooling," Int. J. of Heat and Mass Transfer, Vol. 17, pp. 595-607.

Gritsch, M., Schulz, A., and Wittig, S., 1997a, "Adiabatic Wall Effectiveness Measurements of Film-Cooling Holes with Expanded Exits," ASME Paper No. 97-GT-164.

Gritsch, M., Schulz, A., and Wittig, S., 1997b, "Discharge Coefficient Measurements of Film-Cooling Holes with Expanded Exits," ASME Paper No. 97-GT-165.

Gritsch, M., Schulz, A., and Wittig, S., 1998, "Heat Transfer Coefficient Measurements of Film-Cooling Holes with Expanded Exits," ASME Paper No. 98-GT-28.

Haven, B.A., Yamagata, D.K., Kurosaka, M., Yamawaki, S., and Maya, T., 1997, "Anti-Kidney Pair of Vortices in Shaped Holes and Their Influence on Film-Cooling Effectiveness," ASME Paper No. 97-GT-45.

Honami, S., Shizawa, T., and Uchiyama, A., 1994, "Behavior of the Laterally Injected Jet in Film Cooling: Measurements of Surface Temperature and Velocity/Temperature Field Within the Jet," ASME J. of Turbomachinery, Vol. 116, pp. 106-112.

Hyams, D.G. and Leylek, J.H., 1997, "A Detailed Analysis of Film-Cooling Physics Part III: Streamwise Injection with Shaped Holes," ASME Paper No. 97-GT-271.

Ito, S., Goldstein, R.J., and Eckert, E.R.G., 1978, "Film Cooling of a Gas Turbine Blade," ASME J. of Engineering for Power, Vol. 100, pp. 476-481.

Kline, S.J. and McClintock, F.A., 1953, "Describing Uncertainties in Single-Sample Experiments," *Mechanical Engineering*, Vol. 75, January, pp. 3-8.

Lee, S.W., Kim, Y.B., and Lee, J.S., 1997, "Flow Characteristics and Aerodynamic Losses of Film-Cooling Jets with Compound Angle Orientations," ASME J. of Turbomachinery, Vol. 119, pp. 310-319.

Ligrani, P.M., Ciriello, S., and Bishop, D.T., 1992, "Heat Transfer, Adiabatic Effectiveness, and Injectant Distributions Downstream of a Single Row and Two Staggered Rows of Compound Angle Film-Cooling Holes," ASME J. of Turbomachinery, Vol. 114, pp. 687-700.

Ligrani, P.M., Wigle, J.M., Ciriello, S., and Jackson, S.M., 1994a, "Film-Cooling from Holes with Compound Angle Orientations: Part 1 – Results Downstream of Two Staggered Rows of Holes with 3d Spanwise Spacing," ASME J. of Turbomachinery, Vol. 116, pp. 341-352.

Ligrani, P.M., Wigle, J.M., and Jackson, S.M., 1994b, "Film-Cooling from Holes with Compound Angle Orientations: Part 2 – Results Downstream of a Single Row of Holes with 6d Spanwise Spacing," ASME J. of Turbomachinery, Vol. 116, pp. 353-362.

McGovern, K.T. and Leylek, J.H., 1997, "A Detailed Analysis of Film-Cooling Physics Part II: Compound-Angle Injection with Cylindrical Holes," ASME Paper No. 97-GT-270.

Pedersen, R.D., 1972, "Effect of Density Ratio on Film Cooling Effectiveness for Injection Through a Row of Holes and for a Porous Slot," Ph.D. Thesis, U. Minnesota, Minneapolis, MN.

Schmidt, D.L., Sen, B., and Bogard, D.G., 1996, "Film Cooling with Compound Angle Holes: Adiabatic Effectiveness," ASME J. of Turbomachinery, Vol. 118, pp. 807-813.

Sen, B., Schmidt, D.L., and Bogard, D.G., 1996, "Film Cooling with Compound Angle Holes: Heat Transfer," ASME J. of Turbomachinery, Vol. 118, pp. 800-806.

Shih, T.-H., Liou, W.W., Shabbir, A., and Zhu, J., 1995, "A New k- $\epsilon$  Eddy-Viscosity Model for High Reynolds Number Turbulent Flows Model Development and Validation," *Computers in Fluids*, Vol. 24(3), pp. 227-238.

Walters, D.K. and Leylek, J.H., 1997a, "A Systematic Computational Methodology Applied to a Three-Dimensional Film-Cooling Flowfield," ASME Journal of Turbomachinery, Vol. 119, pp. 777-785.

Walters, D.K. and Leylek, J.H., 1997b, "A Detailed Analysis of Film-Cooling Physics Part I: Streamwise Injection with Cylindrical Holes," ASME Paper No. 97-GT-269.

Walters, D.K. and Leylek, J.H., 2000, "Impact of Film-Cooling Jets on Aerodynamic Losses," ASME J. of Turbomachinery, Vol. 122, pp. 537-545.

Wolfstein, M., 1969, "The Velocity and Temperature Distribution of One-Dimensional Flow with Turbulence Augmentation and Pressure Gradients," Int. J. of Heat and Mass Transfer, Vol. 12, pp. 301-318.

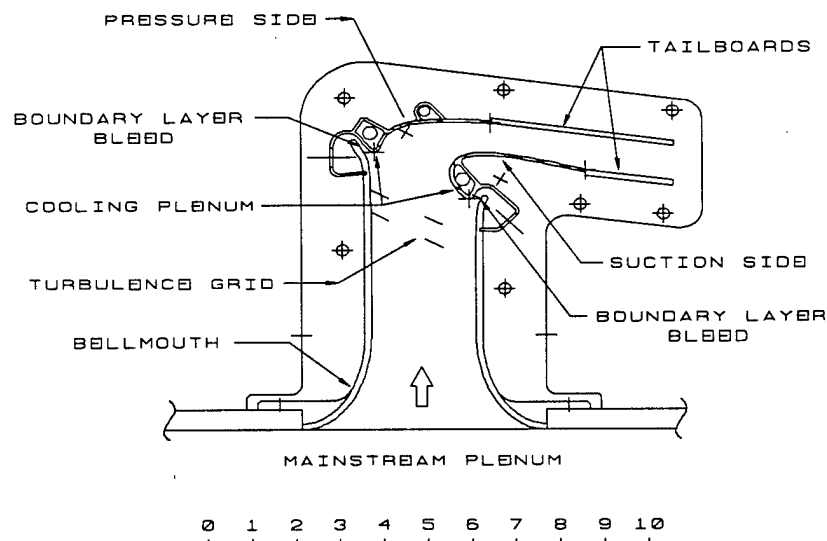


Figure 1. Cross-section view of single airfoil passage test model.



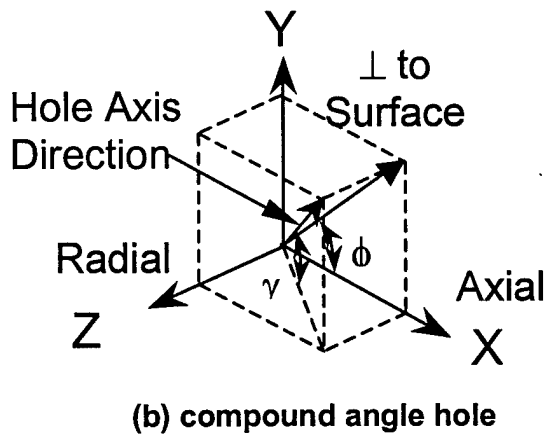
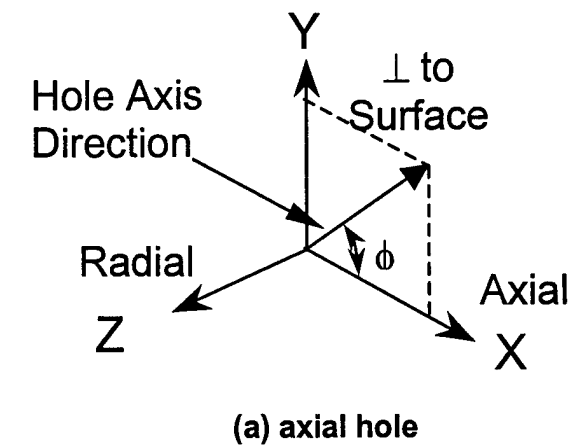


Figure 2. Axial (a) and compound-angle (b) hole definitions.

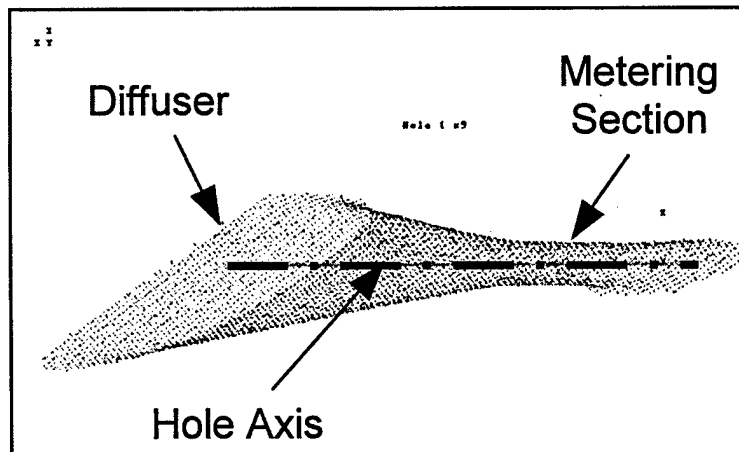


Figure 3. “Cloud” image of edge points defining the interior walls of shaped film hole.

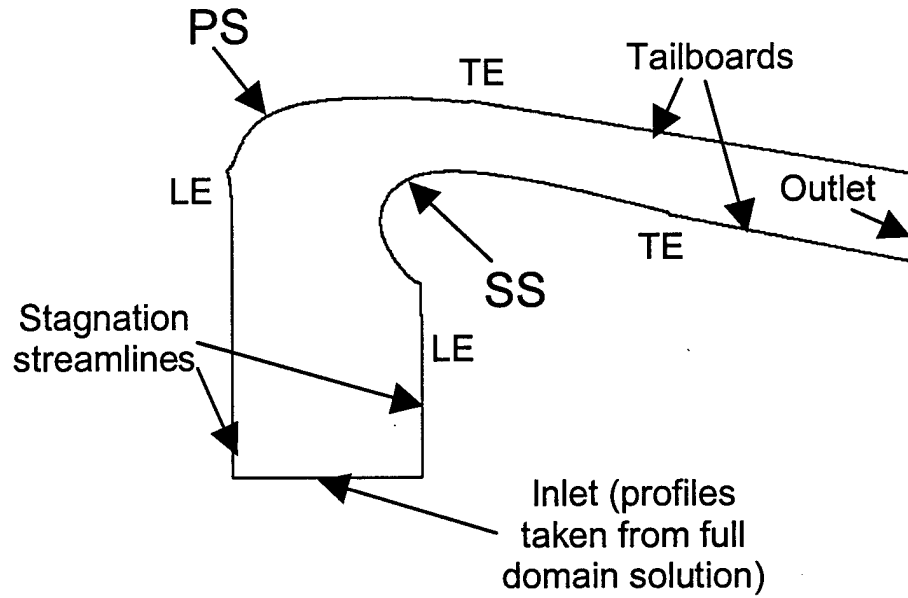


Figure 4. Illustration of single-passage cascade geometry used in the present study.

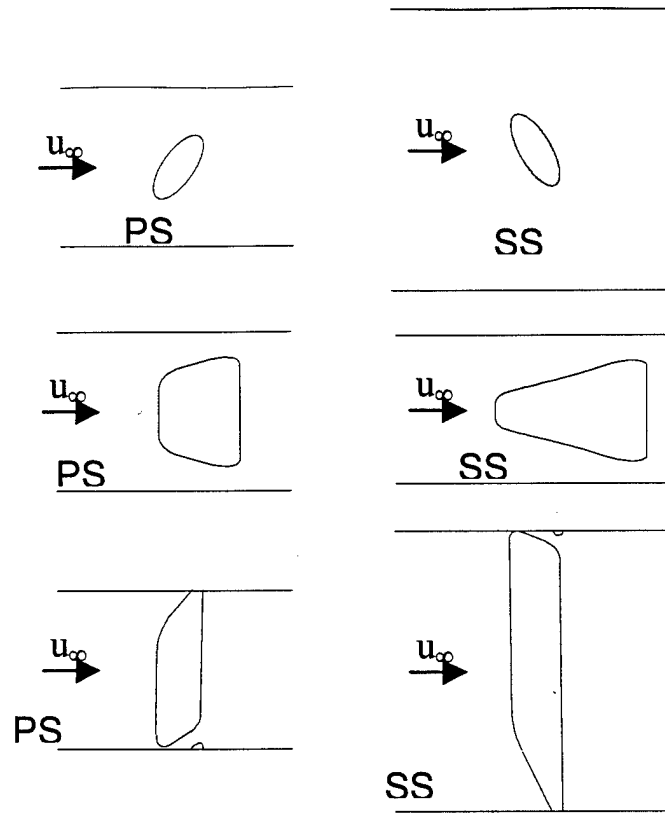


Figure 5. Film-hole breakout geometry for each of the configurations used in the present study.

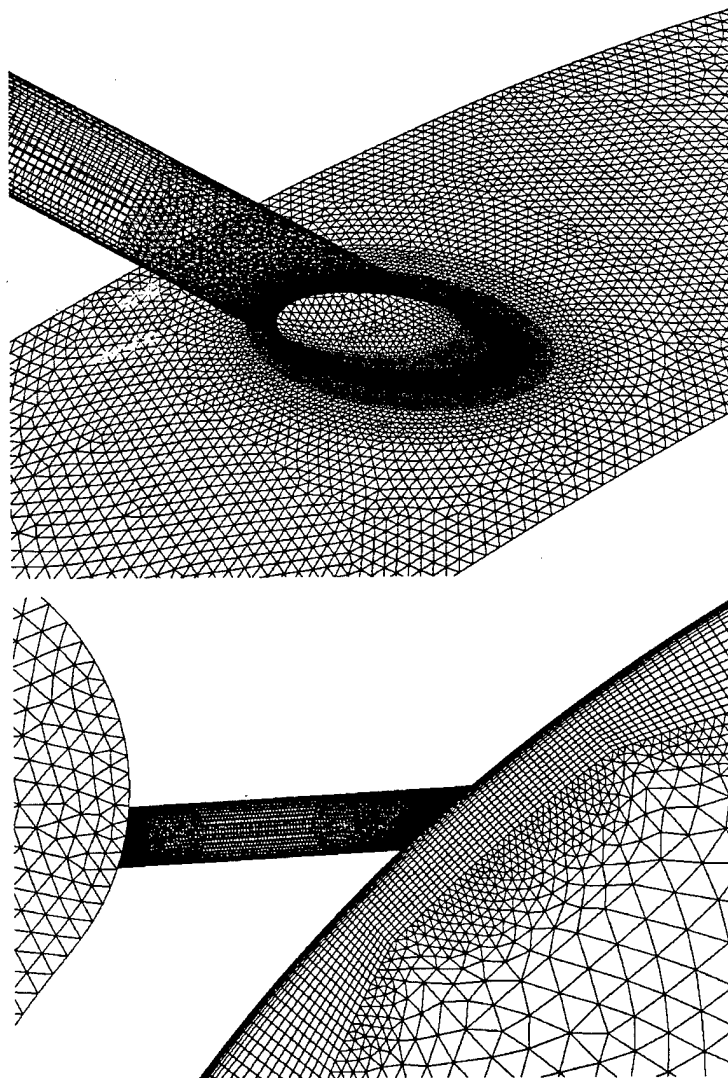


Figure 6. Illustration of the PS CAR grid near the film-hole breakout (a), and depicting the multi-topology near-wall approach (b).

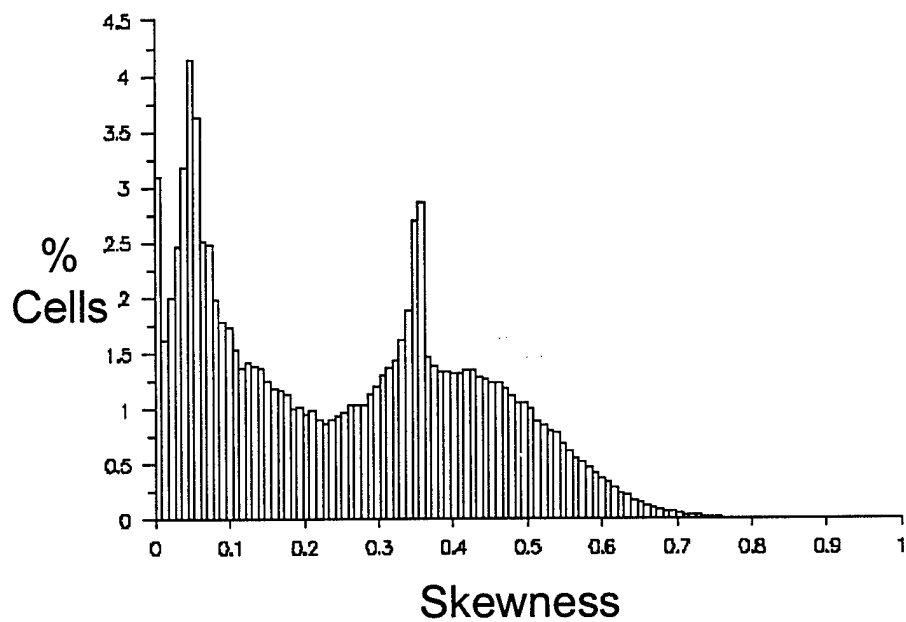


Figure 7. Histogram of cell skewness for the SS CAR case gives an indication of the high grid quality present in all of the cases.

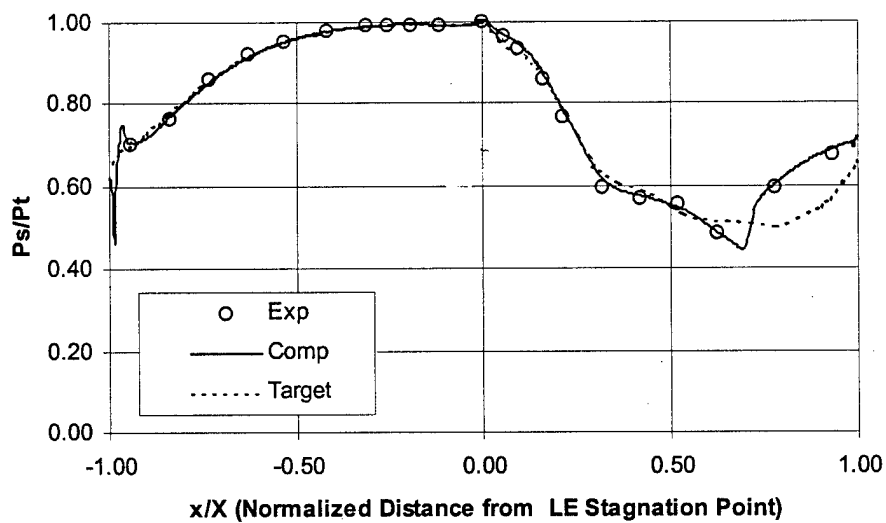


Figure 8. Airfoil loading curve shows agreement between experimental test model and target pressure distribution, and between computations and experiments.

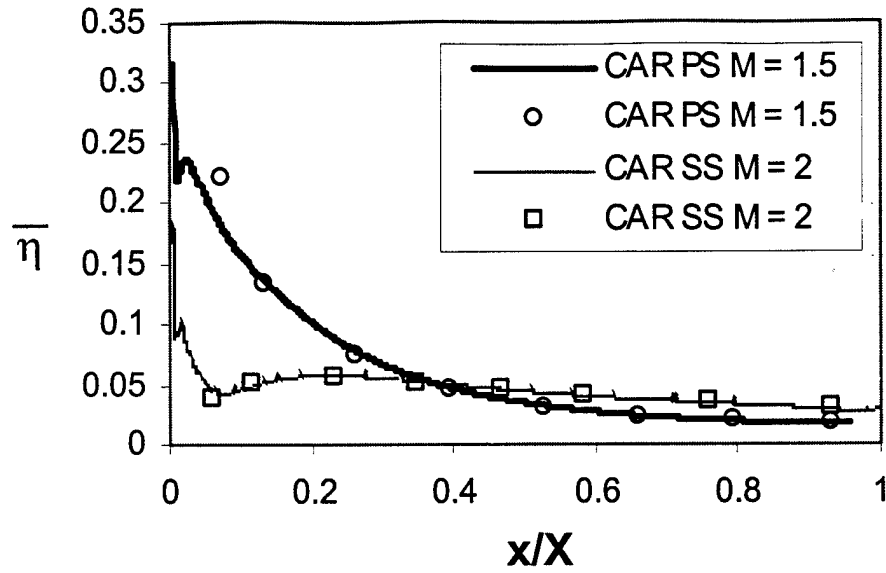


Figure 9. Comparison of computational results using two different averaging techniques. The curves show full-pitch averages, the symbols show averaging at discrete tap locations used in the experiments.

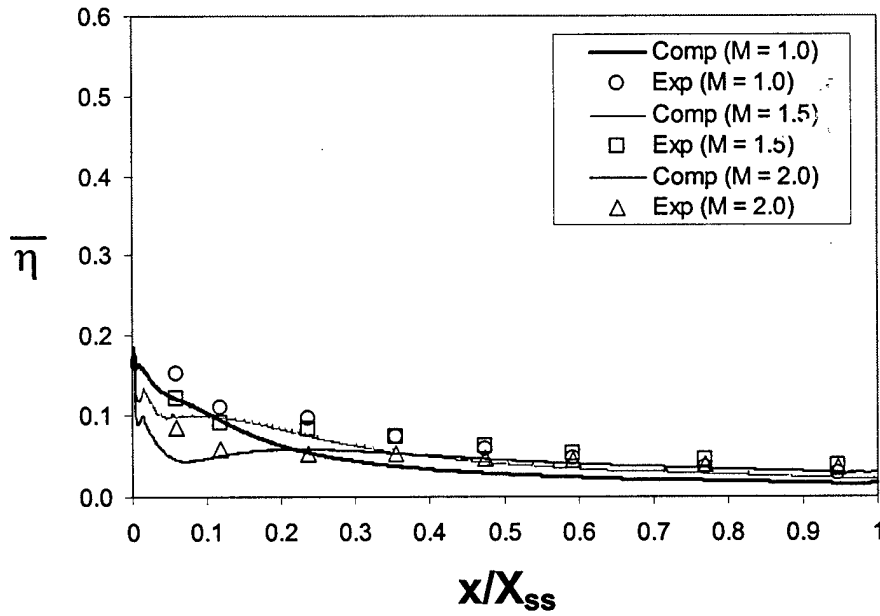


Figure 10. SS CAR cases show reasonable agreement, but consistent underprediction far downstream of injection.

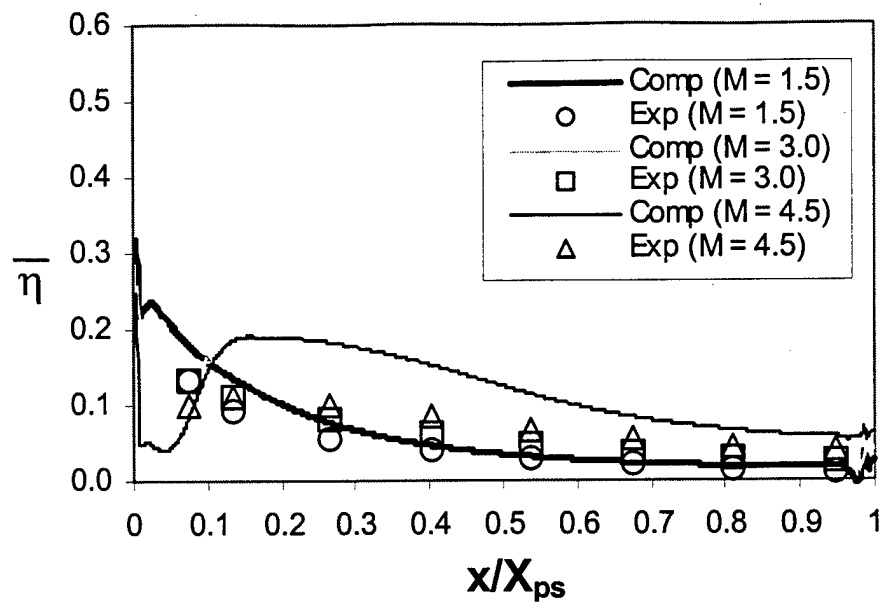


Figure 11. Laterally-averaged adiabatic effectiveness for the PS CAR cases show agreement between computed and measured trends.

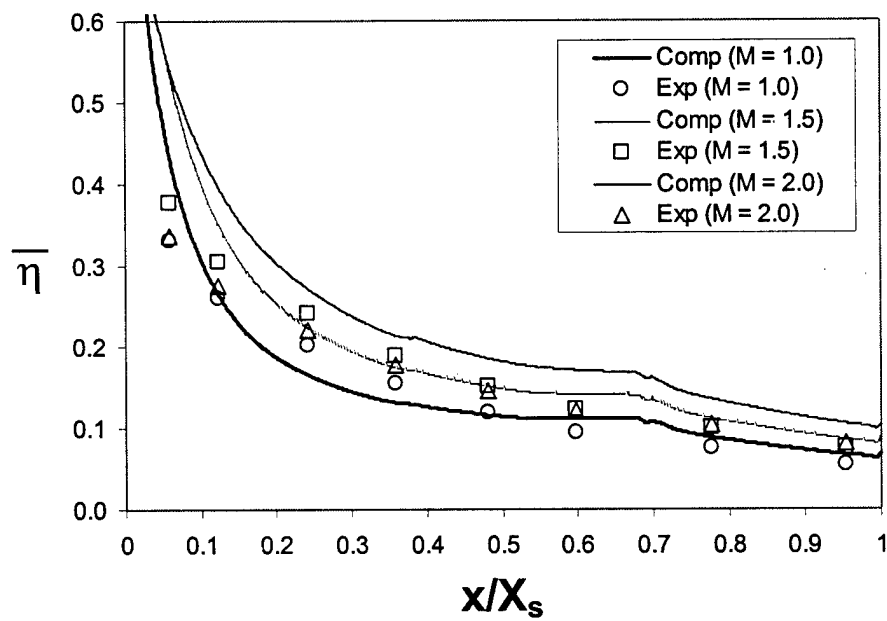


Figure 12. Laterally-averaged effectiveness for SS ASH cases show reasonable agreement with experiments for all blowing ratios.

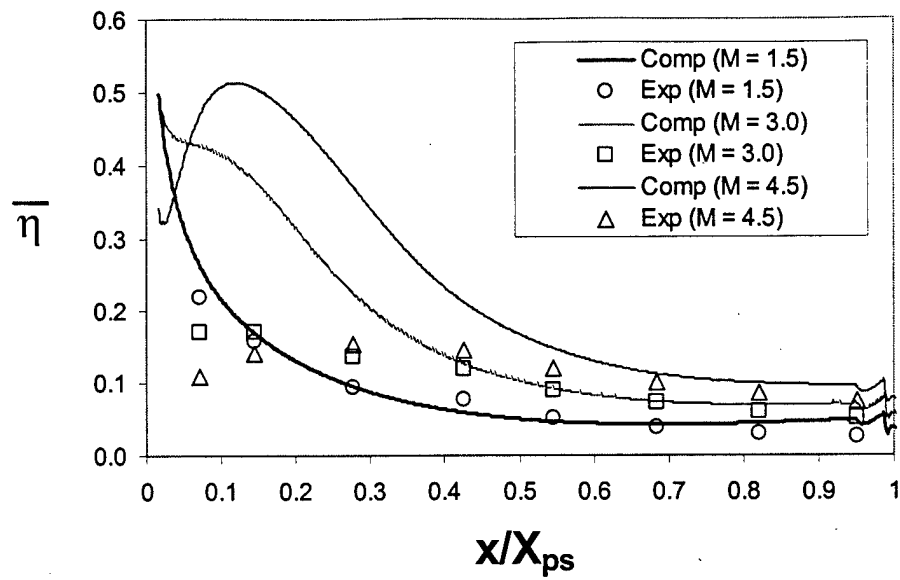


Figure 13. PS ASH cases show relatively good downstream agreement, but overprediction in the near field as blowing ratio increases.

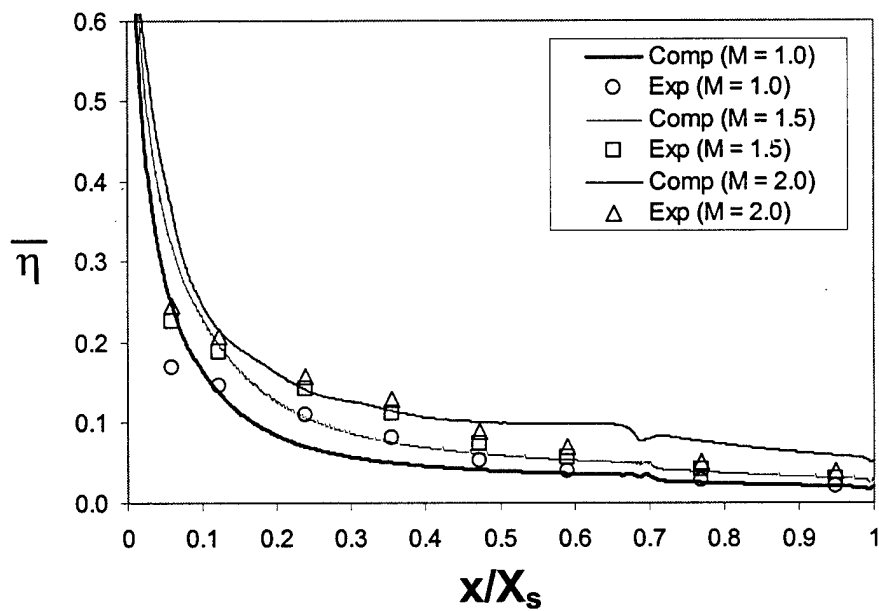


Figure 14. Laterally-averaged adiabatic effectiveness for SS CASH cases.



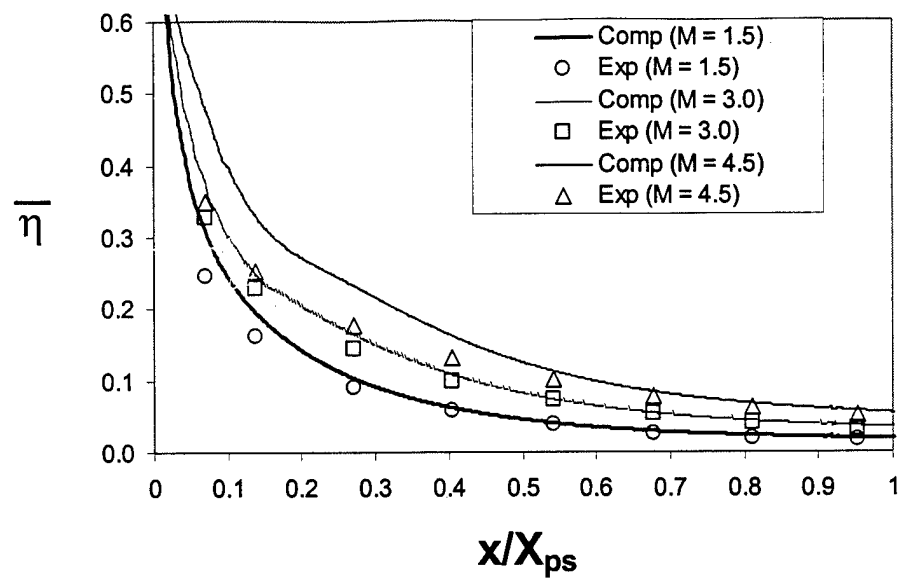


Figure 15. PS CASH results indicate good agreement with experimental data.

## CHAPTER 6

### FILM COOLING ON A MODERN HP TURBINE BLADE PART II: COMPOUND-ANGLE ROUND HOLES

D. Keith Walters, James H. Leylek and Frederick A. Buck

#### NOMENCLATURE

|              |   |
|--------------|---|
| ASH          | <u>a</u> xial <u>s</u> haped <u>h</u> oles                        |
| CAR          | <u>c</u> ompound- <u>a</u> ngle <u>r</u> ound holes               |
| CASH         | <u>c</u> ompound- <u>a</u> ngle <u>s</u> haped <u>h</u> oles      |
| D            | film-hole diameter  |
| DR           | density ratio = $\rho_j/\rho_\infty$                              |
| FHEP         | <u>f</u> ilm- <u>h</u> ole <u>e</u> xit <u>p</u> lane             |
| k            | turbulence kinetic energy   |
| l            | turbulence length scale   |
| L            | film-hole length  |
| M            | blowing ratio = $(\rho u)_j/(\rho u)_\infty$                      |
| P            | film-hole pitch   |
| PS           | <u>p</u> ressure <u>s</u> urface                                  |
| r            | recovery factor   |
| SS           | <u>s</u> uction <u>s</u> urface                                   |
| T            | temperature   |
| $T_{cool}$   | coolant recovery temperature = $T_{s,aw} + r(T_{T,P} - T_{s,aw})$ |
| TE           | <u>t</u> railing <u>e</u> dge                                     |
| u            | local velocity magnitude  |
| U            | non-dimensional local velocity magnitude = $u/u_j$                |
| X            | length of cooled section of airfoil                               |
| $y^+$        | non-dimensional wall distance                                     |
| $\epsilon$   | turbulence dissipation rate                                       |
| $\phi$       | film-hole compound angle  |
| $\gamma$     | film-hole injection angle   |
| $\eta$       | adiabatic effectiveness = $(T_r - T_{s,aw})/(T_r - T_{cool})$     |
| $\bar{\eta}$ | laterally- or spanwise-averaged $\eta$                            |
| $\rho$       | density   |
| $\theta$     | normalized $T_s = (T_p - T_s)/(T_p - T_{T,in})$                   |

#### Subscripts

|          |  |
|----------|--|
| $\infty$ | free-stream condition at location of injection |
| avg      | average  |
| aw       | adiabatic wall                                 |

|    |   |
|----|---|
| ch | airfoil chord                                   |
| fh | film hole                                       |
| in | inlet conditions                                |
| j  | jet conditions in metering section              |
| P  | plenum inlet conditions                         |
| pp | conditions at pierce point (injection location) |
| r  | recovery condition                              |
| s  | static quantity                                 |
| T  | total (stagnation) quantity                     |

## 1. INTRODUCTION

The current four-part paper documents a thorough investigation, using both computational simulations and code-validation quality experimental data, of film cooling on a modern turbine blade. The test cases are meant to reproduce engine-realistic operating conditions, and to examine the influence of complex film-hole configurations on cooling performance. In addition, the results are used to document the physical mechanisms responsible for cooling performance, for each of the different configurations. This part of the four-part paper considers a row of compound-angled, cylindrical film-holes on both the suction and pressure surfaces of the airfoil. Compound-angled holes are known to increase adiabatic effectiveness by imparting a lateral component of momentum to the exiting coolant, and improving downstream coverage. Compound-angled round holes represent the "simplest" of the three complex configurations considered in the present study.

## 2. PRESENT CONTRIBUTIONS

Part I of the paper documented a review of the open literature and identified outstanding issues. The experimental and computational methodologies were outlined in detail, and computational results for each of the configurations were compared to experiments. This part of the paper focuses exclusively on the compound-angle round hole (CAR) configuration, with the following specific objectives:

- Document and analyze the film-cooling effectiveness of CAR configurations under engine-realistic operating conditions;
- Identify the key physical mechanisms, especially those linked to film-hole compound-angle, responsible for the behavior of the jet-and-crossflow interaction;
- Examine the effects of blowing ratio on the physical mechanisms in CAR film-cooling geometries;
- Highlight the performance of the computational methodology -- particularly the turbulence modeling -- for these simulations.

### 3. SIMULATION DETAILS

The computational methodology is outlined in Part I of this paper, and the reader is referred there for a thorough discussion. The computational domain is illustrated in Figure 1, for the SS case. Stagnation streamlines are used to model the single passage cascade without including the SS and PS bleed cavities. Periodic boundary conditions are applied at the spanwise boundaries to model a row of holes. Variation between the different configurations (CAR, ASH, and CASH) is found only in the geometric details of the film-hole geometry, and will be discussed here for the CAR configuration. The suction surface geometry consists of a single row of film-holes oriented with injection angle ( $\gamma$ ) equal to  $23^\circ$  and a compound angle ( $\phi$ ) equal to  $59.6^\circ$ . The film-hole pitch-to-diameter ratio ( $P/D$ ) equals 8.8. For the pressure surface,  $\gamma = 25^\circ$  and  $\phi = 54^\circ$ , with  $P/D = 5$ . Figure 2 shows a close-up representation of the SS and PS film-hole geometries with definition of injection and compound angle. For the SS and PS cases,  $L/D = 12.4$  and  $7.8$ , respectively. The cases were gridded as described in Part I, with the background meshes containing 2.3 million cells for the SS cases and 1.8 million cells for the PS cases. Refined grids used to establish grid independence contained approximately 20% more cells than the background grids, with cells concentrated in regions with high gradients of primary variables.

The passage conditions for these cases included inlet  $Ma = 0.2$ , up to  $Ma$  slightly greater than one downstream of the throat, and  $Re_{ch}$  from 600,000 at the inlet to 2,000,000 at the throat, which were intended to model actual engine flow. The turbulence intensity at the center of the passage leading edge plane was 8%, and the turbulence length scale was taken as 5% of the passage inlet height. The coolant-to-mainstream density ratio (DR) for all cases was nominally 1.52. This density ratio was achieved through foreign gas injection in the experiments, but through a temperature difference in the simulations. All walls were adiabatic in the simulations. Table 1 shows the parameters used for each of the different cases with the CAR configuration.

As discussed in Part I, the simulations were run using the Fluent 5 software from Fluent, Inc. The discretization was second-order linear reconstruction scheme, and the turbulence model was the RNG  $k-\epsilon$  model. The two-layer near-wall treatment was used in order to resolve the flow very near surfaces, especially in the film-hole breakout region.

Pre- and post-processing work was performed on Sun Ultra 10 machines with 300 MHz CPUs and 1GB of RAM and a Sun Ultra 4000 machine with ten 250 MHz CPUs and 5GB of RAM. All simulations for the present work were run on 5 to 12 CPUs on the aforementioned Sun Ultra 4000 and a Sun HPC 6000 machine with 16 CPUs and 4GB of RAM. I-DEAS Master Series 6A from SDRC, T-Grid from Fluent, Inc., and GAMBIT from Fluent, Inc. were used in the pre-processing phases of the simulations.

Table 1. Summary of Parameters for SS and PS Simulations

| Configuration | Case Name | M   | DR   |
|---------------|-----------|-----|------|
| SS            | SS-LOW    | 1.0 | 1.52 |
|               | SS-MID    | 1.5 | 1.52 |
|               | SS-HIGH   | 2.0 | 1.52 |
| PS            | PS-LOW    | 1.5 | 1.52 |
|               | PS-MID    | 3.0 | 1.52 |
|               | PS-HIGH   | 4.5 | 1.52 |

## 4. RESULTS AND DISCUSSION

### 4.1 Suction Surface

Figure 3 shows the comparison of downstream spanwise-averaged adiabatic effectiveness ( $\bar{\eta}$ ) for computed results versus measured data for the three blowing ratio cases on the SS. It is apparent that the SS effectiveness is somewhat low ( $< 0.2$ ) for all three M. This is in large part due to the relatively large pitch-to-diameter ratio ( $P/D = 8.8$ ) for this geometry. Comparison indicates reasonable agreement, although the computational results consistently underpredict the experiments. The degree of underprediction seems to vary inversely with M, as the  $M = 2$  case shows the best downstream agreement, and the  $M = 1$  case shows the worst agreement. The qualitative behavior is well captured for all cases, which suggests that the computations reproduce the essential mean-flow physical mechanisms, if not the relative "strength" of those mechanisms. As such, the mean-flow physics for the SS cases is discussed below.

#### 4.1.1 Blade Surface

Figure 4 highlights the distribution of adiabatic effectiveness near the film holes for the three blowing ratios on the SS. The figure highlights the inverse dependence of the near-field effectiveness on blowing ratio, or more accurately momentum flux ratio. As M (or I) increases for these cases, the coolant is lifted farther from the surface, reducing the near-hole effectiveness. This is apparent by the fact that the  $M = 1$  case shows the influence of the coolant immediately downstream of the hole in a relatively wide band, while the size of that band grows progressively thinner as M increases. Farther downstream, near the right-hand edge of the figure, it can be seen that the coolant footprint is widest for the  $M = 1.5$  case. Apparently, as M increases from 1 to 1.5, additional coolant results in a wider coolant footprint. However, as M increases to 2.0, the coolant jets lift-off from the surface, thus narrowing the footprint. This effect is compounded on the suction surface, since higher momentum coolant jets tend to get

pushed away from the surface by the pressure gradient normal to the surface (see Ito et al., 1978). This behavior will be addressed again in section 4.1.3.

#### 4.1.2 Film Hole and Plenum

The separation, flow turning, and coolant jetting within the film-hole has been well documented (e.g. Walters and Leylek, 1997). The complex flow in the film-hole influences the flow distribution at the film-hole exit plane (FHEP), which in turn influences the downstream effectiveness and heat transfer characteristics (e.g. Garg and Gaugler, 1995). For the present SS cases, the film hole is relatively long ( $L=12.4 D$ ), and the coolant flow relaxes to a full profile at the FHEP, as shown in Figure 5 for  $M = 1.5$ . The vectors are plotted in a plane through the center of the film hole at four different locations, and the contours demonstrate the tendency of the coolant to exit from the downstream portion of the film-hole, due to the blockage effect of the crossflow (Leylek and Zerkle, 1994). As will be seen in parts III and IV of this paper, those cases with strong coolant jetting at the FHEP can result in the ingestion of mainstream fluid into the film hole. Ingestion is not present, however, in any of the six simulations of the CAR configuration.

#### 4.1.3 Near Field

Figure 6 shows velocity vectors in a plane normal to the passage flow for the  $M = 1.5$  case at a location  $2D$  downstream of the film-hole trailing edge. The region just downstream of film-cooling injection has been shown to be dominated by the formation of streamwise vortices. For simple streamwise injection, a symmetric, counter-rotating vortex pair forms due primarily to the streamwise-oriented vorticity exiting the film hole near its lateral sides (Walters and Leylek, 1997). For compound-angle injection it is known that one of the vortices becomes dominant, and for a steep enough compound-angle, one leg of the pair disappears leaving a single dominant vortex (SDV). The SDV for the present case is clearly visible in Figure 6. Less obvious, but still apparent, are the remains of the weaker vortex, which still slightly influences the flow in the near field.

The SDV, being deposited relatively far from the airfoil surface, can persist for some distance downstream, entraining coolant as well as hot mainstream fluid. The strength of the SDV increases as blowing ratio increases. Figure 7 highlights the influence of the SDV on the distribution of coolant in the near field for the SS cases. At the lowest blowing ratio, the SDV exerts little influence and the coolant remains relatively close to the surface. As  $M$  increases, the coolant is lifted away from the surface by entrainment into the SDV. This explains the inverse dependence of  $\bar{\eta}$  on  $M$  in the near field, evidenced by Figure 3. Except for in the immediate vicinity of the film hole, lift-off of the coolant entrained in the SDV is also influenced by the airfoil curvature. For the SS cases, high momentum-flux ratios result in coolant being pushed away from the wall by the pressure gradient normal to the surface, increasing the already present tendency for higher  $I$  cases to lift-off farther from the surface. Evidence of this effect is visible in the effectiveness contours in Figure 4.

#### 4.1.4 Far Field

Far downstream of injection, the secondary motion caused by the SDV weakens, and the coolant is simply carried downstream and diffused by turbulent mixing. Likewise, the momentum difference between coolant and passage flow becomes small, minimizing the influence of airfoil curvature. In this region, at low blowing ratios, the near-field trend reverses: higher  $M$  means more available coolant and more “thermal capacity”, so downstream effectiveness tends to increase. At some blowing ratio, however, increase in  $M$  will result in a decrease in  $\bar{\eta}$ , regardless of downstream location. This phenomenon is referred to as “blow off” or “penetration” and is evident on the SS in the experimental data between  $M = 1.5$  and 2. The computations do not reproduce blow-off far downstream in these cases, a fact apparently related to the underprediction of  $\bar{\eta}$  at low  $M$  on the suction surface, and which is discussed in more detail below.

### **4.2 Pressure Surface**

The spanwise-averaged adiabatic effectiveness ( $\bar{\eta}$ ) for the PS cases is shown in Figure 8. The pitch-to-diameter ratio is smaller for this geometry ( $P/D = 5$ ) and the range of blowing ratios is considerably larger than for the SS cases. Despite this, the overall levels of  $\bar{\eta}$  are close to those on the SS, highlighting the relative difficulty in cooling the pressure surface of an airfoil. Comparison of computational results with experimental data indicates an overprediction by the computations. The degree of overprediction tends to increase as  $M$  increases, with the lowest blowing ratio ( $M = 1.5$ ) showing the best agreement. This contrasts the SS results, which showed best agreement at the highest blowing ratios. Possible reasons for these trends are discussed in section 4.3. As on the SS, the accurate reproduction of data trends suggests that the physical mechanisms – if not their absolute strength – are being simulated.

#### 4.2.1 Blade Surface

Figure 9 shows contours of adiabatic effectiveness on the airfoil surface. Immediately downstream of the film holes, the contours show similar trends to the SS, that is a wide coolant footprint downstream of the holes for low  $M$ , and a narrower footprint as  $M$  increases. However, after a short distance downstream, the trend reverses, and higher  $M$  cases show wider footprints. The two highest  $M$  cases show a complete merging between neighboring coolant footprints after only a relatively short distance. On the PS, increase in  $M$  results not only in additional coolant, but it also increases the coolant momentum, which reacts to the blade-normal pressure gradient in an opposite way as on the SS. Higher momentum coolant tends to get pushed toward the airfoil, resulting in the wider coolant footprints shown as well as higher downstream  $\bar{\eta}$  values, as seen in Figure 8 for both computations and experiments.

#### 4.2.2 Film Hole and Plenum

The flow in the film hole and plenum for the PS cases is similar to the SS cases, and is not illustrated here. A relatively long film-hole length ( $L/D = 7.8$ ) allows a relatively full coolant velocity profile at the film-hole exit plane.

#### 4.2.3 Near Field

The single dominant vortex discussed in section 4.1.3 is also present for the PS cases downstream of injection. The strength of this vortex, as well as its distance from the airfoil surface, is related to the coolant momentum flux. Since the PS cases have a considerably higher range of blowing ratio, the SDV is therefore quite strong, and is deposited relatively far from the surface for the high  $M$  cases. As a result, entrained coolant is deposited far from the airfoil surface in the very near field, as shown in Figure 10. This explains the inverse dependence of  $\bar{\eta}$  on  $M$  in the very near field, as shown in Figure 8. Noting the  $M = 4.5$  case, it is apparent that a massive amount of coolant is present, and that it is mostly deposited far from the surface. The coolant also has considerably higher momentum than the mainstream fluid. As it moves downstream, the coolant gets pushed toward the surface and increases effectiveness. This mechanism is apparently overestimated by the computations, possible reasons for which are discussed below.

#### 4.2.4 Far Field

Far downstream of injection, the secondary motion (SDV) becomes small, and the momentum difference between coolant and mainstream flow becomes negligible. Beyond this point, the coolant is simply carried downstream and is mixed (diffused) by turbulence. Increasing  $M$  increases the “thermal capacity” of the coolant, resulting in an increase in  $\bar{\eta}$ . It is interesting to note that for the PS cases, there is no coolant blow off downstream of about  $x/X_{ps} = 0.1$  in the computations or  $x/X_{ps} = 0.2$  in the experiments, as shown in Figure 8. This is due to the curvature effect, and the upstream shift of the zero blow-off location in the computations—relative to the experiments—is again evidence of the overprediction of this effect.

### **4.3 Discussion**

The current systematic computational methodology is used to isolate the turbulence model performance for these cases. The results above can be used to highlight the performance of the RNG model with a two-layer near-wall treatment. It is known *a priori* that eddy-viscosity models are isotropic with respect to diffusivity, and so cannot exactly resolve the lateral spreading of coolant downstream of injection. Without spanwise-resolved measurements for comparison, it is impossible to exactly determine the impact of isotropic eddy-diffusivity on the coolant distribution, but it is reasonable to assume that spreading is underpredicted, based on numerous cases found in the open literature. The lack of anisotropy needs to be addressed for these problems.

Pertinent to the results presented above is the role of curvature effects on turbulence production. It is known, for instance, that boundary layers on convex surfaces



tend to have reduced turbulence levels, while those on concave surfaces have increased turbulence levels. The RNG model, like most two-equation models, does not include the effect of streamline curvature on turbulence production, and so may introduce error as a consequence. Considering for example the PS results above, it appears that the computations overpredict the impact of concave curvature on the *mean* flow. That is, the coolant jet appears to retain its relatively high momentum for a considerable distance downstream, becoming overly susceptible to the influence of the curvature. It is possible that this behavior is related to improper resolution of increased turbulence in the PS boundary layer. Increased turbulence would presumably diffuse the high-momentum jet, reducing the influence of the blade-normal pressure gradient on the coolant. Conversely, underprediction of effectiveness on the SS may be a result of too high turbulence in the computations, since the attenuating effect of convex curvature on turbulence production is not accounted for.

Finally, it is interesting to note that the relative overprediction of adiabatic effectiveness by the computations shows a definite dependence on the blowing ratio. That is, as  $M$  increases, the ratio of computed-to-measured  $\bar{\eta}$  increases, on both the suction and pressure surfaces. This trend is also observed for the other film-hole geometries, as reported in parts III and IV of this paper. The reason for this is believed to be related to the fact that as  $M$  increases, more of the coolant penetrates through the boundary layer into the mainstream passage flow. If the turbulence mixing in the mainstream is underpredicted, it will lead to the observed trends. Underprediction of turbulent mixing in the mainstream is likely from two sources. One, the RNG model differs from the standard  $k$ - $\epsilon$  model primarily through the additional term in the turbulent dissipation rate equation. In the mainstream, this term will respond to irrotational straining by increasing production of  $\epsilon$ , reducing the turbulent length scale and consequently the turbulent viscosity/diffusivity. Two, recall from part I that a relatively small turbulent length scale (5% of the passage height) was applied at the passage inlet in order to accurately reproduce the turbulence kinetic energy field in the passage. It is believed that both of the above contribute to reduced coolant mixing in the mainstream, and to some extent to the observed behavior of effectiveness with blowing ratio. It is also possible that pressure-gradient and curvature effects on the mainstream turbulence are significant, and are not being resolved by the current turbulence treatment.

All of the above suggest that future improvements to turbulence modeling should include representation of the anisotropy of diffusivity, include the influence of curvature on the turbulence production, and provide a more reasonable means of calculating the correct turbulence field in the passage mainstream.

## 6. CONCLUSIONS

This four-part paper describes a joint experimental and computational effort to analyze film-cooling performance of several complex film-hole geometries on a modern turbine airfoil, and to document the underlying physics responsible for that performance. The study models realistic engine conditions, including Reynolds and Mach numbers

typical of those found in actual turbines. Validation quality experimental results have been obtained using a single passage cascade (SPC) model that reproduces the geometry and flow features of a highly loaded turbine cascade. A foreign gas sampling technique provides laterally-averaged adiabatic effectiveness data with uncertainty less than 10% at all downstream locations. The computational methodology as outlined is intended to minimize geometry and grid-based errors and place the simulations against the limits of a commonly used eddy-viscosity turbulence model, RNG, with a two-layer near-wall treatment.

This study highlights the manner in which experiments and CFD augment one another. The experimental results serve to anchor and validate the computations, while the CFD results provide detailed insight into complex physical mechanisms and aid in understanding the measurements.

Conclusions specific to the current part include the following:

- Computational results show qualitative agreement with measured data. This suggests that the relevant physical mechanisms responsible for film-cooling performance are resolved by the simulations, if not their overall magnitude.
- The major mechanism in the near field downstream of the film holes is a single dominant vortex formed primarily by the streamwise-oriented vorticity exiting the film hole at the top of the coolant jet. This vortex entrains coolant and mainstream fluid, and its position depends on the jet momentum-flux ratio and the curvature of the airfoil.
- SS cases show coolant “blow off” far downstream of injection. Blow off occurs when the benefit of added coolant mass is overpowered by the deposition of the coolant far from the airfoil surface. On the PS, where the influence of curvature acts oppositely with respect to increased momentum-flux ratio, there is no blow-off except very near the film holes.
- The computations show consistent underprediction of measured data on the suction surface, and consistent overprediction on the pressure surface, for the blowing ratios considered. This trend is likely due to the choice of turbulence model in these cases.
- The computational results are believed to be limited only by the turbulence treatment. Comparison to experiments suggests that future improvement will include accurate representation of anisotropy and curvature effects, and more realistic treatment of the turbulence in the passage flow.

## REFERENCES

Garg, V.K. and Gaugler, R.E., 1997, “Effect of Velocity and Temperature Distribution at the Hole Exit on Film Cooling of Turbine Blades,” *Journal of Turbomachinery*, Vol. 119, pp. 343-351.

Leylek, J., and Zerkle, R., 1994, "Discrete-Jet Film Cooling: A Comparison of computational Results with Experiments," *Journal of Turbomachinery*, Vol. 116, pp. 358-368.

Walters, D., and Leylek, J., 1997, "A Detailed Analysis of Film-Cooling Physics - Part I: Streamwise Injection with Cylindrical Holes," ASME Paper No. 97-GT-269.

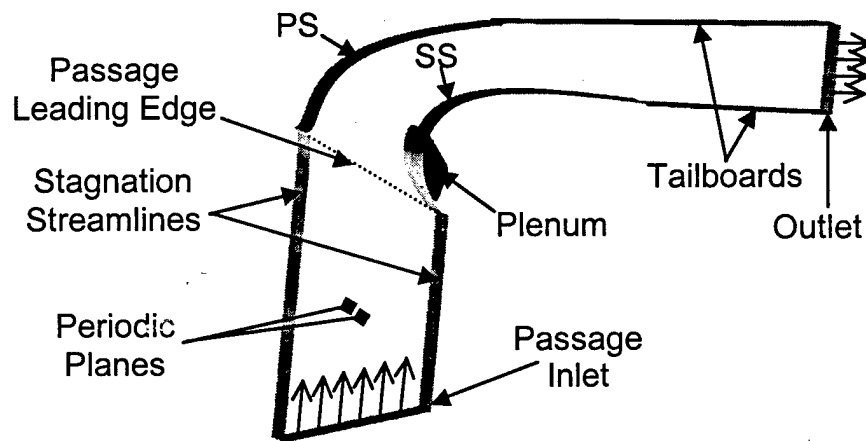


Figure 1. Illustration of 3-D domain for the CAR SS cases, including passage, film-hole, and coolant supply plenum regions.

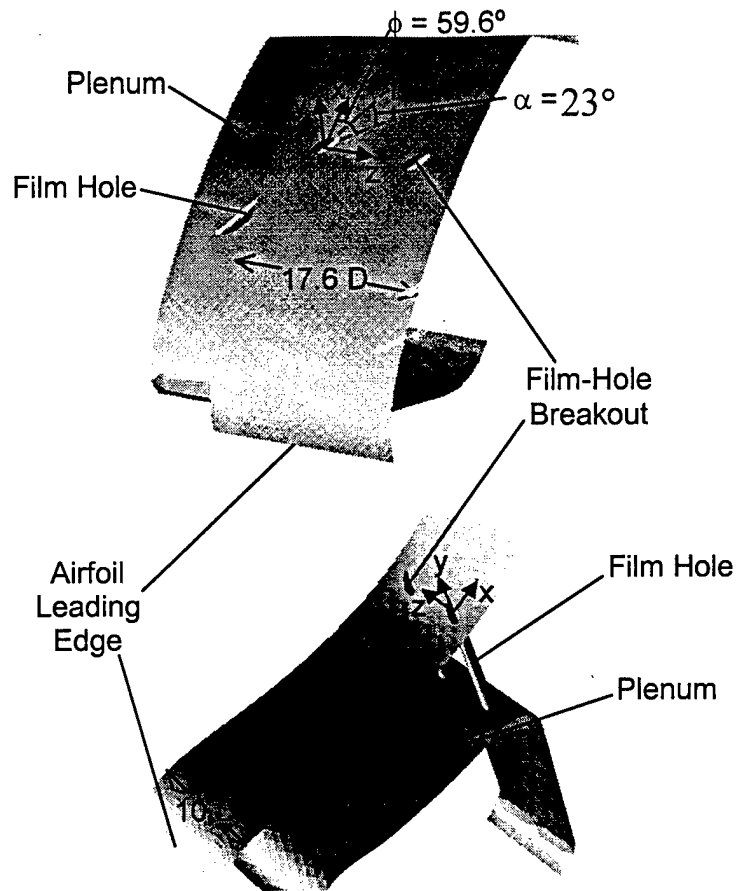


Figure 2. Axial (a) and compound-angle (b) hole definitions.

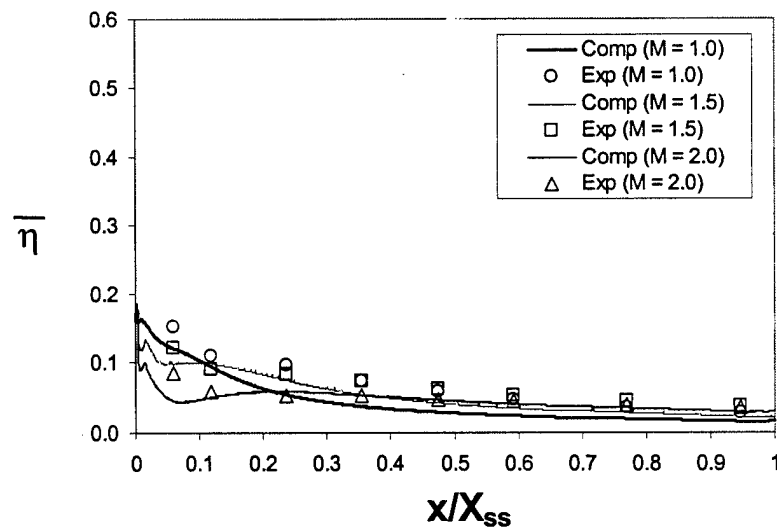


Figure 3. Spanwise-averaged adiabatic effectiveness for all three SS cases, computational results versus experimental data.

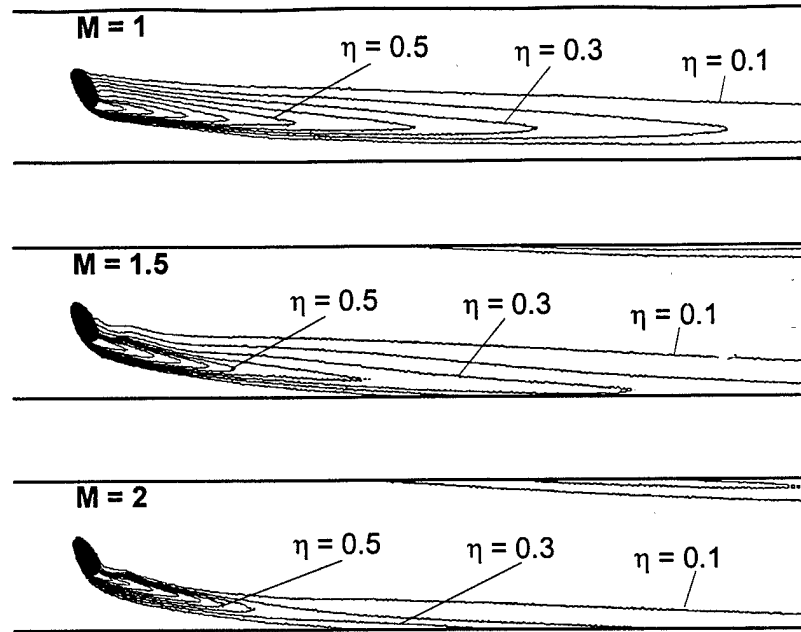


Figure 4. Contours of adiabatic effectiveness for the SS cases indicate low overall effectiveness, and significant spanwise variation.

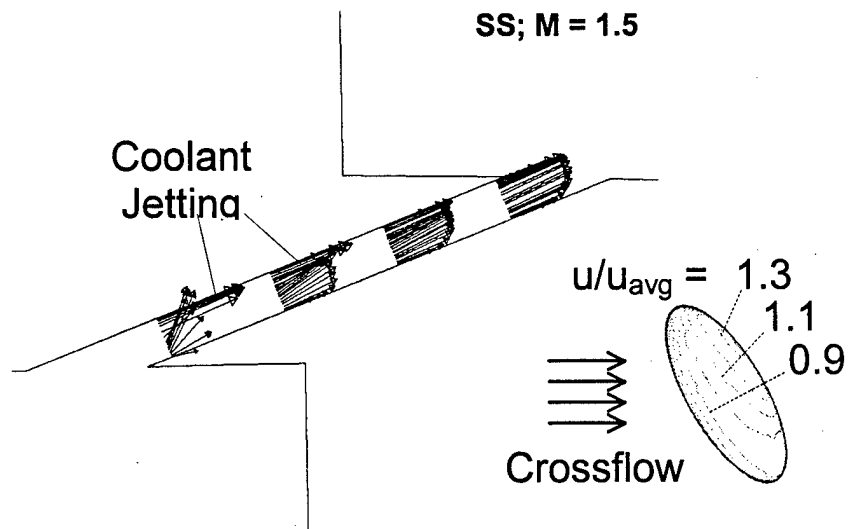


Figure 5. Film-hole breakout geometry for each of the configurations used in the present study.

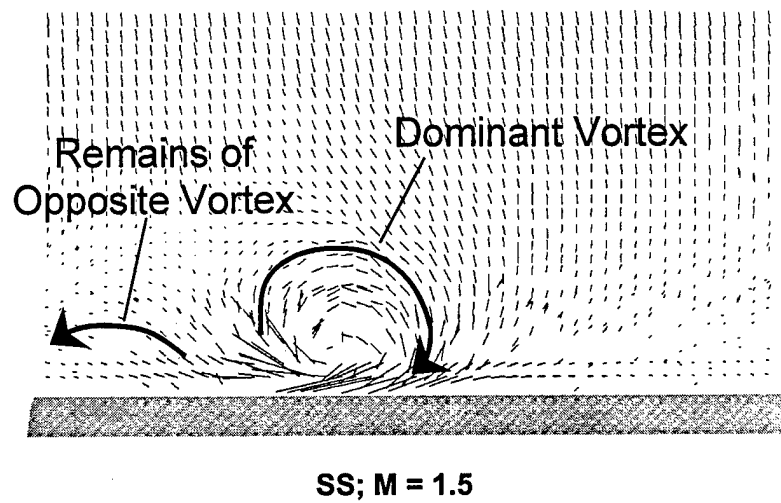


Figure 6. Velocity vectors in a plane normal to the passage flow and 2D downstream of film-hole leading edge.

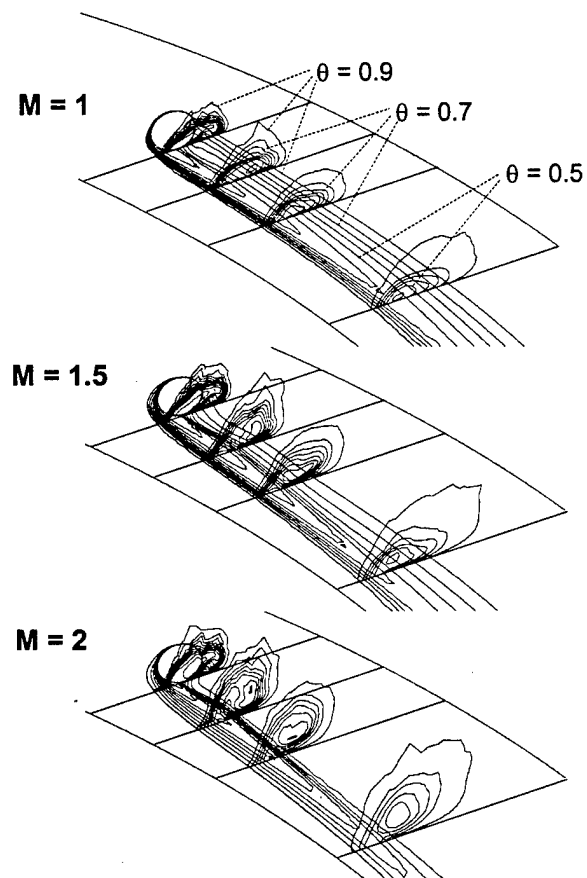


Figure 7. Contours of normalized temperature on SS surface and planes normal to passage flow highlights the near-field coolant distribution for all three blowing ratios.

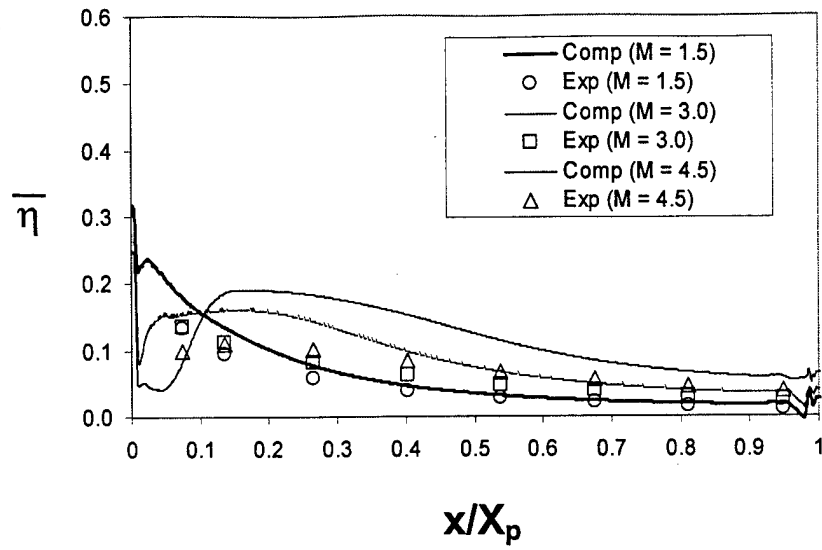


Figure 8. Spanwise-averaged adiabatic effectiveness for the PS cases, comparison of computations and experiments.

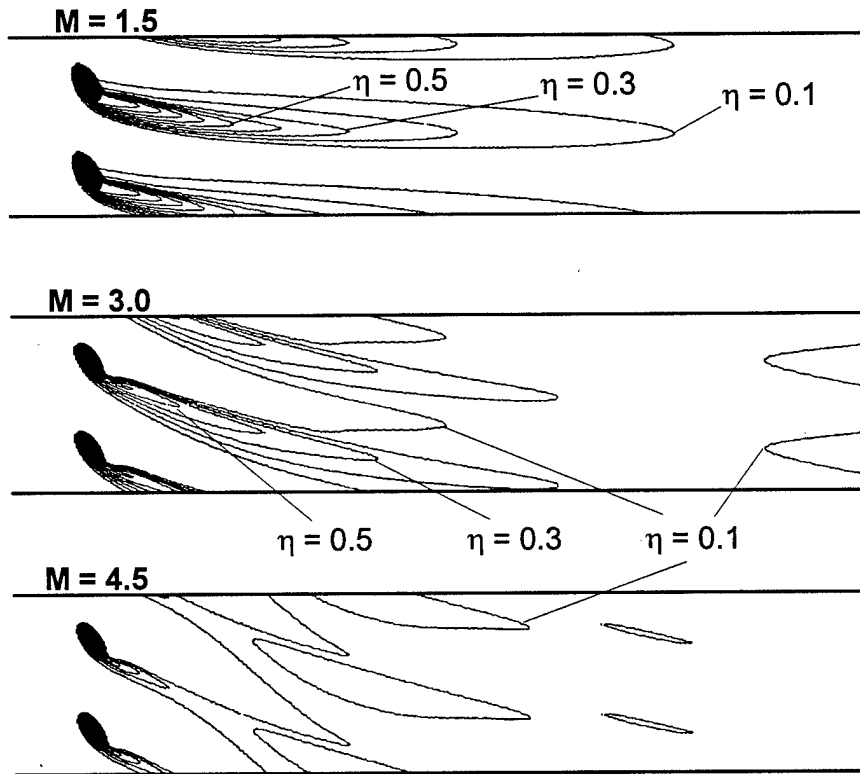


Figure 9. Contours of adiabatic effectiveness on the pressure surface.

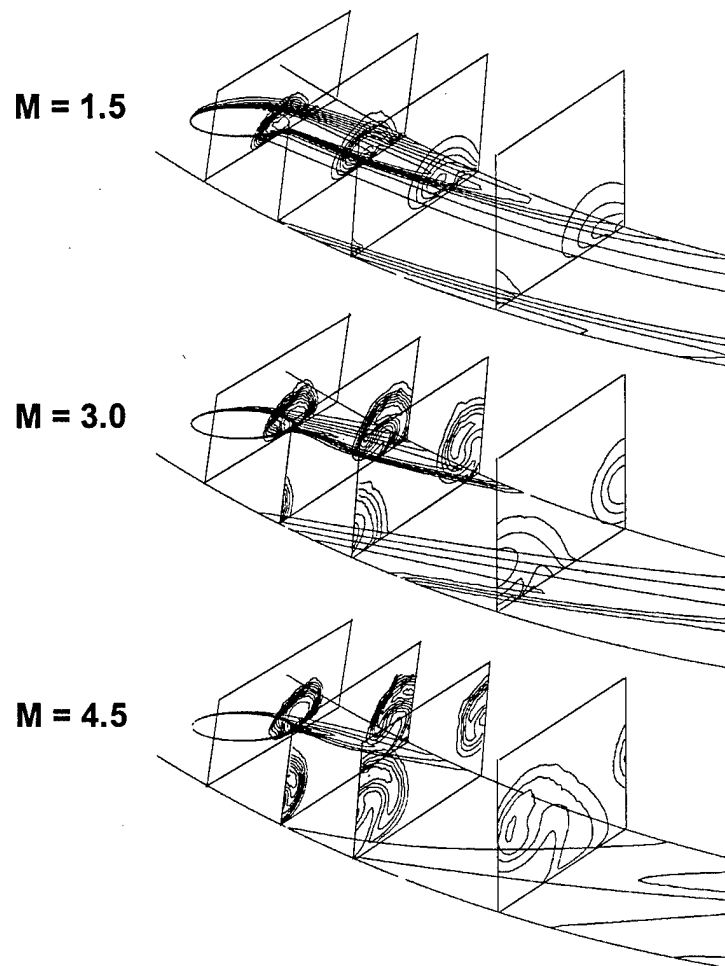


Figure 10. Contours of normalized temperature on the airfoil PS and on planes normal to the passage flow, illustrating penetration at high blowing ratio.



## CHAPTER 7

### FILM COOLING ON A MODERN HP TURBINE BLADE PART III: AXIAL SHAPED HOLES

Jeffrey D. Ferguson, James H. Leylek and Frederick A. Buck

#### NOMENCLATURE

|                   |  |
|-------------------|--|
| ASH               | <u>a</u> xial <u>s</u> haped <u>h</u> oles                                     |
| C <sub>p</sub>    | pressure coefficient = $\frac{P_s - P_{pp}}{\frac{1}{2} \rho_{pp} u_\infty^2}$ |
| D                 | film hole metering section diameter  |
| DR                | density ratio = $\rho_{pp}/\rho_\infty$  |
| FHEP              | <u>f</u> ilm- <u>h</u> ole <u>e</u> xit <u>p</u> lane                          |
| k                 | turbulence kinetic energy  |
| l                 | turbulence length scale  |
| L                 | film hole length   |
| LE                | <u>l</u> eading <u>e</u> dge   |
| M                 | blowing ratio = $(\rho u)_{pp}/(\rho u)_\infty$                                |
| P                 | film-hole pitch  |
| PS                | <u>p</u> ressure <u>s</u> urface   |
| r                 | recovery factor  |
| SS                | <u>s</u> uction <u>s</u> urface  |
| T                 | temperature  |
| T <sub>cool</sub> | coolant recovery temperature = $T_{s,aw} + r (T_{T,P} - T_{s,aw})$             |
| TE                | <u>t</u> railing <u>e</u> dge  |
| u                 | local velocity magnitude   |
| U                 | non-dimensional local velocity magnitude                                       |
| U <sub>norm</sub> | U component normal to FHEP   |
| X                 | length of cooled section of airfoil  |
| y <sup>+</sup>    | non-dimensional wall distance  |
| ε                 | turbulence dissipation rate  |
| η                 | adiabatic effectiveness = $(T_r - T_{s,aw})/(T_r - T_{cool})$                  |
| $\bar{\eta}$      | laterally- or spanwise-averaged η  |
| ρ                 | density  |
| θ                 | normalized T <sub>s</sub> = $(T_p - T_s)/(T_p - T_{T,in})$                     |

#### Subscripts

|    |  |
|----|--|
| ∞  | free-stream condition at location of injection |
| aw | adiabatic wall                                 |
| in | inlet conditions                               |

|    |   |
|----|---|
| j  | jet conditions in metering section              |
| P  | plenum inlet conditions                         |
| pp | conditions at pierce point (injection location) |
| r  | recovery condition                              |
| s  | static quantity                                 |
| T  | total (stagnation) quantity                     |

## 1. INTRODUCTION

As gas turbine designers continue to increase turbine inlet temperatures, film cooling has become a critical area of the design process. Advanced Computational Fluid Dynamics (CFD) techniques and sophisticated supercomputers have revolutionized the empiricism and one-dimensionality found in many modern design practices with great advances in rapid prototyping and predictive capabilities. However, the complexity of new film-cooling configurations, the often transonic nature of the flowfield in a modern turbine blade passage, and the lack of high-quality experimental data have prevented many serious computational studies of film cooling under realistic engine conditions. The present study combines validation-quality data obtained in a companion experimental study and a well-tested computational methodology to investigate the physics of axial-injected, shaped-hole (ASH) film cooling on the pressure and suction surfaces of a modern HP turbine blade under realistic conditions.

## 2. PRESENT CONTRIBUTIONS

The present study is Part III in a four-part paper. An extensive review of the open literature and a detailed description and validation of the computational methodology used in the current work are provided in Part I of this series. The present paper addresses the outstanding issues in the open literature outlined in Part I by investigating the physics of axial-injected, shaped-hole film cooling on a modern HP turbine blade under realistic engine conditions. The objectives of the present work are as follows:

- Document and analyze the adiabatic film-cooling effectiveness of ASH configurations in realistic engine conditions;
- Identify the key physical mechanisms, especially those linked to hole shaping, responsible for the behavior of the jet-and-crossflow interaction;
- Examine the effects of blowing ratio on the physical mechanisms in ASH film-cooling geometries;
- Comment on possible means of improving film-cooling performance in ASH configurations.

### 3. SIMULATION DETAILS

The present study uses the computational methodology outlined in Part I of this paper, and the reader is referred there for a thorough discussion. Figure 1 shows the computational domain for the PS case. For each case on the PS and SS, a row of ASH configurations was examined. Because of manufacturing limitations, the experimental film holes showed variations in geometry. Therefore, as described in Part I, a nominal geometry, based on average characteristics from the experimental holes, was used in the simulations. For the PS case, the forward and laterally diffused hole configuration had  $L/D=5.2$  and  $P/D=5$ . For the SS, a similar shaped-hole configuration was used with  $L/D=10$  and  $P/D=4.4$ . Figure 2 shows the breakouts for each configuration. For the SS geometry, blowing ratios of 1.0, 1.5, and 2.0 were examined. For the PS,  $M=1.5$ , 3.0, and 4.5 were studied. These three blowing ratios will often be referred to as LOW, MID, and HIGH. All cases maintained a nominal DR of 1.52. Table 1 summarizes the boundary conditions used for each case.

Table 1. Summary of Parameters for SS and PS Simulations

| Configuration | Case Name | M   | DR   |
|---------------|-----------|-----|------|
| SS            | SS-LOW    | 1.0 | 1.50 |
|               | SS-MID    | 1.5 | 1.52 |
|               | SS-HIGH   | 2.0 | 1.55 |
| PS            | PS-LOW    | 1.5 | 1.51 |
|               | PS-MID    | 3.0 | 1.52 |
|               | PS-HIGH   | 4.5 | 1.54 |

All cases were meshed as described in Part I, and background meshes contained 1,142,783 cells for the SS case and 948,258 for the PS case. Grid independence in each case was established when a significant addition of cells (at least 15-20%) in the high-gradient regions produced negligible changes (less than 5%) in the surface and field results.

The passage conditions for these cases included inlet  $Ma = 0.2$ , up to  $Ma$  slightly greater than one downstream of the throat, and  $Re_{ch}$  from 600,000 at the inlet to 2,000,000 at the throat, which were intended to model actual engine flow. The turbulence intensity at the center of the passage leading edge plane was 8%, and the turbulence length scale was taken as 5% of the passage inlet height. Because of the problems with the two-layer model highlighted in Ferguson et al. (1997), the plenum region was set to be a laminar zone.

The simulations were run using the Fluent 5 software, as discussed in Part I. Discretization was an upwind second-order scheme, and the turbulence model was RNG k- $\epsilon$  with a two-layer near-wall treatment. Pre- and post-processing work was performed on Sun Ultra 10 machines with 300 MHz CPUs and 1GB of RAM and a Sun Ultra 4000 machine with ten 250 MHz CPUs and 5GB of RAM. All simulations for the present work were run on 5 to 12 CPUs on the aforementioned Sun Ultra 4000 and a Sun HPC 6000 machine with 16 CPUs and 4GB of RAM. I-DEAS Master Series 6A from SDRC, T-Grid from Fluent, Inc., and GAMBIT from Fluent, Inc. were used in the pre-processing phases of the simulations.

## 4. RESULTS AND DISCUSSION

### 4.1 Suction Surface

The following sections outline the physical mechanisms present for the SS-MID case with  $M=1.5$ , and  $DR=1.52$ .

#### 4.1.1 Blade Surface

Figure 3 shows reasonably good agreement between trends for computations and experiments for  $\bar{\eta}$  on the blade SS. Contours of  $\theta$  on the blade surface are shown in Figure 4(b). The coolant does not lift off of the surface but is deposited rather evenly on the blade. However, the crossflow does “pinch” in on the coolant, preventing increased lateral spreading and allowing the “hot streaks” between holes to continue further downstream. The “pinching” is due to the counter-rotating vortex (CRV) structure formed from the streamwise-oriented vorticity in the film-hole boundary layers documented in Walters and Leylek (1997). Though not shown, the CRV structure was observed in velocity vector plots for this case.

#### 4.1.2 Film Hole and Plenum

The relevant physical mechanisms for the flow in the plenum and film-hole regions have been well documented (Walters and Leylek, 1997). Figure 5(b) shows contours of  $U$  along the film-hole centerline, where  $U$  is the local velocity magnitude normalized by the average jet velocity in the metering section for the SS-MID case. As the flow turns to enter the film hole, a separation region is formed on the downstream wall and the coolant jets along the upstream wall. A CRV structure is produced by the lateral pressure gradients formed from the streamline curvature at the film-hole inlet.

The metering section of this configuration is long (about  $6D$ ) so that the flow entering the diffusing section of the film hole is nearly fully developed, as shown in Figure 5(b). Because the jetting region is mostly eliminated by the time the coolant reaches the diffuser, the flow diffuses as intended. However, because of the adverse pressure gradient generated by the relatively steep forward diffusion angle, a small recirculation region is formed on the downstream wall in the diffuser section.

Contours of  $U_{\text{norm}}$  on the FHEP, shown in Figure 6(e), show that the coolant exits the film hole in a uniform manner. No jetting or crossflow ingestion is evident, and the coolant is injected into the crossflow boundary layer as desired. The primary mechanism resulting in the even distribution of coolant by the ASH configuration is the long metering section because it allows the coolant to develop and eliminate jetting before being diffused.

#### 4.1.3 Near Field

Contours of  $\hat{\theta}$  on the film hole wall, shown in Figure 6(b), indicate that some sections of the laterally diffused sides of the film hole are heated. This heating is not due to crossflow ingestion, but to diffusive effects. Because the coolant exits the film hole in a uniform manner, the crossflow does not encounter a major obstacle at the film-hole TE. Instead, the crossflow rides over the coolant. However, the low momentum of the crossflow and film-hole boundary layer fluid allows diffusive effects to transfer energy from the crossflow to the coolant, heating the film-hole wall. Although the wall heating in the present study is relatively small, the same mechanism could potentially result in serious heating in different shaped-hole configurations.

#### 4.1.4 Far Field

Contours of  $\theta$  on several crossplanes, shown in Figure 4(e), demonstrate the tendency of the coolant to remain close to the surface. The CRV structure that causes the crossflow to “pinch” the coolant is weak, and turbulent diffusion dominates the mixing downstream of  $x/D=5$ . The high TL of the crossflow quickly dissipates the jet in the far field.

### **4.2 Pressure Surface**

The following sections outline the dominant physical mechanisms present for the PS-MID case with  $M=3.0$ , and  $DR=1.52$ .

#### 4.2.1 Blade Surface

Figure 7 compares computational and experimental results for  $\bar{\eta}$  on the blade PS. The computations show excellent agreement in the far-field regions, but significantly over-predict in the near-field. As described in Parts I and II, the possible explanations for this discrepancy include the limitations of the nominal geometry to exactly match the experiments, and/or the inability of the simulations to fully capture jet penetration of the crossflow boundary layer because of the inadequacies of the turbulence modeling. Regardless, the computational capturing of the key trends in the experimental data indicates that useful information on physical mechanisms in the flow can be extracted from the simulations.

Figure 8(b) shows contours of  $\theta$  along the blade PS. The crossflow “pinching” and “hot streaks” evident in the SS-MID case are also evident here. However, the

coolant exiting the film hole TE approaches the crossflow temperature. Therefore, either the jet has lifted off the surface or massive crossflow ingestion occurs in this configuration.

#### 4.2.2 Film Hole and Plenum

As in the SS case, the coolant separates along the downstream wall, causing a jetting region along the upstream side of the film hole, as shown in Figure 9(b). Because the metering section in the PS configuration is not long enough to allow the flow to fully develop, the jetting coolant is not effectively diffused and maintains enough momentum to overcome the adverse pressure gradient caused by the diffuser and penetrates into the crossflow. Most of the coolant from the metering section boundary layer and core is carried away from the blade surface by this jetting coolant and is ineffective for cooling the near-field region. The low-momentum fluid in the separation region at the film-hole inlet is on the same side of the hole as the diffuser and is slowed further. This portion of the coolant does not have enough momentum to exit the film hole and a large recirculation region is formed in the diffuser section.

Contours of  $C_p$  on the film-hole wall and FHEP in Figure 10(b,e) show the pressure gradients that are formed as a result of the jetting and recirculating coolant. Low-momentum coolant in the crossflow boundary layer is very susceptible to these pressure gradients and the hot crossflow is pulled into the film hole, as shown by contours of velocity normal to the FHEP in Figure 9(e).

#### 4.2.3 Near Field

Figure 10 shows the effects on the crossflow of the pressure gradients in the film-hole region. Pathlines of particles released near the wall upstream of the film-hole LE (Figure 11(a)) show that the crossflow boundary layer fluid is pulled into the film hole and caught up in the recirculation region in the diffuser section. Fluid higher in the crossflow boundary layer, which has higher momentum, is also pulled into the film hole. However, as Figure 11(b) shows, it has enough momentum that it impinges on the film hole wall creating the stagnation region seen near the film hole TE in Figure 10(b). This ingestion results in heating of the film hole wall as shown in Figure 12(b). Although McGrath and Leylek (1999) show that the reoriented leg of the horseshoe vortex causes the ingestion in the compound-angle shaped hole investigated in their study, pressure gradients due to the jetting and recirculation regions in the film hole are the primary causes of ingestion in the PS configuration in the present work. The reoriented horseshoe vortex, while helping to promote ingestion, is not the primary cause in this study. The effects of crossflow ingestion may be significant but unfortunately cannot be fully evaluated without performing a conjugate conduction analysis.

The hot crossflow ingestion observed in the present work significantly heats the coolant in the recirculation region and results in a relatively low near-field cooling effectiveness. The fluid exiting the TE of the film hole has already been heated to near-crossflow temperatures and causes the PS ASH configuration to be inefficient and ineffective. Jet blow-off, except for the coolant jetting out of the TE of the film hole, is

not evident in the simulations. That is, increase in blowing ratio results in an increase in effectiveness over most of the airfoil, within the range of blowing ratios considered. Thus, the authors hypothesize that the possible causes of the discrepancy between computations and experiments in this configuration include the inability of the nominal geometry to fully capture the extent of crossflow ingestion in the “as-built” experimental geometries, and perhaps more importantly the inability of the turbulence models to fully capture the physics of the flow when the strong ingestion is present. However, the computational capturing of the experimental trends shows that CFD can be used to predict the physical mechanisms of various film-hole configurations.

#### 4.2.4 Far Field

Figure 8(e) shows contours of  $\theta$  at several crossplanes. Much of the coolant has been carried away from the blade PS by the coolant jetting out of the film-hole TE. However, as in the SS case, turbulent diffusion dominates the mixing in the far-field region. The high turbulence of the crossflow diffuses the coolant quickly so that even the coolant that was deposited far from the blade in the near-field region serves to cool the blade in the far field.

### **4.3 Effects of Blowing Ratio**

For each film-cooling configuration investigated, two additional blowing ratios were simulated to determine the effects, if any, of higher or lower  $M$ . Including the mid-point, the blowing ratios examined were  $M=1.0$ ,  $1.5$ , and  $2.0$  for the blade SS and  $M=1.5$ ,  $3.0$ , and  $4.5$  for the blade PS.

#### 4.3.1 Suction Surface

Figure 3 shows reasonably good agreement between computational and experimental trends in  $\bar{\eta}$  for a range of blowing ratios on the SS configuration. As  $M$  decreases, the agreement increases. Figure 4(a-c) shows contours of  $\theta$  on the blade surface for each  $M$ . As more coolant is injected into the crossflow, the effectiveness increases, leading to the conclusion that for each  $M$  the coolant is staying close to the blade, and lift off does not occur.

A comparison of the flow-fields for each blowing ratio reveals no new physical mechanisms governing the flow. However, the mechanisms examined in previous sections show subtle, non-linear differences with changes in  $M$ . Figure 5(a-c) shows contours of  $U$  along the centerline plane of the SS film hole. For all cases, the jetting region along the upstream wall is evident. In addition, the coolant flow at the end of the metering section is nearly fully-developed for each  $M$ . However, the SS-HIGH case does not have the recirculation region in the diffuser section that is evident in the two lower  $M$  cases. Instead, the coolant has too much momentum to be evenly slowed by the diffuser, and the coolant jets through the middle of the film hole. Some coolant is diffused, and low-momentum regions develop near the upstream and downstream sides of the diffuser. Though caused by different mechanisms, the SS-LOW case also shows low-momentum

coolant in these same regions. In this case,  $M$  is low and the diffuser further lowers the coolant momentum downstream of the metering section.

Figure 6(e-f) shows contours of  $U_{\text{norm}}$  on the FHEP for each  $M$ . Because the coolant on the upstream edge of the film hole in the SS-LOW and SS-HIGH cases is of such low momentum, it is blocked at the FHEP by the crossflow. Thus, the coolant rides under the crossflow and exits the film hole further downstream. This provides more time for the crossflow to heat the coolant, and the film hole wall is heated in the shallow regions of the laterally-diffused sides. As the coolant exits uniformly, the SS-MID case has less wall heating than the other two cases, as shown in Figure 6(a-c). This phenomenon highlights the non-linear effects of varying  $M$  in ASH configurations.

For each  $M$ , the coolant is injected into the crossflow boundary layer and remains near the surface, as shown in Figure 4(e-f). Thus, because no ingestion or jet lift off occurs, increases in  $M$  for the range investigated result in increases in surface effectiveness.

#### 4.3.2 Pressure Surface

As in the SS cases, changes in  $M$  do not introduce new flow physics to the PS configuration; instead, the extent to which the mechanisms discussed above affect the flow physics varies with  $M$ . Comparisons between predicted and measured  $\bar{\eta}$  are shown in Figure 7. The computations significantly over-predict experiments in the near field for the PS-MID and PS-HIGH cases, while good agreement is shown for the PS-LOW case over the entire range of measurement. As indicated earlier, it is the opinion of the authors that the primary cause of this discrepancy is due to an inability of the current turbulence modeling treatment to accurately resolve the physics of the jet-crossflow interaction when strong ingestion is present. A secondary cause may be that the actual geometry generated more ingestion than the nominal geometry used in the computations; thus, as  $M$  decreases, the ingestion decreases, and agreement increases. Figure 8(a-c) shows contours of  $\theta$  on the blade PS. As  $M$  increases, the near-field effectiveness decreases, highlighting the ingestion phenomenon.

Figure 9(a-c) shows contours of  $U$  along the film hole centerline plane. As  $M$  decreases, the severity of the jetting region also decreases. Thus, the computations and experiments match well at  $M=1.5$  because the jetting region does not fully penetrate the crossflow boundary layer. As shown in Figure 10, the pressure-gradients on the film-hole wall and FHEP become more steep as  $M$  increases. These steeper pressure gradients force more crossflow into the film hole, resulting in more massive crossflow ingestion as  $M$  increases. Contours of  $U_{\text{norm}}$  in Figure 9(d-f) show the increased ingestion for higher  $M$ . In addition, as more crossflow is pulled into the film hole, the coolant is heated more, as is shown by contours of  $\theta$  on the film-hole wall in Figure 12.

Because the jetting region is more severe with increased  $M$ , more coolant is carried away from the blade. Therefore, in the near-field, this coolant is unable to cool the surface and effectiveness decreases with increasing  $M$ . As shown in Figure 8(e-f), the



coolant is diffused quickly by the high turbulence in the crossflow, the blade feels the effects of the coolant, and far-field effectiveness increases with  $M$ .

## 5. CONCLUSIONS

This four-part paper describes a joint experimental and computational effort to analyze film-cooling performance of several complex film-hole geometries on a modern turbine airfoil, and to document the underlying physics responsible for that performance. The study models realistic engine conditions, including Reynolds and Mach numbers typical of those found in actual turbines. Validation quality experimental results have been obtained using a single passage cascade (SPC) model that reproduces the geometry and flow features of a highly loaded turbine cascade. A foreign gas sampling technique provides laterally-averaged adiabatic effectiveness data with uncertainty less than 10% at all downstream locations. The computational methodology as outlined is intended to minimize geometry and grid-based errors and place the simulations against the limits of a commonly used eddy-viscosity turbulence model, RNG, with a two-layer near-wall treatment.

This study highlights the manner in which experiments and CFD augment one another. The experimental results serve to anchor and validate the computations, while the CFD results provide detailed insight into complex physical mechanisms and aid in understanding the measurements.

Conclusions specific to the current part include the following:

- Computational results show good agreement with experimental trends for all cases, with the exception of the highest  $M$  case on the suction surface. It is apparent, however, that the overall magnitudes show considerable difference, especially for the  $M = 3$  and  $M = 4.5$  PS cases. Nevertheless, the combination of experiments and computations can be used to elucidate physical mechanisms responsible for cooling performance.
- The near field of the jet-crossflow interaction displays the classic counter-rotating vortex pair and crossflow "pinching", although its strength is diminished by the diffusing section of the shaped-hole geometry.
- At higher blowing ratios, the PS cases show significant crossflow ingestion into the film hole. This ingestion is caused by separation of the coolant within the film hole and a corresponding low-pressure zone at the film-hole exit plane.
- The experiments indicate blow off for the SS cases only at the highest blowing ratio. On the PS, both experiments and computations show that blow off does not occur far downstream of the film holes over the range of blowing ratios examined, similar to the results in part II. In the near field, however, blow-off is indicated by the experiments by  $M = 0.3$ , due to the increased momentum of the exiting coolant. The computations indicate blow-off by  $M = 4.5$ .
- Except for the SS  $M = 2$  case mentioned above, the computations consistently show underprediction of the measurements on the SS and overprediction on the PS. As

discussed in part II, this trend is likely due to the turbulence modeling used in these cases.

## REFERENCES

Ferguson, J., Walters, D., and Leylek, J., 1998, "Performance of Turbulence Models and Near-Wall Treatments in Discrete-Jet Film-Cooling Simulations," ASME Paper No. 98-GT-438.

Fluent, Inc., 1997, *Fluent 5 Users Manual*, Lebanon, NH.

Leylek, J., and Zerkle, R., 1994, "Discrete-Jet Film Cooling: A Comparison of computational Results with Experiments," *Journal of Turbomachinery*, Vol. 116, pp. 358-368.

McGrath, E., and Leylek, J., 1999, "Physics of Hot Crossflow Ingestion in Film Cooling," *Journal of Turbomachinery*, Vol. 121, pp. 1-10.

Walters, D., and Leylek, J., 1997, "A Systematic Computational Methodology Applied to a Three-Dimensional Film-Cooling Flowfield," *Journal of Turbomachinery*, Vol. 119, pp. 777-785.

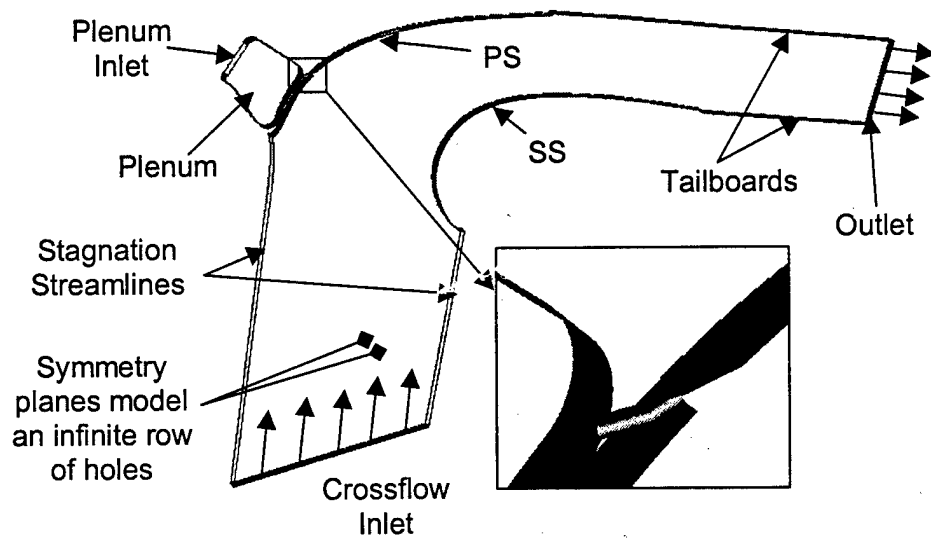


Figure 1. PS geometry shows how the computational domain models the three-way coupling of the film hole, crossflow, and plenum flow.

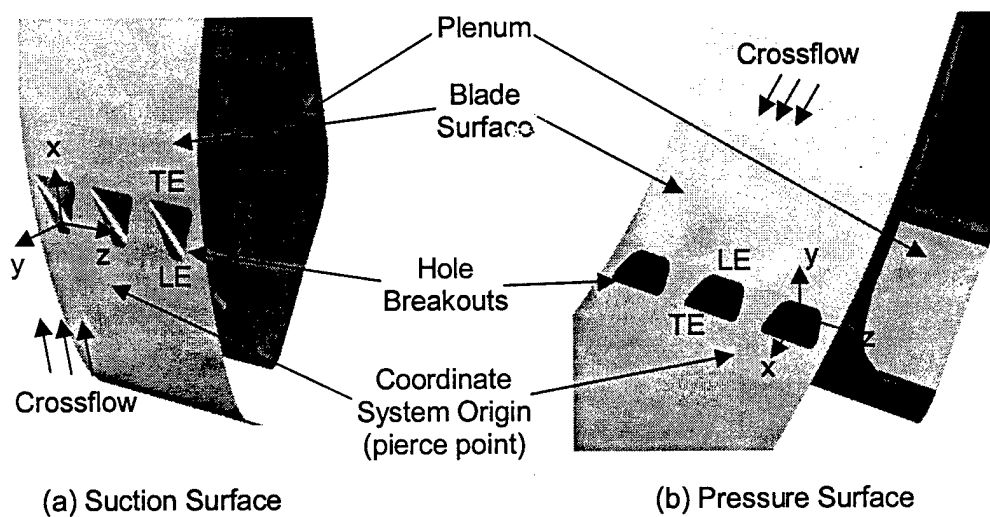


Figure 2. Similar hole shaping produces different breakouts in the (a) SS and (b) PS geometries.

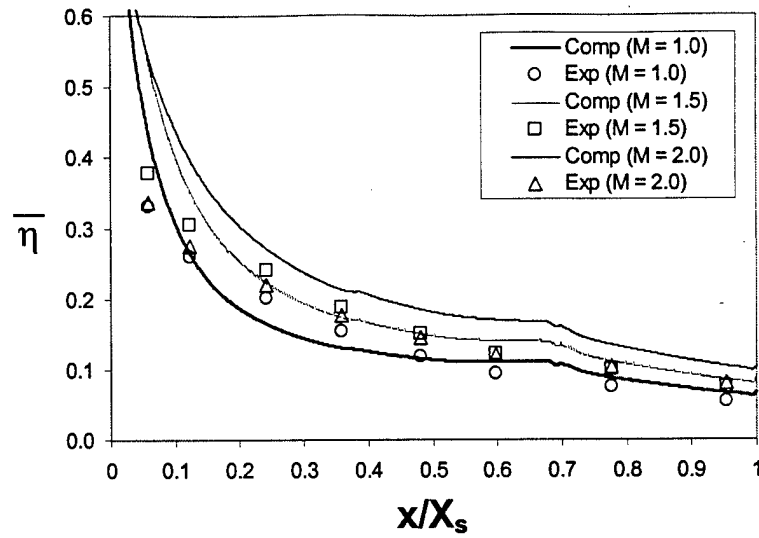


Figure 3. Comparison of laterally averaged  $\eta$  shows reasonably good agreement with experiments on the blade SS.

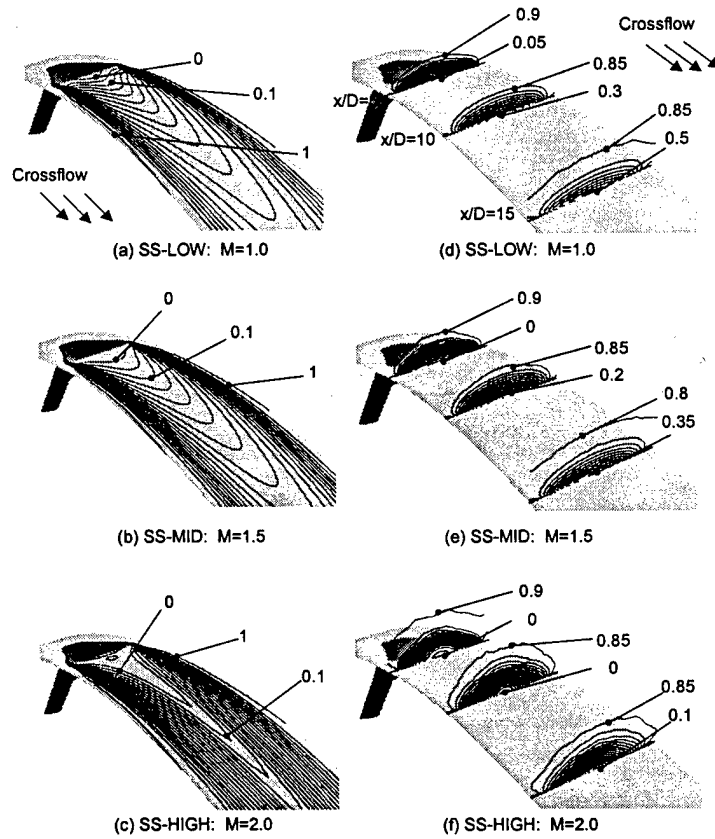


Figure 4. Contours of  $\theta$  on the SS for (a) SS-LOW, (b) SS-MID, and (c) SS-HIGH and at crossflow crossplanes of  $x/D=5, 10$ , and  $15$  for (d) SS-LOW, (e) SS-MID, and (f) SS-HIGH show the lateral spreading and diffusion of the coolant.

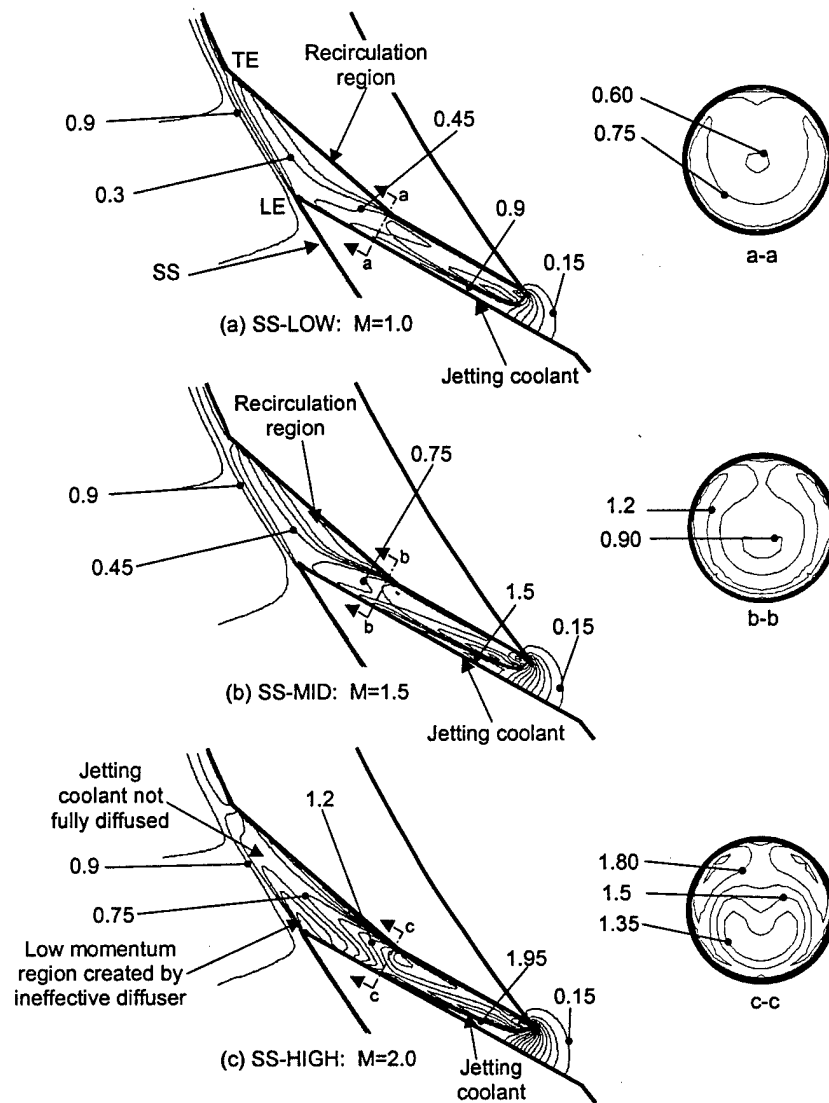


Figure 5. . Contours of  $U$  demonstrate the varying effectiveness of the diffuser for (a) SS-LOW, (b) SS-MID, and (c) SS-HIGH.

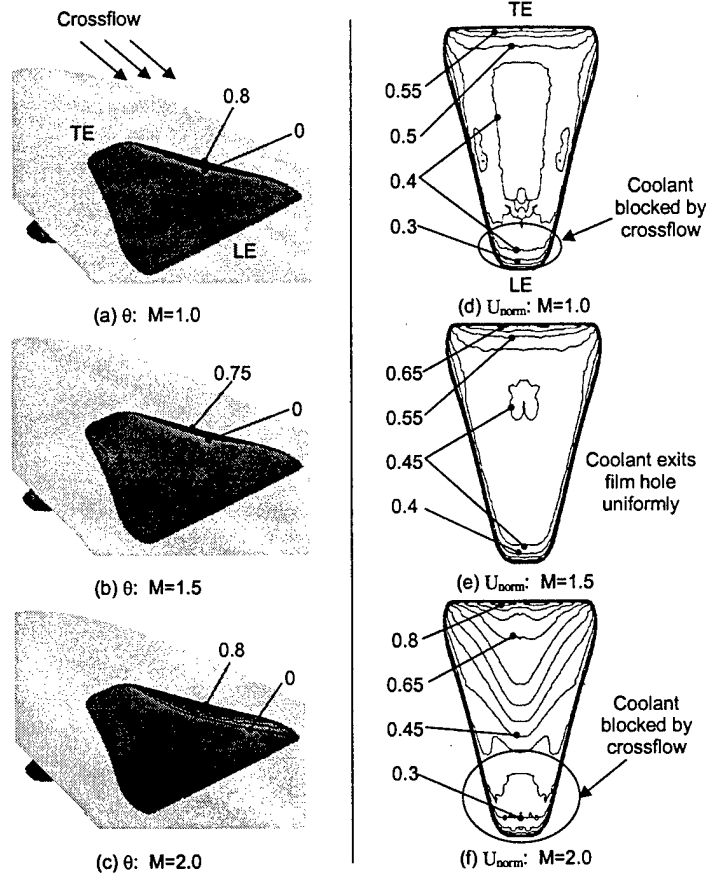


Figure 6. Contours of  $\theta$  on the film-hole wall show the wall heating for (a) SS-LOW, (b) SS-MID, and (c) SS-HIGH and contours of  $U_{\text{norm}}$  on the FHEP show different coolant exit patterns for (d) SS-LOW, (e) SS-MID, and (f) SS-HIGH.

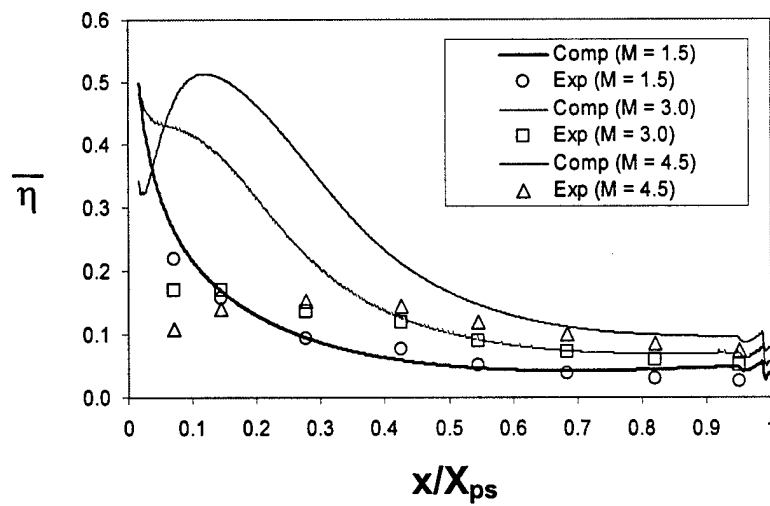


Figure 7. Laterally averaged  $\eta$  comparison with experiments shows that computations capture all major trends on the blade PS.

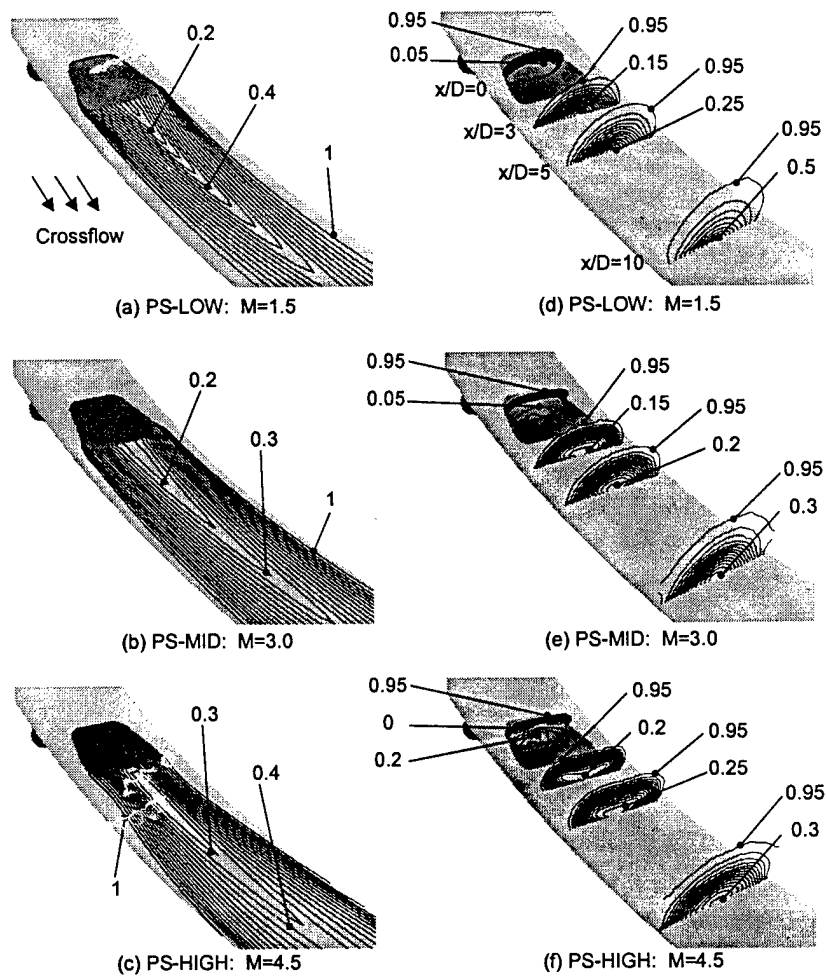


Figure 8. Contours of  $\theta$  on the PS for (a) PS-LOW, (b) PS-MID, and (c) PS-HIGH and on crossflow crossplanes of  $x/D=0, 3, 5$ , and  $10$  for (d) PS-LOW, (e) PS-MID, and (f) PS-HIGH show the lateral spreading and diffusion of the coolant.

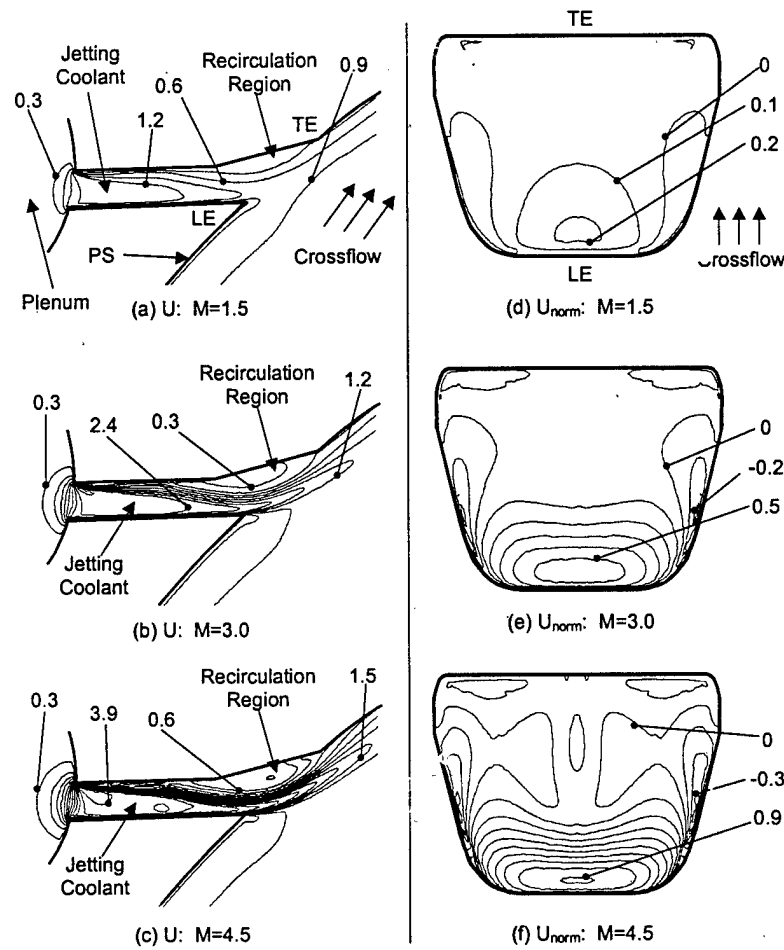


Figure 9. Contours of  $U$  along the film hole centerline show the jetting and recirculation regions for (a) PS-LOW, (b) PS-MID, and (c) PS-HIGH and contours of  $U_{norm}$  on the FHEP show the resulting crossflow ingestion for (e) PS-LOW, (f) PS-MID, and (g) PS-HIGH.



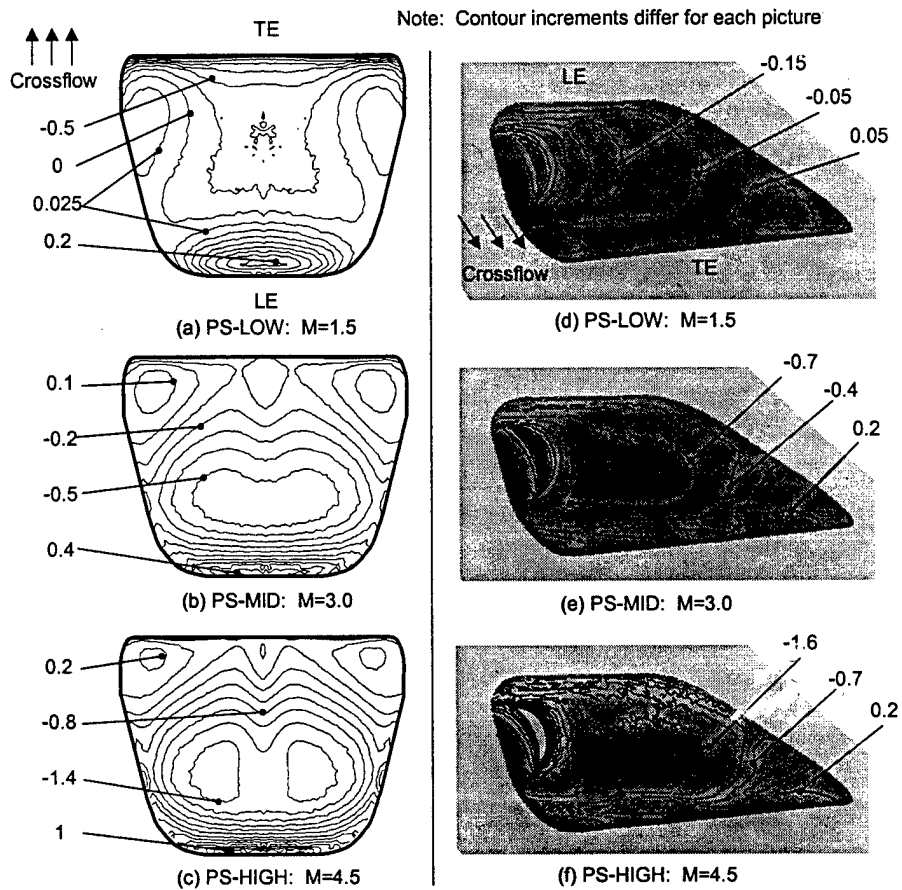
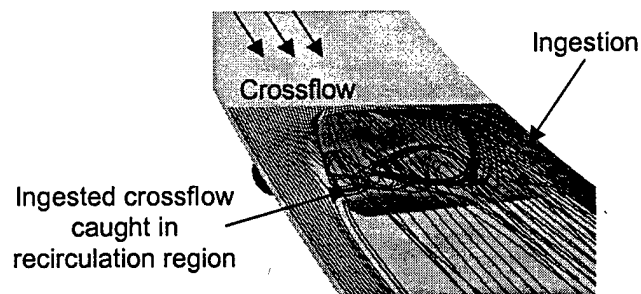
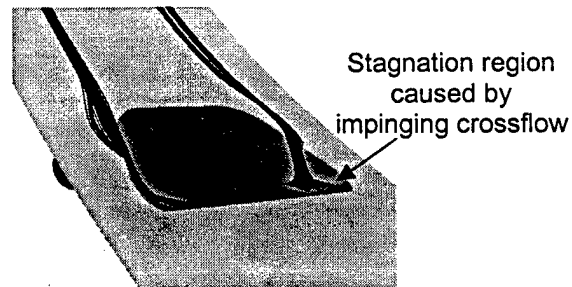


Figure 10. Contours of normalized temperature on the airfoil PS and on planes normal to the passage flow, illustrating penetration at high blowing ratio.

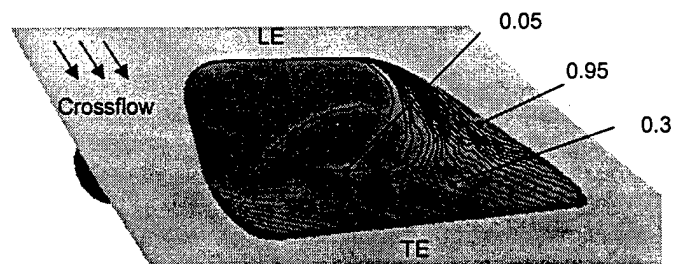


(a) PS-MID: Particles released in crossflow boundary layer just upstream of hole LE

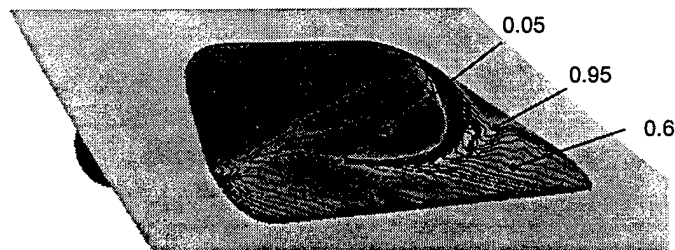


(b) PS-MID: Particles released in stagnation region near hole TE

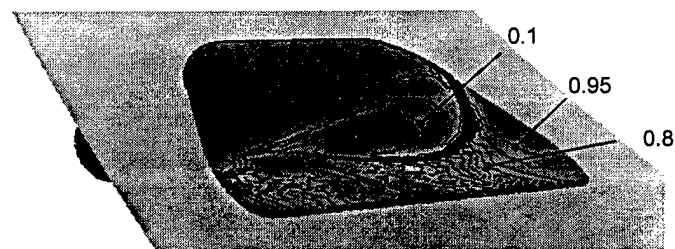
Figure 11. Crossflow ingestion is shown by (a) particles released near the PS upstream of the hole LE and (b) reverse-flow particles released in the stagnation region near the hole TE.



(a) PS-LOW:  $M=1.5$



(b) PS-MID:  $M=3.0$



(c) PS-HIGH:  $M=4.5$

Figure 12. Contours of  $\theta$  on the film-hole wall show the effects of crossflow ingestion.

## CHAPTER 8

### FILM COOLING ON A MODERN HP TURBINE BLADE PART IV: COMPOUND-ANGLE SHAPED HOLES

E. Lee McGrath, James H. Leylek and Frederick A. Buck

#### NOMENCLATURE

|            |   |
|------------|---|
| CASH       | compound-angle shaped holes   |
| $C_p$      | pressure coefficient = $(P - P_\infty)/(\rho_\infty v_\infty^2/2)$    |
| D          | film hole diameter  |
| DR         | coolant-to-mainstream density ratio = $\rho_j/\rho_\infty$            |
| FHEP       | film hole exit plane  |
| k          | turbulent kinetic energy  |
| L          | film hole length  |
| $L_M$      | length of hole metering section                                       |
| M          | blowing ratio = $\rho_c v_c/\rho_\infty v_\infty$                     |
| P          | local static pressure (psi), film hole lateral pitch                  |
| PS         | pressure surface  |
| r          | recovery factor = $(T_{aw,0} - T_\infty)/(T_{t,\infty} - T_\infty)$   |
| SS         | suction surface   |
| T          | local static temperature  |
| $T_{cool}$ | coolant recovery temperature = $T_c + r(T_{t,c} - T_c)$               |
| TL         | turbulence level = $(2k/3)^{0.5}/v_\infty$                            |
| v          | local velocity magnitude  |
| $v_c$      | nominal coolant velocity magnitude based on hole metering section     |
| VR         | velocity ratio = $v/v_\infty$   |
| $W_H$      | lateral width of hole   |
| x          | streamwise coordinate at hole centerline pierce point                 |
| X          | length of cooled section of airfoil                                   |
| y          | coordinate normal to test surface at hole pierce point                |
| z          | spanwise coordinate at hole centerline pierce point                   |
| $\alpha$   | injection angle with respect to x-z plane                             |
| $\phi$     | compound angle with respect to x-y plane                              |
| $\gamma$   | half angle of hole diffuser   |
| $\eta$     | adiabatic effectiveness = $(T_{aw,0} - T_{aw})/(T_{aw,0} - T_{cool})$ |
| $\theta$   | non-dimensional temperature = $(T - T_c)/(T_\infty - T_c)$            |
| $\rho$     | density   |
| $\omega$   | vorticity magnitude   |
| $\xi$      | helicity = $\vec{\omega} \cdot \vec{v}$                               |

$\psi$  normalized helicity =  $\xi/(v_\infty v_c/D)$

### **Subscripts**

|          |   |
|----------|---|
| $\infty$ | free-stream condition at injection location |
| aw       | adiabatic wall                              |
| c        | coolant                                     |
| ps       | pressure surface                            |
| ss       | suction surface                             |
| t        | total                                       |
| 0        | no film cooling                             |

## **1. INTRODUCTION**

Film cooling is essential to providing thermal protection for a turbine airfoil. This four-part paper series presents companion experimental and computational results in an effort to document the effect of film-hole geometry on film cooling of a modern turbine airfoil under engine-realistic operating conditions. Part I of this series contains the literature review and a detailed description of the robust computational methodology that is utilized to study the physics of streamwise shaped, compound-angle-round, and compound-angle shaped holes in Parts II, III, and IV.

## **2. OBJECTIVES**

The objectives of this research are:

- Document the physics of CASH film cooling on both SS and PS of a modern airfoil under realistic engine conditions
- Examine the effects of blowing ratio
- Demonstrate the ability of CFD as a robust predictive design tool for film cooling

## **3. COMPUTATIONAL DETAILS**

Since the computational methodology is detailed in Part I, only the geometry of the current CASH holes is presented here. Figure 1 contains a picture of the PS film hole geometry, while Figure 2 contains the SS film hole geometry. Two key differences are that the metering length ( $L_M$ ) of the PS hole is 27% of the SS  $L_M$ . In addition, the diffuser half angles ( $\gamma$ ) are much larger for the SS hole, with the largest being on the "short side" of the diffuser. The total background grid size for PS film cooling was 1,541,252 cells, with an average skewness of 0.18. Background grid for SS film cooling was 1,249,865 cells, with an average skewness of 0.16. Skewness of 0 indicates a perfect cell, whereas a value of 1 is a degenerate cell. Hanging node adaption was used to obtain grid independence, which required an approximate 250,000 cell addition in the areas of high gradients in the jet-in-crossflow region. All computations were performed at

DR=1.52. Blowing ratios simulated on the PS were  $M=1.5$ , 3.0, and 4.48, and on the SS were  $M=1.0$ , 1.52, and 2.0.

## 4. RESULTS

### 4.1 Pressure Surface Physics

#### 4.1.1 Flow Inside Hole

The flow in the metering section of the hole is identical to flow typically found in a cylindrical film hole, such as that documented by Leylek and Zerkle (1994). Flow entering the hole from the plenum accelerates and turns up to  $135^\circ$ , producing a 3-dimensional separation region on the inside of the angle at the entrance of the hole. As a result of the velocity deficit in the separation region, the coolant "jets" on the outside of the inlet angle, as seen in Figure 3. In long film holes, the turbulent diffusion of momentum would flatten the velocity profile, but the short metering section does not allow time for diffusion to occur. The resulting non-uniformity of momentum at the end of the metering section reduces the effectiveness of the diffuser, and the velocity profile becomes even more non-uniform in the diffuser. The adverse pressure gradient in the diffuser causes the low momentum coolant to separate from the wall. This separated fluid forms a large 3-dimensional recirculation region on the long side of the diffuser, as marked in Figure 3. Though not presented here, the recirculation was clearly visible from velocity vector plots. Due to the "blockage" formed in the diffuser by the recirculation region, the jetting coolant does not diffuse as much as intended and jets out of the left side of hole when viewed from downstream (maximum  $VR=1.8$  in Figure 4(a)). The jetting coolant exiting the hole contains a high turbulence level (TL) of 25%. The main source of turbulence production inside the hole is the shear layer between the jetting coolant and the coolant in the inlet separation region.

#### 4.1.2 Flow at Hole Exit

Figure 4(a,b) shows the highly non-uniform velocity profile and injection angle profile of the coolant exiting the film hole. Over a large part of the FHEP little coolant exits because of the recirculation region inside the diffuser. The jetting coolant produces blockage of the crossflow, resulting in a high pressure region upstream, as shown in Figure 5. This high pressure causes the crossflow boundary layer to separate from the wall, and the strong vorticity in the separated fluid causes a horseshoe vortex to form. The right leg of the horseshoe vortex is the "ingestion vortex" described by McGrath and Leylek (1999). The ingestion shown in Figure 4(b) is the result of the ingestion vortex, and some heating of the wall inside the film hole occurs. Also, the ingestion causes an increase in the coolant temperature before it exits the hole, as shown in Figure 4(c). The left leg of the horseshoe vortex is absorbed by opposite vorticity produced inside the film-hole boundary layer and exiting with the jetting coolant.

#### 4.1.3 Flow Downstream of Hole

Figure 6 shows the  $\theta$  contours on the blade surface for  $M=3.0$ , which show significant lateral non-uniformity. Immediately downstream of the hole, a "stripe" of low  $\theta$  contours is present on the left side of the hole behind the jetting coolant. To the left of the stripe, the surface  $\theta$  quickly goes above 0.8. As a result, a large temperature gradient line is present next to the stripe. At the pointed corner on the right side of the hole, the exiting coolant has low momentum and moves laterally toward the adjacent hole in response to the low pressure pocket shown in Figure 5. In addition, downstream of the middle of the hole, the surface  $\theta$  starts at roughly 0.4 because of the ingestion. The significant non-uniformity of the surface temperatures persists for up to 30 diameters downstream.

The large  $\theta$  gradient line on the blade is a consequence of vorticity in the flow. Figure 7 is a composite view of  $\theta$  on the blade surface and  $\psi$  on a crossflow plane normal to the blade at  $x/D=3$  and angled at  $15^\circ$  from the axial direction in order to be perpendicular to the flow. The parameter  $\psi$  is non-dimensional helicity ( $\xi$ ), which is the amount of vorticity that is aligned with the streamwise flow,  $\xi = \vec{\omega} \cdot \vec{v}$ . Helicity indicates the presence of a vortex. When contours of helicity are shown in this discussion, a location of positive helicity indicates a counter-clockwise vortex when viewed from downstream, whereas negative helicity indicates a clockwise vortex. The large pocket of positive helicity in Figure 7 is the alpha vortex (single dominant vortex) produced by the vorticity from the film hole boundary layer exiting on the left side of the hole with the jetting coolant. As viewed from downstream, the alpha vortex rotates the hot crossflow under the coolant in a counter-clockwise motion. At the same time, the alpha vortex rotates the coolant away from the blade. Since the crossflow is rotated down to the surface, high  $\theta$  contours result on the surface under the alpha vortex. The tucking of the crossflow under the coolant can be seen in Figure 8 which shows contours of  $\theta$  on both the blade surface and on a crossflow plane downstream of the hole at 1D for  $M=1.5$  & 4.48 and at 8D for  $M=4.48$ . At the higher blowing ratio, the alpha vortex is stronger since the greater coolant velocity through the hole produces more vorticity in the boundary layer inside the hole. The stronger alpha vortex tucks more crossflow under the coolant.

Figure 5 shows a low pressure pocket downstream of the jetting coolant on the left side of the hole trailing edge. This low pressure is similar to that formed behind a cylinder in crossflow, but is also associated with the turning of the jetting coolant as it exits the hole. A trail of lower pressure extends downstream of this location and traces the path of the alpha vortex. A lateral pressure gradient results, and the low momentum near-wall flow downstream of the middle of the hole is influenced to move laterally to the left, contrary to the rightward motion induced by the compound injection into the flow. Because of the no-slip wall, this leftward lateral motion of the near-wall flow produces vorticity that is aligned opposite to the mainstream flow (negative helicity). This negative helicity is shown in Figure 7, and will be called the "anti-lift" vortex, since its effect is to take some of the coolant from the alpha vortex and rotate it down onto the blade surface. The stripe of low  $\theta$  temperatures on the blade are directly the result of the anti-lift vortex, even though it is smaller, weaker, and remains closer to the wall than the alpha vortex. The large temperature gradient on the blade is located where the hot

crossflow pulled under the alpha vortex ends and the coolant in the anti-lift vortex begins. Without the anti-lift vortex, the alpha vortex would detach even more of the coolant from the blade, and the thermal protection of the blade might be poor. Since the anti-lift vortex is sustained by the lateral pressure gradient produced by the low pressure trail of the alpha vortex, the anti-lift vortex persists as long as the alpha vortex at a relative strength.

A key mechanism that helps the anti-lift vortex retain its coolant is the suppression of turbulence. The free-stream is turbulent, and the core of the jetting coolant has a turbulence level of ~25%. Near the wall where the anti-lift vortex is located, the turbulent length scale is reduced and the blade acts as a turbulence sink. Thus, the coolant lifted off the blade by the alpha vortex diffuses quickly into the crossflow as shown in Figure 8(c), while the coolant in the anti-lift vortex near the wall experiences less diffusion and stays cool longer.

#### 4.1.4 Effect of Blowing Ratio

The qualitative physical mechanisms governing the film cooling produced by the current geometry are not dependent on  $M$  over the range studied, and only the quantitative strength of the mechanisms is influenced. As  $M$  increases, the magnitude of the turbulence, vorticity, and lateral motion is increased. The strength of the ingestion vortex does not change, however, since its source of vorticity is the upstream boundary layer, which is not dependent on  $M$ . Since the alpha vortex is weaker at low  $M$ , the coolant stays closer to the blade and provides more thermal protection, as shown in Figure 8(a). At high  $M$ , more coolant is present, but the alpha vortex is stronger, so most of the coolant is detached from the blade. Thus, the hole configuration is more efficient at low  $M$  since a greater percentage of the coolant actually protects the blade.

Figure 9 shows a plot comparing  $\bar{\eta}$  for each of the blowing ratios. Included are the results from the experiments. The thermal protection of the blade is good in the very near field at all blowing ratios, with values staying above 0.6 until roughly  $x/X_{ps}=0.05$ . The cooling performance of the geometry is not much better at  $M=3.0$  than at  $M=1.5$ , considering the fact that twice as much coolant is used. For example, at  $x/X_{ps}=0.18$ ,  $\bar{\eta}$  is 0.16 for  $M=1.5$  but is only 0.22 for  $M=3.0$ , an increase of only 25%. At the same location  $\bar{\eta}$  is 0.29 for  $M=4.5$ , which is only an 81% increase over that of  $M=1.5$  despite the fact that three times as much coolant is being used. In the far field the vortices dissipate and turbulent diffusion of the coolant dominates. After about  $x/X_{ps}=0.5$ , the increase in  $\bar{\eta}$  is proportional to the increase in  $M$ .

### **4.2 Suction Surface Physics**

#### 4.2.1 Flow Inside Hole and at Hole Exit

The flow physics inside the SS film hole is similar to that in the PS hole, and flow separation at the hole inlet and jetting coolant are both present. A key difference is that the metering section of the SS hole is  $5.7D$  longer, which allows more time for turbulent diffusion of the jetting coolant in the metering section and results in a fairly flat velocity



profile entering the diffuser. Figure 10 shows the flow inside the diffuser when  $M=1.5$ . No jetting coolant is present, but the flow still separates on the long side of the diffuser and a 3-dimensional recirculation region is formed.

Figure 11 shows the VR and  $\alpha$  of the flow at the FHEP. The majority of the coolant exits the hole on the right side, as viewed from downstream, whereas the coolant is essentially blocked by the crossflow from exiting a large portion of the hole especially near the leading edge. This region of coolant blockage corresponds to the recirculation region inside the hole. As discussed by McGrath and Leylek (1999), heat is able to diffuse into the film hole through the slow moving coolant in the blocked region of the film hole since convection out of the hole is hampered. As a result, slight heating of the film hole wall is present in the shallow region of the hole.

#### 4.2.2 Flow Downstream of Hole

The physics of the flow downstream of the SS hole is also similar to that downstream of the PS hole. Figure 12 shows the  $\theta$  contours on the blade surface in the near field for  $M=1.52$ . There is little lateral motion downstream of the hole, since the coolant is easily turned by the crossflow at low  $M$ . A coolant stripe is evident extending from the right side of the hole where the majority of the coolant exits. Because of the blockage of coolant at the FHEP, little coolant is present across most of the span and the thermal protection dissipates quickly in between the coolant stripes. Also because  $M$  is small, the vorticity exiting the hole is weak. The majority of the coolant stays close to the blade because the alpha vortex is weak and mainly hampers lateral spreading instead of rotating the coolant off the blade. The long extension of the coolant stripe can be attributed to the lower turbulence level ( $TL < 12\%$ ) and to the flow pushing the coolant onto the blade in response to the mainstream pressure gradients normal to the blade.

#### 4.2.3 Effect of Blowing Ratio

At the lower  $M$  of 1.0, the flowfield is qualitatively the same, except the coolant diffuses even more inside the film hole. Thus, at the FHEP the velocity profile across the lateral span of the hole is close to uniform, with coolant blockage everywhere except the trailing edge. The coolant spreads very well in the near field since the streamwise vortices are extremely weak, and all the coolant stays in a thin layer over the blade.

At the higher blowing ratio of  $M=2$ , the flowfield changes significantly inside the film hole, as shown in Figure 13. In this case the boundary layer separates on the short side (right side) of the diffuser rather than on the long side (left side) of the diffuser. The reason is that the higher momentum coolant cannot negotiate the large  $\gamma$  of  $25^\circ$  on the short side of the diffuser. As a result of the separation, the pressure on the short side of the diffuser remains low, and the effect of the low pressure can be felt by the crossflow outside of the hole. Figure 14 shows contours of  $C_p$  on the blade, which indicate the presence of the strong low pressure inside the hole on the right side. As shown in Figure 15 the low pressure in the hole causes ingestion of the crossflow into the hole greater than that caused by the ingestion vortex in the PS hole. The ingested crossflow hits the metal

inside the hole on the downstream side of the diffuser and then becomes entrained in a large recirculation region inside the diffuser. The effect of the ingestion is heating of the metal as shown in Figure 16. Contours of  $\theta > 0.8$  extend a distance of almost 1D down into the hole, and contours of  $\theta > 0.5$  extend almost to the end of the hole metering section. As a result of the ingestion, a majority of the coolant is significantly warmed before exiting the film hole, thus lowering  $\eta$  in the near field. In addition, a hot streak is present downstream of the region of ingestion since no coolant is exiting the hole and only crossflow is present at that location, as shown in Figure 17. A large lateral temperature gradient is also present between the hot streak and the coolant exiting from the adjacent hole on the right. The effects of crossflow ingestion may be significant but unfortunately cannot be fully evaluated without performing a conjugate conduction analysis.

Figure 18 is a plot of  $\bar{\eta}$  vs.  $x/X_{ss}$  for the three M's. The dips in the curves at  $x/X_{ss}=0.7$  are the result of the weak shock between the suction surface and the pressure side tailboard. The curves increase as M increases, except in the immediate near field where  $\bar{\eta}$  is lower at M=2.0 because of the ingestion. The ingestion at M=2.0 cannot be detected simply by looking at the curves. Only once the flow at the hole was examined could the lower  $\bar{\eta}$  in the near field be attributed to ingestion.

## 5. CONCLUSIONS

This four-part paper describes a joint experimental and computational effort to analyze film-cooling performance of several complex film-hole geometries on a modern turbine airfoil, and to document the underlying physics responsible for that performance. The study models realistic engine conditions, including Reynolds and Mach numbers typical of those found in actual turbines. Validation quality experimental results have been obtained using a single passage cascade (SPC) model that reproduces the geometry and flow features of a highly loaded turbine cascade. A foreign gas sampling technique provides laterally-averaged adiabatic effectiveness data with uncertainty less than 10% at all downstream locations. The computational methodology as outlined is intended to minimize geometry and grid-based errors and place the simulations against the limits of a commonly used eddy-viscosity turbulence model, RNG, with a two-layer near-wall treatment.

This study highlights the manner in which experiments and CFD augment one another. The experimental results serve to anchor and validate the computations, while the CFD results provide detailed insight into complex physical mechanisms and aid in understanding the measurements.

Conclusions specific to the current part include the following:

- Computational results match experimental trends for all cases. Additionally, the results show the best overall quantitative agreement for the present configuration.
- The effectiveness of CASH film cooling is dominated by vorticity. Turbulence also plays an important role, but it is secondary to the vorticity.

- Hot crossflow ingestion can occur when the boundary layer inside the diffuser separates on the short side of the diffuser and a low pressure pocket forms near the hole exit plane. In the present cases, this occurs for suction surface injection for the case of  $M = 2$ .
- Less severe ingestion can be caused by the ingestion vortex, which is actually one leg of horseshoe vortices formed from the upstream blade boundary layer wrapping around jetting coolant.
- Both the experiments and computations indicate that coolant blow off does not occur on either the SS or the PS for all of the blowing ratios considered. This is due to the fact that the film hole is effective in diffusing the coolant momentum and depositing the coolant jet close to the airfoil surface.
- Similar to the previous configurations discussed in parts II and III, the computations tend to overpredict the measurements as blowing ratio is increased. As discussed previously, this is likely due to the turbulence modeling used in the present study.

## REFERENCES

Leylek, J., and Zerkle, R., 1994, "Discrete-Jet Film Cooling: A Comparison of Computational Results with Experiments," Journal of Turbomachinery, Vol. 116, pp. 358-368.

McGrath, E. L., and Leylek, J., 1999, "Physics of Hot Crossflow Ingestion in Film Cooling," Journal of Turbomachinery, Vol. 121, pp. 1-10.

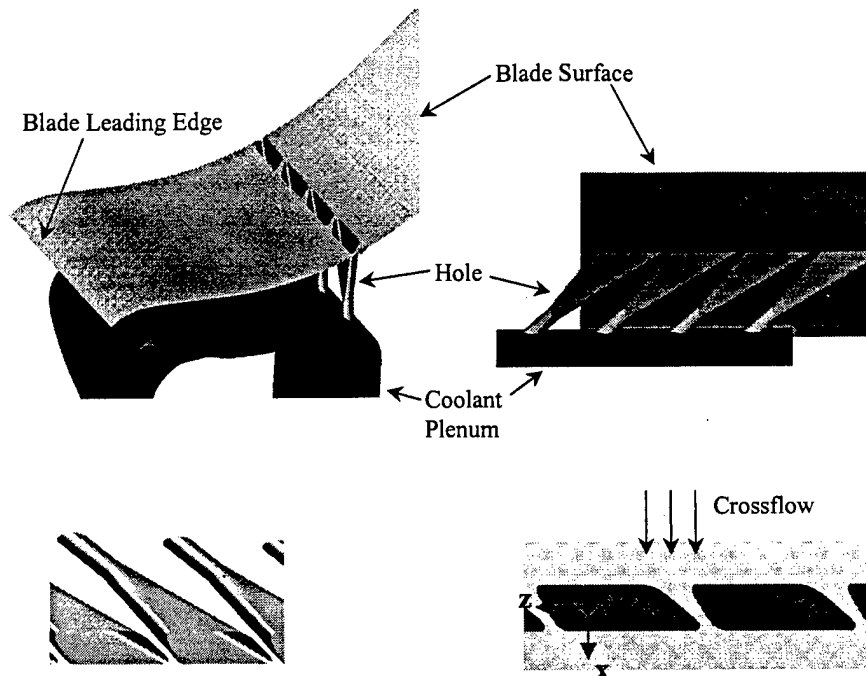


Figure 1. CASH film hole geometry on the blade PS.

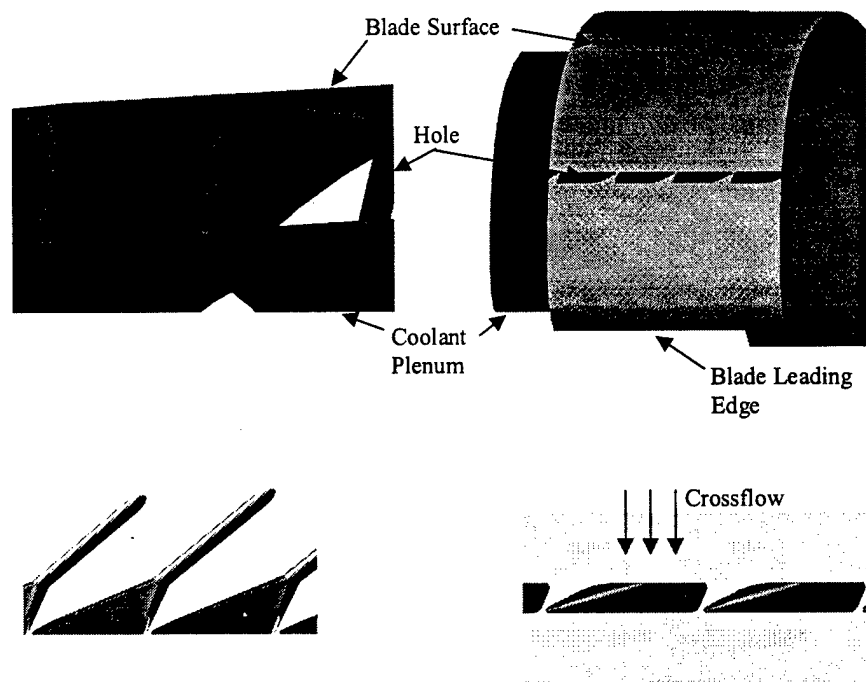


Figure 2. CASH film hole geometry on the blade SS.

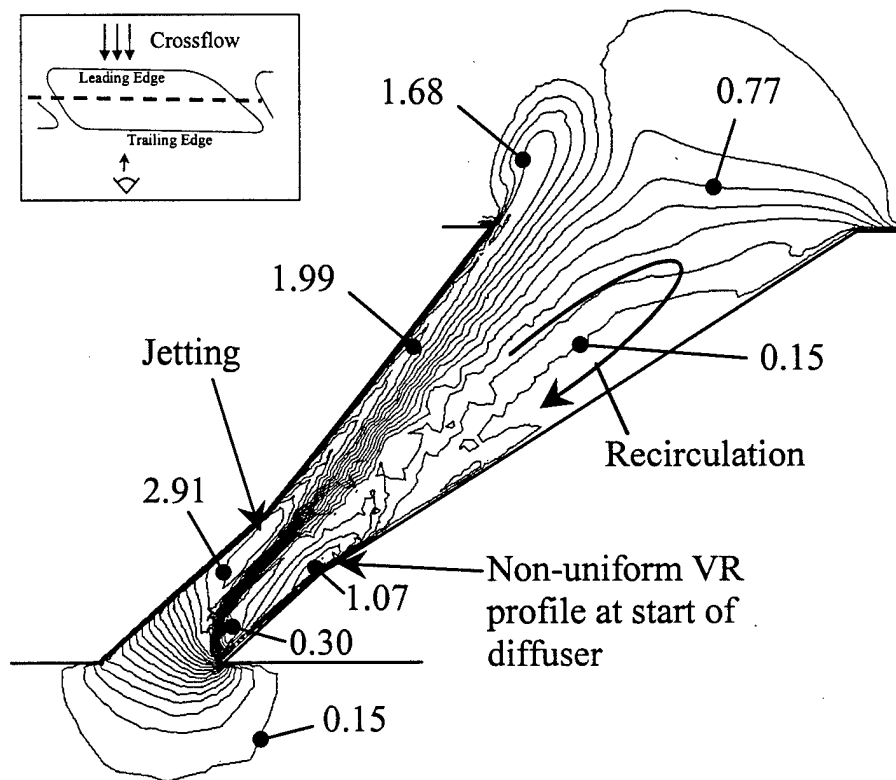


Figure 3. Contours of VR on lateral cross-section of PS hole when  $M=3.0$ .

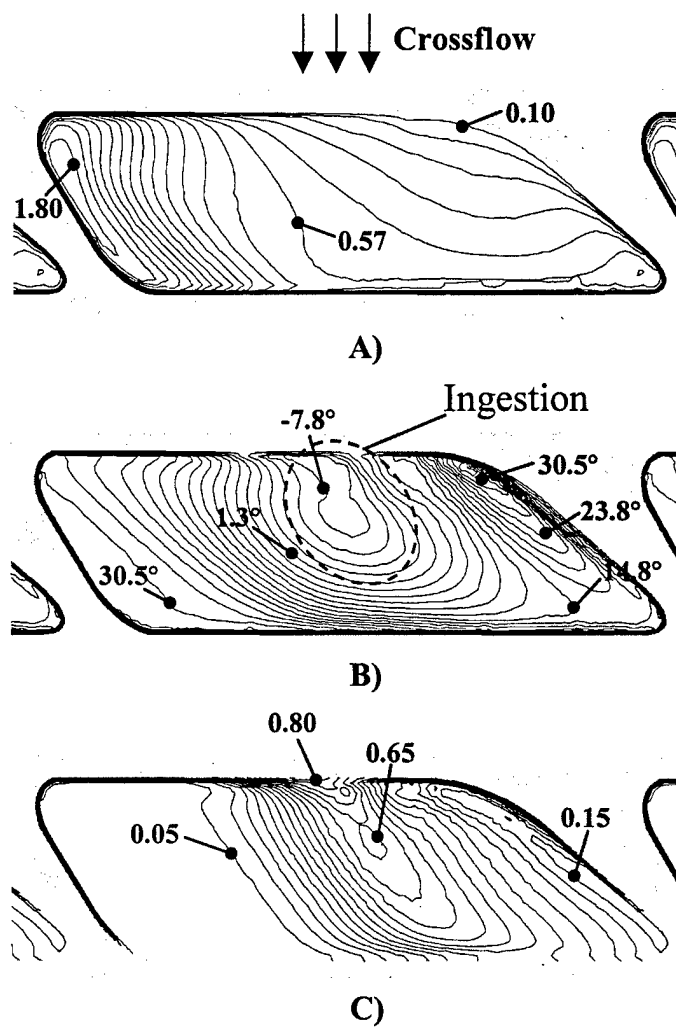


Figure 4. Contours of A) VR, B)  $\alpha$ , and C)  $\theta$  on PS FHEP for  $M=3$ .

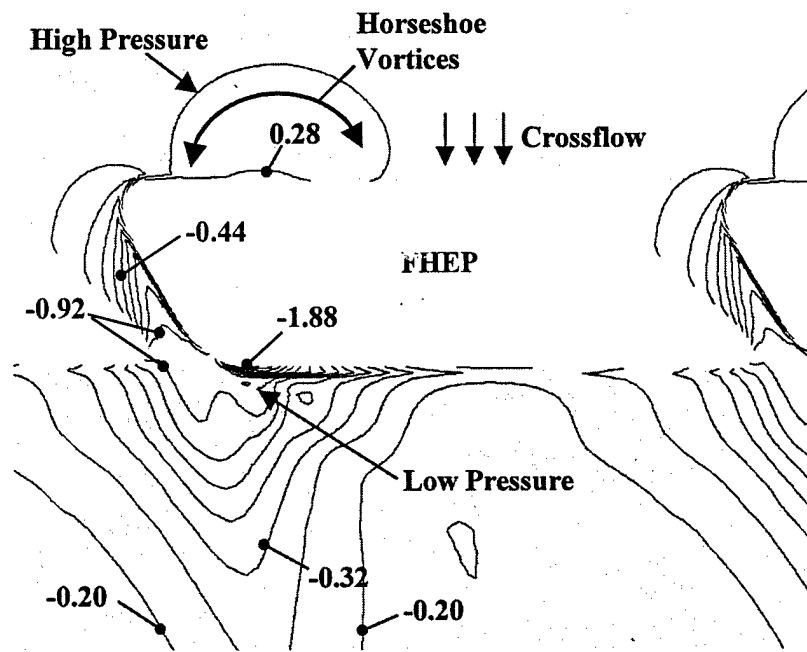


Figure 5. Contours of  $C_p$  on PS blade for  $M=3$ .

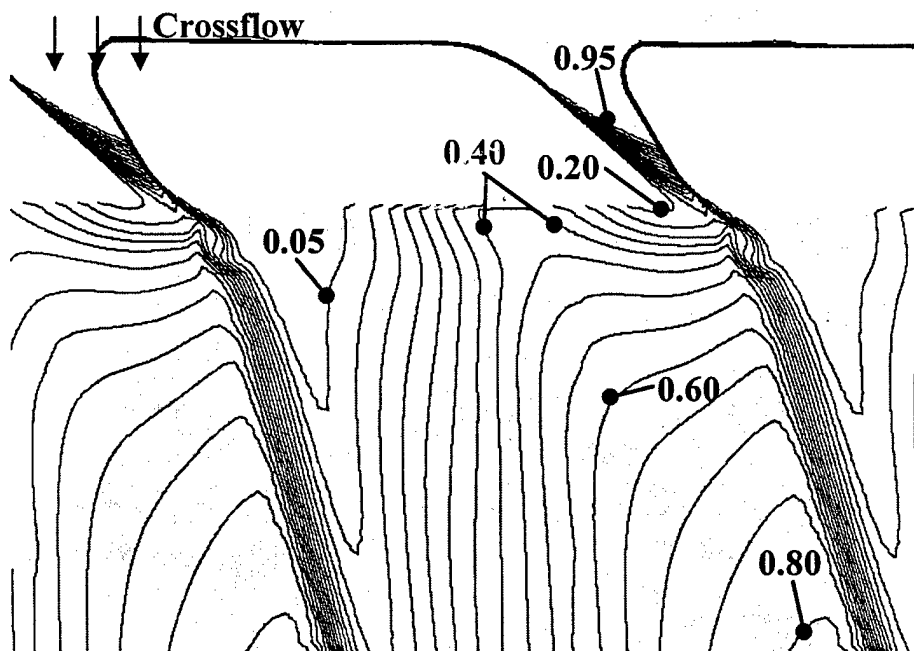


Figure 6. Contours of  $\theta$  on PS blade for  $M=3$  showing lateral gradients and inefficient coolant spreading.

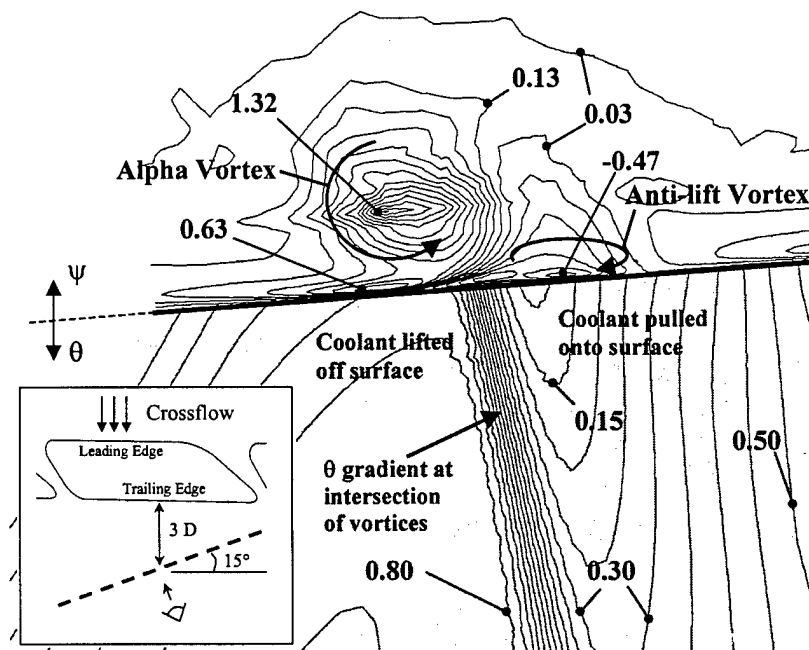


Figure 7. Contours of  $\theta$  on blade and  $\psi$  on crossflow plane at  $x/D=3.8$  show influence of vortices on blade  $\theta$  at  $M=3.0$ .



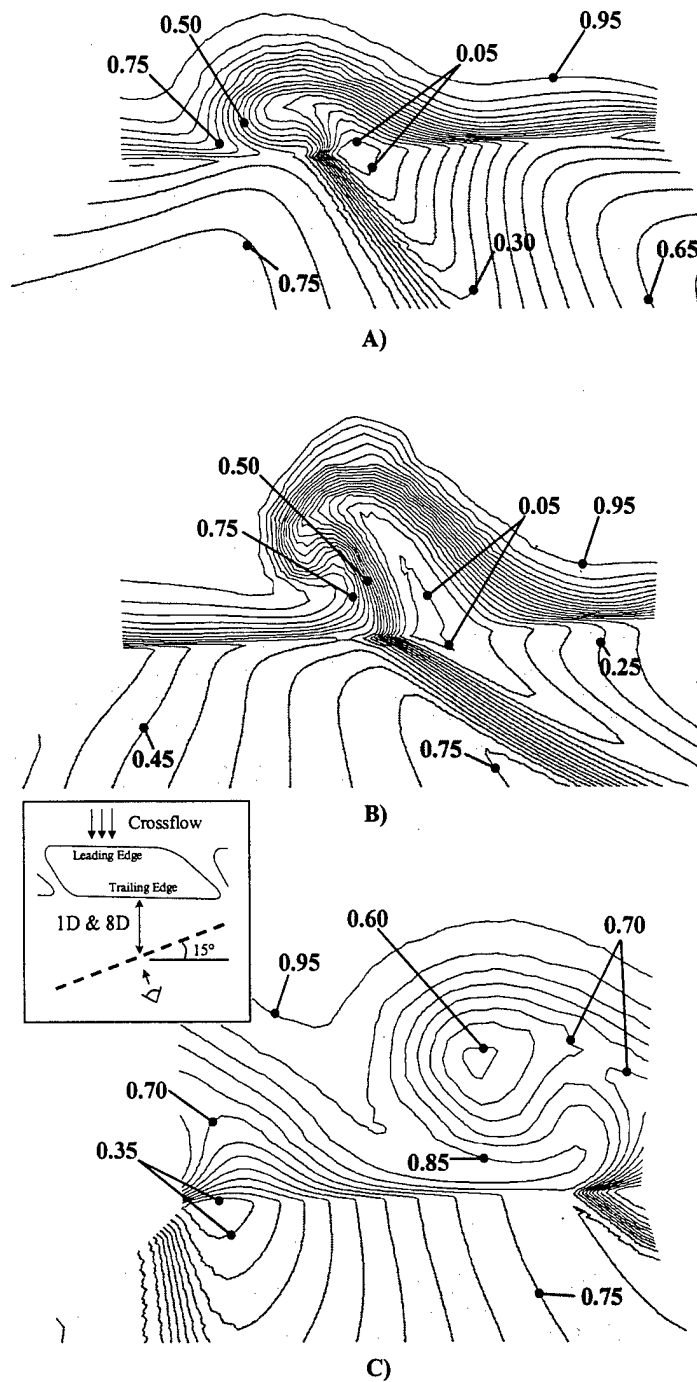


Figure 8. Contours of  $\theta$  on PS blade and crossflow plane angled at  $15^\circ$  at A)  $x/D=1$  for  $M=1.5$ , B)  $x/D=1$  for  $M=4.48$ , and C)  $x/D=8$  for  $M=4.48$ .

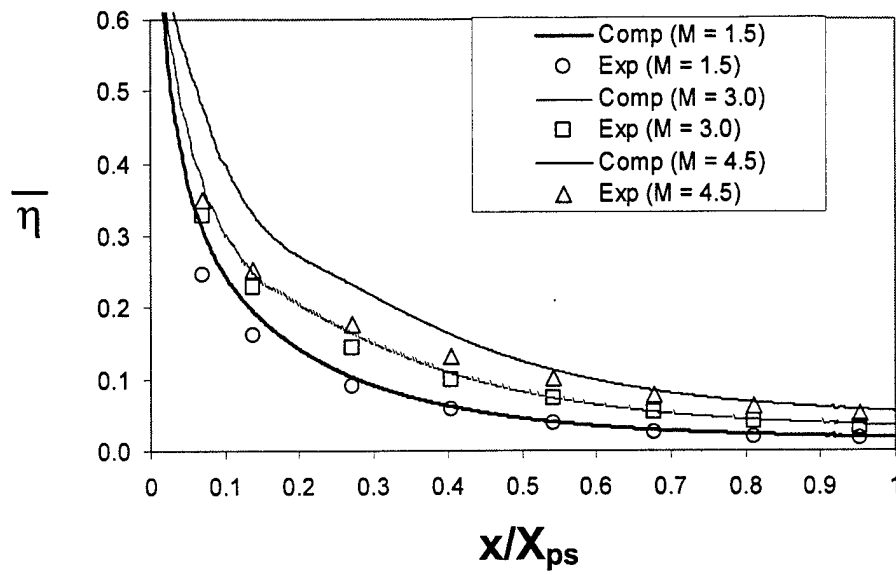


Figure 9. Variation of PS  $\bar{\eta}$  with M and comparison of computations versus experiments.

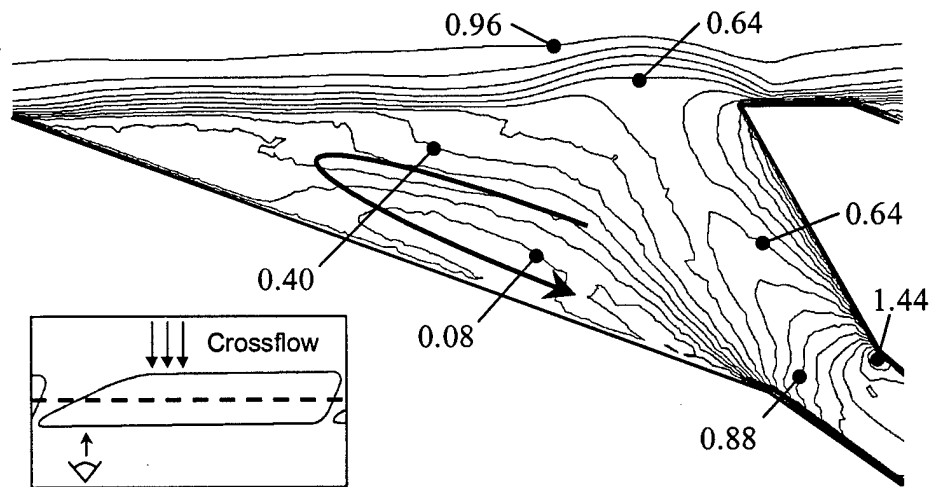


Figure 10. Contours of VR on a lateral cross-section of SS hole diffuser for  $M = 1.52$ .

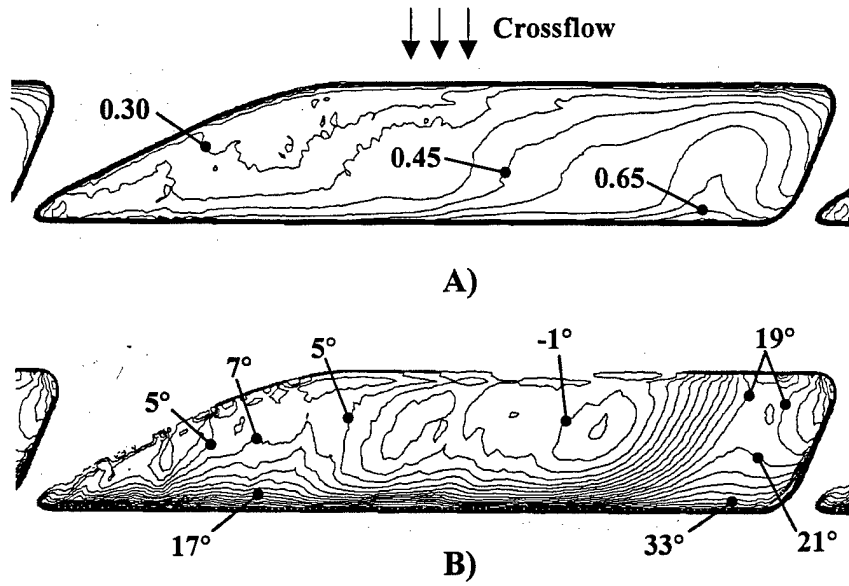


Figure 11. Contours of A) VR and B)  $\alpha$  at the SS FHEP showing coolant blockage by crossflow at  $M=1.52$ .

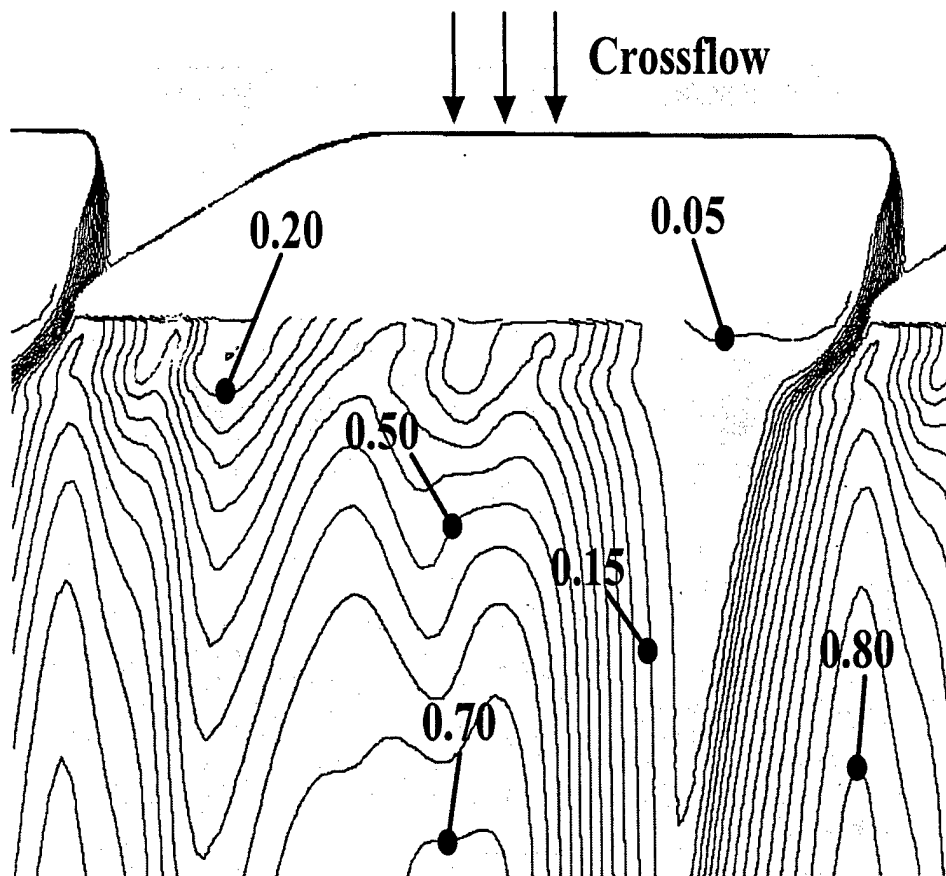


Figure 12. Contours of  $\theta$  on SS blade surface for  $M=1.52$ .

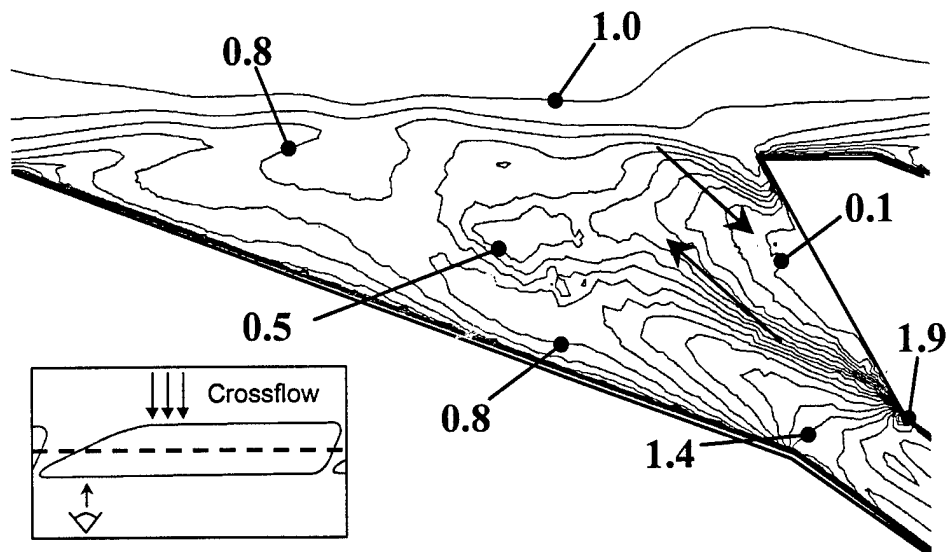


Figure 13. Contours of VR on lateral cross-section of SS hole diffuser at  $M=2.0$  showing coolant separation and resulting ingestion.

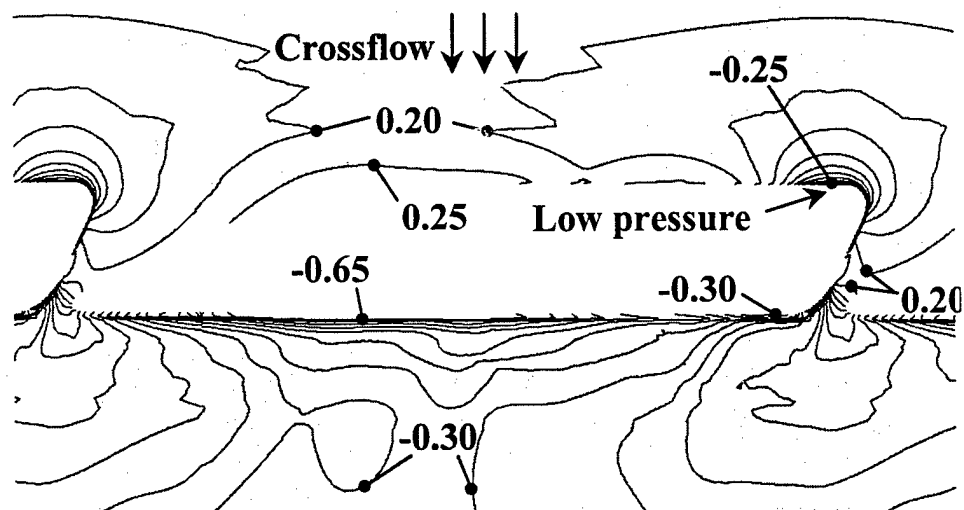


Figure 14. Contours of  $C_p$  on SS blade surface showing low pressure at region of ingestion for  $M=2.0$ .

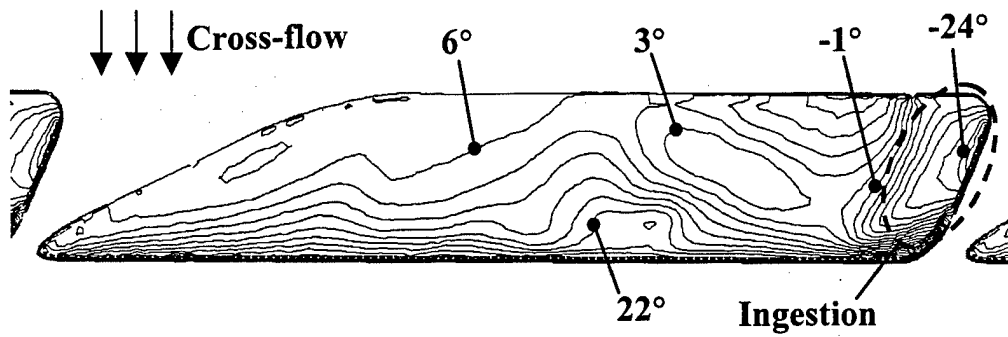


Figure 15. Contours of  $\alpha$  at SS FHEP for  $M=2.0$  showing ingestion of crossflow.

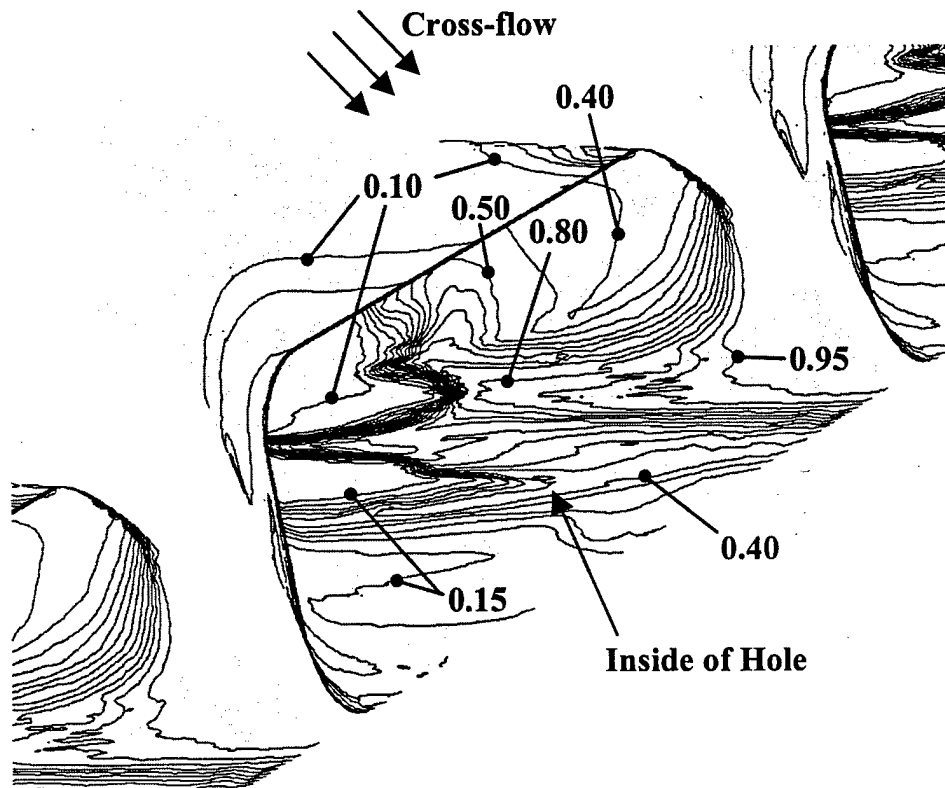


Figure 16. Isometric view of contours of  $\theta$  on wall inside SS film hole showing significant heating of the wall due to ingestion.

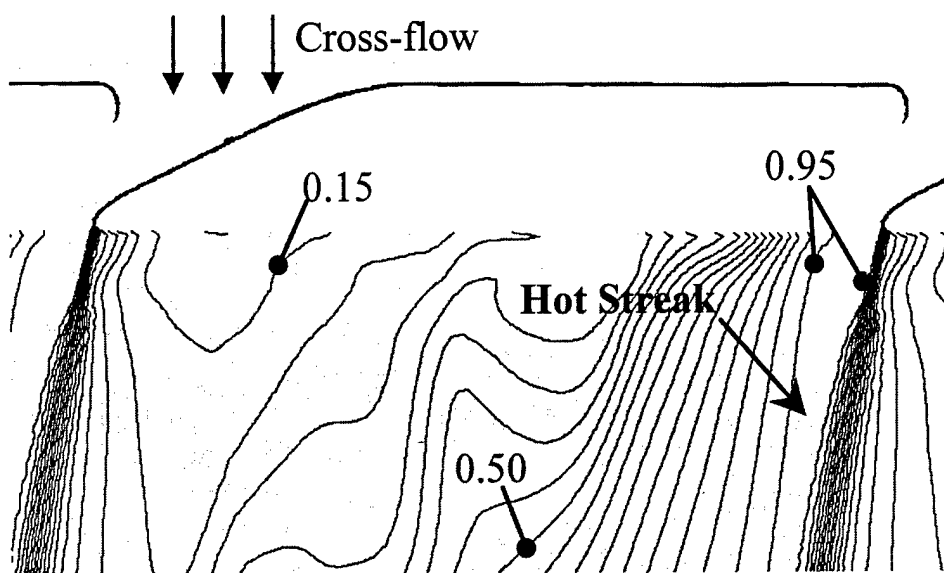


Figure 17. Contours of  $\theta$  on SS blade surface for  $M=2.0$ .

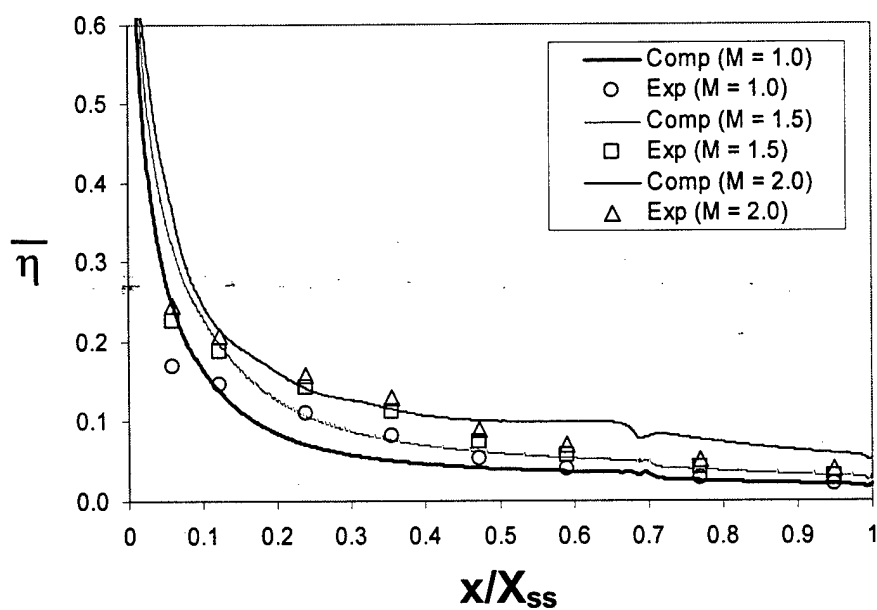


Figure 18. Variation of SS  $\eta$  with  $M$  and comparison of computations versus experiments.